



HAL
open science

Cryo-MMC - a Modular Multilevel Converter with Superconducting Coupled Arm Coils

Rafael Coelho Medeiros

► **To cite this version:**

Rafael Coelho Medeiros. Cryo-MMC - a Modular Multilevel Converter with Superconducting Coupled Arm Coils. Electric power. Université Paris-Saclay, 2022. English. NNT : 2022UPAST026 . tel-03883261

HAL Id: tel-03883261

<https://theses.hal.science/tel-03883261>

Submitted on 3 Dec 2022

HAL is a multi-disciplinary open access archive for the deposit and dissemination of scientific research documents, whether they are published or not. The documents may come from teaching and research institutions in France or abroad, or from public or private research centers.

L'archive ouverte pluridisciplinaire **HAL**, est destinée au dépôt et à la diffusion de documents scientifiques de niveau recherche, publiés ou non, émanant des établissements d'enseignement et de recherche français ou étrangers, des laboratoires publics ou privés.

Cryo-MMC : a Modular Multilevel Converter with Superconducting Coupled Arm Coils

*Cryo-MMC : un convertisseur modulaire
multiniveau avec des bobines de bras
supraconductrices couplées*

Thèse de doctorat de l'université Paris-Saclay

École doctorale n°575 : Electrical, optical, bio : physics and engineering
(EOBE)

Spécialité de doctorat : Génie électrique

Graduate School : Sciences de l'ingénierie et des systèmes

Référent : CentraleSupélec

Thèse préparée dans le Laboratoire de Génie Electrique et Electronique
de Paris, Université Paris-Saclay, CentraleSupélec, CNRS, sous la
direction de Jean-Claude Vannier, professeur des universités à
CentraleSupélec, le co-encadrement de Jing Dai, maître de conférences
à CentraleSupélec, Loïc Quéval, maître de conférences à
CentraleSupélec et du tuteur Philippe Egrot, ingénieur chercheur senior
à l'EDF R&D

Thèse soutenue à Paris-Saclay, le 24 mars 2022, par

Rafael Coelho-Medeiros

Composition du jury

Philippe Ladoux

Professeur des Universités, Université de Toulouse

Bertrand Raison

Professeur des Universités, Université Grenoble Alpes

Bruno Douine

Professeur des Universités, Université de Lorraine

François Costa

Professeur des Universités, Université Paris Est Créteil

Jean-Claude Vannier

Professeur des Universités, CentraleSupélec

Président

Rapporteur/Examineur

Rapporteur/Examineur

Examineur

Directeur de thèse

"Sometimes science is more art than science."
Rick Sanchez

Acknowledgements

Throughout the development of this thesis, I have received great support and assistance from countless people to whom I am deeply grateful.

I would like to express my gratitude to my supervisor, Prof. Jean-Claude Vannier, for his prompt assistance and support whenever needed. His actions were of the utmost importance to accomplishing this work.

I would like to express my gratitude to my co-supervisor, Dr. Jing Dai, for his guidance through scientific writing. I have significantly benefited from his wealth of knowledge and meticulous editing. I am highly grateful for all the time he consecrated revising all my work over these years.

I would like to express my gratitude to my co-supervisor, Dr. Loïc Quéval, for his guidance through the practical research. His plentiful experience and knowledge have lightened my path and taught me too many valuable skills. I am proud of and grateful for my time working with him.

I would like to express my gratitude to my tutor, Sr. Engr. Philippe Egrot, for offering me advice and encouragement throughout the years. I am privileged for been enlightened by his tremendous expertise. I am thankful for the extraordinary opportunities he provided for my professional and personal growth.

I would like to acknowledge all the members of the evaluation committee: Prof. Philippe Ladoux, Prof. Bertrand Raison, Prof. Bruno Douine, Prof. François Costa, and Dr. Florent Morel. Their suggestions were vital to the improvement of this manuscript.

I am thankful to all the highly skilled professionals I have worked with, too many to name. I acknowledge every precious moment among my colleagues from the M2A team at EDF. Thank you all for providing me with inspiration and valuable suggestions during this thesis. I am grateful to all my colleagues from the GeePs laboratory for every stimulating discussion and support they granted me.

I am thankful to every one of my friends who helped me to stay put through the toughest times: João Vitor, Vinícius, Guilherme, Mylena, Lívia, Marcio, Lucas, Frédéric, Julien, Emeric, Cedric, Rúbia, Paulo Ricardo, Natália and Juliana.

I am grateful for my family's unconditional and unequivocal loving support. I am thankful to my mother, Margaret, who tough me to pursue my dreams. I am thankful to my father, Marco, who tough me discipline. I am thankful to my brothers and sisters, Thiago, Thais, Fernando and Suélin for teaching me teamwork. I am thankful to my grandparents, Júlia, Marco, Maria, and Orlando and my godson, Jonas, for teaching me the treasured value of every moment spent together.

Contents

Acknowledgements	iii
Contents	v
List of Figures	ix
List of Tables	xiii
Acronyms	xv
Cryo-MMC : un convertisseur modulaire multiniveau avec des bobines de bras supraconductrices couplées	xvii
Introduction	1
Context	1
Objectives of the Thesis	1
Propositions	2
Thesis Content	2
Publications	3
I Review of HVDC Grids	5
I.1 Yesterday's HVDC Grids	5
I.1.1 Today's HVDC Grids	6
I.2 Tomorrow's HVDC grids	8
I.3 Focus on VSC-HVDC Systems	11
I.3.1 VSC Topologies	11
I.3.2 Protection	14
I.4 Reference case: a Point-to-Point MMC-HVDC Link	17
I.5 Summary	20
II Harmonic State-Space Modeling of the Modular Multi-level Converter	23
II.1 Review on the Modeling of the MMC	23
II.2 State-Space Representations of the MMC	25
II.2.1 Overview and Conventions	25
II.2.2 Half-bridge Submodule's Dynamics	26
II.2.3 Equivalent Submodule's Dynamics	27
II.2.4 Arm Dynamics	28
II.2.5 $UL-\Delta\Sigma$ Transformation	30

	II.2.6	External Dynamics	31
	II.2.7	Internal Dynamics	32
	II.2.8	State-Space Representation in abc Frame	34
	II.2.9	Harmonic State-Space Representation in abc Frame	35
II.3		Harmonic State-Space Models for the MMC	42
	II.3.1	Averaged-Arm HSS model	42
	II.3.2	Detailed-Arm HSS model	43
	II.3.3	Validation	44
II.4		Summary	45
III		Study of a Modular Multilevel Converter with Coupled Arm Coils	47
III.1		Review on the Arm Coil Sizing for the MMC	47
III.2		Steady-State Performance Indicators	49
	III.2.1	Capacitor Voltage Ripple	49
	III.2.2	Maximum and Minimum Arm Currents	50
	III.2.3	Weighted Total Harmonic Distortion of the AC-modulated Voltage	50
	III.2.4	Arm Coil Losses	51
	III.2.5	Conduction and Switching Losses of Solid-State Devices	52
III.3		Arm Inductance Sizing Using the HSS model	52
	III.3.1	Uncoupled Arm Coils	53
	III.3.2	Directly-Coupled Arm Coils	56
III.4		Steady-State Analysis	59
III.5		Transient Analysis	60
	III.5.1	Modeling	60
	III.5.2	Behavior during Normal Operation	61
	III.5.3	Behavior during a Pole-to-Pole Fault	66
III.6		Summary	68
IV		Study of a Modular Multilevel Converter with Coupled High Temperature Superconducting Arm Coils	71
IV.1		Design of coupled HTS arm coils	72
	IV.1.1	Requirements	72
	IV.1.2	Overview of the Coupled HTS Arm Coils	72
	IV.1.3	High-Temperature Superconducting Tapes	72
	IV.1.4	HTS pancake coil	76
	IV.1.5	HTS double pancake coil	77
	IV.1.6	HTS module	77
	IV.1.7	Coupled HTS Arm Coils	80
	IV.1.8	Refrigeration system	82
IV.2		Steady-State Analysis	86
IV.3		Transient Analysis	86
	IV.3.1	Modeling	86

	IV.3.2	Behavior during Normal Operation	90
	IV.3.3	Behavior during a Pole-to-Pole Fault	94
IV.4		Economical Assessment	96
	IV.4.1	Conventional Arm Coils	96
	IV.4.2	HTS Arm Coils	97
	IV.4.3	Cryo-MMC	98
IV.5		Summary	101
V		Laboratory-Scale Cryo-MMC Prototype	103
V.1		Prototype Specifications and Overview	103
	V.1.1	Arm Submodules	105
	V.1.2	Control Structure	106
	V.1.3	Uncoupled/Coupled HTS Arm Coils	106
V.2		Experimental Results	111
	V.2.1	Comparison Between Different Arm Coil Configurations	112
	V.2.2	Cryo-MMC Behavior During Normal Operation	113
V.3		Summary	115
		Conclusion	117
		Appendices	121
A		Linear Systems and Harmonic State Space	123
A.1		Mathematical Preliminaries	123
A.2		Linear Systems	124
	A.2.1	Linear Time-Variant System	125
	A.2.2	Linear Time-Invariant System	125
	A.2.3	Linear Time-Periodic System	125
A.3		Solution of Linear Systems	126
	A.3.1	Solution of LTV Systems	126
	A.3.2	Solution of LTI Systems	128
	A.3.3	Solution of LTP Systems	128
A.4		Transfer Function of Linear Systems	130
	A.4.1	Transfer function of LTI Systems	130
	A.4.2	Transfer Function of LTP Systems	133
B		Data for a 1 GW ± 320 kV Point-to-Point MMC-Based Link	147
C		Design of Dry-Type Air-Core Coils	151
C.1		Coil parameters	151
	C.1.1	Coil Inductance	151
	C.1.2	Single Coil Inductance	152
	C.1.3	Coupled Coils Inductance	153
	C.1.4	Coil Resistance	153

Contents

	C.1.5	Other parameters	153
C.2		Design	154
D		Losses Calculation for the Modular Multilevel Converter	157
D.1		Conduction Losses	158
D.2		Switching Losses	161
E		Grid-Following Control of the Modular Multilevel Converter	167
E.1		Low-Level Control	167
	E.1.1	Nearest-Level Modulation	168
	E.1.2	Voltage-Balancing Control	170
E.2		High-Level Control	172
	E.2.1	External Dynamics Control: Inner Control Loop	172
		Bibliography	181

List of Figures

I.1	Cumulative installed power of P2P HVDC links (data from [8]). Merc designates mercury-valve converters, Thyr designates LLC, IGBT designates VSC.	7
I.2	Ratings of today's P2P LCC-HVDC and VSC-HVDC links (data from [8]).	8
I.3	Number of P2P HVDC links per continent and per valve technology (data from [8]).	9
I.4	A vision of the future: integration of HV-MTDC grid with HVAC grids.	11
I.5	VSC topologies in commercial HVDC links.	13
I.6	AC-side modulated voltages for the 2L-VSC, 3L-NPC, 3L-ANPC, and the HB-MMC with 50 SMs per arm. We consider a modulation index amplitude of 0.8 with a frequency of fundamental frequency of 50 Hz, a constant DC voltage $u_{dc}(t) = U_{dc}$ and a switching frequency of 1 kHz for the 2L-VSC, 3L-NPC, and 3L-ANPC. The AC modulated voltage is represented in purple, and the fundamental voltage is represented in green. . .	15
I.7	HB-MMC after SMs blocking under a DC pole-to-pole fault. The arrows indicate the fault current direction.	16
I.8	Point-to-Point (P2P) scheme.	17
I.9	Typical Architecture and Electric Circuit of an MMC-HVDC Station.	18
I.10	Components of an MMC-HVDC station.	20
I.11	Breakdown of the capital cost, weight, and losses for the reference MMC. "SMs" includes the HB-SMs, the valve building, the cooling plant, and control.	20
II.1	Computation time per fundamental period $T_0 = 20$ ms for different models of the HB-MMC [62].	25
II.2	Overview and conventions for the grid connected HB-MMC. The AC grid is modeled by an ideal AC voltage source in series with resistance R_f and an inductance L_f	26
II.3	Half-bridge submodule. The indices u and l stand for the upper and lower arms, respectively. The index p denotes a generic phase.	27
II.4	Coupled coils between the upper and lower arms of the same phase.	29
II.5	Upper- and lower-arm switching function for the DA-HSS model represented in green and purple, respectively.	44

List of Figures

II.6	AA model (solid line), AA-HSS model (dashed line), DA-HHS (dotted line) steady-state waveforms for the MMC at the nominal operation point.	45
III.1	Operation set-point for the MMC with uncoupled arm coils. . .	54
III.2	Evolution of the performance indicators for the MMC with uncoupled arm coils.	55
III.3	Operation set-point for the MMC with directly-coupled arm coils.	56
III.4	Evolution of the performance indicators of the MMC with directly-coupled arm coils.	58
III.5	Mock-up of the coupled air-core arm coils.	59
III.6	P2P HVDC link circuit.	60
III.7	Arm model with blocking capacity.	61
III.8	Simulation results for the start-up sequence from 0 s to 4.5 s. Dotted lines represent the MCC #0, dashed lines represent the MMC #1 and solid lines represent the MMC #2.	62
III.9	Simulation results for the nominal power transfer from 4.5 s to 9 s. Dotted lines represent the MCC #0, dashed lines represent the MMC #1 and solid lines represent the MMC #2.	65
III.10	Simulation results for the pole-to-pole fault from 9 s to 13.5 s. Dotted lines represent the MCC #0, dashed lines represent the MMC #1 and solid lines represent the MMC #2.	67
IV.1	Overview of a coupled HTS arm coil system.	72
IV.2	Commercial HTS tapes structure (not to scale).	73
IV.3	I-V characteristic of the Amperium Type 8502-350 YBCO tape.	74
IV.4	Amperium Type 8502-350 YBCO tape critical current.	75
IV.5	HTS pancake.	76
IV.6	HTS module.	78
IV.7	HTS Module magnetic flux density distribution for a current equal to the critical current in both DPC. The component parallel to the tape surface is B_z . The one perpendicular to it is B_r . . .	79
IV.8	2-D I-V characteristic of each DPC of one HTS module.	80
IV.9	HTS modules layout.	82
IV.10	Mock-up of the coupled HTS arm coils.	82
IV.11	Overview of the coupled HTS coils system.	83
IV.12	PTC cooling performances.	83
IV.13	Lumped-parameter electric circuit of the coupled HTS arm coils.	87
IV.14	Lumped-parameter thermal circuit of one HTS module.	88
IV.15	Liquid Nitrogen convective heat transfer coefficient at atmospheric pressure. Data from [95].	90
IV.16	Simulation results for the start-up sequence from 0 s to 4.5 s. Dashed lines represent the response of MMC #0 and solid lines represent the response of MMC #4	91

IV.17	Simulation results for the nominal power transfer from 4.5 s to 9 s. Dashed lines represent the response of MMC #0 and solid lines represent the response of MMC #4	93
IV.18	Simulation results for the pole-to-pole fault from 9 s to 13.5 s. Dashed lines represent the response of MMC #0 and solid lines represent the response of MMC #4.	95
IV.19	HTS coils thermal behavior.	96
IV.20	Yearly cost evolution for the MMC with different arm coil configurations.	100
V.1	Cryo-MMC prototype.	104
V.2	Cryo-MMC prototype HB-SMs assembly.	105
V.3	Cryo-MMC prototype control structure.	106
V.4	Measured I-V characteristic of the HT-CA BSCCO tape.	107
V.5	HTS pancake coil.	108
V.6	Winding of an HTS pancake coil.	109
V.7	HTS Coils #1u and #1l I-V Measurement.	110
V.8	Δ -modulation index sequence.	111
V.9	Measurements for different arm coil configurations.	112
V.10	Measurements for the MMC #2e.	114
C.1	Dry-type air-core coils.	151
C.2	Dry-type air-core aluminium coil inductance, resistance, mass and volume as a function of N_v for the parameters listed in Table C.1.	155
D.1	Converter for the i -th SM in the upper and lower arm of phase p	157
D.2	Typical transistor's on-state collector-emitter voltage and diode's on-state forward voltage for an IGBT module with a rated collector-emitter voltage $V_{CE} = 4.5$ kV and a rated collector current $I_C = 3$ kA.	159
D.3	Typical transistor switching energies for an IGBT module with a rated collector-emitter voltage $V_{CE} = 4.5$ kV and a rated collector current $I_C = 3$ kA.	164
E.1	Typical control structure for the MMC in grid-following operation.	167
E.2	Low-level control structure for the MMC.	168
E.3	Nearest-level modulation scheme.	168
E.4	Voltage balancing control scheme.	170
E.5	Controlled-switching-frequency voltage balancing algorithm flowchart.	171
E.6	Individual and total SM capacitor's voltages using the CSF-VBA. Simulation for the thesis's study case with $N = 50$ and $C = 3.3$ mF for $P = 1$ GW and $Q = 300$ MVar.	172

List of Figures

E.7	High-level control structure for the MMC in grid-following operation.	173
E.8	Inner dq - Δ -current control.	175
E.9	Active and reactive power control structures.	176
E.10	DC-voltage control structure.	177
E.11	Open-loop bode diagrams of the proposed control structures considering $F_{SM} = 150$ Hz.	180

List of Tables

I.1	Comparison of LCC-HVDC and VSC-HVDC technologies. Source: [18].	9
I.2	Parameters of the reference MMC system.	17
III.1	Dry-type air-core arm coils specifications. Mass and conductor length, computed in Appendix C, are given for a set of 2 coils. .	58
III.2	MMCs #0, #1 and #2 performance indicators evaluated for $P = P_{nom}$ and $Q = Q_{nom}$	59
IV.1	Parameters for the Amperium Type 8502-350 YBCO tape. "Substrate" designates the buffer and substrate layers together. .	74
IV.2	Parameters of the Amperium Type 8502-350 YBCO tape fitted from data provided in [84].	76
IV.3	HTS pancake coil specifications.	77
IV.4	HTS module specifications.	78
IV.5	Coupled HTS arm coils specifications. Data are given for a set of 2 coils. RT denotes the room temperature. The mass includes the weight of HTS modules and of the cryostat full of LN2. . . .	81
IV.6	Cryocooler specifications. Cooling power given for a water cooled configuration with 15°C water temperature at the heat rejecter.	84
IV.7	Circulating pump specifications.	85
IV.8	LN2 Buffer Tank Specifications.	85
IV.9	MMCs #0, #3 and #4 Performance indicators evaluated for $P = P_{nom}$ and $Q = Q_{nom}$	86
IV.10	Thermal circuit parameters for the HTS module.	89
IV.11	Refrigeration system sizing.	97
IV.12	Coil's capital cost.	98
IV.13	MMC capital cost for different arm coil configurations.	98
IV.14	MMC energy loss for different arm coil configurations.	99
IV.15	Coupled HTS arm coils mass and footprint, including the refrigeration system.	101
V.1	Cryo-MMC prototype specifications.	105
V.2	Parameters for the HT-CA BSCCO tape. This tape has a copper reinforcement layer.	107
V.3	HTS pancake coil specifications.	108
V.4	Measured HTS pancake coil parameters.	109
V.5	Measured HTS coil parameters. RT stands for room temperature.	111
V.6	Measurements for $M_{\Delta} = 0.95$ and $\theta_{\Delta} = 0$	113

List of Tables

B.1	Modular multilevel converter parameters.	147
B.2	AC-grid parameters [49, p. 177].	148
B.3	Transformer parameters [49, p. 181].	148
B.4	DC cable parameters [49, p. 78].	149
C.1	Parameters for the dry-type air-core aluminium coil.	155
E.1	Controller's parameters for the MMCs #0, #1, #2 and #4.	179

Acronyms

2L-VSC Two-Level Voltage Source Converter.

3L-ANPC Three-Level Active Neutral Point Clamp Converter.

3L-NPC Three-Level Neutral Point Clamp Converter.

AA Averaged-Arm.

AA-HSS Averaged-Arm Harmonic State Space.

AC Alternative Current.

DA Detailed-Arm.

DA-HSS Detailed-Arm Harmonic State Space.

DC Direct Current.

DPC Double Pancake Coil.

EMTI Exponentially Modulated Time Invariant.

EMTP Exponentially Modulated Time Periodic.

HB-SM Half-Bridge Submodule.

HSS Harmonic State Space.

HTS High-Temperature Superconductor.

HV High Voltage.

HVAC High Voltage Alternative Current.

HVDC High Voltage Direct Current.

IGBT Insulated-Gate Bipolar Transistor.

KCL Kirchhoff's Current Law.

KVL Kirchhoff's Voltage Law.

LCC Line-Commutated Converter.

LN2 Liquid Nitrogen.

LTI Linear Time Invariant.

LTP Linear Time Periodic.

LTV Linear Time Variant.

MMC Modular Multilevel Converter.

NLM Nearest-Level Modulation.

P2P Point-to-Point.

PC Pancake Coils.

PI Performance Indicator.

PTC Pulse Tube Cryocooler.

ScFCL Superconducting Fault-Current Limiter.

SM Submodule.

SSTI State-Space Time Invariant.

THD Total Harmonic Distortion.

VBA Voltage Balancing Algorithm.

VSC Voltage-Source Converters.

WTHD Weighted Total Harmonic Distortion.

Cryo-MMC : un convertisseur modulaire multiniveau avec des bobines de bras supraconductrices couplées

Introduction

Dans cette thèse, nous visons à améliorer la conception du convertisseur modulaire multiniveau (MMC) pour les applications de transport en courant continu et haute tension (HVDC) afin de fournir une alternative robuste pour la gestion de défauts aux systèmes MMC-HVDC. Nous concentrons nos efforts sur la conception des bobines de bras puisqu'elles représentent une partie non négligeable du coût, des pertes et de la masse d'un MMC. Nos objectifs sont les suivants :

- (i) Réduire la taille et la masse des bobines de bras, diminuant ainsi l'encombrement de la station MMC-HVDC. Ce point est particulièrement important dans les applications embarquées en mer ;
- (ii) Réduire les pertes des bobines de bras, augmentant ainsi l'efficacité de la station MMC-HVDC;
- (iii) Fournir une fonction de limitation du courant de défaut DC au MMC. En limitant les courants de défaut, les contraintes sur le convertisseur et sur tous les équipements associés de la station MMC-HVDC seront réduites. Cela pourrait également simplifier la conception des disjoncteurs DC.

Afin de répondre aux objectifs de ces travaux, nous proposons deux étapes :

- Premièrement, nous proposons de coupler magnétiquement les bobines de bras du MMC. Nous estimons qu'un couplage direct nous permettra de réduire la taille et la masse des bobines de bras (objectif (i)).
- Deuxièmement, nous proposons de remplacer les bobines de bras conventionnelles à noyau d'air par des bobines de bras supraconductrices à haute température (HTS). Cela devrait nous permettre de réduire les pertes de conversion (objectif (ii)) tout en assurant la fonction de limitation du courant de défaut (objectif (iii)) en se comportant comme un limiteur de courant de défaut supraconducteur.

Chapitre I. Les Réseaux HVDC

Le transport d'électricité en courant continu et haute tension (HVDC) apparait en 1954 en tant qu'une alternative pour les systèmes en haute tension courant alternatif (HVAC) dans certaines applications, tels les liens par câble en souterrain ou sous-marin et cela grâce à l'absence de l'effet capacitif en courant continu. Depuis, le HVDC a été utilisé sur d'autres applications où il s'avère avantageux, comme par exemple : pour la connexion de réseaux asynchrones, pour de liaisons aériennes sur de longues distances transportant de grandes puissances, pour des liaisons sous-marines comme dans l'éolien en mer, entre autres.

Trois technologies de convertisseurs ont été historiquement déployées dans de liaisons HVDC : les redresseurs à vapeur de mercure, basés sur les diodes à vapeur de mercure, parus en 1954, les convertisseurs commutés par la ligne (LCC), basés sur les thyristors, parus en 1970 et les convertisseurs source de tension (VSC), basés sur les transistors bipolaires à grille isolée, parus en 1999. Parmi ces trois technologies, le LCC et le VSC coexistent à nos jours. Les LCCs sont majoritairement utilisées dans de liaisons en dessus les 2000 MW et notamment dans des liaisons aériennes sur de très longues distances. Le plus grand nombre de liens LCC-HVDC se retrouvent en Asie grâce à un déploiement massif de cette technologie depuis 2010. Cela s'explique par l'aptitude de cette technologie à transporter de l'énergie sur de longues distances, comme par exemple depuis le centre de production du nord-ouest de la Chine jusqu'aux centres de consommation du sud-est. Les VSCs sont majoritairement utilisées dans de liaisons en dessous les 2000 MW et notamment dans des liens souterrains ou sous-marins. Le plus grand nombre de liaisons VSC-HVDC se retrouvent en Europe et sont utilisées pour le transport d'énergie par des câbles souterrains comme la liaison INELFE, pour les câbles sous-marins utilisés pour connecter des réseaux insulaires comme le projet COMETA et pour connecter des centrales éoliennes en mer du nord comme la liaison DolWin3.

Dans l'avenir, un réseau multi-terminaux HVDC (MT-HVDC) pourrait compléter les infrastructures actuelles en HVAC, ce qui permettrait notamment une connexion efficace de sites européen avec grande potentialité de production d'énergie renouvelable, notamment localisés en mer du nord pour l'éolien et en méditerranée pour le solaire photovoltaïque, aux grands centres de consommation. Actuellement, les VSCs sont aperçus comme les meilleurs candidats au déploiement de réseaux HVDC, étant donné qu'ils sont plus adaptés à une connexion parallèle en DC. Contrairement aux LCCs, les VSCs n'inversent jamais leur polarité de tension mais seulement la direction de leur courant en fonction de la direction du flux du puissance ce qui lui rend plus adapté aux topologies de réseaux HVDC envisagées.

Dans cette thèse, nous nous concentrons dans les VSCs et plus particulièrement dans le convertisseur modulaire multiniveau avec de sous-modules (SMs) en demi-pont (HB-SM) qui est l'état de l'art industriel dans le VSC-HVDC. Ce convertisseur, qui a été proposé en 2001, a été mis en service dans une première

réalisation industrielle en 2010 dans le San Francisco trans bay project, une liaison DC sous-marine de 86 km reliant San Francisco à Pittsburg, dimensionnée pour une tension de 200 kV et une puissance de 400 MW.

En comparaison à la première génération de convertisseurs VSC pour le HVDC, notamment des VSCs à 2 et 3 niveaux de tension, le MMC présente certains avantages tels :

- Sa modularité : Un MMC est composé par une association série de plusieurs sous-modules qui sont composés par l'association d'un circuit électronique de puissance à de condensateurs. Cela offre une modularité qui est industriellement intéressante puis que tous les sous-modules sont fabriqués de la même façon et le convertisseur peut être adapté pour tout niveaux de tension DC en fonction du nombre de SMs.
- Sa tension modulée : un MMC à l'échelle industrielle en HVDC est composé d'une centaine de SMs en demi-point qui offrent chacun un niveau de tension. Avec plusieurs niveaux de tensions, une tension modulée presque sinusoïdale est générée même en gardant une fréquence de commutation de 150-300 Hz par SM. Par conséquent, le MMC génère moins de pertes de commutation comparées aux VSCs à 2 et 3 niveaux.
- Sa robustesse : avec un bon agencement du nombre de SMs, le convertisseur peut perdre une certaine quantité de SMs sans préjudice à son fonctionnement. Typiquement, les SMs défectueux sont contournés par un interrupteur mécanique et échangés lors d'une maintenance annuelle.

Un verrou industriel qui doit être encore levé concerne la gestion des défauts dans une liaison HVDC basées sur des HB-MMCs. Un HB-MMC n'est pas capable de contrôler un défaut DC et une fois le convertisseur bloqué, le réseau AC alimente directement le défaut DC à travers les diodes des HB-SMs. Ceci est notamment critique dans un schéma MTDC où un défaut avec une durée plus longue que 10 ms peut entraîner l'effondrement de la tension DC et par conséquent la perte du transport de puissance. Le développement des liaisons MTDC est donc dépendant du développement des technologies capables d'interrompre le courant continu de défaut DC dans moins de 10 ms.

Chapitre II. Modélisation du convertisseur modulaire multiniveau basé sur la représentation d'espace d'état harmonique

Ce chapitre est consacré au développement d'un modèle adapté à la conception du HB-MMC. Ce modèle, que nous avons baptisé le DA-HSS, est capable d'estimer les variables du convertisseur en régime permanent avec un temps de calcul réduit et une faible erreur par rapport aux approches classiques. Le

DA-HSS est basée sur la représentation d'espace d'état harmonique (HSS) des équations différentielles modélisant le comportement dynamique du HB-MMC. L'originalité du DA-HSS est de prendre en compte les harmoniques générées par toute technique de modulation.

Afin d'obtenir le DA-HSS, Nous développons les équations du HB-MMC triphasé dans le domaine temporel et sa respective représentation en espace d'état, ensuite, nous obtenons la représentation HSS du HB-MMC triphasé en suivant la procédure décrite dans l'appendice A. Le modèle DA-HSS a été validé en comparaison à un modèle circuit électrique pour le cas de référence de cette thèse : un HB-MMC dimensionnée pour une liaison point-à-point à 1 GW et ± 320 kV définie dans l'appendice B.

Chapitre III. Etude d'un convertisseur modulaire multiniveau avec des bobines de bras couplées

Ce chapitre aborde le dimensionnement des bobines de bras du MMC. Plus précisément, nous utilisons le modèle DA-HSS pour sélectionner la valeur de l'inductance de bras du HB-MMC. Cette sélection est réalisée en fonction de plusieurs indicateurs de performance en régime établi qui ont été définis : l'ondulation de la tension des condensateurs des SMs, les courants de bras maximales et minimales, le taux de distorsion harmonique pondéré de la tension modulée, les pertes dans les bobines de bras et les pertes de conduction et commutation dans les composants actifs de SMs.

Nous concluons qu'un MMC avec des bobines de bras en couplage direct peut être conçu avec différents objectifs par rapport au MMC de référence : conserver une taille similaire tout en améliorant les performances en régime permanent ou réduire la taille tout en conservant les mêmes performances en régime permanent. Néanmoins, les performances en cas de défaillance peuvent se détériorer. Par exemple :

- Un HB-MMC avec des bobines de bras directement couplées ayant $L = 50,9$ mH et $K_{u,l} = 0,6517$ a la même masse et une taille similaire aux bobines du MMC de référence. La masse de ces deux bobines de bras couplées est de 85 t, et leur volume est de $171,2$ m³ (réduction de 22,5%). Ce MMC a des performances améliorées en régime permanent. En particulier, les pertes de conversion sont réduites de 12,56%. De plus, le courant DC de défaut est réduit de 37%.
- Un HB-MMC avec des bobines de bras directement couplées ayant $L = 27,3$ mH et $K_{u,l} = 0,6740$ a des bobines de bras plus petites que le bobines du MMC de référence. La masse de ces deux bobines de bras couplées est de 48 t (réduction de 43,6%), et leur volume est de $122,15$ m³ (réduction de 44,7%). Ce MMC a des performances similaires

au MMC de référence en régime permanent, néanmoins le courant DC de défaut augmente de 6%.

Chapitre IV. Etude d'un convertisseur modulaire multiniveau avec des bobines de bras supraconductrices couplées

Ce chapitre développe une étude techno-économique d'un cryo-MMC dimensionnée pour un lien point-à-point de 1 GW et ± 320 kV. Ce convertisseur est un MMC avec 400 HB-SMs et des bobines de bras supraconductrices à haute température directement couplées. Cette intégration devrait nous permettre de réduire les pertes des bobines de bras (objectif (ii)) tout en assurant la fonction de limitation du courant de défaut (objectif (iii)) en se comportant comme un limiteur de courant de défaut supraconducteur.

Les bobines de bras supraconductrices couplées et leur circuit de refroidissement cryogénique sont dimensionnés pour deux températures d'opération, l'une à 77 K et l'autre à 65 K. On évalue les performances des cryo-MMC avec ces bobines en régime établi et transitoire ainsi qu'en termes de coût d'investissement et opération. Cette analyse a abouti aux résultats suivants :

- Un HB-MMC avec des bobines de bras HTS directement couplées avec $L = 28,3$ mH et $K_{u,l} = 0,8788$ opérées à 77 K a des bobines de bras plus petites que le MMC de référence. La masse de deux bobines de bras HTS couplées (y compris le système de refroidissement) est de 31.1 t (une réduction de 63.4%), et son volume est de 47 m³ (réduction de 78.6%). Ce MMC a des performances améliorées en régime permanent. En particulier, les pertes de conversion sont réduites de 12,5%. De plus, le courant DC de défaut est réduit de 80%. Le coût d'investissement d'un tel convertisseur est estimé à 118,77 millions d'euros (soit une augmentation de 8 %) et son coût sur cycle de vie à 40 ans s'est élevé à 189,3 millions d'euros (soit une augmentation de 0.8%).
- Un HB-MMC avec des bobines HTS de bras directement couplées avec $L = 27,7$ mH et $K_{u,l} = 0,8788$ opérées à 65 K a des bobines de bras plus petites que le MMC de référence. Le poids des bobines de bras HTS couplées (y compris leur système de refroidissement) est de 20,6 t (réduction de 75,8%), et son volume est de $40,7$ m³ (réduction de 82%). Un tel MMC a des performances améliorées en régime permanent. En particulier, les pertes de conversion sont réduites de 7,7%. Le courant DC de défaut est réduit de 80%. Le coût d'investissement d'un tel convertisseur est estimé à 111 M€ (soit une augmentation de 0.95%) et son coût sur cycle de vie à 40 ans s'est élevé à 172,7 millions d'euros (soit une réduction de 7,9%).

Nous rappelons au lecteur que l'analyse technico-économique repose sur de nombreuses hypothèses et dépend fortement des données relatives aux coûts.

Les valeurs relatives sont probablement plus fiables que les valeurs absolues. Les résultats doivent donc être interprétés avec prudence. Dans ce sens, il semble qu'un cryo-MMC fonctionnant à 65 K soit compétitive par rapport à au MMC de référence.

Chapitre V. Le prototype du Cryo-MMC

Ce chapitre décrit la conception, la construction et les tests du premier cryo-MMC au monde. Nous reportons le fonctionnement d'un prototype du cryo-MMC à l'échelle du laboratoire pendant le fonctionnement normal. Cela place le cryo-MMC dans un niveau de maturité technologique (TRL) de 3-4.

Tout d'abord, nous avons conçu, bobiné et testé 8 bobines inductives supraconductrices à haute température du type pancake (PC). Chaque PC est composée de 47 m de ruban HTS 1G et a une inductance de 1,2 mH. Les PCs sont connectées en série et empilées pour obtenir les bobines de bras HTS à couplage direct. Nous avons mesuré une inductance propre de $L = 4$ mH et un coefficient de couplage $K_{u,l} = 0.88$. Le courant critique mesuré à 77 K est de 120 A.

Deuxièmement, le HB-MMC avec des bobines de bras HTS directement couplées (cryo-MMC) a été conçu, construit et testé. Ce prototype a 5 sous-modules demi-pont par bras. Le prototype a fonctionné comme prévu, en mode onduleur pour une tension continue de 150 V jusqu'à 760 W. Les pertes normalisées des bobines de bras sont 10 fois plus faibles pour le cryo-MMC que pour le HB-MMC avec des bobines de bras en cuivre non couplées.

Conclusion

Ce chapitre résume les résultats essentiels et propose des directions de recherche futures pour les développements réalisés de cette thèse.

Dans le deuxième chapitre, un modèle DA-HSS a été développé et validé pour le HB-MMC. Ce modèle permet de calculer avec précision les valeurs en régime permanent des variables d'état du convertisseur en étant dix fois plus rapide que les modèles classiques dans le domaine temporel. Son originalité par rapport à d'autres modèles classiques d'espace d'état est sa capacité à prendre en compte les harmoniques créées par la modulation. Des travaux futurs pourraient appliquer la même méthodologie à d'autres convertisseurs électroniques de puissance où l'effet des harmoniques de modulation est plus critique, comme le 2L-VSC.

Dans le troisième chapitre, nous avons défini les indicateurs de performance en régime permanent qui doivent être pris en compte lors de la conception d'un MMC. Ensuite, nous avons étudié la possibilité de coupler magnétiquement les bobines de bras du HB-MMC dans le but de réduire leur taille. Nous avons utilisé le modèle DA-HSS pour dimensionner les bobines de bras du HB-MMC, à la fois pour les cas non couplés et directement couplés. Trois configurations

de bobines de bras ont été sélectionnées et comparées à l'aide d'une simulation transitoire dans le domaine temporel d'un lien HVDC P2P de 1 GW pm 320 kV. Nous avons montré que les bobines de bras à couplage direct peuvent être conçues pour : garder une taille similaire tout en améliorant les performances, ou réduire la taille tout en gardant les mêmes performances. Par exemple, un MMC avec des bobines de bras en couplage direct ayant une inductance propre de $L = 27,3$ mH et un coefficient de couplage de $K_{u,l} = 0,6740$ aurait des performances similaires à celles du MMC industriel de référence tout en réduisant la masse de la bobine de bras de 43,6% et son volume de 44,7%.

Dans le quatrième chapitre, nous avons étudié la possibilité de remplacer les bobines de bras conventionnelles à noyau d'air par des bobines de bras supraconductrices à haute température pour fournir une fonction de limitation du courant de défaut au HB-MMC. Nous avons conçu les bobines de bras HTS et leur système de réfrigération en considérant le HB-MMC de 1 GW \pm 320 kV. Nous avons utilisé le modèle DA-HSS pour calculer les indicateurs de performance en régime permanent. Nous avons montré que le cryo-MMC peut améliorer les performances en régime permanent par rapport au MMC de référence. Une analyse transitoire a confirmé la stabilité thermique et électrique du cryo-MMC. Les bobines de bras HTS ont réduit les courants de défaut prospectifs DC et AC d'un facteur cinq. De plus, le cryo-MMC permet de diviser par quatre la masse des bobines de bras tout en réduisant leur encombrement par un facteur de 1,6. Nous avons évalué le coût économique d'un cryo-MMC et montré que la configuration avec des bobines de bras HTS directement couplées et fonctionnant à 65 K entraîne une augmentation du coût d'investissement de 0.95% par rapport à la MMC de référence. Des travaux futurs pourraient étudier d'autres architectures de systèmes de réfrigération afin d'améliorer l'efficacité du refroidissement et ainsi réduire les pertes opérationnelles du cryo-MMC.

Dans le cinquième chapitre, nous avons décrit la conception, la construction et les tests du cryo-MMC avec des bobines de bras HTS en couplage direct. Les résultats reportés confirment la faisabilité de l'intégration de bobines supraconductrices à haute température dans un HB-MMC.

Les travaux futurs sur le cryo-MMC peuvent se concentrer sur les aspects suivants.

- Le système de réfrigération conçu au quatrième chapitre a une efficacité d'environ 5% et 3% à 77 K et 65 K. De travaux futurs devraient porter sur des systèmes de réfrigération plus efficaces afin de réduire les coûts opérationnels du cryo-MMC.
- Des études sur l'intégration du cryo-MMC dans un réseau HV-MTDC devraient être réalisées pour évaluer l'impact de ce convertisseur dans un systèmes à courant continu plus grand que les liaison point-à-point.
- L'association du cryo-MMC et des disjoncteurs DC (DC-CB) doit être analysée afin d'évaluer la technologie de disjoncteur la plus appropriée en

termes d'aspects fonctionnels et économiques. Cette analyse permettrait également de comparer un cryo-MMC associé à un DC-CB avec une topologie capable de bloquer les défauts, comme le MMC avec des sous-modules en pont complet.

- La capacité de courant de défaut de la cryo-MMC doit encore être testée à l'échelle du laboratoire.

Le cryo-MMC peut également constituer une solution appropriée pour les lignes aériennes MMC-HVDC en raison de sa capacité de limitation du courant de défaut. Actuellement, les lignes aériennes HVDC ne sont pas susceptibles de déployer en utilisant le HB-MMC, car elles sont plus sujettes à de courts-circuits fugitifs DC que les liaisons par câble en raison des conditions environnementales et météorologiques. Le MMC avec de SM en pont complet (FB-MMC) est considérée comme la topologie préférée pour les lignes aériennes de transmission en courant continu. Néanmoins, l'association du cryo-MMC et d'un DC-CB peut être une alternative moins coûteuse.

L'industrialisation du cryo-MMC nécessiterait un effort conjoint entre deux industries : Les fabricants de convertisseurs électroniques de puissance pour le HVDC et les fabricants d'équipements supraconducteurs. La construction des bobines de bras HTS du cryo-MMC peut s'inspirer des projets réussis de limiteurs de courant de défaut supraconducteurs dans le monde entier.

Introduction

Context

High-voltage direct current (HVDC) systems are steadily being implemented all around the globe to connect load and generation centers in some particular applications where they outperform classical high-voltage alternated current (HVAC) systems. These HVDC links are currently employed for bulk power transportation through overhead lines with hundreds or even thousands of kilometers, for underground cable links where overhead lines are disregarded due to project complexity, environmental and societal impacts, and undersea cable links to connect insular systems and offshore wind power plants.

An essential component of HVDC links is the power electronic converter. It interfaces the AC and DC transmission systems. The Modular Multilevel Converter (MMC) is currently state of the art in HVDC links for power ratings under 2000 MW. This converter has been employed in the last few years to link offshore wind power plants to mainland networks with voltage ratings up to ± 525 kV. Nowadays, MMCs are mainly used in point-to-point (P2P) HVDC links connecting two AC systems over one HVDC line. In the future, the MMC may be used to create multi-terminal direct-current (MTDC) grids that would enable efficient integration of massive amounts of renewable energy from remote areas and increase the interconnection of actual HVAC grids.

In this work, we focus our attention on the design of the MMC with half-bridge submodules (HB-SMs). In particular, we explore several options for the arm coils of the MMC. They are often designed to perform different tasks. In normal conditions, the arm coils allow for the control of the power flow in grid following mode, filter the modulation harmonics on the AC-side current and limit the circulating currents. In fault conditions, the arm coils limit the fault current.

Objectives of the Thesis

In this thesis, we aim to improve the MMC design to make it more cost-effective and provide robust fault contingency to MMC-HVDC systems. We focus our efforts on the design of the arm coils since they impact the cost, losses, and weight of the MMC.

Our objectives are to:

- (i) Reduce the size and weight of the arm coils, thereby decreasing the footprint of the MMC-HVDC station. This point is particularly important for offshore applications.

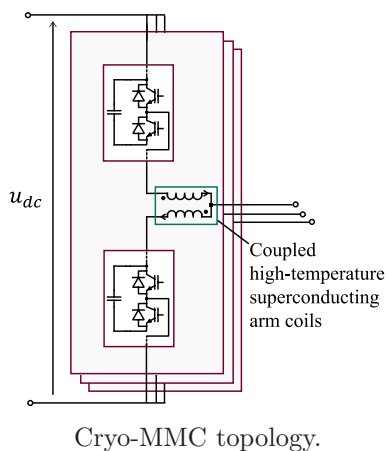
- (ii) Reduce the losses of the arm coils, thereby increasing the efficiency of the MMC-HVDC station.
- (iii) Provide a DC fault current limitation function to the HB-MMC. By limiting the fault currents, the constraints on the converter and on all of the associated equipment of the MMC-HVDC station will be reduced. This could simplify the design of the DC-circuit breakers too.

Propositions

First, we propose to magnetically couple the arm coils of the HB-MMC. It is expected that a direct-coupling will allow us to reduce the size and weight of the arm coils (objective (i)). This proposition has been patented [1].

Second, we propose replacing the conventional dry-type air-core arm coils with high-temperature superconducting arm coils. It is expected that it will allow us to reduce conversion losses (objective (ii)) while providing the fault current limitation function (objective (iii)) by behaving like a superconducting fault current limiter. This proposition has been patented [2].

The resulting topology is an HB-MMC with high temperature superconducting directly-coupled arm coils that we propose to call “cryo-MMC”.



Thesis Content

The rest of this thesis is organized as follows.

- In Chapter I, we update key numbers describing the historical and technical evolution of HVDC grids. Additionally, we define an industrial-scale reference HVDC system to be used as a point of comparison in future analysis.

- In Chapter II, we propose, develop and validate a detailed-arm harmonic state-space (DA-HSS) model of the three-phase MMC. This tool is used in the next chapters to study the impact of the arm coil design on the steady-state performances of the HB-MMC.
- In Chapter III, we study the HB-MMC with coupled dry-type air-core arm coils. After sizing the coupled dry-type air-core coils, we compare the performances of this MMC with the reference case through simulations in steady-state and transient operation.
- In Chapter IV, we study the HB-MMC with high temperature superconducting coupled arm coils. After sizing the coils, we compare the performances of the MMC with the reference case through simulations in steady-state and transient operation. An economic assessment completes the discussion.
- In Chapter V, we detail the design, construction, and tests of our laboratory-scale HB-MMC with high temperature superconducting coupled arm coils.
- In Chapter V.3, we summarize the key findings and propose future research directions.

The thesis is completed by several appendices.

- In Appendix A, we develop the mathematical framework behind the harmonic state-space model.
- In Appendix B, we summarize the data of the reference 1 GW \pm 320 kV HB-MMC.
- In Appendix C, we design a conventional dry-type air-core coil for industrial-scale MMC.
- In Appendix D, we develop a semi-analytical method to compute the conduction and switching losses of an HB-MMC.
- In Appendix E, we remind the classical control structure used in HB-MMCs when operating in grid-following mode.

Publications

The work presented in this thesis was partially reported in the following documents.

- P. Egrot, R. Coelho-Medeiros. “Convertisseur alternatif-continu de type MMC”. French pat. FR3110304, May 18, 2020.

- P. Egrot, R. Coelho-Medeiros. “Convertisseur alternatif-continu de type MMC”. French pat. FR2004974, May 18, 2020.
- R. Coelho-Medeiros, B. Džonlaga, J. Dai, L. Queval, J.-C. Vannier and P. Egrot, “A Comparison between Different Models of the Modular Multilevel Converter,” 2020 22nd European Conference on Power Electronics and Applications (EPE'20 ECCE Europe), 2020, pp. 1-10.
- R. Coelho-Medeiros, L. Queval, J. Dai, J.-C. Vannier and P. Egrot, “Modeling of High-Temperature Superconducting Pancake Coils using the Axisymmetric Partial Element Equivalent Circuit Method,” 7th International Workshop on Numerical Modelling of High-Temperature Superconductors, 2021, Nancy, France.
- R. Coelho-Medeiros, L. Queval, J. Dai, J. -C. Vannier and P. Egrot, “Cryo-MMC: a Modular Multilevel Converter with Superconducting Arm Coils,” 2021 23rd European Conference on Power Electronics and Applications (EPE'21 ECCE Europe), 2021, pp.1-8.
- R. Coelho-Medeiros, L. Queval, J. Dai, J. -C. Vannier and P. Egrot, "Integration of HTS Coils in a Lab-Scale Modular Multilevel Converter," in *IEEE Transactions on Applied Superconductivity*, vol. 32, no. 4, pp. 1-4, June 2022.

Chapter I

Review of HVDC Grids

In this chapter, we review today's high-voltage direct current (HVDC) transmission systems and highlight some technical issues yet to be solved in order to enable a full-scale deployment of multi-terminal direct current (DC) grids.

The objectives of this chapter are:

- To update key numbers describing the history and evolution of HVDC systems.
- To define a reference HVDC system used as a point of comparison in future analysis.

This chapter is organized as follows. In Section I.1, we review the historical evolution of HVDC grids. In Section I.1.1, we describe some technical aspects of today's HVDC grids. In Section I.2, we attempt to forecast the evolution of HVDC grids. Section I.3, we analyze the latest converter's technology for HVDC systems. In Section I.4, we define a reference industrial-scale HVDC system that will be used as a point of comparison in future analysis. In Section I.5, we summarize the essential findings of this chapter.

I.1 Yesterday's HVDC Grids

Electrical power systems arose from street lighting and achieved commercial scale in Europe by the mid-1870s and in North America by 1880 [3]. At that time, arc lamp street lighting ran on alternating current (AC), and incandescent lighting ran on direct current (DC). Edison General Electric company first introduced the DC incandescent lighting systems in 1882, which were deployed for indoor lighting on a large scale. However, a DC generating station could only cover a radius of three kilometers due to the economic limitation of DC-voltage transportation at low-voltage levels (110 V). This limitation bound early DC systems to serve high-density loads in relatively small urban areas. In the meantime, an AC power system was demonstrated in 1881 by Lucien Gaulard, and John Gibbs [4] which used transformers to step voltages up and down, thus reducing current ratings for transportation. In 1888, the Westinghouse Electric Company bought several patents on polyphase AC motors, power transmission, generators, transformers, and lighting from Nikola Tesla and employed the inventor. It set off what is known as the "battle of the currents", where Edison's DC power system competed with Westinghouse's AC power system from 1888

to 1892. The AC power system triumphed over its DC counterpart [4], and the rest is history, until the early 1950s [5].

For many decades, high-voltage AC (HVAC) prevailed over high-voltage DC (HVDC) for electric power transmission. This history started to bustle with the invention of the mercury arc rectifier in 1902. In the 1930s, research efforts on HVDC transmission technology intensified, focusing on the AC-DC static converters, converter valves, economic aspects of DC lines, insulation, and transient performance of overhead DC lines [5]. At that time, many research works already pointed out that HVDC would be cheaper than HVAC for undersea cable links and long-distance overhead lines [5].

The first commercial HVDC system was an undersea cable between the Swedish mainland and the island of Gotland. The link Gotland 1, commissioned in 1954, had a rated DC voltage of 100 kV and a rated power of 20 MW and used mercury-valve converters. The mercury-valve technology disappeared in 2004 with the decommissioning of the mercury-valve rectifier of the Bipole 1 of the Nelson river DC transmission system.

In the 1970s, the thyristor took over the mercury-arc valves in HVDC applications. The thyristor-based converters, also called line-commutated converters (LCC), had higher reliability, lower cost, simpler maintenance, and lower environmental risk when compared to mercury-valve rectifiers [5]. From the 1970s until today, LCC-HVDC links have massively been deployed. In 1970, the prior mercury-valve-based Gotland 1 link was re-engineered to employ thyristors and became the world's first commercial LCC-HVDC link, with a rated DC voltage of +150 kV and a rated power of 30 MW. The Brazilian Itaipu 1 and 2 projects, commissioned in 1984, marked a substantial step-up with a rated DC-voltage of ± 600 kV and a rated power of 3150 MW in two 800 km overhead lines [5].

In the 2000s, voltage-source converters (VSC) using Insulated-Gate Bipolar Transistors (IGBT) started to be developed for HVDC applications. The first commercial VSC-HVDC project was the 70 km submarine Gotland 3 HVDC link, commissioned in 1999, with a rated DC voltage of ± 80 kV and a rated power of 50 MW [6]. The NordLink project [7], commissioned in 2020, was the first VSC-HVDC link to employ a DC-voltage of ± 525 kV.

In Fig. I.1, the cumulative installed power of point-to-point (P2P) HVDC links is plotted from 1954 (the beginning of commercial HVDC) to 2021.

I.1.1 Today's HVDC Grids

Today LCC-HVDC links correspond to 89.5% of the installed power capacity for point-to-point (P2P) HVDC links. A panorama of the ratings of LCC-HVDC links is presented in Fig. I.2. China's Changji-Guquan ultra-high-voltage direct current (UHVDC) transmission line holds every record of this technology. It is a 3324 km overhead line with a rated DC voltage of ± 1100 kV and a rated power of 12 GW [9].

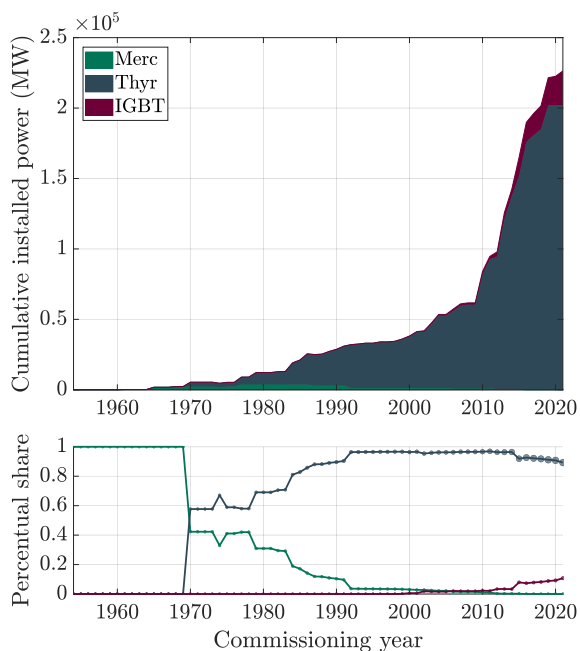


Figure I.1: Cumulative installed power of P2P HVDC links (data from [8]). Merc designates mercury-valve converters, Thyr designates LLC, IGBT designates VSC.

Today VSC-HVDC links correspond to 11.5% of the installed power capacity for P2P HVDC links. A panorama of the ratings of VSC-HVDC links is presented in Fig. I.2. The INELFE link between France and Spain is the most powerful VSC-HVDC link in operation, with a rated power of 2000 MW. The 32 km underground link has a rated DC voltage of ± 320 kV [10]. The Nord Sea Link [11], a 730 km submarine cable between the UK and Norway, commissioned in 2021, is the longest VSC-HVDC link in operation with a rated DC voltage of ± 525 kV and a rated power of 1400 MW.

Beyond technical reasons, economic reasons are an important factor explaining the development of HVDC transmission. It is well documented that for HV links, there is a break-even distance from which the total cost of an HVDC link becomes smaller than the total cost of its HVAC counterpart [12, 13, 14, 15]. Although the initial capital cost of an HVDC system is higher than in HVAC, the cost of HVDC cables and the associated losses are lower [15]. For a 1 GW HVDC link, the break-even distance is between 310 and 800 km for overhead lines; and between 30 and 70 km for submarine cables [12, 13, 14, 15].

Besides P2P links for bulk power transmission, LCC-HVDC and VSC-HVDC

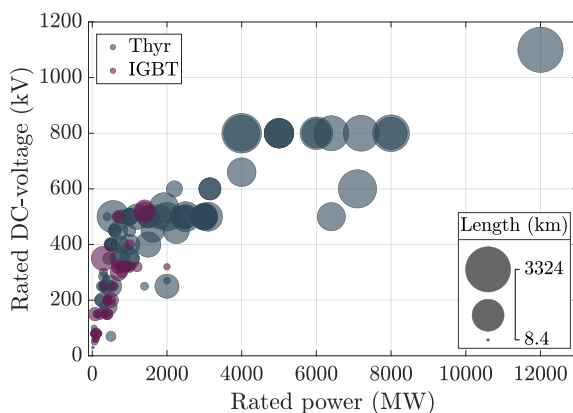


Figure I.2: Ratings of today’s P2P LCC-HVDC and VSC-HVDC links (data from [8]).

have been implemented using several architectures (back-to-back, multi-terminal DC) and configurations (asymmetrical monopolar, symmetrical monopolar, bipolar, homopolar) adapted to many different applications. For a complete overview, we refer the reader to the many excellent works, all too briefly, cited here [12, 16, 17].

Each technology has its advantages and drawbacks, and they coexist today, together and with the AC transmission grid. A short summary is proposed in Table I.1. In today’s scenario, LCCs are mainly used in HVDC links between strong AC systems exceeding 2000 MW, and VSCs are mainly used in HVDC links under 2000 MW and can operate with weak or even passive AC systems.

I.2 Tomorrow’s HVDC grids

In an attempt to forecast the evolution of HVDC grids, let’s look at which technology has been implemented and where. To do so, we counted the number of P2P HVDC links per continent and per valve technology. The results are plotted in Fig. I.3 and permit us to highlight two facts.

First, a massive deployment of LCC-HVDC links has occurred in Asia since 2010. This is explained by the suitability of this technology to carry out bulk power over long-distance, from the production center in the North-West of China to the consumption centers in the South-East [19, 20, 21].

Second, VSC-HVDC links outnumbered LCC-HVDC in Europe in 2021. They are used for bulk power transport through underground cables as the INELFE link [10], for submarine cables used to connect insular grids such as the COMETA project [22] and to connect offshore wind power plants as the DolWin3 link [23].

	LCC-HVDC	VSC-HVDC
Switching device	Thyristor	IGBT
Onshore station footprint for 1 GW	600 m × 360 m	220 m × 80 m
Active power reversal	Upon DC voltage polarity reversal in 0.5–1 s	upon DC current reversal in 0.1 s
DC conductor	Mainly Mass-Impregnated insulated conductors	Mainly Cross-linked Polyethylene conductors
Independent PQ control	No	Inherent within the control
Losses per station	0.6–0.8%	1.5–2%
Power rating per station	Up to 12000 MW	Up to 2000 MW
Application with AC systems	Connection to strong systems only ($SCR > 3$)	Connection to weak and passive systems

Table I.1: Comparison of LCC-HVDC and VSC-HVDC technologies. Source: [18].

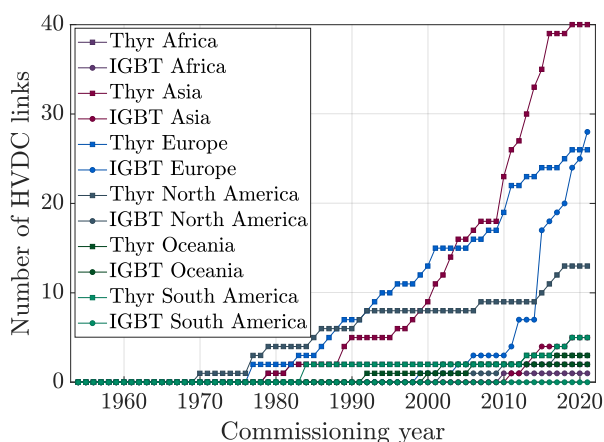


Figure I.3: Number of P2P HVDC links per continent and per valve technology (data from [8]).

These two facts are in agreement with the objectives of decarbonization of the energy systems underlined by many road maps for the energy transition [24, 25, 26]. The tendency is, therefore, likely to continue.

From the electricity generation point of view, sites with the best wind and solar photovoltaic potential are often located far from load centers. For example, the best European sites for wind power plants are located in the North Sea and Western Europe, while suitable sites for large-scale solar power plants are located around the Mediterranean Sea [27]. These elements indicate a shift in the location of future generation plants towards the borders of the European power system, thus moving the new generation sources farther from load centers than classical generation sources, such as fossil fuels and nuclear plants.

The evolution of the future grid to integrate renewable energy sources requires a transmission grid that supports highly varying power flow and transports large amounts of power over long distances through different links in a cost-effective manner [27, 28]. In addition, the deployment of offshore wind power plants and the multiple barriers to new overhead line projects drive an increasing need for HV cable links. In this context, future infrastructures may transit from overhead lines to cable technology in onshore applications [28].

An high-voltage multi-terminal DC (MTDC) grid complementing the existing HVAC infrastructures can provide a valuable interconnection between the many renewable energy sources and compensate for their intrinsic intermittency [16, 29, 30, 31, 32]. In the future, VSC-HVDC links may integrate offshore wind farms and remote land-based wind farms into the HVAC grid. Bulk power transmission from large and remote energy sources such as hydro-power plants can be integrated with LCC-HVDC. Ancillary services to improve HVAC grid performance can be provided by VSC-HVDC. Cross-border capacity for power exchange between regions and countries can be developed using LCC and VSC-HVDC. Underground cables VSC-HVDC can supply power and provide voltage support to large urban areas where the development of new overhead lines is cumbersome. An illustration of the integration of an HV-MTDC grid into the existing HVAC infrastructure is illustrated in Fig. I.4.

Future MTDC grids will be developed in a parallel-connected configuration where all converters share a common DC bus [16, 17]. The parallel multi-terminal connections of LCCs can be built but with performance and cost penalties [17, 18, 33] since they require a DC-DC interface to manage the LLC's variable DC-voltage polarity related to bidirectional power flow. The parallel connection of converters on the DC side is better handled with VSCs due to their fixed DC voltage polarity, making this technology more suitable for developing multi-terminal DC (MTDC) grids. The effective deployment of such systems is conditioned to multiple challenges, namely the operation and control of converters, strategies for fault contingency, and the development of HVDC grid codes [13, 32].

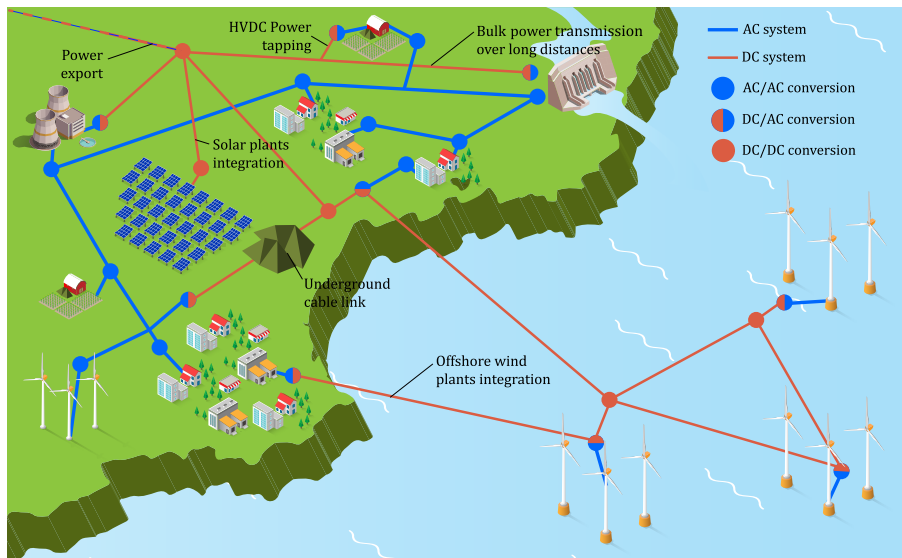


Figure I.4: A vision of the future: integration of HV-MTDC grid with HVAC grids.

For all these reasons, VSC-HVDC is considered to be the backbone of future HVDC grids. Therefore we will focus on this technology from now on.

I.3 Focus on VSC-HVDC Systems

In 1999, a two-level voltage source converter (2L-VSC) was first employed in a P2P HVDC link. From 2000 to 2006, VSC topologies providing two or three voltage level modulated voltage have been used in HVDC-links up to ± 150 kV and 350 MW. The arrival of the modular multilevel converter, firstly deployed in 2010, stepped up both the voltage and power of VSC-HVDC links, whose current ratings can be up to ± 525 kV and 1400 MW for a single converter.

VSCs have been employed in HVDC cable links, particularly to integrate offshore wind plants, and are seen as the backbone of future HVDC grids. Nonetheless, a critical issue of VSC-based HVDC grids yet to be addressed at the industrial scale is the development of appropriate strategies and devices for DC-fault contingency.

I.3.1 VSC Topologies

Four topologies of voltage source converters have been employed in commercial VSC-HVDC links [34]: The two-level voltage source converter (2L-VSC) illustrated in Fig. I.5a, the three-level neutral point clamp converter (3L-NPC) illustrated in Fig. I.5b, the three-level active neutral point clamp converter

(3L-ANPC) illustrated in Fig. I.5c, and the modular multilevel converter (MMC) with half-bridge submodules (HB-SMs) illustrated in Fig. I.5d.

The Estlink, an undersea cable link of 105 km between Estonia and Finland, commissioned in 2006, employs a 2L-VSC and has a rated DC voltage of ± 150 kV and a rated power of 350 MW [35]. The Eagle Pass back-to-back station, commissioned in 2000, employs a 3L-NPC and has a rated DC voltage of ± 15 kV and a rated power of 36 MW. The Cross Sound Cable, an undersea cable link of 40 km between Connecticut and New York, commissioned in 2002, employs a 3L-ANPC and has a rated DC voltage of ± 150 kV and a rated power of 330 MW [36].

The 2L-VSC, the 3L-NPC, and the 3L-ANPC were mainly employed on VSC-HVDC links at DC-voltage levels up to 150 kV. Many IGBTs need to be associated in series to reach these voltage levels since IGBTs modules are limited to a couple of kilovolts (1.7-6.5 kV) [37]. A sinusoidal pulse-width modulation is usually adopted on the low-level control of these converters with a switching frequency between 1-1.5 kHz [37]. The AC-modulated voltage for the 2L-VSC is illustrated in Fig. I.6a and for the 3L-NPC and that for the 3L-ANPC is illustrated in Fig. I.6c. Some shortcomings of these topologies are [37]:

- The series association of IGBTs requires special attention to ensure equal voltage sharing among the series-connected switches during static and dynamic states.
- The AC modulated voltages, illustrated in Figs. I.6a and I.6c, contain significant harmonic components at multiples of the switching frequency, thus requiring passive-filtering. Increasing the switching frequency to improve filtering leads to excessive losses at HVDC power levels.
- The AC modulated voltage is switched at the total DC voltage of the link in around 1 microsecond. These transitions result in a high voltage slope dv/dt that generates significant insulation stress on the equipment connected to the converter's AC terminal.

In 2001, a new converter topology has been proposed in [38] for HVDC applications. The Modular Multilevel Converter consists of a modular VSC topology composed of a series association of smaller VSCs, called submodules. Each phase comprises an upper and a lower arm composed of a stack of submodules in series connected to an arm coil. The midpoint between the two arms is connected to the converter's AC terminal, as illustrated in Fig. I.5d. Some essential differences from the above three topologies are:

- The modular design avoids the series association of IGBT and provides scalability to different voltage levels. The converter can be easily adapted to any DC-voltage rating by adjusting the number of submodules [39].

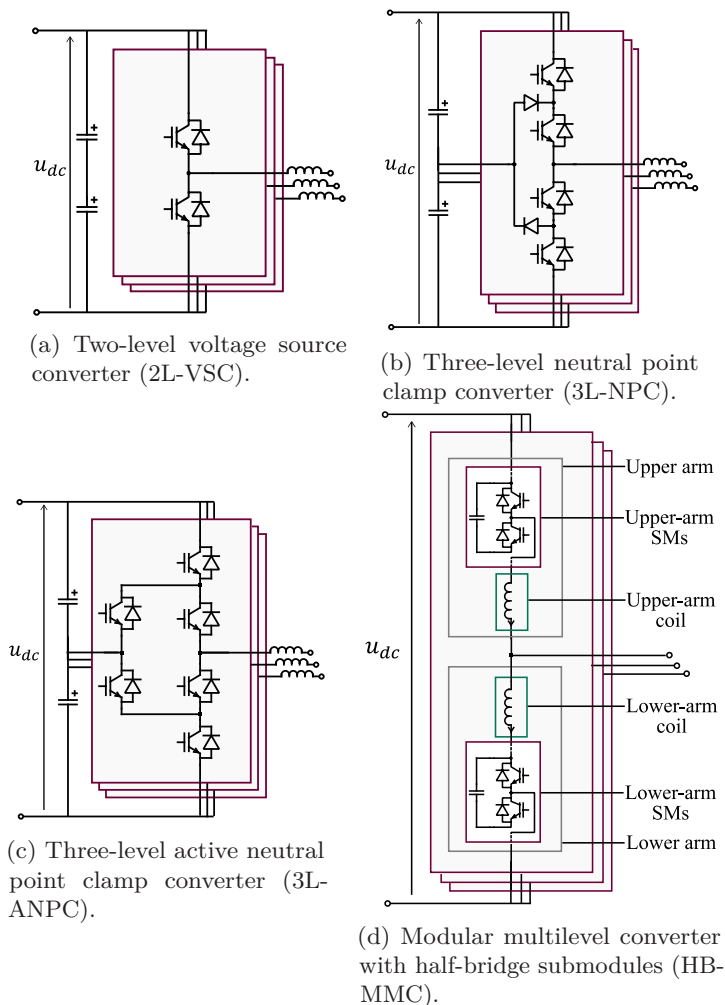


Figure I.5: VSC topologies in commercial HVDC links.

- The MMC has distributed capacitors in the submodules, and practical MMCs for HVDC applications can have hundreds of submodules per arm, providing a multitude of voltages levels.
- By applying multilevel modulation techniques [40, 41], a nearly sinusoidal modulated voltage can be synthesized as illustrated in Fig. I.6e, thus eliminating the need for AC-filtering.
- With proper multilevel modulation techniques [40], only one submodule is commutated, corresponding to a small fraction of the DC-link voltage.

This significantly reduces the voltage variation step and relaxes insulation requirements on the equipment connected to the converter's AC terminal.

- The nearest level modulation, a carrier-less modulation technique, is mainly employed for the MMC in HVDC. This technique reduces the commutation losses compared to the prior topologies since the submodules are switched at an average frequency of 150-300 Hz [42, 43].
- The DC-side harmonics generated by the MMC are very low and eliminate the DC-filtering requirement. Consequently, the converter can be controlled much faster when compared to others VSCs, and LCCs [39, 44].

The first commercial MMC was commissioned in 2010 in the San Francisco trans bay project, a submarine cable link with a rated DC voltage of 200 kV and a rated power of 400 MW [34]. Since then, the MMC has gained considerable attention and development owing to its advantages over more classical topologies. MMCs with HB-SMs are mainly employed in commercial HVDC applications.

In the light of the above considerations, we focus our attention on MMC-HVDC links from now on. The protection being a strong constraint, we review the behavior of such a system during faults.

I.3.2 Protection

In HVDC systems, the MMC terminals can be subject to symmetrical and asymmetrical AC and DC faults. While the HB-MMC can control AC fault currents, DC faults currents are uncontrollable. Consequently, DC-fault clearance is one of the most significant challenges in current HVDC systems using the HB-MMC [32].

Once a DC fault is detected, the IGBTs of the HB-MMC are blocked, and the converter behaves as a diode-bridge rectifier with the anti-parallel diodes creating an uncontrollable path for the fault to be fed by the AC system. The HB-MMC behavior during a DC fault when SMs are blocked is illustrated in Fig. I.7. A protective bypass thyristor is often used to conduct the fault current and avoid overcurrent damage to the anti-parallel diodes in parallel to each submodule.

The impact of a DC fault on an HB-MMC-HVDC link depends on the system's configuration, the fault type, and the grounding configuration [45]. In the absence of any protection device, a pole-to-ground fault results in a high-valued prospective fault current for low-impedance grounded grids and high prospective overvoltages on the healthy converters for a high-impedance grounded grid. For a pole-to-pole fault, whatever the grounding configuration, the DC fault current quickly increases and reaches a high steady-state value.

In a P2P link, once the converters are blocked, trip signals are sent to the circuit breakers (CB) located on the converter's AC side. The CBs are opened in around two to three fundamental periods, namely 40-60 ms in a 50 Hz system.

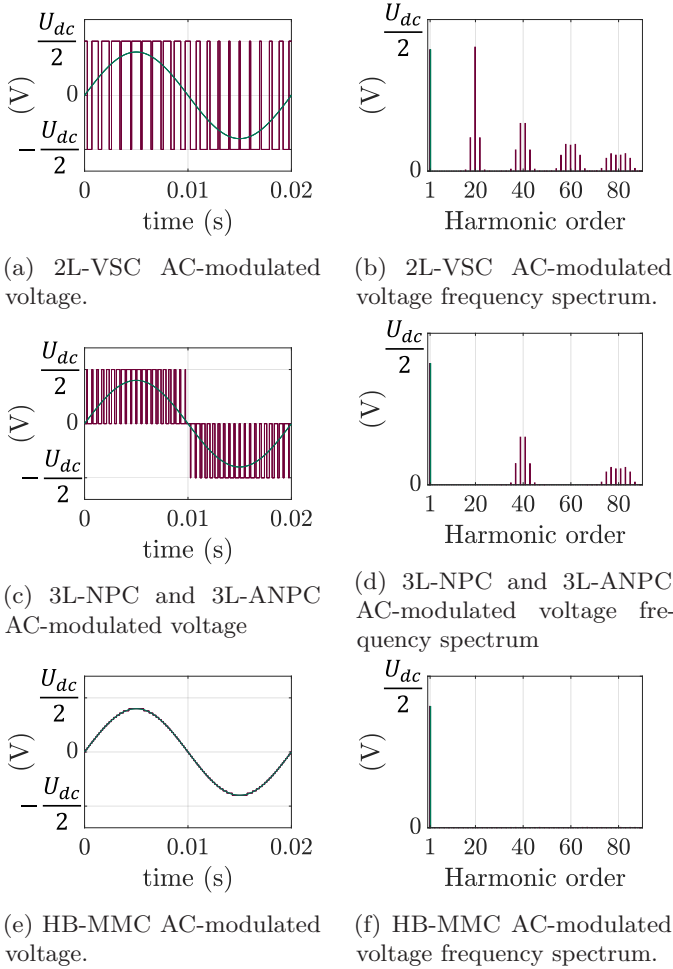


Figure I.6: AC-side modulated voltages for the 2L-VSC, 3L-NPC, 3L-ANPC, and the HB-MMC with 50 SMs per arm. We consider a modulation index amplitude of 0.8 with a frequency of fundamental frequency of 50 Hz, a constant DC voltage $u_{dc}(t) = U_{dc}$ and a switching frequency of 1 kHz for the 2L-VSC, 3L-NPC, and 3L-ANPC. The AC modulated voltage is represented in purple, and the fundamental voltage is represented in green.

During this time span, the converter station must withstand the fault current, which represents a critical constraint on the station design.

These DC faults also propagate rapidly across the DC network due to their low impedance [16]. A DC fault longer than 10 ms in an MTDC scheme composed of HB-MMCs would lead to the collapse of the DC grid voltage and, consequently, a power outage [16]. Moreover, all the connected converters

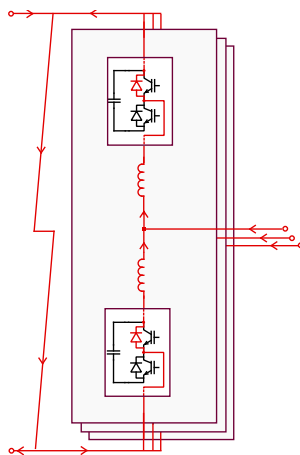


Figure I.7: HB-MMC after SMs blocking under a DC pole-to-pole fault. The arrows indicate the fault current direction.

would potentially contribute to the fault current, and the fault condition would be propagated into all the AC systems. While the protection systems for AC grids operate in the range of 25–100 ms, the protection systems of DC grids will be required to work in the 5-10 ms range [32].

Three DC-fault clearing strategies for DC systems are classified in the CIGRE's TB 739 [46]:

- Non-selective fault clearing: In the case of a fault, the entire HVDC grid is entirely de-energized, and the faulted component is identified and isolated using DC high-speed switches. Thereafter, the remaining part of the HVDC grid is reenergized, and power flow is reestablished.
- Partially-selective fault clearing: The HVDC grid is subdivided into protection zones using devices with fault-current blocking capability at the zones' boundaries. In the case of a fault, the faulted zone is isolated from the healthy ones of the grid. Subsequently, the faulted component is identified and isolated using DC high-speed switches. Thereafter, the healthy portion of the prior faulted zone is reenergized and reconnected to the healthy parts of the grid.
- Fully-selective fault clearing: Several devices with fault-current blocking capability are employed throughout the grid, creating a highly selective system. In the case of a fault, the faulted component can be individually isolated, and the healthy parts of the grid continue to operate unaffected by the fault. This strategy is similar to the standard practice in AC grid protection.

Suitable equipment to interrupt DC fault currents are either DC-circuit breakers (DC-CBs) [47] or MMCs using SMs with fault blocking capability [48]. Therefore the deployment of MTDC HVDC grids lies on the development of such devices [32]. However, both solutions increase the cost and power losses of HVDC grids and are still in earlier stages of industrialization [32].

I.4 Reference case: a Point-to-Point MMC-HVDC Link

In this section, we define a reference industrial-scale HVDC system that will be used as a point of comparison in future analysis.

We consider a 1 GW ± 320 kV HB-MMC point-to-point (P2P) scheme with symmetrical monopolar configuration, inspired from the CIGRE TB832 [49]. An overview of such P2P link is shown in Fig. I.8. The main parameters are summarized in Table I.2, and the full list of parameters is in Appendix B.

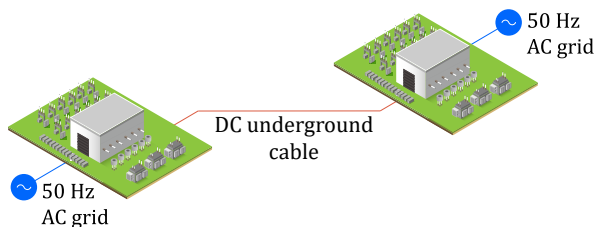
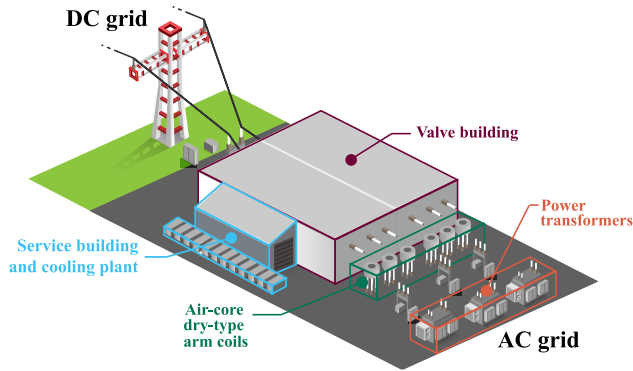


Figure I.8: Point-to-Point (P2P) scheme.

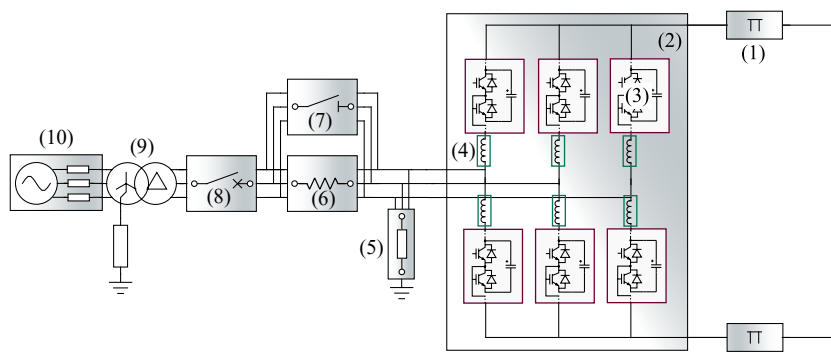
Quantity	Symbol	Value
Rated Active Power [MW]	P_{nom}	1000
Rated Reactive Power [MVar]	Q_{nom}	300
Rated DC Voltage [kV]	U_{dc}	± 320
Grid Voltage L-L RMS [kV]	V_g	400
DC Cable Length [km]	l_{cable}	70

Table I.2: Parameters of the reference MMC system.

One MMC station is located at each end of the line. A typical architecture of the station is shown in Fig. I.9a with the corresponding electric circuit shown in Fig. I.9b. Its main components are:



(a) Architecture.



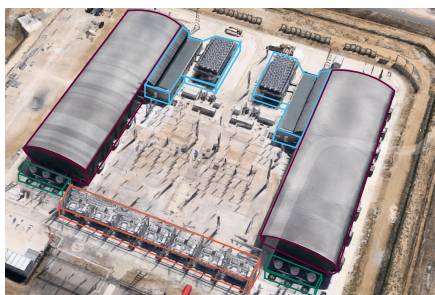
(b) Electric Circuit.

Figure I.9: Typical Architecture and Electric Circuit of an MMC-HVDC Station.

- (1) DC conductors: MMC-HVDC uses mainly XLPE cables. The parameters for the DC conductors of the reference HVDC link are provided in Table B.4.
- (2) Modular Multilevel Converter: The reference converter parameters are listed in Table. B.1.
- (3) Half-Bridge submodules: the reference MMC has 400 SMs per arm with an SM capacitance of 11 mF.
- (4) Arm coils: there is one arm coil per arm. We estimate that each arm coil has a resistance of $R = 90.4 \text{ m}\Omega$, an inductance of $L = 50.9 \text{ mH}$, a mass of 42.5 t, and a volume of 110 m^3 (see Appendix C).

- (5) Grounding Reactor: connected between the AC terminals and the ground, these devices provide a high impedance to ground at the converter's AC side.
- (6) Pre-Insertion Resistors: these high-valued resistors are intended to limit the inrush currents when the converter is connected to the grid. They are only used during the start-up sequence of the system.
- (7) Bypass switches: used to bypass the pre-insertion resistors.
- (8) AC Circuit Breakers: used to connect and disconnect the converter station to the AC grid.
- (9) Power Transformer: this equipment adapt the voltage at the AC-side of the converter to the AC-grid voltage level, provides galvanic isolation between the DC and the AC system, and, due to the wye-delta configuration, prevents any zero-sequence current exchange between the AC and DC grids. The parameters for the transformers of the reference MMC-HVDC station are provided in Table. B.2.
- (10) AC grid: the reference-case MMC is connected to a 400 kV AC grid for which parameters are given in Table. B.3.

In Fig. I.10, we present some pictures of a 1 GW ± 320 KV HVDC station using an HB-MMC.



(a) Baixas HVDC station: two 1 GW ± 320 KV HB-MMCs. Source: Google Maps.



(b) Valve building: HB-SMs assembly. Source: [50].



(c) Transformers for the Baixas HVDC station. Source: <https://www.inelfe.eu>.

(d) Arm coils of a 1 GW and ± 320 kV HB-MMC. Source: <https://www.inelfe.eu>.

Figure I.10: Components of an MMC-HVDC station.

The breakdown of an MMC-station capital cost, weight, and losses are shown in Fig. I.11. The SM system accounts for 96% of the capital cost and 91% of the nominal losses. Despite being seemingly minor components, the arm coils account for up to 4% of the cost and 9% of the losses. When considering the weight, their contribution reaches 42% of the weight of the MMC [51]. Therefore the arm coils represent a fundamental component of the MMC-HVDC station.

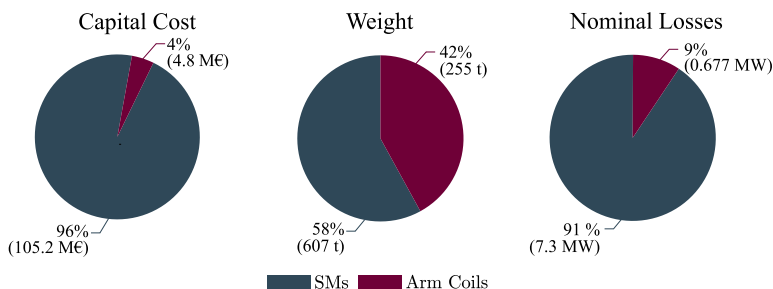


Figure I.11: Breakdown of the capital cost, weight, and losses for the reference MMC. "SMs" includes the HB-SMs, the valve building, the cooling plant, and control.

I.5 Summary

In this chapter, we reviewed yesterday’s and today’s HVDC grids and attempted to forecast the evolution of tomorrow’s HVDC grids. Some key findings are:

- LCC-HVDC and VSC-HVDC links will, most likely, coexist in the years to come. LCCs will continue to be used for bulk power transportation with ratings exceeding 2000 MW. VSCs will be principally used under 2000 MW in many applications, such as HVDC links for offshore wind power plants, for example.

- VSC-HVDC links correspond to 11.5% of the installed power capacity in today's P2P HVDC links, and LCCs correspond to 89.5%. and can operate with weak or even passive AC systems.
- A massive deployment of LCC-HVDC links has been taking place in Asia since 2010. This is explained by the suitability of this technology to carry out bulk power over long-distance.
- VSC-HVDC links outnumbered LCC-HVDC in Europe in 2021. They are used for bulk power transport through underground cables, submarine cables used to connect insular grids, and offshore wind power plants.
- Possible Multi-terminal DC (MTDC) grids will be developed using VSC-HVDC due to the fixed DC voltage polarity of VSCs.
- A major technical issue yet to be solved is the fault contingency in MTDC HVDC grids. The protection systems of DC grids will be required to respond in the 5-10 ms range.
- We have defined an industrial-scale MMC rated for a 1 GW and ± 320 kV and pointed out the impact of the arm coils on the HB-MMC. Despite being seemingly minor components, the arm coils account for up to 4% of the cost and 9% of the losses. When considering the weight, their contribution reaches 42% of the weight of the MMC.

Chapter II

Harmonic State-Space Modeling of the Modular Multilevel Converter

In this chapter, we look for a model that is suitable for the fast design of HB-MMC. Such a model should estimate the converter steady-state variables with a reduced computational burden and low error compared to classical approaches. We foresee that Harmonic State-Space (HSS) models have great potential. They are the focus of this chapter.

The objectives of this chapter are:

- To propose a detailed-arm harmonic state-space (DA-HSS) model of the three-phase HB-MMC that accounts for the harmonics generated by any arbitrary modulation technique.
- To implement and validate this model by comparison with a circuit simulation.

This chapter is completed by Appendix A where the theory behind the harmonic state-space representation of linear time-periodic systems is developed.

This chapter is organized as follows. In Section II.1, we review different modeling techniques for the MMC. In Section II.2, we derive the set of differential equations describing the dynamic behavior of the MMC with coupled arm coils and two state-space representations in the abc reference frame. In Section II.3, we develop the DA-HSS model and validate its results in comparison with the averaged-arm HSS and time-domain models on a benchmark. In Section II.4, we summarize the essential findings of this chapter.

II.1 Review on the Modeling of the MMC

When modeling the MMC, one can rely on time-dependent models such as the detailed-arm (DA) model [52, 53] and the averaged-arm (AA) model [54, 55]. In the AA and DA models, the time-dependent differential equations of the converter are solved using fixed or variable time-step numerical methods. The simulation of time-dependent models with large numbers of state variables can be a major challenge in computing time and memory requirements. Alternatively, the state-space time-invariant (SSTI) model [56, 57, 58] and the averaged-arm harmonic state-space (AA-HSS) model [59, 60, 61] eliminate the time dependence of the converter equations. In the SSTI and the AA-HSS

models, the steady-state response of the system can be obtained through sparse-matrix inversion leading to a shorter simulation time than their time-dependent counterparts.

The DA model reproduces each solid-state device of the MMC, namely transistors and diodes, and one must provide the turn ON/OFF gate signals for each solid-state device. In the DA model, the reference of the arm modulated voltages are converted into the switching patterns of transistors by a modulation technique associated with a capacitor voltage balancing control if necessary. The AA model assumes an identical capacitor voltage in all submodules (SM) of an arm, thus represented by a single equivalent arm SM. This equivalent SM is controlled by the arm switching function corresponding to the sum of the SMs switching functions of the arm. Additionally, only the zero and the fundamental harmonic of each arm switching function is considered, and the model only reproduces the MMC behavior in low frequencies.

Both the SSTI and the AA-HSS models are derived from the time-dependent differential equations of the averaged-arm model. The SSTI model is obtained by truncating the converter dynamics at the second harmonic and writing them in two rotating reference frames at the fundamental frequency f_0 and at the second harmonic $2f_0$ using the dq0-transformation. The harmonic state-space model is obtained by transposing the converter equations from the time domain to the frequency domain using the HSS decomposition of linear time-periodic (LTP) systems. A fundamental difference between these two time-independent models lies in their mathematical derivation. The SSTI model employs the dq0 decomposition for each modeled frequency, which is less straightforward than the HSS decomposition of linear time-periodic systems (see Appendix A) used in the AA-HSS model. If one wants to model the converter behavior at higher frequencies, it is simpler to increase the model's harmonic order by using the HSS decomposition.

Each of these models is suitable for a different range of applications. The DA model is ideal for studying capacitor voltage balancing control, modulation techniques and accurately describing semiconductors' losses. The AA model is suitable for power flow, high-level control, and stability analysis. The SSTI and AA-HSS models have the same range of applications as the AA. Due to their good performance in computation time for the system's steady-state response, they are suitable for parametric variation studies and the MMC design. As shown in Fig. II.1, the SSTI and the AA-HSS models are up to ten times faster than the AA model [62].

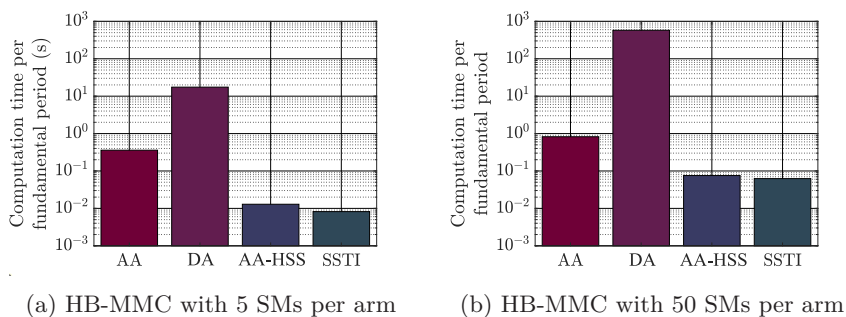


Figure II.1: Computation time per fundamental period $T_0 = 20$ ms for different models of the HB-MMC [62].

The derivation of the AA-HSS model for the MMC can be found in multiple works that focus on the stability analysis of the converter [59, 60, 61, 63, 64, 65, 66]. The MMC and its controllers are modeled in these works that present a standard procedure. Firstly the time-domain equations of the averaged-arm model are derived. When adding the controller dynamics, the model becomes non-linear. Thus, this model is linearized to obtain an LTP model. Thirdly, the HSS decomposition is applied to obtained LTP model, which yields the AA-HSS model of the MMC.

II.2 State-Space Representations of the MMC

In the following, we derive the state-space representation of the MMC in abc frame and the harmonic state-space representation of the MMC in abc frame. The reader can jump to sections II.2.8 and II.2.9 for a summary of these representations.

II.2.1 Overview and Conventions

In this section, we derive the equations of the dynamics of an MMC with half-bridge SMs interfacing a DC and an AC system, with the power conventions shown in Fig. II.2.

In the rest of this chapter, bold characters represent matrix and vector quantities and all the equations will be developed for a generic phase p , for sake of clarity and conciseness.

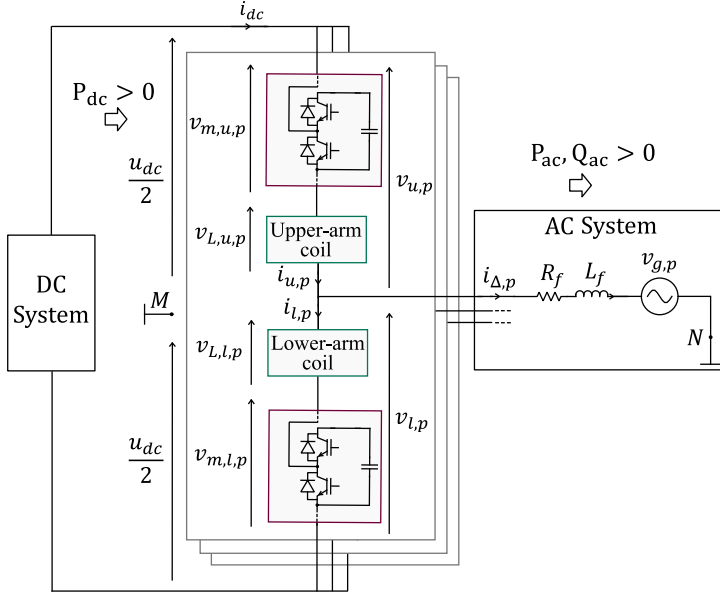


Figure II.2: Overview and conventions for the grid connected HB-MMC. The AC grid is modeled by an ideal AC voltage source in series with resistance R_f and an inductance L_f .

II.2.2 Half-bridge Submodule's Dynamics

In this work, we consider the half-bridge submodule (HB-SM) as the building block for the MMC. We adopt the notations shown in Fig. II.3. The indices u and l stand for the upper and lower arms, respectively, the index p stand for a generic phase and the i for the i -th SM.

The i -th submodule's modulated voltage $v_{m,(u,l),p}^{(i)}$ and its capacitor current $i_{c,(u,l),p}^{(i)}$ are

$$v_{m,(u,l),p}^{(i)} = u_{(u,l),p}^{(i)} v_{c,(u,l),p}^{(i)} \quad (\text{II.1a})$$

$$i_{c,(u,l),p}^{(i)} = u_{(u,l),p}^{(i)} i_{(u,l),p}^{(i)} \quad (\text{II.1b})$$

where $u_{(u,l),p}^{(i)} \in \{0, 1\}$ is the SM switching function, $v_{c,(u,l),p}^{(i)}$ is the SM capacitor voltage, and $i_{(u,l),p}^{(i)}$ is the arm current.

Apply the Kirchoff's Voltage Law (KVL) and the Kirchoff's Current Law (KCL) to obtain,

$$-i_{k1,(u,l),p}^{(i)} + i_{k2,(u,l),p}^{(i)} = i_{(u,l),p}^{(i)} \quad (\text{II.2a})$$

$$v_{k1,(u,l),p}^{(i)} + v_{k2,(u,l),p}^{(i)} = v_{c,(u,l),p}^{(i)} \quad (\text{II.2b})$$

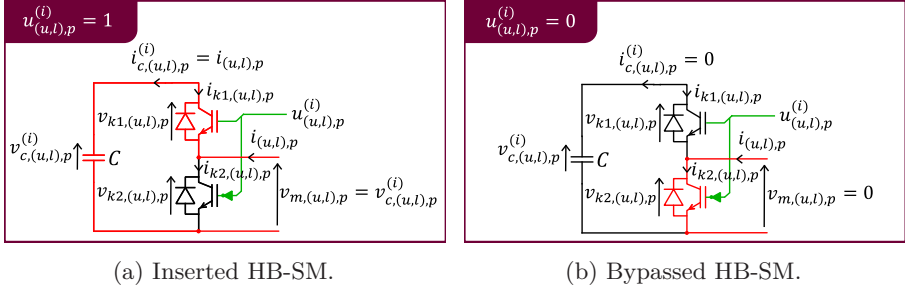


Figure II.3: Half-bridge submodule. The indices u and l stand for the upper and lower arms, respectively. The index p denotes a generic phase.

where $i_{k1,(u,l),p}^{(i)}$ and $v_{k1,(u,l),p}^{(i)}$ are the current and the voltage of the HB-SM k1 switch and $i_{k2,(u,l),p}^{(i)}$ and $v_{k2,(u,l),p}^{(i)}$ are the current and the voltage of the HB-SM k2 switch.

Additionally, the voltage and current at the HB-SM switches can be written as

$$i_{k1,(u,l),p}^{(i)} = -u_{(u,l),p}^{(i)} i_{(u,l),p}^{(i)} \quad (\text{II.3a})$$

$$v_{k1,(u,l),p}^{(i)} = \left(1 - u_{(u,l),p}^{(i)}\right) v_{c,(u,l),p}^{(i)} \quad (\text{II.3b})$$

$$i_{k2,(u,l),p}^{(i)} = \left(1 - u_{(u,l),p}^{(i)}\right) i_{(u,l),p}^{(i)} \quad (\text{II.3c})$$

$$v_{k2,(u,l),p}^{(i)} = u_{(u,l),p}^{(i)} v_{c,(u,l),p}^{(i)} \quad (\text{II.3d})$$

From Eq. (II.3), we conclude that the limits in current and voltage of the SMs' switches correspond to the maximum value of $i_{(u,l),p}^{(i)}$ and $v_{c,(u,l),p}^{(i)}$, respectively.

From Eq. (II.1b), the voltage dynamics of upper-and lower-arm capacitors, assuming that all SMs have the same capacitance, can be written as

$$C \frac{d}{dt} v_{c,(u,l),p}^{(i)} = u_{(u,l),p}^{(i)} i_{(u,l),p}^{(i)} \quad (\text{II.4})$$

where C is the capacitance of the i -th SM capacitor.

II.2.3 Equivalent Submodule's Dynamics

The set of equations defined in Section II.2.2 model the individual behavior of each SMs. We adopt an equivalent representation of submodules developed in the following paragraphs in this work.

Define the equivalent SMs capacitor voltage for an arm in phase p , denoted by $v_{c,(u,l),p}$, as the sum of all individual SM capacitors voltages,

$$v_{c,(u,l),p} \triangleq \sum_{i=1}^N v_{c,(u,l),p}^{(i)} \quad (\text{II.5})$$

Use Eqs. (II.4),(II.5) to obtain the dynamics of the equivalent SMs capacitor voltage,

$$C \frac{d}{dt} v_{c,(u,l),p} = u_{(u,l),p} i_{(u,l),p} \quad (\text{II.6})$$

where $u_{(u,l),p}$ is the arm switching function defined as

$$u_{(u,l),p} \triangleq \sum_{i=1}^N u_{(u,l),p}^{(i)} \quad (\text{II.7})$$

We assume that the capacitor voltages are the same at all time for all SMs of a given arm, which can be mathematically written as

$$v_{c,(u,l),p}^{(i)} \stackrel{\text{hyp.}}{=} \frac{v_{c,(u,l),p}}{N} \quad (\text{II.8})$$

Also, the arm modulated voltage is written as

$$v_{m,(u,l),p} = \sum_{i=1}^N v_{m,(u,l),p}^{(i)} = \sum_{i=1}^N u_{(u,l),p}^{(i)} v_{c,(u,l),p}^{(i)} \quad (\text{II.9})$$

which can be further simplified from Eq. (II.8) as

$$v_{m,(u,l),p} = u_{(u,l),p} \frac{v_{c,(u,l),p}}{N} \quad (\text{II.10a})$$

II.2.4 Arm Dynamics

The voltage of each arm $v_{(u,l),p}$ is written as,

$$v_{(u,l),p} = v_{m,(u,l),p} + v_{L,(u,l),p} \quad (\text{II.11})$$

where $v_{L,(u,l),p}$ the arm coil's voltage written as

$$v_{L,(u,l),p} = R i_{(u,l),p} + \frac{d}{dt} \lambda_{(u,l),p} \quad (\text{II.12})$$

with R denoting the arm coil's resistance and $\lambda_{(u,l),p}$ its flux linkage.

From the KVL at each arm we can derive the following equations.

$$\begin{aligned}
 -\frac{u_{dc}}{2} + v_{m,u,p} + \frac{d}{dt}\lambda_{u,p} + R i_{u,p} + \\
 L_g \frac{d}{dt}i_{\Delta,p} + R_g i_{\Delta,p} + v_{g,p} + v_{NM} = 0 \quad (\text{II.13a})
 \end{aligned}$$

$$\begin{aligned}
 \frac{u_{dc}}{2} - v_{m,l,p} - \frac{d}{dt}\lambda_{l,p} - R i_{l,p} + \\
 L_g \frac{d}{dt}i_{\Delta,p} + R_g i_{\Delta,p} + v_{g,p} + v_{NM} = 0 \quad (\text{II.13b})
 \end{aligned}$$

where $v_{g,p}$ and $i_{\Delta,p}$ are the AC voltage and current, v_{NM} is the differential voltage between the two reference points N and M and u_{dc} is the DC voltage.

For arm coils coupled between the upper and lower arm of phase p (Fig. II.4), the flux linkages are written as,

$$\lambda_{u,p} = L i_{u,p} + M i_{l,p} \quad (\text{II.14a})$$

$$\lambda_{l,p} = L i_{l,p} + M i_{u,p} \quad (\text{II.14b})$$

where L is the coil's self inductance and M its mutual inductance.

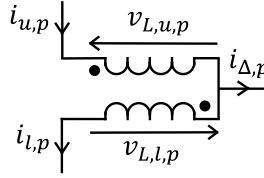


Figure II.4: Coupled coils between the upper and lower arms of the same phase.

Furthermore, the coupling coefficient these arm coils is defined as

$$K = \frac{M}{L} \quad (\text{II.15})$$

with $K \in [-1, 1]$.

If the coupling coefficient $K \in]0, 1]$, the coils are directly coupled, meaning that any arbitrary direct currents entering at the polarity marks of coils generate adding magnetic flux linkages. On the contrary, if $K \in [-1, 0[$, the coils are inversely coupled, meaning that any arbitrary direct currents entering at the polarity marks of coils generate subtracting magnetic flux linkages. Moreover, $K = 0$ denotes two uncoupled coils.

Replace Eq. (II.14) into (II.13) to obtain the arm dynamics,

$$\begin{aligned}
 -\frac{u_{dc}}{2} + v_{m,u,p} + R i_{u,p} + L \frac{d}{dt}i_{u,p} + M \frac{d}{dt}i_{l,p} + \\
 L_g \frac{d}{dt}i_{\Delta,p} + R_g i_{\Delta,p} + v_{g,p} + v_{NM} = 0 \quad (\text{II.16a})
 \end{aligned}$$

$$\begin{aligned} \frac{u_{dc}}{2} - v_{m,l,p} - R i_{l,p} - L \frac{d}{dt} i_{l,p} - M \frac{d}{dt} i_{u,p} + \\ L_g \frac{d}{dt} i_{\Delta,p} + R_g i_{\Delta,p} + v_{g,p} + v_{NM} = 0 \end{aligned} \quad (\text{II.16b})$$

The grid current can be written from the KCL at the converter's AC side as

$$i_{\Delta,p} = i_{u,p} - i_{l,p} \quad (\text{II.17})$$

Combining Eq. (II.17) and Eq. (II.16) leads to

$$\begin{aligned} -\frac{u_{dc}}{2} + v_{m,u,p} + (L + L_g) \frac{d}{dt} i_{u,p} + (R + R_g) i_{u,p} \\ - (L_g - M) \frac{d}{dt} i_{l,p} - R_g i_{l,p} + v_{g,p} + v_{NM} = 0 \end{aligned} \quad (\text{II.18a})$$

$$\begin{aligned} \frac{u_{dc}}{2} - v_{l,p} - (L + L_g) \frac{d}{dt} i_{l,p} - (R + R_g) i_{l,p} \\ + (L_g - M) \frac{d}{dt} i_{u,p} + R_g i_{u,p} + v_{g,p} + v_{NM} = 0 \end{aligned} \quad (\text{II.18b})$$

Notice that the voltage v_{NM} was defined between the grid reference point N and the virtual reference point M and it can be controlled to any arbitrary value by the converter modulated upper and lower arm voltages. From here on out, we consider $v_{NM} = 0$.

II.2.5 UL- $\Delta\Sigma$ Transformation

To represent the converter's dynamics given in Eq. (II.18) in a more convenient form, a transformation of variables was proposed in [67] where the upper and lower (UL) arm quantities are converted to delta (Δ) and sigma (Σ) quantities as follows.

$$i_{\Delta,p} \triangleq i_{u,p} - i_{l,p} \quad (\text{II.19a})$$

$$i_{\Sigma,p} \triangleq \frac{i_{u,p} + i_{l,p}}{2} \quad (\text{II.19b})$$

$$v_{\Delta c,p} \triangleq \frac{-v_{c,u,p} + v_{c,l,p}}{2} \quad (\text{II.19c})$$

$$v_{\Sigma c,p} \triangleq \frac{v_{c,u,p} + v_{c,l,p}}{2} \quad (\text{II.19d})$$

$$v_{\Delta m,p} \triangleq \frac{-v_{m,u,p} + v_{m,l,p}}{2} \quad (\text{II.19e})$$

$$v_{\Sigma m,p} \triangleq \frac{v_{m,u,p} + v_{m,l,p}}{2} \quad (\text{II.19f})$$

$$u_{\Delta,p} \triangleq -u_{u,p} + u_{l,p} \quad (\text{II.19g})$$

$$u_{\Sigma,p} \triangleq u_{u,p} + u_{l,p} \quad (\text{II.19h})$$

The upper and lower arm variables can be written as a function of $\Delta\Sigma$ quantities by inverting the previous relations,

$$i_{u,p} = i_{\Sigma,p} + \frac{i_{\Delta,p}}{2} \quad (\text{II.20a})$$

$$i_{l,p} = i_{\Sigma,p} - \frac{i_{\Delta,p}}{2} \quad (\text{II.20b})$$

$$v_{c,u,p} = -v_{\Delta c,p} + v_{\Sigma c,p} \quad (\text{II.20c})$$

$$v_{c,l,p} = v_{\Delta c,p} + v_{\Sigma c,p} \quad (\text{II.20d})$$

$$v_{m,u,p} = v_{\Sigma m,p} - v_{\Delta m,p} \quad (\text{II.20e})$$

$$v_{m,l,p} = v_{\Sigma m,p} + v_{\Delta m,p} \quad (\text{II.20f})$$

$$u_{u,p} = \frac{-u_{\Delta,p} + u_{\Sigma,p}}{2} \quad (\text{II.20g})$$

$$u_{l,p} = \frac{u_{\Delta,p} + u_{\Sigma,p}}{2} \quad (\text{II.20h})$$

II.2.6 External Dynamics

The external dynamics of the MMC, corresponds to its AC- and DC-side dynamics. But we are only interested in the AC dynamics which are obtained by computing (II.18a) + (II.18b),

$$v_{m,u,p} - v_{m,l,p} + (L - M + 2L_g) \frac{d}{dt} (i_{u,p} - i_{l,p}) + (R + 2R_g) (i_{u,p} - i_{l,p}) + 2v_{g,p} = 0 \quad (\text{II.21})$$

Insert Eqs. (II.19a), (II.19e) into Eq. (II.21) and arrange it to obtain

$$\frac{d}{dt} i_{\Delta,p} = -\frac{R_{\Delta}}{L_{\Delta}} i_{\Delta,p} + \frac{1}{L_{\Delta}} v_{\Delta m,p} - \frac{1}{L_{\Delta}} v_{g,p} \quad (\text{II.22})$$

with

$$L_{\Delta} \triangleq \frac{L - M + 2L_g}{2} \quad (\text{II.23a})$$

$$R_{\Delta} \triangleq \frac{R + 2R_g}{2} \quad (\text{II.23b})$$

In Eq. (II.22), the Δ -modulated voltage $v_{\Delta m,p}$ is the control variable imposing the AC power.

At this point, we rewrite the Δ -modulated voltage in terms of the Δ and the Σ capacitor's voltage. Insert Eq. (II.10a) into (II.19e),

$$v_{\Delta m,p} = -u_{u,p} \frac{v_{c,u,p}}{2N} + u_{l,p} \frac{v_{c,l,p}}{2N} \quad (\text{II.24})$$

Insert Eqs.(II.20c), (II.20d), (II.20g), (II.20h) into (II.24),

$$v_{\Delta m,p} = - \left(\frac{-u_{\Delta,p} + u_{\Sigma,p}}{2} \right) \left(\frac{-v_{\Delta c,p} + v_{\Sigma c,p}}{2N} \right) + \left(\frac{u_{\Delta,p} + u_{\Sigma,p}}{2} \right) \left(\frac{v_{\Delta c,p} + v_{\Sigma c,p}}{2N} \right) \quad (\text{II.25})$$

Reorganize (II.25) to obtain

$$v_{\Delta m,p} = \frac{u_{\Delta,p}}{2N} v_{\Sigma c,p} + \frac{u_{\Sigma,p}}{2N} v_{\Delta c,p} \quad (\text{II.26})$$

Insert (II.26) into (II.22) to obtain

$$\frac{d}{dt} i_{\Delta,p} = - \frac{R_{\Delta}}{L_{\Delta}} i_{\Delta,p} + \frac{u_{\Delta,p}}{2N} \frac{1}{L_{\Delta}} v_{\Sigma c,p} + \frac{u_{\Sigma,p}}{2N} \frac{1}{L_{\Delta}} v_{\Delta c,p} - \frac{1}{L_{\Delta}} v_{g,p} \quad (\text{II.27})$$

II.2.7 Internal Dynamics

The MMC internal dynamics correspond to the SM capacitor's voltage fluctuations and circulating current dynamics.

The circulating-current $i_{\Sigma,p}$ dynamics are obtained by computing (II.18a) - (II.18b),

$$- u_{dc} + v_{m,u,p} + v_{m,l,p} + (L + M) \frac{d}{dt} (i_{u,p} + i_{l,p}) + R (i_{u,p} + i_{l,p}) = 0 \quad (\text{II.28})$$

Insert Eqs. (II.19b), (II.19f) into Eq. (II.28) and reorganize it to obtain

$$\frac{d}{dt} i_{\Sigma,p} = - \frac{R}{L_{\Sigma}} i_{\Sigma,p} - \frac{1}{L_{\Sigma}} v_{\Sigma m,p} + \frac{1}{L_{\Sigma}} \frac{u_{dc}}{2} \quad (\text{II.29})$$

with

$$L_{\Sigma} \triangleq L + M \quad (\text{II.30})$$

Eq. (II.29) corresponds to the internal dynamics of the MMC, where the Σ modulated voltage $v_{\Sigma m,p}$ is the control variable.

Let us rewrite the Σ -modulated voltage as a function of the Δ and the Σ capacitor's voltage. Start by inserting Eq. (II.10a) into (II.19f),

$$v_{\Sigma m,p} = u_{u,p} \frac{v_{c,u,p}}{2N} + u_{l,p} \frac{v_{c,l,p}}{2N} \quad (\text{II.31})$$

Insert Eqs.(II.20c), (II.20d), (II.20g), (II.20h) into (II.31),

$$v_{\Sigma m,p} = \left(\frac{-u_{\Delta,p} + u_{\Sigma,p}}{2} \right) \left(\frac{-v_{\Delta c,p} + v_{\Sigma c,p}}{2N} \right)$$

$$+ \left(\frac{u_{\Delta,p} + u_{\Sigma,p}}{2} \right) \left(\frac{v_{\Delta c,p} + v_{\Sigma c,p}}{2N} \right) \quad (\text{II.32})$$

Reorganize (II.32) to obtain

$$v_{\Sigma m,p} = \frac{u_{\Delta,p}}{2N} v_{\Delta c,p} + \frac{u_{\Sigma,p}}{2N} v_{\Sigma c,p} \quad (\text{II.33})$$

Insert (II.33) into (II.29),

$$\frac{d}{dt} i_{\Sigma,p} = -\frac{R}{L_{\Sigma}} i_{\Sigma,p} - \frac{u_{\Delta,p}}{2N} \frac{1}{L_{\Sigma}} v_{\Delta c,p} - \frac{u_{\Sigma,p}}{2N} \frac{1}{L_{\Sigma}} v_{\Sigma c,p} + \frac{1}{L_{\Sigma}} \frac{u_{dc}}{2} \quad (\text{II.34})$$

The capacitor Δ -voltage dynamic equation is obtained by computing the difference between the upper and lower arm capacitor's dynamics from (II.6) divided by 2,

$$C \frac{d}{dt} \left(\frac{-v_{c,u,p} + v_{c,l,p}}{2} \right) = \frac{1}{2} (-u_{u,p} i_{u,p} + u_{l,p} i_{l,p}) \quad (\text{II.35})$$

Insert Eqs. (II.19c), (II.20a), (II.20b), (II.20g), (II.20h) into Eq. II.35,

$$C \frac{d}{dt} v_{\Delta c,p} = - \left(\frac{-u_{\Delta,p} + u_{\Sigma,p}}{4} \right) \left(i_{\Sigma,p} + \frac{i_{\Delta,p}}{2} \right) + \left(\frac{u_{\Delta,p} + u_{\Sigma,p}}{4} \right) \left(i_{\Sigma,p} - \frac{i_{\Delta,p}}{2} \right) \quad (\text{II.36})$$

Reorganize Eq. (II.36) to obtain the capacitor Δ -voltage dynamic equation,

$$\frac{d}{dt} v_{\Delta c,p} = -\frac{u_{\Sigma,p}}{4C} i_{\Delta,p} + \frac{u_{\Delta,p}}{2C} i_{\Sigma,p} \quad (\text{II.37})$$

The capacitor Σ -voltage dynamic equation is obtained by computing the difference of the upper and lower arm capacitor's dynamics from (II.6) divided by 2,

$$C \frac{d}{dt} \left(\frac{v_{c,u,p} + v_{c,l,p}}{2} \right) = \frac{1}{2} (u_{u,p} i_{u,p} + u_{l,p} i_{l,p}) \quad (\text{II.38})$$

Insert Eqs. (II.19d), (II.20a), (II.20b), (II.20g), (II.20h) into Eq. (II.38),

$$C \frac{d}{dt} v_{\Sigma c,p} = \left(\frac{-u_{\Delta,p} + u_{\Sigma,p}}{4} \right) \left(i_{\Sigma,p} + \frac{i_{\Delta,p}}{2} \right) + \left(\frac{u_{\Delta,p} + u_{\Sigma,p}}{4} \right) \left(i_{\Sigma,p} - \frac{i_{\Delta,p}}{2} \right) \quad (\text{II.39})$$

Reorganize Eq. (II.39) to obtain the capacitor Σ -voltage dynamic equation,

$$\frac{d}{dt} v_{\Sigma c,p} = -\frac{u_{\Delta,p}}{4C} i_{\Delta,p} + \frac{u_{\Sigma,p}}{2C} i_{\Sigma,p} \quad (\text{II.40})$$

II.2.8 State-Space Representation in abc Frame

The state variables are chosen to be the Δ -current $i_{\Delta,p}$, the Σ -current $i_{\Sigma,p}$, the Δ -capacitor voltage $v_{\Delta c,p}$ and the Σ -capacitor voltage $v_{\Sigma c,p}$.

The state-space representation for the phase p of the MMC can be expressed from Eqs. (II.27),(II.34) (II.37), (II.40) as

$$\frac{d}{dt}\mathbf{x}_p = \mathbf{A}_p \mathbf{x}_p + \mathbf{B}_p \mathbf{u}_p \quad (\text{II.41a})$$

$$\mathbf{y}_p = \mathbf{C}_p \mathbf{x}_p + \mathbf{D}_p \mathbf{u}_p \quad (\text{II.41b})$$

with

$$\mathbf{x}_p = \begin{bmatrix} i_{\Delta,p} \\ i_{\Sigma,p} \\ v_{\Delta c,p} \\ v_{\Sigma c,p} \end{bmatrix} \quad (\text{II.42a})$$

$$\mathbf{u}_p = \begin{bmatrix} v_{g,p} \\ u_{dc} \end{bmatrix} \quad (\text{II.42b})$$

$$\mathbf{A}_p = \begin{bmatrix} -\frac{R_{\Delta}}{L_{\Delta}} & 0 & \frac{u_{\Sigma,p}}{2N L_{\Delta}} & \frac{u_{\Delta,p}}{2N L_{\Delta}} \\ 0 & -\frac{R}{L_{\Sigma}} & -\frac{u_{\Delta,p}}{2N L_{\Sigma}} & -\frac{u_{\Sigma,p}}{2N L_{\Sigma}} \\ -\frac{u_{\Sigma,p}}{4C} & \frac{u_{\Delta,p}}{2C} & 0 & 0 \\ -\frac{u_{\Delta,p}}{4C} & \frac{u_{\Sigma,p}}{2C} & 0 & 0 \end{bmatrix} \quad (\text{II.42c})$$

$$\mathbf{B}_p = \begin{bmatrix} -\frac{1}{L_{\Delta}} & 0 \\ 0 & \frac{1}{2L_{\Sigma}} \\ 0 & 0 \\ 0 & 0 \end{bmatrix} \quad (\text{II.42d})$$

$$\mathbf{C}_p = \mathbb{I}_4 \quad (\text{II.42e})$$

$$\mathbf{D}_p = \mathbb{0}_{4 \times 2} \quad (\text{II.42f})$$

where \mathbb{I}_4 is the 4×4 identity matrix, $\mathbb{0}_{4 \times 2}$ the 4×2 zero matrix, and \mathbf{y}_p is chosen to be \mathbf{x}_p for simplicity.

Subsequently, the state-space representation of the three-phase MMC is

$$\frac{d}{dt}\mathbf{x} = \mathbf{A} \mathbf{x} + \mathbf{B} \mathbf{u} \quad (\text{II.43a})$$

$$\mathbf{y} = \mathbf{C} \mathbf{x} + \mathbf{D} \mathbf{u} \quad (\text{II.43b})$$

with

$$\mathbf{x} = \begin{bmatrix} \mathbf{x}_a \\ \mathbf{x}_b \\ \mathbf{x}_c \end{bmatrix} \quad (\text{II.44a})$$

$$\mathbf{u} = \begin{bmatrix} \mathbf{u}_a \\ \mathbf{u}_b \\ \mathbf{u}_c \end{bmatrix} \quad (\text{II.44b})$$

$$\mathbf{A} = \begin{bmatrix} \mathbf{A}_a & \mathbf{0}_4 & \mathbf{0}_4 \\ \mathbf{0}_4 & \mathbf{A}_b & \mathbf{0}_4 \\ \mathbf{0}_4 & \mathbf{0}_4 & \mathbf{A}_c \end{bmatrix} \quad (\text{II.44c})$$

$$\mathbf{B} = \begin{bmatrix} \mathbf{B}_a & \mathbf{0}_{4 \times 2} & \mathbf{0}_{4 \times 2} \\ \mathbf{0}_{4 \times 2} & \mathbf{B}_b & \mathbf{0}_{4 \times 2} \\ \mathbf{0}_{4 \times 2} & \mathbf{0}_{4 \times 2} & \mathbf{B}_c \end{bmatrix} \quad (\text{II.44d})$$

$$\mathbf{C} = \begin{bmatrix} \mathbf{C}_a & \mathbf{0}_4 & \mathbf{0}_4 \\ \mathbf{0}_4 & \mathbf{C}_b & \mathbf{0}_4 \\ \mathbf{0}_4 & \mathbf{0}_4 & \mathbf{C}_c \end{bmatrix} = \mathbb{1}_{12} \quad (\text{II.44e})$$

$$\mathbf{D} = \begin{bmatrix} \mathbf{D}_a & \mathbf{0}_{4 \times 2} & \mathbf{0}_{4 \times 2} \\ \mathbf{0}_{4 \times 2} & \mathbf{D}_b & \mathbf{0}_{4 \times 2} \\ \mathbf{0}_{4 \times 2} & \mathbf{0}_{4 \times 2} & \mathbf{D}_c \end{bmatrix} = \mathbf{0}_{12 \times 6} \quad (\text{II.44f})$$

where $\mathbf{0}_4$ represents the 4×4 zero matrix.

II.2.9 Harmonic State-Space Representation in abc Frame

We assume that $u_{\Delta,p}$ and $u_{\Sigma,p}$ are periodic. Thereby the matrices \mathbf{A}_p , \mathbf{B}_p , \mathbf{C}_p and \mathbf{D}_p of (II.41) are T-periodic, and the system (II.43) is a linear time-periodic (LTP) system.

The HSS method can transform an LTP system into a linear-time invariant (LTI) system, called the ‘‘harmonic state-space system.’’ The full mathematical background of this method is developed in Appendix A. In the following, we derive the detailed-arm harmonic state-space representation of the MMC in abc frame. The reader can jump to section II.3.3 for a comparison of this model with the averaged-arm HSS model and the time-domain averaged-arm model.

To transform the LTP system (II.43) into an LTI system using the HSS transformation, we need to write its matrices in terms of Fourier series and its state, input, and output vectors as exponentially modulated time-periodic (EMTP) signals.

Start by writing the following EMTP signals,

$$i_{\Delta,p} = e^{st} \sum_{k=-\infty}^{\infty} I_{\Delta,p,k} e^{jk\omega_0 t} \quad (\text{II.45a})$$

$$i_{\Sigma,p} = e^{st} \sum_{k=-\infty}^{\infty} I_{\Sigma,p,k} e^{jk\omega_0 t} \quad (\text{II.45b})$$

$$v_{\Delta c,p} = e^{st} \sum_{k=-\infty}^{\infty} V_{\Delta c,p,k} e^{jk\omega_0 t} \quad (\text{II.45c})$$

$$v_{\Sigma c,p} = e^{st} \sum_{k=-\infty}^{\infty} V_{\Sigma c,p,k} e^{jk\omega_0 t} \quad (\text{II.45d})$$

where $I_{\Delta,p,k}$, $I_{\Sigma,p,k}$, $V_{\Delta c,p,k}$ and $V_{\Sigma c,p,k}$ are the Fourier coefficients for the k -th harmonic of the system's state variables and $\omega_0 = 2\pi F_0$ with F_0 being the fundamental frequency.

The state vector \mathbf{x}_p of Eq. (II.41) can be written from Eq. (II.45) as

$$\mathbf{x}_p = e^{st} \sum_{k=-\infty}^{\infty} \begin{bmatrix} I_{\Delta,p,k} \\ I_{\Sigma,p,k} \\ V_{\Delta c,p,k} \\ V_{\Sigma c,p,k} \end{bmatrix} e^{jk\omega_0 t} \quad (\text{II.46})$$

or alternatively,

$$\mathbf{x}_p = e^{st} \sum_{k=-\infty}^{\infty} \mathbf{X}_{p,k} e^{jk\omega_0 t} \quad (\text{II.47})$$

with

$$\mathbf{X}_{p,k} = \begin{bmatrix} I_{\Delta,p,k} \\ I_{\Sigma,p,k} \\ V_{\Delta c,p,k} \\ V_{\Sigma c,p,k} \end{bmatrix} \quad (\text{II.48})$$

Also, let us define the AC-grid voltage and the DC voltage as EMTP signals,

$$v_{g,p} = e^{st} \sum_{k=-\infty}^{\infty} V_{g,p,k} e^{jk\omega_0 t} \quad (\text{II.49a})$$

$$u_{dc} = e^{st} \sum_{k=-\infty}^{\infty} U_{dc,k} e^{jk\omega_0 t} \quad (\text{II.49b})$$

where $V_{g,p,k}$ and $U_{dc,k}$ are the Fourier coefficients of the AC voltage and DC voltage, respectively.

The input vector \mathbf{u}_p of Eq. (II.41) can be written from (II.49) as,

$$\mathbf{u}_p = e^{st} \sum_{k=-\infty}^{\infty} \begin{bmatrix} V_{g,p,k} \\ V_{dc,k} \end{bmatrix} e^{jk\omega_0 t} \quad (\text{II.50})$$

or alternatively,

$$\mathbf{u}_p = e^{st} \sum_{k=-\infty}^{\infty} \mathbf{U}_{p,k} e^{jk\omega_0 t} \quad (\text{II.51})$$

with

$$\mathbf{U}_{p,k} = \begin{bmatrix} V_{g,p,k} \\ V_{dc,k} \end{bmatrix} \quad (\text{II.52})$$

Let us express the output vector of Eq. (II.41) as an EMTP signal,

$$\mathbf{y}_p = e^{st} \sum_{k=-\infty}^{\infty} \mathbf{Y}_{p,k} e^{jk\omega_0 t} \quad (\text{II.53})$$

Let us write the Fourier series of $u_{\Delta,p}$ and $u_{\Sigma,p}$,

$$u_{\Delta,p} = \sum_{k=-\infty}^{\infty} U_{\Delta,p,k} e^{jk\omega_0 t} \quad (\text{II.54a})$$

$$u_{\Sigma,p} = \sum_{k=-\infty}^{\infty} U_{\Sigma,p,k} e^{jk\omega_0 t} \quad (\text{II.54b})$$

Also, the other constant terms of the matrix \mathbf{A}_p in Eq. (II.42c) can be written as Fourier series,

$$\frac{R_{\Delta}}{L_{\Delta}} = \sum_{k=-\infty}^{\infty} \frac{R_{\Delta}}{L_{\Delta}} \delta_{0,k} e^{jk\omega_0 t} \quad (\text{II.55a})$$

$$\frac{R}{L_{\Sigma}} = \sum_{k=-\infty}^{\infty} \frac{R}{L_{\Sigma}} \delta_{0,k} e^{jk\omega_0 t} \quad (\text{II.55b})$$

where the operand $\delta_{0,k}$ denotes the Kronecker Delta defined more generically as

$$\delta_{m,k} \triangleq \begin{cases} 1, & \text{if } m = n, \\ 0, & \text{otherwise.} \end{cases} \quad (\text{II.56})$$

Insert Eqs.(II.54), (II.55) into (II.42c) to obtain,

$$\mathbf{A}_p = \sum_{k=-\infty}^{\infty} \begin{bmatrix} -\frac{R_{\Delta}}{L_{\Delta}} \delta_{0,k} & 0 & \frac{U_{\Sigma,p,k}}{2N L_{\Delta}} & \frac{U_{\Delta,p,k}}{2N L_{\Delta}} \\ 0 & -\frac{R}{L_{\Sigma}} \delta_{0,k} & -\frac{U_{\Delta,p,k}}{2N L_{\Sigma}} & -\frac{U_{\Sigma,p,k}}{2N L_{\Sigma}} \\ -\frac{U_{\Sigma,p,k}}{4C} & \frac{U_{\Delta,p,k}}{2C} & 0 & 0 \\ -\frac{U_{\Delta,p,k}}{4C} & \frac{U_{\Sigma,p,k}}{2C} & 0 & 0 \end{bmatrix} e^{jk\omega_0 t} \quad (\text{II.57})$$

or alternatively,

$$\mathbf{A}_p = \sum_{k=-\infty}^{\infty} \mathbf{A}_{p,k} e^{jk\omega_0 t} \quad (\text{II.58})$$

with

$$\mathbf{A}_{p,k} = \begin{bmatrix} -\frac{R_{\Delta}}{L_{\Delta}} \delta_{0,k} & 0 & \frac{U_{\Sigma,p,k}}{2N L_{\Delta}} & \frac{U_{\Delta,p,k}}{2N L_{\Delta}} \\ 0 & -\frac{R}{L_{\Sigma}} \delta_{0,k} & -\frac{U_{\Delta,p,k}}{2N L_{\Sigma}} & -\frac{U_{\Sigma,p,k}}{2N L_{\Sigma}} \\ -\frac{U_{\Sigma,p,k}}{4C} & \frac{U_{\Delta,p,k}}{2C} & 0 & 0 \\ -\frac{U_{\Delta,p,k}}{4C} & \frac{U_{\Sigma,p,k}}{2C} & 0 & 0 \end{bmatrix} \quad (\text{II.59})$$

The input matrix \mathbf{B}_p of Eq. (II.42) can be written as a complex Fourier series,

$$\mathbf{B}_p = \sum_{k=-\infty}^{\infty} \mathbf{B}_{p,k} e^{jk\omega_0 t} \quad (\text{II.60})$$

with

$$\mathbf{B}_{p,k} = \begin{bmatrix} -\frac{1}{L_{\Delta}} \delta_{0,k} & 0 \\ 0 & \frac{1}{2 L_{\Sigma}} \delta_{0,k} \\ 0 & 0 \\ 0 & 0 \end{bmatrix} \quad (\text{II.61})$$

The output matrix \mathbf{C}_p of Eq. (II.42) can be written as a complex Fourier series,

$$\mathbf{C}_p = \sum_{k=-\infty}^{\infty} \mathbf{C}_{p,k} e^{jk\omega_0 t} \quad (\text{II.62})$$

with

$$\mathbf{C}_{p,k} = \mathbb{1}_4 \delta_{0,k} \quad (\text{II.63})$$

The feed-forward matrix \mathbf{D}_p of Eq. (II.42) can be written as a complex Fourier series,

$$\mathbf{D}_p = \sum_{k=-\infty}^{\infty} \mathbf{D}_{p,k} e^{jk\omega_0 t} \quad (\text{II.64})$$

with

$$\mathbf{D}_{p,k} = \mathbf{0}_4 \quad (\text{II.65})$$

At this point, the matrices and vectors of the three-phase system given in Eq. (II.44) can be written as complex Fourier series and EMTP signals.

The state vector \mathbf{x} of Eq. (II.44) can be written as an EMTP signal,

$$\mathbf{x} = e^{st} \sum_{k=-\infty}^{\infty} \mathbf{X}_k e^{jk\omega_0 t} \quad (\text{II.66})$$

with

$$\mathbf{X}_k = \begin{bmatrix} \mathbf{X}_{a,k} \\ \mathbf{X}_{b,k} \\ \mathbf{X}_{c,k} \end{bmatrix} \quad (\text{II.67})$$

where the state vector's Fourier series coefficients for the generic phase p are given by Eq. (II.48).

The input vector of (II.44) is written as

$$\mathbf{u} = e^{st} \sum_{k=-\infty}^{\infty} \mathbf{U}_k e^{jk\omega_0 t} \quad (\text{II.68})$$

with

$$\mathbf{U}_k = \begin{bmatrix} \mathbf{U}_{a,k} \\ \mathbf{U}_{b,k} \\ \mathbf{U}_{c,k} \end{bmatrix} \quad (\text{II.69})$$

where the input vector's Fourier series coefficients for the generic phase p are given by Eq. (II.52).

The output vector of (II.44) is written as

$$\mathbf{y} = e^{st} \sum_{k=-\infty}^{\infty} \mathbf{Y}_k e^{jk\omega_0 t} \quad (\text{II.70})$$

with

$$\mathbf{Y}_k = \begin{bmatrix} Y_{a,k} \\ Y_{b,k} \\ Y_{c,k} \end{bmatrix} \quad (\text{II.71})$$

the output vector's Fourier coefficients have the same form of the state vector's Fourier series coefficients provided in Eq. (II.48) for the generic phase p .

The state matrix \mathbf{A} of Eq. (II.44) can be written as a complex Fourier series,

$$\mathbf{A} = \sum_{k=-\infty}^{\infty} \mathbf{A}_k e^{jk\omega_0 t} \quad (\text{II.72})$$

with

$$\mathbf{A}_k = \begin{bmatrix} \mathbf{A}_{a,k} & \mathbf{0}_4 & \mathbf{0}_4 \\ \mathbf{0}_4 & \mathbf{A}_{b,k} & \mathbf{0}_4 \\ \mathbf{0}_4 & \mathbf{0}_4 & \mathbf{A}_{c,k} \end{bmatrix} \quad (\text{II.73})$$

where the state matrix's Fourier series coefficients for the generic phase p are given by Eq. (II.59).

The input matrix \mathbf{B} of Eq. (II.44) can be written as a complex Fourier series,

$$\mathbf{B} = \sum_{k=-\infty}^{\infty} \mathbf{B}_k e^{jk\omega_0 t} \quad (\text{II.74})$$

with

$$\mathbf{B}_k = \begin{bmatrix} \mathbf{B}_{a,k} & \mathbf{0}_{4 \times 2} & \mathbf{0}_{4 \times 2} \\ \mathbf{0}_{4 \times 2} & \mathbf{B}_{b,k} & \mathbf{0}_{4 \times 2} \\ \mathbf{0}_{4 \times 2} & \mathbf{0}_{4 \times 2} & \mathbf{B}_{c,k} \end{bmatrix} \quad (\text{II.75})$$

where the input matrix's Fourier series coefficients for the generic phase p are given by Eq. (II.61).

The output matrix \mathbf{C} of Eq. (II.44) can be written as a complex Fourier series,

$$\mathbf{C} = \sum_{k=-\infty}^{\infty} \mathbf{C}_k e^{jk\omega_0 t} \quad (\text{II.76})$$

with

$$\mathbf{C}_k = \begin{bmatrix} \mathbf{C}_{a,k} & \mathbf{0}_{4 \times 2} & \mathbf{0}_{4 \times 2} \\ \mathbf{0}_{4 \times 2} & \mathbf{C}_{b,k} & \mathbf{0}_{4 \times 2} \\ \mathbf{0}_{4 \times 2} & \mathbf{0}_{4 \times 2} & \mathbf{C}_{c,k} \end{bmatrix} \quad (\text{II.77})$$

where the output matrix's Fourier series coefficients for the generic phase p are given by Eq. (II.63). The feed-forward matrix \mathbf{D}_p of Eq. (II.44) can be written as a complex Fourier series,

$$\mathbf{D} = \sum_{k=-\infty}^{\infty} \mathbf{D}_k e^{jk\omega_0 t} \quad (\text{II.78})$$

with

$$\mathbf{D}_k = \mathbf{0}_{12} \quad (\text{II.79})$$

Finally, the HSS representation of the system given in (II.44) is obtained by applying the same steps detailed in Appendix A and has the form,

$$s \mathbf{X} = (\mathcal{A} - \mathbf{N}) \mathbf{X} + \mathcal{B} \mathbf{U} \quad (\text{II.80a})$$

$$\mathbf{Y} = \mathcal{C} \mathbf{X} + \mathcal{D} \mathbf{U} \quad (\text{II.80b})$$

where \mathbf{X} , \mathbf{U} and \mathbf{Y} are vectors composed of the Fourier coefficients of Eqs. (II.67), (II.69) and (II.71), respectively, as defined in Eq. (A.102), the matrix \mathbf{N} is a block diagonal matrix as defined in Eq. (A.105e), and the matrices \mathcal{A} , \mathcal{B} , \mathcal{C} and \mathcal{D} are composed of the Fourier coefficients of Eqs. II.73, II.75, II.77 and II.2.9, respectively, and have a Toeplitz form as defined in Eq. (A.1.7). These matrices describe the evolution of the Fourier coefficients of \mathbf{x} , \mathbf{u} and \mathbf{y} as defined in Eqs. (II.66), (II.68) and (II.70), respectively.

The steady-state response of the system can be obtained by finding the limit for $s \rightarrow 0$ in (II.80a) and putting the obtained \mathbf{X} vectors into (II.80b) leading to,

$$\mathbf{Y} = \left(-\mathcal{C} (\mathcal{A} - \mathbf{N})^{-1} \mathcal{B} + \mathcal{D} \right) \mathbf{U} \quad (\text{II.81})$$

For practical reasons, the solution of the HSS system of equations can only be realized for an arbitrary finite number of harmonics. Consequently, the number of harmonics has to be truncated to a certain order. The truncated HSS representation is presented in Section A.4.2.4 of Appendix A.

II.3 Harmonic State-Space Models for the MMC

In this section, we develop two distinct HSS models for the MMC, the Averaged Arm-HSS model, and the proposed Detailed-Arm HSS (DA-HSS) model, which includes modulation indexes obtained by an arbitrary modulation technique. All equations used to obtain these models were developed in Section II.2.9.

For both models, we define the Δ -modulation $m_{\Delta,p}$ index for each phase as

$$\begin{bmatrix} m_{\Delta,a} \\ m_{\Delta,b} \\ m_{\Delta,c} \end{bmatrix} \triangleq \begin{bmatrix} M_{\Delta,1} \cos(\omega_0 t + \theta_{\Delta,1}) \\ M_{\Delta,1} \cos\left(\omega_0 t - \frac{2\pi}{3} + \theta_{\Delta,1}\right) \\ M_{\Delta,1} \cos\left(\omega_0 t + \frac{2\pi}{3} + \theta_{\Delta,1}\right) \end{bmatrix} \quad (\text{II.82})$$

where $M_{\Delta,1}$ is the modulation index amplitude and $\theta_{\Delta,1}$ the modulation index angle.

We also chose to write the AC and the DC-voltages as

$$u_{dc} = U_{dc} \quad (\text{II.83a})$$

$$\begin{bmatrix} v_{g,a} \\ v_{g,b} \\ v_{g,c} \end{bmatrix} = \begin{bmatrix} V_g \cos(\omega_0 t + \theta_g) \\ V_g \cos\left(\omega_0 t - \frac{2\pi}{3} + \theta_g\right) \\ V_g \cos\left(\omega_0 t + \frac{2\pi}{3} + \theta_g\right) \end{bmatrix} \quad (\text{II.83b})$$

where U_{dc} is the DC-voltage assumed to be constant, V_g corresponds to be AC voltage amplitude, which is the same for all phases in the balanced condition, and $\theta_{g,p}$ is the AC-voltage angle.

Then, the Fourier coefficients of Eq. (II.49) are written from (II.83) for the AA-HSS and DA-HSS models as

$$V_{g,p,k} = \frac{V_g}{2} \delta_{1,|k|} e^{jk\theta_{g,p}} \quad (\text{II.84a})$$

$$U_{dc,k} = U_{dc} \delta_{0,k} \quad (\text{II.84b})$$

The Fourier coefficients of the vector \mathbf{u}_p as defined in (II.51) can be written from (II.84) as

$$\mathbf{u}_{p,k} = \begin{bmatrix} \frac{V_g}{2} \delta_{1,|k|} e^{jk\theta_{g,p}} \\ U_{dc} \delta_{0,k} \end{bmatrix} \quad (\text{II.85})$$

II.3.1 Averaged-Arm HSS model

For the AA-HSS model, the arm modulation indices are defined as

$$u_{u,p} \triangleq \frac{N}{2} (1 - m_{\Delta,p}) \quad (\text{II.86a})$$

$$u_{l,p} \triangleq \frac{N}{2} (1 + m_{\Delta,p}) \quad (\text{II.86b})$$

From (II.86), the Δ and Σ arm modulation indices can be written from Eqs. (II.19g), (II.19h) as

$$u_{\Delta,p} = N m_{\Delta,p} \quad (\text{II.87a})$$

$$u_{\Sigma,p} = N \quad (\text{II.87b})$$

Notice that from the definition of the Δ -modulation index in Eq. II.82, the Δ and Σ switching functions, $u_{\Delta,p}$ and $u_{\Sigma,p}$ in Eq. II.87 are indeed periodic as assumed in Section II.2.9.

Consequently, the Fourier coefficients of Eq. (II.54) are written from (II.87) for the AA-HSS model as

$$U_{\Delta,p,k} = N \frac{M_{\Delta,1}}{2} \delta_{1,|k|} e^{jk\theta_{\Delta,p,1}} \quad (\text{II.88a})$$

$$U_{\Sigma,p,k} = N \delta_{0,k} \quad (\text{II.88b})$$

Subsequently, the Fourier coefficients of the matrix \mathbf{A}_p as defined in (II.58), can be written from (II.59) as

$$\mathbf{A}_{p,k} = \begin{bmatrix} -\frac{R_{\Delta}}{L_{\Delta}} \delta_{0,k} & 0 & \frac{1}{2L_{\Delta}} \delta_{0,k} & \begin{pmatrix} \frac{M_{\Delta,1}}{4L_{\Delta}} \delta_{1,|k|} \\ e^{jk\theta_{\Delta,p,1}} \end{pmatrix} \\ 0 & -\frac{R}{L_{\Sigma}} \delta_{0,k} & -\begin{pmatrix} \frac{M_{\Delta,1}}{4L_{\Sigma}} \delta_{1,|k|} \\ e^{jk\theta_{\Delta,p,1}} \end{pmatrix} & -\frac{\delta_{0,k}}{2L_{\Sigma}} \\ -\frac{N\delta_{0,k}}{4C} & \begin{pmatrix} \frac{NM_{\Delta,1}}{4C} \delta_{1,|k|} \\ e^{jk\theta_{\Delta,p,1}} \end{pmatrix} & 0 & 0 \\ -\begin{pmatrix} \frac{NM_{\Delta,1}}{8C} \delta_{1,|k|} \\ e^{jk\theta_{\Delta,p,1}} \end{pmatrix} & \frac{N\delta_{0,k}}{2C} & 0 & 0 \end{bmatrix} \quad (\text{II.89})$$

II.3.2 Detailed-Arm HSS model

For the DA-HSS model the arm modulation indices are defined as

$$u_{u,p} \triangleq \text{round} \left(\frac{N}{2} (1 - m_{\Delta,p}) \right) \quad (\text{II.90a})$$

$$u_{l,p} \triangleq \text{round} \left(\frac{N}{2} (1 + m_{\Delta,p}) \right) \quad (\text{II.90b})$$

The arms switching functions $u_{u,p}$, $u_{l,p}$ are obtained in the time domain from (II.90) and are converted to the frequency domain using a discrete Fast Fourier Transform (FFT) algorithm [68]. Also we write the AC and the DC-voltages in (II.83).

II.3.3 Validation

To validate the developed AA-HSS and DA-HSS models, we compare their steady-state simulation results with the time-domain averaged-arm model. For all the models, we consider the MMC with uncoupled arm coils whose parameters are listed in Appendix B. The AA-HSS and the DA-HSS models are implemented with a MATLAB® script where harmonics are truncated at the 2-nd and the 100th orders. The time-domain AA model is built with PLECS® following the procedure explained in [55].

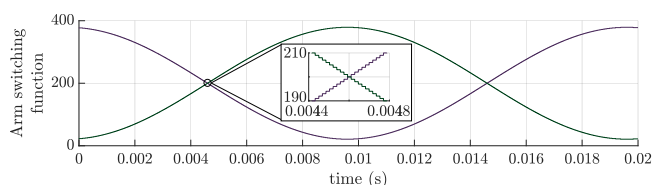
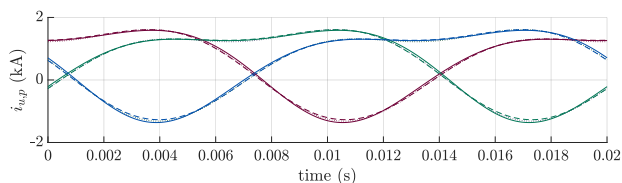
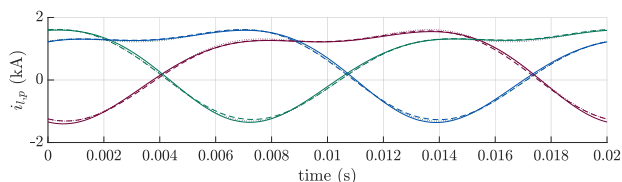


Figure II.5: Upper- and lower-arm switching function for the DA-HSS model represented in green and purple, respectively.

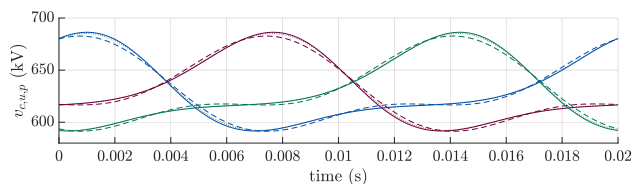
In Fig. II.6, we plot simulation results for the operation point P_{nom}, Q_{nom} . This operation point is set in the AA-HSS model with $M_{\Delta} = 0.8954$ and $\theta_{\Delta} = 0.1269$ and $M_{\Delta} = 0.8947$ and $\theta_{\Delta} = 0.1252$ in the DA-HSS model. Both models adopt an AC-voltage angle of $\theta_g = 0$.



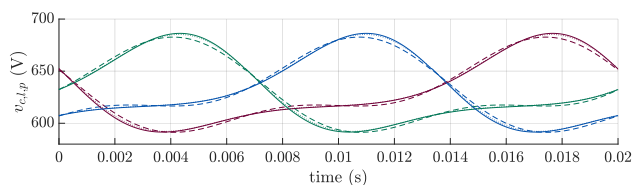
(a) Upper-arm currents.



(b) Lower-arm currents.



(c) Sum of the upper-arm capacitor voltages.



(d) Sum of the lower-arm capacitor voltages.

Figure II.6: AA model (solid line), AA-HSS model (dashed line), DA-HSS (dotted line) steady-state waveforms for the MMC at the nominal operation point.

The results are summarized in Fig. II.6. The different models are in good agreement. The difference is justified since the three models do not have the same harmonic range. In particular, the AA-HSS is truncated at the 2-nd harmonic, and alongside the AA model, they consider purely sinusoidal arm switching functions as defined in II.86. On the other hand, the DA-HSS model includes harmonic due to modulation by adopting arm switching functions as defined in Eq. (II.90) and representing up to the 100-th harmonic. Also, the difference between models is negligible since we are analyzing an MMC with 400 SMs capable of synthesizing a nearly-sinusoidal modulated voltage.

II.4 Summary

This chapter developed, implemented, and validated the proposed DA-HSS model for the reference HB-MMC introduced in Section I.4. This model will be used in the following chapters to estimate the steady-state performances of various proposed converters.

Chapter III

Study of a Modular Multilevel Converter with Coupled Arm Coils

In this chapter, we use the DA-HSS model developed in the previous chapter to design the arm coils of an HB-MMC. We propose to magnetically couple the arm coils. It is expected that a direct-coupling will allow us to reduce the size and weight of the arm coils (objective (i)). This proposition has been patented [1].

The objectives of this chapter are:

- To define steady-state performance indicators that need to be considered when designing an MMC.
- To design uncoupled and directly-coupled arm coils for the reference MMC defined in I.4.
- To assess the transient performance in normal and fault operation for the proposed MMCs.

This chapter is organized as follows. In Section III.1, we review current techniques and works focusing on arm inductance selection for the MMC. In section III.2, we define steady-state performance indicators for the MMC to evaluate a given converter design. In section Section III.3, we develop an arm inductance selection analysis based on the DA-HSS model for the HB-MMC with uncoupled and directly-coupled arm coils. In Section III.4, we compute the steady-state performance of the MMCs with arm coils configurations selected in the previous section. In Section III.5, we evaluate the transient performance in normal and fault operation conditions for HB-MMCs with uncoupled and directly-coupled arm coils. In Section III.6, we summarize the essential findings of this chapter.

III.1 Review on the Arm Coil Sizing for the MMC

The arm coils of the MMC should be designed to fulfill three different requirements [69]:

- (i) Filter the modulation harmonics on the AC current $i_{\Delta,p}$;
- (ii) Limit the harmonics of the circulating current $i_{\Sigma,p}$;

(iii) Limit the fault current.

The first requirement is usually the least restrictive since the AC current harmonics are very low in the MMC for HVDC applications. This is justified by the converter's high number of voltage levels leading to an AC modulated voltage with very low harmonic distortion.

The second requirement shall avoid the resonance of even-harmonics in the converter's arm currents and typically leads to an inductance value of 0.05 p.u. fulfilling simultaneously the requirements (i) and (ii). Alternatively, circulating current control loops can be added to suppress these harmonics.

The third requirement is the most restrictive and typically leads to an inductance value of 0.10–0.15 p.u. fulfilling simultaneously the requirements (i), (ii) and (iii).

In [70], the authors use an averaged-arm model to evaluate the impact of the arm inductance on the converter's arm currents. The work points out a resonance effect on the arm currents' second and fourth-order harmonic where arm currents' steady-state peak value can be up to six times the AC current. The authors conclude that the resonance region must be avoided by adequately selecting the parameters of passive components in consideration of all possible resonances.

In [71], the authors employ the time-independent phasor model to study the impact of the arm inductance on the second-order harmonic of the arm current. This phasor model is derived from the averaged-arm state-space representation of the MMC and can reproduce any quantity up to the second harmonic. The authors point out the existence of a resonance effect of the second harmonic of the arm currents and conclude that suppressing these harmonics by adequately selecting the arm inductance, despite its feasibility, would lead to bulky arm coils, which make this strategy rather ineffective.

In [72], the authors present a technique to minimize the values of arm inductances and SM capacitances based on the analytical formulation of the MMC. The work points out a resonance effect on the arm currents' second and fourth-order harmonic and chooses the arm inductance to operate the converter between the second and fourth harmonic resonance. This choice leads to a small arm inductance that provides suitable arm current levels but cannot ensure the limitation current in the case of a short-circuit on the converter's DC side.

In [73], the authors investigate the selection of arm inductance for the MMC using a time-dependent model where the converter is either modulated by a phase-shift or a phase-disposition pulse width technique. This work analyzes the impact of the arm inductance on the efficiency of the MMC by calculating the switching and conduction losses on the converter's solid-state devices. Equally important, the work studies the impact of the arm inductance on the AC-side harmonic performance by evaluating the total harmonic distortion (THD) of the AC modulated voltage.

In [74], the author studies the impact of the arm coils' inductance and resistance in the PQ diagram of the converter, which is a tool to evaluate whether the designed MMC can cover the required active and reactive power requirement. This study concludes that the arm inductance and resistance have a similar effect on the converter PQ diagram's and increasing either of the two parameters decreases the converter's operating area.

In this chapter, we propose a novel analysis by including the influence of modulation harmonics considering the nearest level modulation technique and adopting arm coils' inductance and resistance values obtained from a designed-based analysis of dry-type air-core coils. In the following paragraphs, we develop this analysis based on the MMC DA-HSS model presented in Section II.3.2.

The main improvements in the following analysis, with regard to previous studies, are:

- Contrarily to [70], [71] and [72], we do not truncate the MMC state variables' harmonics at the second or the fourth-order, and thus the influence of any other low-order harmonics is reproduced.
- We include the effect of the nearest level modulation technique, the standard technique for MMCs in HVDC applications.
- When varying the arm inductance, we also change the arm resistance with values obtained from the design of dry-type air-core coils. In [70],[71], [72] and [73], the arm coil resistance is kept constant for every inductance value, whose impact has only been evaluated in [74].
- To compare the performance of the MMC for different pairs of arm inductance and resistance, the converter is set to operate at the most restrictive operating point inside its PQ requirements. In [70], [72] and [73], the arm inductance and resistance are changed for a constant pair of Σ - Δ -modulation indices. Consequently, for each pair of arm inductance and resistance, the converter operates at different points, and comparing these points among them seems somewhat inaccurate.

III.2 Steady-State Performance Indicators

To size the arm inductance, we need to define some performance indicators (PIs). These indicators have been selected to quantify the voltage and current stress in the solid-state switches, the converter's harmonic performance, and its overall steady-state efficiency.

III.2.1 Capacitor Voltage Ripple

The capacitor voltage ripple depends on both the SM capacitance and the arm inductance and resistance. For designing the latter, Ref. [69] proposed a

common rule of thumb for HVDC applications, whereby the average stored energy is chosen based on the power rating to be in the range of 45 kJ/MVA and 60 kJ/MVA.

In order to evaluate the capacitor voltage waveform for a given design, we define the total capacitor voltage ripple as

$$\Delta v_{c,(u,l),p} = \frac{1}{V_{c,(u,l),p,0}} \left(\max_{t \in [(k-1)T_0, kT_0]} \{v_{c,(u,l),p}\} - \min_{t \in [(k-1)T_0, kT_0]} \{v_{c,(u,l),p}\} \right) \quad (\text{III.1})$$

The ripple on the SMs capacitor voltages in the MMC is an indicator of central importance since all the off-state switching devices of a given SM are subjected to its capacitor voltage. A suitable design must ensure that the peak value of individual capacitor voltages does not surpass the collector-emitter breakdown voltage of the IGBT module. Equally important, the failure rate of IGBTs is strongly dependent on the applied voltage, which is also an aspect to be considered when analyzing the obtained capacitor's voltage waveform for a given design [75].

III.2.2 Maximum and Minimum Arm Currents

To evaluate the arm current's extreme values for a given set of passive components, we define the maximum and the minimum arm currents as

$$i_{(u,l),p}^{max} \triangleq \max_{t \in [(k-1)T_0, kT_0]} \{i_{(u,l),p}\} \quad (\text{III.2a})$$

$$i_{(u,l),p}^{min} \triangleq \min_{t \in [(k-1)T_0, kT_0]} \{i_{(u,l),p}\} \quad (\text{III.2b})$$

The extreme values of the MMC's arm currents must be kept lower than the rated collector-emitter current of IGBTs modules employed in each SM. The set of passive components values leading to the resonance of arm current should be avoided by design since arm currents are substantially high in these regions and can jeopardize SMs.

III.2.3 Weighted Total Harmonic Distortion of the AC-modulated Voltage

The modulated voltage of any VSC contains undesirable harmonics due to the inherent switching behavior of power electronic equipment. These harmonics are directly transferred to the AC currents, and one must quantify the harmonic injection during the converter's operation.

In the MMC, the Δ -modulated voltage is filtered by inductive equipment, namely the arm coils and any other inductance between the converter AC

midpoint and the AC grid. For that reason, the performance index to quantify harmonic distortion is chosen to be the weighted total harmonic distortion (WTHD) of the modulated voltage.

The Δ -modulated voltage WTHD is calculated from its complex Fourier coefficients as

$$WTHD\{v_{\Delta m,p}\} = \sqrt{\frac{1}{|V_{\Delta m,p,1}|^2} \sum_{k=2}^{\infty} \frac{|V_{\Delta m,p,k}|^2}{k^2}} \quad (\text{III.3})$$

The WTHD, defined in [76], is a measurement of the harmonic distortion present in a given signal. Its difference regarding the classical THD is that the WTHD weights the voltage harmonics inversely with their frequencies. Thus the lower portion of the frequency spectra is weighted more heavily (i.e., inversely with frequency), providing a picture of the expected AC current's harmonics filtered by an inductive load.

III.2.4 Arm Coil Losses

The arm coil resistive losses impact the overall conversion efficiency. Consequently, the resistance of these coils should be kept as low as possible. The instantaneous arm coil losses can be computed as

$$p_{coil,p} = R_{coil} (i_{u,p}^2 + i_{l,p}^2) \quad (\text{III.4})$$

The average coil losses per phase of the MMC can be computed as

$$P_{coil,p} = R_{coil} \frac{1}{T_0} \int_{(k-1)T_0}^{kT_0} (i_{u,p}^2 + i_{l,p}^2) dt \quad (\text{III.5})$$

or alternatively

$$P_{coil,p} = R_{coil} \left((i_{u,p}^{rms})^2 + (i_{l,p}^{rms})^2 \right) \quad (\text{III.6})$$

The total average coil's losses for the MMC are given by

$$P_{coil} = P_{coil,a} + P_{coil,b} + P_{coil,c} \quad (\text{III.7})$$

The resistance of a coil is directly correlated with its physical design and construction. In Appendix C, we develop an approach to design dry-type air-core coils based on the physical form of these devices using analytical inductance formulas. Notice that the inductance (in Henrys) and the rated current are initial design constraints when designing a coil, and its resistance is a consequence of its physical design and construction. For instance, the evolution of inductance and resistance of dry-type air-core coils designed for a nominal current of 1.75 kA is shown in Fig. C.2.

III.2.5 Conduction and Switching Losses of Solid-State Devices

The MMC's IGBTs and diodes generate both steady-state conduction losses and switching losses during the converter operation.

Conduction losses occur while the IGBT or its freewheeling diode is on and conducting current. Since both IGBTs and diodes have non-zero on-state voltages, a certain amount of energy is lost during conduction.

Switching losses occur during the state transition of the solid-state device when both the current through and the voltage across the device are non-zero, thus leading to instantaneous power loss.

A procedure to calculate the switching and conduction losses for the HB-MMC is fully developed in Appendix D.

The average conduction losses for the MMC are computed as

$$P_{cond} = P_{cond,a} + P_{cond,b} + P_{cond,c} \quad (\text{III.8})$$

where $P_{cond,a}$, $P_{cond,b}$ and $P_{cond,c}$ are the conduction losses for the converter's arm for the phase a , b , and c , respectively.

The average switching losses for the MMC are computed as

$$P_{sw} = P_{sw,a} + P_{sw,b} + P_{sw,c} \quad (\text{III.9})$$

where $P_{cond,a}$, $P_{sw,b}$ and $P_{sw,c}$ are the switching losses for the converter's arm for the phase a , b , and c , respectively.

III.3 Arm Inductance Sizing Using the HSS model

In this section, we size the arm inductance based on the steady-state PIs defined in Section III.2 for an HB-MMC with uncoupled and directly-coupled arm coils based on the parameters of the reference MMC presented in section I.4.

To calculate the MMC state variables and its steady-state PIs over the set of arm inductance and resistance values given in Fig. C.2, obtained in Appendix C from the design dry-type air-core coils with physical considerations, we employ the DA-HSS model truncated at the 100-th harmonic as developed in Section II.3.2. Notice that the SM capacitance is kept at $C = 11$ mF for any arm inductance and resistance.

The Σ -modulation index is adopted to be $m_{\Sigma,p} = 1$ in order to impose the Σ -modulated voltage equal to $v_{\Sigma m} = U_{dc}/2$ (see Appendix E.1.1). The Δ -modulation index $m_{\Delta,p}$, defined in Eq. (E.8), is computed to impose the desired active and reactive power references, denoted P^* and Q^* , respectively, on the converter's AC side.

In particular, to obtain the Δ -modulation index amplitude and phase, $M_{\Delta m,p}$ and $\theta_{\Delta,p}$, respectively, that imposes the active and reactive equal to their references, we solve the following non-linear least-squares minimization problem,

$$\min_{M_{\Delta,p}, \theta_{\Delta,p}} \left(|P - P^*|^2 + |Q - Q^*|^2 \right) \quad (\text{III.10})$$

where P and Q are the active and reactive power on the AC side of the converter computed using the DA-HSS model (see Section II.3.2), and they depend on the Δ -modulation index with $M_{\Delta m,p} \in [0, 1.2]$ and $\theta_{\Delta m,p} \in [-\pi, \pi]$.

The total arm coil's losses and the conduction and switching losses for the converter are determined from Eqs. (III.7), (III.8) and (III.9). To account for the losses generated by the voltage balancing control, we adopt the voltage balancing algorithm presented in Appendix E.1.2 in which we allow three additional SMs switching events at each arm switching function transition. In addition, we assume the junction temperature for every solid-state device of the MMC to be $T_j = 85^\circ\text{C}$. Besides, we consider each submodule composed of a single IGBT module with a rated collector-emitter voltage of $V_{CE} = 4.5$ kV and a rated collector current of $I_C = 3$ kA. The on-state voltages for this IGBT module can be found in Fig. D.2, and its on, and off-switching energies are shown in Fig. D.3.

For each pair of (L, R) under consideration, the operation of the converter is swept through all possible operating points, that is, the area defined by $P \in [-P_{nom}, P_{nom}]$ and $Q \in [-Q_{nom}, Q_{nom}]$. Among all of these operation points, we find the one that maximizes all of the steady-state performance indicators defined in Section III.2. It turns out that all the steady-state PIs reach their extreme values when the MMC injects the nominal active and reactive power to the AC-grid, i.e., $P = P_{nom}$ and $Q = Q_{nom}$.

III.3.1 Uncoupled Arm Coils

In Figs. III.1 and III.2, we present the results for the HB-MMC with uncoupled arm coils, from which we draw the following conclusions.

- In Figs. III.1a and III.1b, we plot the values of the Δ -modulation index amplitude and angle for which the MMC with different uncoupled coils operate at (P_{nom}, Q_{nom}) as shown in Fig. III.1c.
- In Figs. III.2a and III.2b, three resonances are identified at which the extreme values of arm currents are substantially high. The points (1), (2), and (3) correspond respectively to the resonance of the 6-th, 4-th, and 2-nd arm current harmonics. For the reference case defined in Appendix B where $L = 50.9$ mH (star marker), the maximum absolute value of arm currents is 1.53 kA.
- Fig. III.2c shows the evolution of the capacitor voltage ripple in terms of the arm inductance. For the reference case, the capacitor voltage ripple is $\Delta V_{c,(u,l),p} = 0.14$ p.u. Also, the inductance value leading to the 2-nd harmonic resonance yields a substantially high capacitor voltage ripple of $\Delta V_{c,(u,l),p} = 0.85$ p.u. for $L = 20.64$ mH. The inductance values in the zone around it shall be avoided to maintain $\Delta V_{c,(u,l),p} \leq 0.2$ p.u. The

minimum voltage ripple is obtained for the lowest arm inductance value $L = 0.082$ mH where $\Delta V_{c,(u,l),p} = 0.064$ p.u.

- The evolution of the WTHD is shown in Fig. (III.2d). For the reference case the WTHD of the Δ -modulated voltage is $WTHD\{v_{\Delta mp}\} = 3.88 \cdot 10^{-5}$. Smaller values for the $WTHD\{v_{\Delta mp}\}$ than the reference case are obtained for arm inductances $L > 50.9$ mH but also for the $L \leq 4.2$ mH.
- The evolution of the arm coil losses and the conduction and switching losses of solid-state devices in terms of the arm inductance is shown in Fig. III.2e. For the reference MMC, switching losses accounts for 68 % of losses while conduction and arm coil losses accounts for 23 % and 9%, respectively. Fig. (III.2f) shows the total converter losses normalized by the converted active power $P = P_{nom}$. The normalized losses for the reference case is 0.79% of P_{nom} . Since resonance points lead to relatively high losses, they should be avoided by design, for $L = 20.54$ mH losses achieve 8.7 % of P_{nom} .

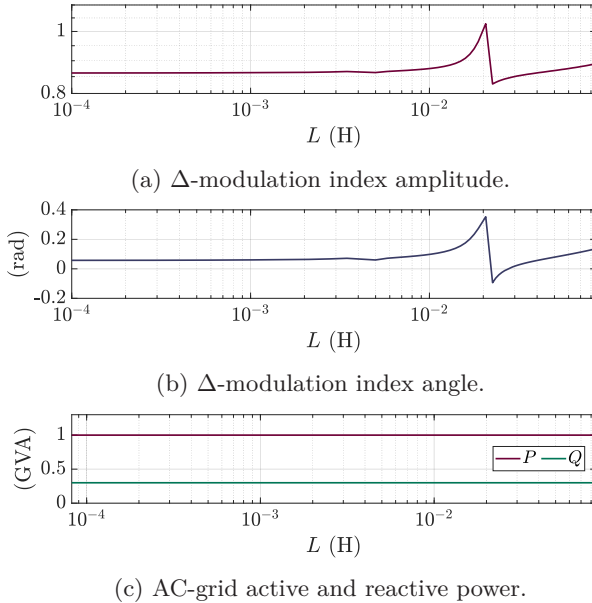


Figure III.1: Operation set-point for the MMC with uncoupled arm coils.

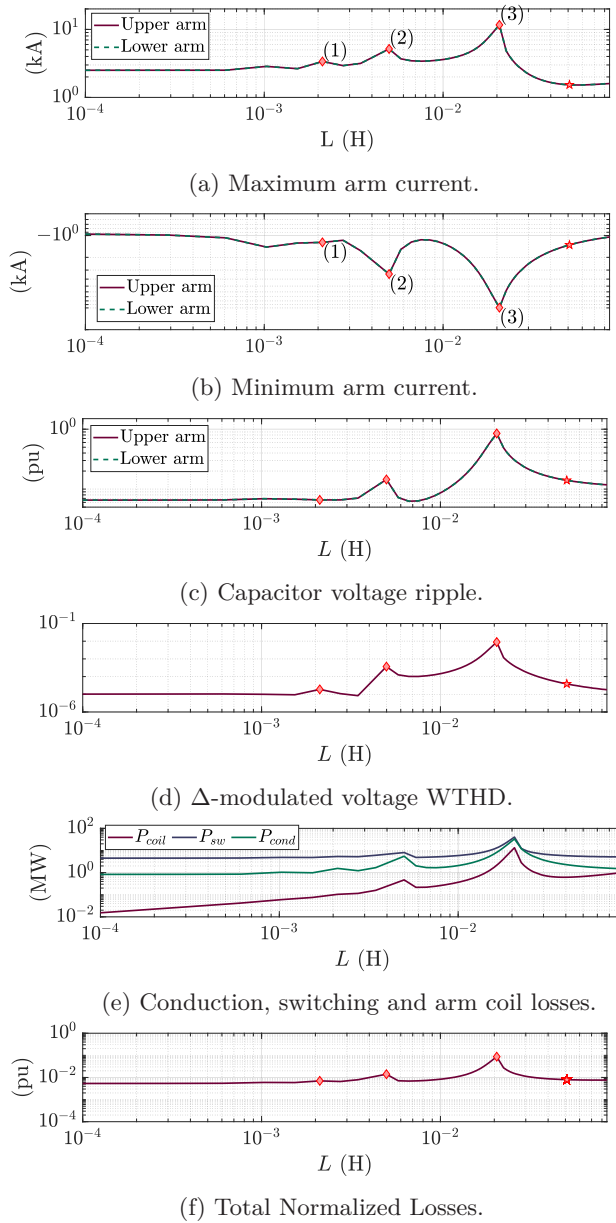


Figure III.2: Evolution of the performance indicators for the MMC with uncoupled arm coils.

III.3.2 Directly-Coupled Arm Coils

In Figs. III.3, III.4, we present the results for directly-coupled arm coils with a coupling coefficient $K_{(u,l)}$ extracted from Fig. C.2b, from which we draw the following conclusions.

- In Figs. III.4a and III.4b, three resonances are identified as indicated by the points (1), (2), and (3) corresponding respectively to the resonance of the 6-th, 4-th, and 2-nd arm current harmonics. To keep the absolute value of arm currents at the reference MMC's level, we can adopt $L = 27.3$ mH.

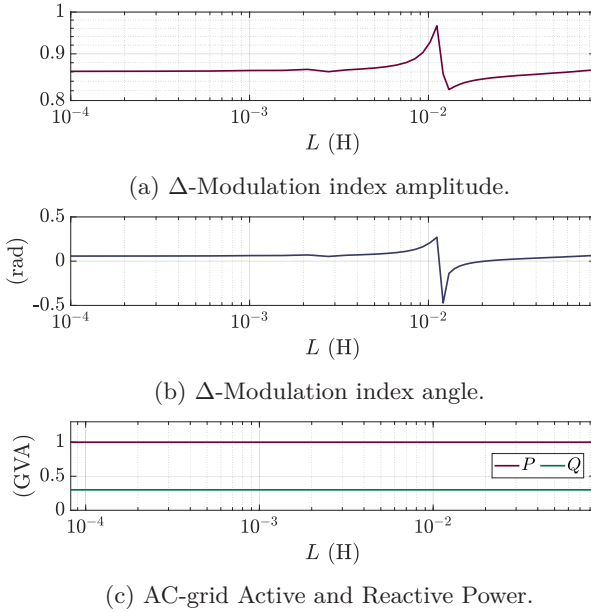
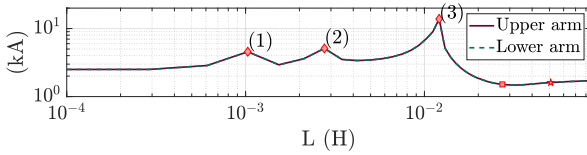


Figure III.3: Operation set-point for the MMC with directly-coupled arm coils.

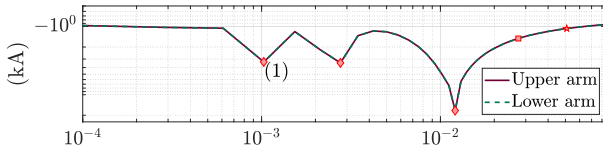
- Fig. III.4c shows the evolution of the capacitor voltage ripples in terms of the arm self-inductance for directly-coupled arm coils. Directly-coupling two reference coils with $L = 50.9$ mH (star marker) would lead to $\Delta V_{cup} = 0.117$ p.u. while coupling two coils with $L = 27.3$ mH (square marker) would lead to $\Delta V_{cup} = 0.1480$ p.u. corresponding to the reference MMC's voltage ripple level.
- The evolution of the WTHD is shown in Fig. (III.4d) in terms of the arm self-inductance for directly-coupled arm coils. Directly-coupling two reference coils would lead to $WTHD\{v_{\Delta mp}\} = 1.9 \cdot 10^{-5}$ while coupling

two coils with $L = 27.3$ mH would lead to $WTHD\{v_{\Delta mp}\} = 5.2 \cdot 10^{-5}$ which is higher than the reference value $WTHD\{v_{\Delta mp}\} = 3.88 \cdot 10^{-5}$.

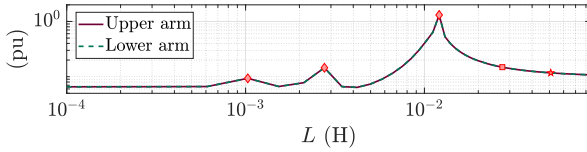
- The evolution of the arm coil losses and the conduction and switching losses of solid-state devices in terms of the arm self-inductance for directly-coupled arm coils is shown in Fig. III.4e. Fig. (III.4f) shows the total converter losses normalized by the converted active power $P = P_{nom}$. Directly-coupling two reference coils would lead to a normalized losses level of 0.69% of P_{nom} , thus reducing losses by 12.67% compared to the reference case. Coupling two coils with $L = 27.3$ mH would lead to a normalized losses level of 0.785 % of P_{nom} which equals the reference level.



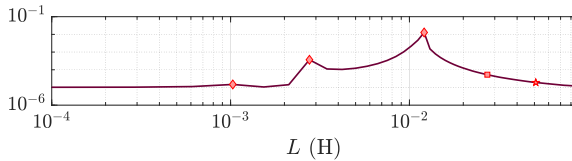
(a) Maximum arm current.



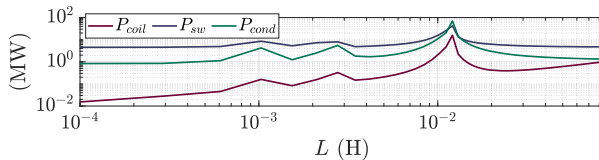
(b) Minimum arm current.



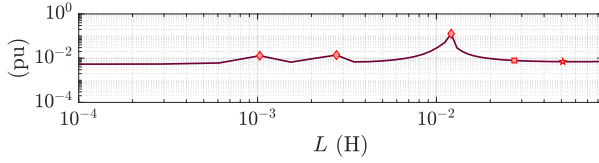
(c) Capacitor voltage ripple.



(d) Δ -modulated voltage WTHD.



(e) Conduction, switching and arm coil losses.



(f) Total Normalized Losses.

Figure III.4: Evolution of the performance indicators of the MMC with directly-coupled arm coils.

In conclusion, directly-coupled arm coils can be designed with different objectives: keep a similar size while improving the performances, or reduce the size while keeping similar performance.

Therefore, we define three MMC configurations:

- MMC #0: an MMC with 400 HB-SMs and conventional uncoupled dry-type air-core arm coils. It corresponds to the reference MMC defined in Section I.4.
- MMC #1: an MMC with 400 HB-SMs and directly-coupled arm coils, that are designed to keep the similar size while improving the performances.
- MMC #2: an MMC with 400 SMs and directly-coupled arm coils, that are designed to reduce the size while keeping the same performances.

The corresponding specifications are summarized in Table III.1. A visual comparison of the coupled air-core arm coils with the reference uncoupled coils is proposed in Fig. III.5.

	MMC		
	#0	#1	#2
R [Ω]	$90.4 \cdot 10^{-3}$	$90.4 \cdot 10^{-3}$	$51.2 \cdot 10^{-3}$
L [H]	$50.9 \cdot 10^{-3}$	$50.9 \cdot 10^{-3}$	$27.3 \cdot 10^{-3}$
$K_{u,l}$	0	0.6517	0.6740
Conductor length [m]	$5.98 \cdot 10^3$	$5.98 \cdot 10^3$	$3.38 \cdot 10^3$
Mass [t]	85	85	48

Table III.1: Dry-type air-core arm coils specifications. Mass and conductor length, computed in Appendix C, are given for a set of 2 coils.

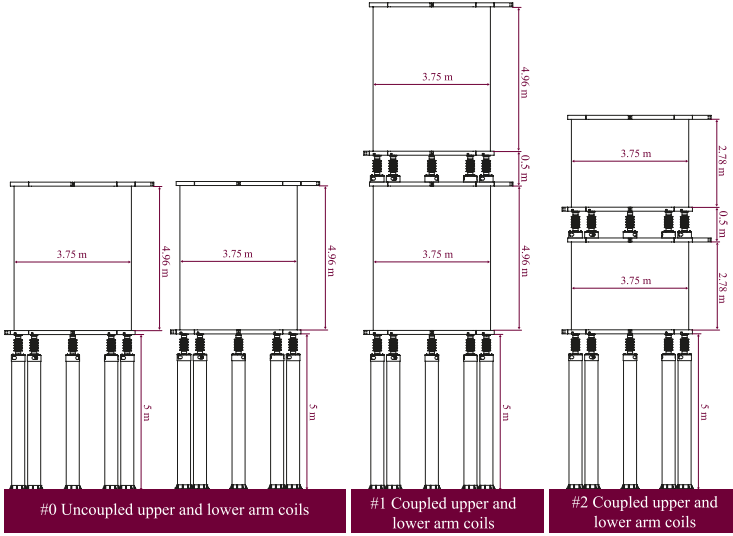


Figure III.5: Mock-up of the coupled air-core arm coils.

III.4 Steady-State Analysis

In this section, we evaluate the steady-state performances of the proposed MMCs with coupled arm coils and compare them with the reference MMC #0. This is done by calculating the performance indicators defined in section III.2 using the DA-HSS model developed in section II and the data from Table III.1. The results are summarized in Table III.2.

	MMC		
	#0	#1	#2
P_{cond} [kW]	1860.60	1472.5	2002.49
P_{sw} [kW]	5422.9	4875.5	5415.60
P_{coil} [kW]	677.21	619.43	401.89
$\Delta v_{c,(u,l),p}$ [p.u.]	0.1401	0.1172	0.1488
$WTHD\{v_{\Delta m,p}\}$	$3.9 \cdot 10^{-5}$	$1.9 \cdot 10^{-5}$	$5.2 \cdot 10^{-5}$
$\max\{i_{(u,l),p}\}$ [kA]	1.5316	1.6077	1.5112
$\min\{i_{(u,l),p}\}$ [kA]	-1.3485	-1.0707	-1.4996

Table III.2: MMCs #0, #1 and #2 performance indicators evaluated for $P = P_{nom}$ and $Q = Q_{nom}$.

As shown in Table III.2, the MMC #1 has improved steady-state performance indicators compared to the reference MMC #0. In particular, conversion losses are reduced by 12.67%. The MMC #3 performs similarly to the MMC #0, and both topologies produce the same amount of conversion losses.

III.5 Transient Analysis

In this section, we evaluate the transient performances of the proposed MMCs #1 and #2 and compare them with the reference MMC #0.

III.5.1 Modeling

For the transient analysis, we use a circuit simulation of the reference case defined in section I.4 and illustrated in Fig. III.6. The simulation is carried out with PLECS. We only model the converter CMA1 in detail, while CMC1 is modelled by a controlled DC voltage source.

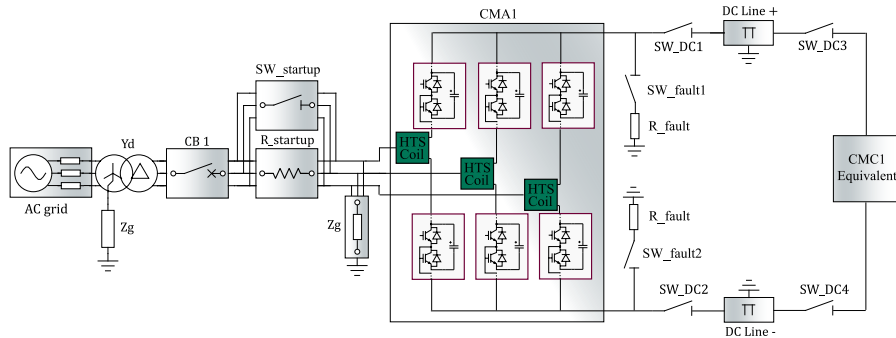


Figure III.6: P2P HVDC link circuit.

For CMA1, the SMs of an arm are modeled as proposed in [77] and illustrated in Fig. III.7. This model makes the same assumptions as the AA-HSS model developed in Chapter II and is also capable of reproducing the MMC’s arm behavior when SMs are blocked. An arm is blocked if all its SM’s IGBTs are turned off. The signal *blk* is introduced to activate the blocking state of the arm, blocked when *blk* = 1 and unblocked when *blk* = 0.

The adopted controller has a conventional cascaded structure in the dq-reference frame. A fast inner current loop controls the converter d- and q-axis currents. Outer slower loops control the active and reactive powers. This control structure in detail led in Appendix E. The controllers of the compared converter are tuned to ensure similar closed-loop control performances, and their values are summarized in Table E.1.

In all the time-domain responses presented in this section, dotted lines represent the MCC #0, dashed lines represent the MMC #1 and solid lines

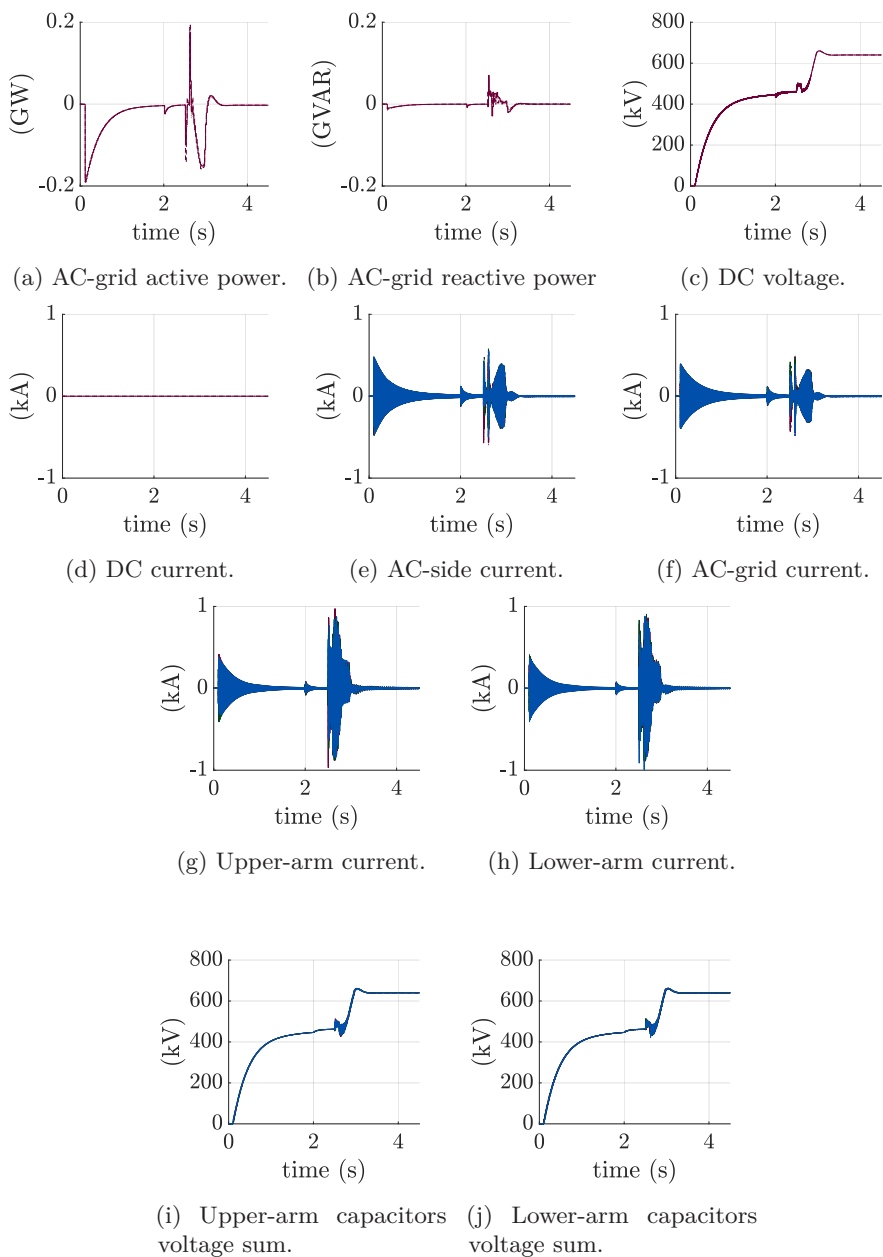


Figure III.8: Simulation results for the start-up sequence from 0 s to 4.5 s. Dotted lines represent the MCC #0, dashed lines represent the MMC #1 and solid lines represent the MMC #2.

During the start-up process, the charging of the SM capacitors and the DC

cable is realized by draining the power from the AC grid, as shown in Figs. III.8a and III.8b.

As plotted in Figs. III.8a and III.8b, after closing $CB1$ at $t = 0.1$ s, the DC cables are charged through the highly resistive start-up resistors and reaches $U_{dc} = 446$ kV at $t = 2$ s. The start-up resistors are bypassed at $t = 2$ s by the switch $SW_{startup}$, and consequently the DC-side voltage reaches a new intermediary value of $U_{dc} = 462$ kV at $t = 2.5$ s. The converter is unblocked at $t = 2.5$ s and the DC-voltage control is activated at $t = 2.6$ s which brings the DC-side voltages to $U_{dc} = 640$ kV at $t = 3.6$ s. The sum of upper- and lower-arm capacitors voltages follows the same behavior as U_{dc} during the start-up process, as shown in Figs. III.8i and III.8j.

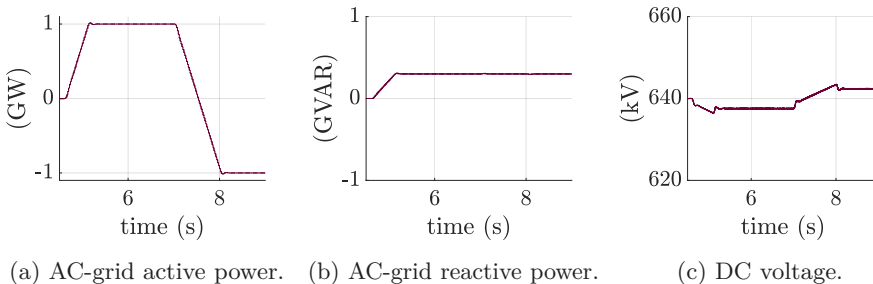
In Figs. III.8e, III.8f, III.8g and III.8h, we identify different inrush currents relative to the charging of capacitors and DC cables.

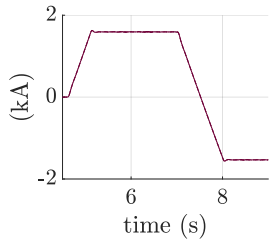
No significant difference was observed when comparing the start-up process between MMCs #0, #1 and #2.

Once the SM capacitors and DC cables have been charged, the converter can start to transfer power which is simulated as follows.

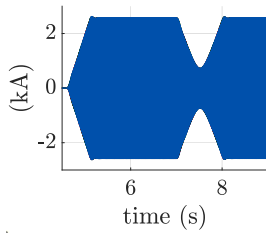
- At $t = 4.55$ s, the switches SW_{DC3} and SW_{DC4} are closed.
- At $t = 4.6$ s, the DC-voltage regulation of CMA1 is turned off, and the PQ control is activated. The converter CMC1 is put in charge of controlling the DC voltage while CMA1 controls the DC active power.
- Once CMA1 is in PQ control mode, the active and reactive powers are ramped up to their nominal values P_{nom}, Q_{nom} .
- At $t = 7$ s, the link active power is ramped down to $-P_{nom}$.

The results for the proposed operation sequence are plotted in Fig. III.9.

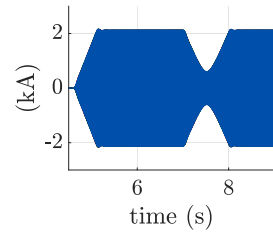




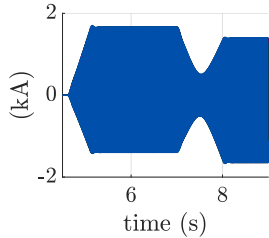
(d) DC current.



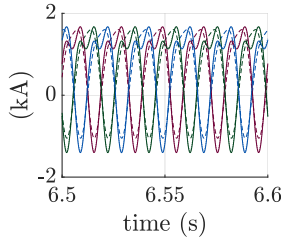
(e) AC-side current.



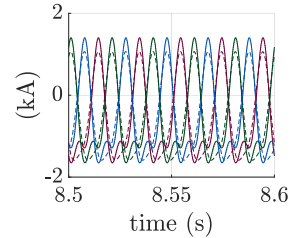
(f) AC-grid current.



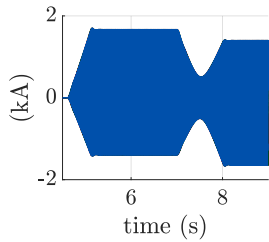
(g) Upper-arm current.



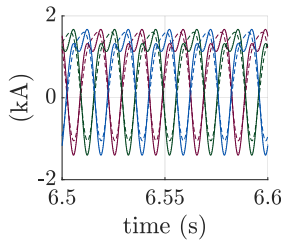
(h) Upper-arm current: zoom between 6.5 s and 6.6 s.



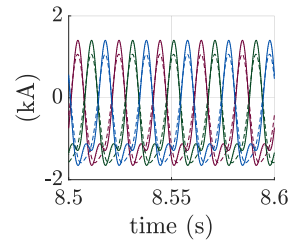
(i) Upper-arm current: zoom between 8.5 s and 8.6 s.



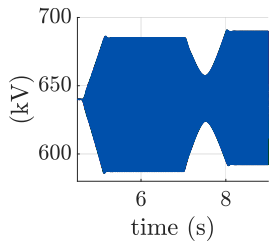
(j) Lower-arm current.



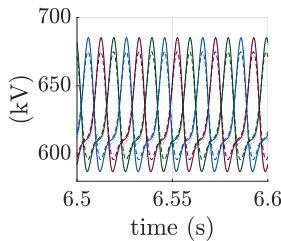
(k) Lower-arm current: zoom between 6.5 s and 6.6 s.



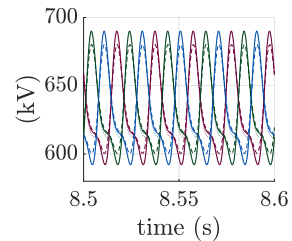
(l) Lower-arm current: zoom between 8.5 s and 8.6 s.



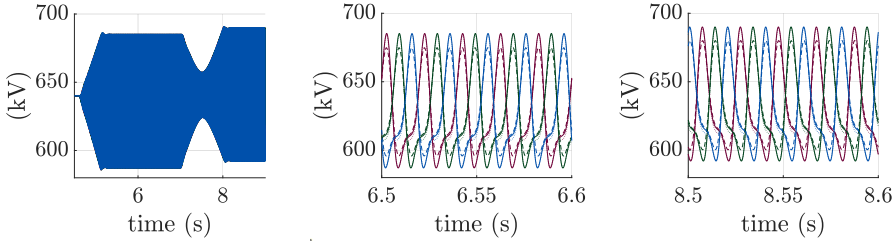
(m) Upper-arm capacitor voltages sum.



(n) Upper-arm capacitor voltages sum: zoom between 6.5 s and 6.6 s.



(o) Upper-arm capacitor voltages sum: zoom between 8.5 s and 8.6 s.



(p) Lower-arm capacitor voltages sum. (q) Lower-arm capacitor voltages sum: zoom between 6.5 s and 6.6 s. (r) Lower-arm capacitor voltages sum: zoom between 8.5 s and 8.6 s.

Figure III.9: Simulation results for the nominal power transfer from 4.5 s to 9 s. Dotted lines represent the MCC #0, dashed lines represent the MMC #1 and solid lines represent the MMC #2.

In Figs. III.9a and III.9b, the MMCs #0, #1 and #2 behaved similarly in terms of active and reactive power control, which confirms that the tuned controllers provide the same closed-loop performances for the various configurations. The active power ramps up to $P = 1$ GW at $t = 5.4$ s. At $t = 7$ s, it starts to ramp down and reaches $P = -1$ GW at $t = 8.2$ s. The reactive power ramps up to $Q = 0.3$ GW at $t = 5.4$ s and is kept at this same value during the analyzed time-span.

In Fig. III.9c, we plot the DC voltage. When $P = 1$ GW, the DC voltage ramps down from $V_{dc} = 640$ kV to 637.48 kV. When $P = -1$ GW, the DC voltage ramps up from the previous value to 642.27 kV.

In Figs. III.9d, III.9e and III.9f, we plot the DC current, the converter's AC current (on the transformer's delta side) and the AC-grid current (on the transformer's wye side), respectively. The power flow inversion in the DC link is realized by a change in the direction of the DC current as expected in VSC-HVDC schemes.

In Figs. III.9g and III.9j, we plot the upper- and lower-arm currents, respectively. In Figs. III.9h and III.9k, when $P = 1$ GW, the MMCs #0 and #2 perform similarly with the arm currents oscillating between -1.40 kA and 1.67 kA while for the MMC #1 it oscillates between -1.05 kA and 1.60 kA. In Figs. III.9i and III.9l, when $P = -1$ GW, the MMCs #0 and #2 also perform similarly with the arm currents oscillating between -1.65 kA and 1.40 kA while for the MMC #1 it oscillates between -1.57 kA and 1.06 kA.

In Figs. III.9m and III.9p, we plot the sum of upper- and lower-arm capacitor voltages, respectively. In Figs. III.9n and III.9q, when $P = 1$ GW, the MMCs #0 and #2 perform similarly with the arm capacitor voltages sum oscillating between 587.01 kV and 685.23 kV while for the MMC #1 it oscillates between 595.85 kV and 674.87 kV. In Figs. III.9o and III.9r, when $P = -1$ GW, the MMCs #0 and #2 also perform similarly with the arm capacitor voltages sum oscillating between 592.11 kV and 690.0 kV while for the MMC #1 it oscillates

between 600.55 kV and 679.7 kV.

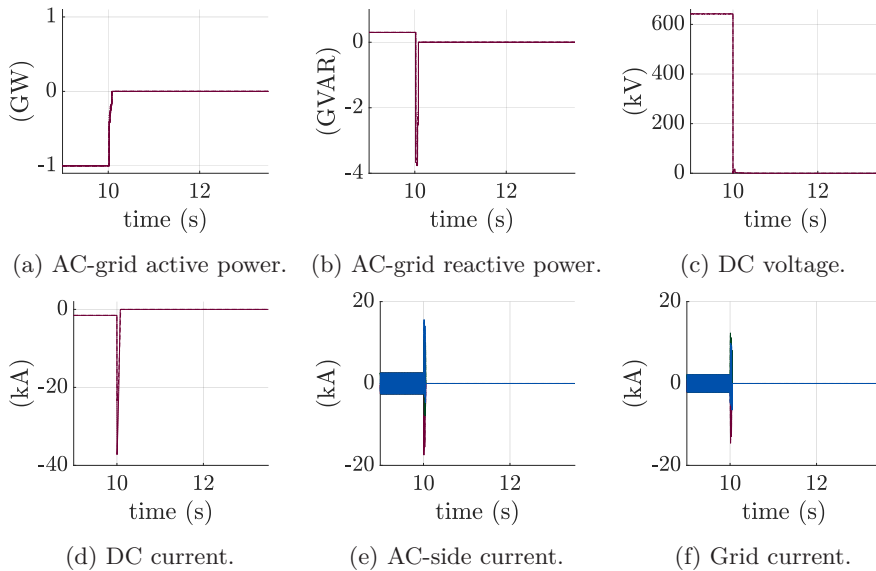
III.5.3 Behavior during a Pole-to-Pole Fault

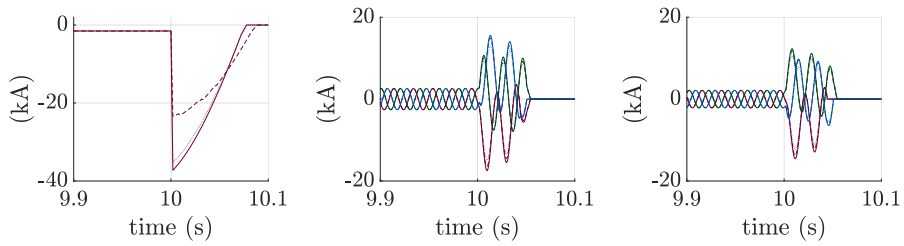
A pole-to-pole short circuit on the MMC DC ports is the most severe fault condition for the converter in a P2P-HVDC scheme. When such a fault is detected, the converters on both sides of the link are immediately blocked, and the AC grid must be isolated as rapidly as possible. If the MMC is implemented with HB-SMs, it will act as an uncontrolled rectifier with the AC grid directly feeding the fault until the AC-CB is opened.

A pole-to-pole short circuit is simulated with the following sequence.

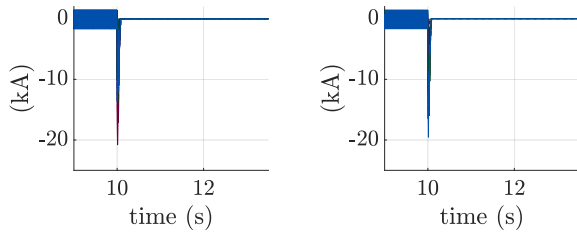
- At $t = 10$ s, a pole-to-pole short circuit occurs at the converter CMA1. The fault is provoked by closing simultaneously the switches SW_{fault1} and SW_{fault2} . The fault resistance is adopted as $R_{fault} = 0.1 \Omega$.
- At $t = 10.002$ s, the fault is detected and CMA1 is blocked.
- At $t = 10.042$ s, CB1 is opened.

The results for the pole-to-pole fault are plotted in Fig. III.10.

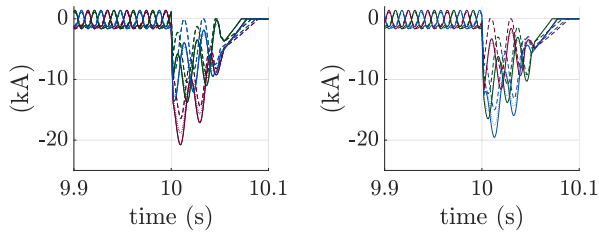




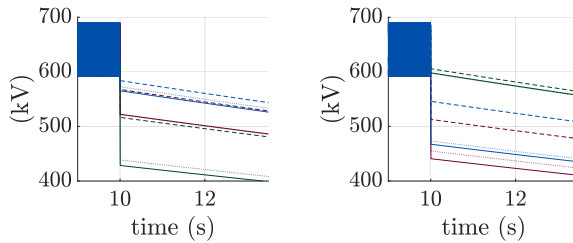
(g) DC current: zoom between 9.9 s and 10.1 s. (h) AC-side current: zoom between 9.9 s and 10.1 s. (i) Grid current: zoom between 9.9 s and 10.1 s.



(j) Upper-arm current. (k) Lower-arm current.



(l) Upper-arm current: zoom between 9.9 s and 10.1 s. (m) Lower-arm current: zoom between 9.9 s and 10.1 s.



(n) Upper-arm capacitor voltages sum. (o) Lower-arm capacitor voltages sum.

Figure III.10: Simulation results for the pole-to-pole fault from 9 s to 13.5 s. Dotted lines represent the MCC #0, dashed lines represent the MMC #1 and solid lines represent the MMC #2.

The results in Figs. III.10a and III.10b show that immediately after the fault, the active power drops from $P = -1$ GW to zero while the reactive power surges to -3.12 GVAR, -3.59 GVAR and -3.76 GVAR for MMCs #0, #1 and #2, respectively.

In Fig. III.10c, we plot the DC voltage which drops from 642.27 kV to zero almost instantly.

The DC current spikes at -35.23 kA, -23.45 kA, -37.22 kA for MMCs #0, #1 and #2, respectively as shown in Figs. III.10d and III.10g. While the MMCs #0 and #2 performs similarly in terms of DC limitation during the pole-to-pole fault, the MMC #1 reduces the DC surge current by around 37 %.

During the fault, the converter's AC-side currents oscillates, between -14.91 kA and 12.91 kA for the MMC #0, between -16.45 kA and 14.90 kA for the MMC #1, and between -17.52 kA and 15.65 kA for the MMC #2, as shown in Fig. III.10h. The AC-grid currents oscillate, between -12.17 kA and 10.62 kA for the MMC #0, between -13.83 kA and 11.65 kA for the MMC #1, and between -14.58 kA and 12.33 kA for the MMC #2, as shown in Fig. III.10i. The MMCs #1 and #2, with directly-coupled arm coils, perform worse in terms of AC-current limitation during the pole-to-pole fault than the MMC #0 with uncoupled arm coils.

The upper- arm and lower-arm currents oscillate during the fault, as shown in Figs. III.10j and III.10k. In Figs. III.10l and III.10m, the arm currents oscillate between -18.84 kA and 0 kA for the MMC #0, between -16.44 kA and 0 kA for the MMC #1, and between -20.7825 kA and 0 kA for the MMC #2.

From the sum of the SM capacitor's voltages shown in Figs. III.10n and III.10o, we can see that after the fault, the SMs capacitors are quickly discharged until the SMs blocking at $t = 10.002$ s. After the blocking, the capacitors are slowly discharged through the loop created by the grounding impedance Z_g and the and the fault resistance R_{fault} .

III.6 Summary

Directly-coupled arm coils can be designed with different objectives: keep the same size while improving the steady-state performances or reduce the size while keeping similar steady-state performances. But the fault operation performance can deteriorate. For instance:

- An HB-MMC with directly-coupled arm coils with $L = 50.9$ mH and $K_{u,l} = 0.6517$ has the same weight and size as the reference MMC. The weight of two coupled arm coils is 85 t, and its volume is 171.2 m³ (reduction of 22.5%). But such MMC has improved steady-state performances. In particular, the conversion losses are reduced by 12.56%. In addition, the DC-fault current is reduced by 37%.

- An HB-MMC with directly-coupled arm coils with $L = 27.3$ mH and $K_{u,l} = 0.6740$ has smaller arm coils than the reference MMC. The weight of two coupled arm coils is 48 t (reduction of 43.6%), and its volume is 122.15 m³ (reduction of 44.7%). Such MMC has similar steady-state performances. But the DC-fault current increases by 6% compared to the reference MMC.

Chapter IV

Study of a Modular Multilevel Converter with Coupled High Temperature Superconducting Arm Coils

In the previous chapter, we have investigated the effect of coupling the arm coils of a 1 GW ± 320 kV HB-MMC. We have shown that a direct-coupling can lead to smaller and lighter coils but that it can deteriorate the fault operation performance.

Therefore in this chapter, we propose to go one step further and to replace the conventional dry-type air-core arm coils with high-temperature superconducting arm coils. It is expected that it will allow us to reduce the losses of the arm coils (objective (ii)) while providing the fault current limitation function (objective (iii)) by behaving like a superconducting fault current limiter. This proposition has been patented [2]. The resulting HB-MMC has directly-coupled high-temperature superconducting arm coils and is called a cryo-MMC.

The objectives of this chapter are:

- To design directly-coupled high temperature superconducting arm coils for the reference MMC defined in I.4.
- To assess the transient performance in normal and fault operation for the proposed MMCs.
- To propose an economic assessment of the cryo-MMC.

This chapter is organized as follows. In Section IV.1, we develop the design of the high-temperature superconducting directly-coupled arm coils system. In Section IV.2, we compute the steady-state performance indicators defined in Section III.2 for the cryo-MMC. In Section IV.3, we evaluate the transient performance in normal and fault operation conditions for the cryo-MMC. In Section IV.4, we develop an economical assessment for the cryo-MMC. In Section IV.5, we summarize the essential findings of this chapter.

IV.1 Design of coupled HTS arm coils

IV.1.1 Requirements

In this section, we design the high-temperature superconducting (HTS) arm coils system for the reference 1 GW ± 320 kV HB-MM (section I.4). The design constraints are its nominal current and its inductance. According to Fig. III.9, the nominal current is 1750 A. Following to the conclusions of chapter III, a suitable design should have directly-coupled arm coils with a self-inductance of $L \approx 27.3$ mH and a coupling coefficient $K_{u,l} \geq 0.6$.

We assume liquid nitrogen (LN2) as the coolant, either right below the LN2 boiling temperature of 77 K or subcooled at 65 K. The study of R-type superconducting fault current limiters in [78] pointed out that a subcooled operation temperature of 65 K yields a most economical solution than at 77 K.

IV.1.2 Overview of the Coupled HTS Arm Coils

The coupled HTS arm coils are shown in Fig. IV.1. Both arm coils are located in the same cryostat, cooled down in an LN2 bath. A set of coupled HTS arm coils is composed of several HTS modules connected in series and parallel. One HTS module is composed of two HTS double pancake coils (DPCs). Each HTS double pancake coils is made of two HTS pancake coils (PCs) connected in series. Each module is magnetically independent. The magnetic coupling is obtained by coupling the DPC within each module. The design is obtained following a bottom-up approach.

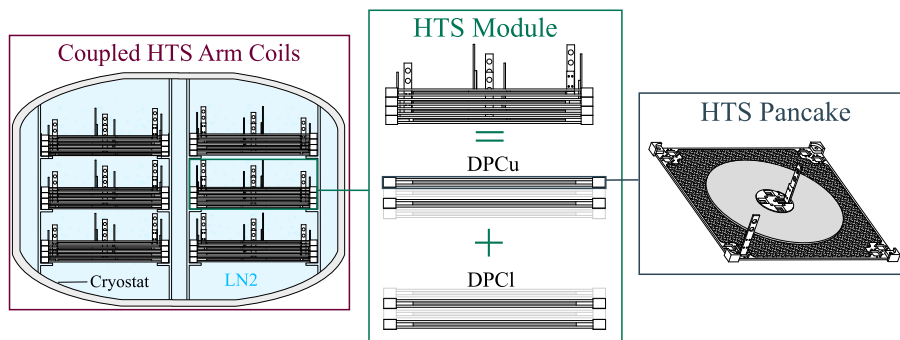


Figure IV.1: Overview of a coupled HTS arm coil system.

IV.1.3 High-Temperature Superconducting Tapes

Given the operating temperature defined in Section IV.1.1, a high-temperature superconducting (HTS) tape can be used to build the arm coils. HTS tapes are now commercially available with high power density, good in-field behavior, and good resistance to mechanical stress [79]. There are two generations of

HTS tapes. The first generation (1G), corresponding to BSCCO tapes, has a multi-filamentary bismuth-based oxide structure surrounded by a silver or silver alloy matrix, potentially coated with a metallic stabilizer layer as shown in Fig. IV.2a. The second generation (2G), corresponding to ReBCO tapes, has a coated structure where a rare-earth-based oxide layer is wrapped by a buffer, a substrate, and stabilizer layers, as shown in Fig. IV.2b.

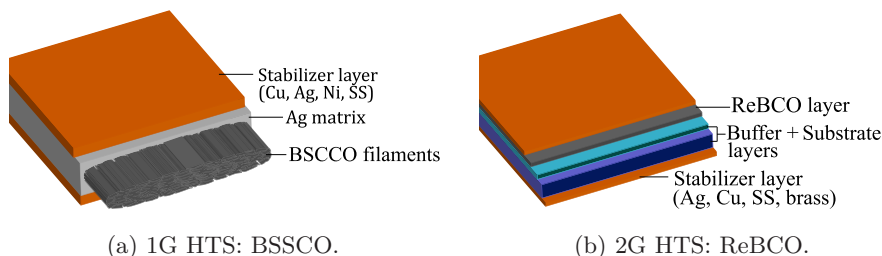


Figure IV.2: Commercial HTS tapes structure (not to scale).

The three parameters used to define an HTS material are its critical current I_c , its critical temperature T_c , and its critical magnetic field B_c . An HTS transits outside its superconducting state (quenches) when its temperature, current or magnetic field is higher than its critical values.

The critical current I_c of an HTS tape is obtained from its I-V characteristic for a given operating temperature in self-field conditions. Its measurement is normalized by the international standard IEC 61788 [80], [81]. The critical current is defined as the value of the DC current for which the electric field criterion of $E_c = 1 \cdot 10^{-4}$ V/m is reached. This is done by measuring the current and voltage of a short-length HTS tape sample. Considering a sample of 10 cm length, the critical current corresponds to a measured voltage of 10 μ V.

For superconducting fault-current limiters (ScFCL) [82], ReBCO tapes are more suitable than BSSCO tapes. During a fault-current limitation, the superconducting layer becomes resistive, and the current flows in the other layers of the tape. To achieve fault current limitation, the other layers of the tape have to be relatively resistant. Unlike 1G tapes fabricated using an Ag matrix, an excellent electrical conductor, 2G HTS tapes have much more resistive layers and are thus more suitable for current limiting applications. In addition, 2G tapes can be fabricated with a high resistance stainless steel stabilizer layer to increase further the tape's resistivity and its capacity to transfer outside the heat generated during the fault [79]. As measured in [83], two similar air-core HTS coils made from 1G and 2G HTS tapes experience an impedance increase by 3 and 42 times, respectively, during fault. Therefore, we adopt a 2G HTS tape to build the arm coils of the cryo-MMC since we seek a fault-current limiting capability.

We selected the reference "Amperium Type 8502-350 YBCO" for which experimental data are provided in [84]. The geometric data for that YBCO

tape are summarized in Table IV.1. In Fig. IV.3, we plot the I-V characteristic of the short sample. It has a critical current of 401.2 A at 77 K.

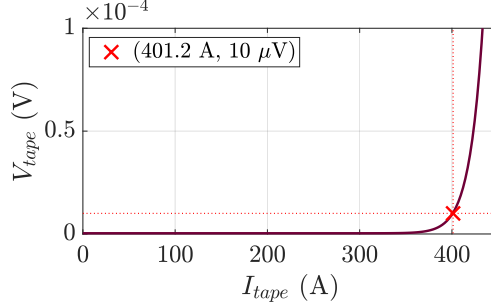


Figure IV.3: I-V characteristic of the Amperium Type 8502-350 YBCO tape.

Quantity	Symbol	Value
Tape width [m]	w_t	$12 \cdot 10^{-3}$
Tape thickness [m]	t_t	$0.258 \cdot 10^{-3}$
Stainless steel stabilizer layer thickness [m]	t_{SS}	$75 \cdot 10^{-6}$
YBCO layer thickness [m]	t_{YBCO}	$0.8 \cdot 10^{-6}$
Substrate thickness [m]	t_H	$100 \cdot 10^{-6}$

Table IV.1: Parameters for the Amperium Type 8502-350 YBCO tape. "Substrate" designates the buffer and substrate layers together.

A phenomenological law introduced by Kim [85, 86] is usually employed to describe the critical current I_c as a function of its temperature T_{sc} and its magnetic flux density parallel B_{\parallel} and perpendicular B_{\perp} components,

$$I_c(T_{sc}, B_{\parallel}, B_{\perp}) = \frac{I_{c0} \left(1 - \frac{T_{sc}}{T_0}\right)^{\alpha_T}}{1 + \left(\frac{\sqrt{k_B^2 B_{\parallel}^2 + B_{\perp}^2}}{B_0}\right)^{\alpha_B}} \quad (\text{IV.1})$$

where I_{c0} , T_0 , α_T , k_B , B_0 , and α_B are material parameters. Note that other authors may have used other formulas to account for the temperature and field

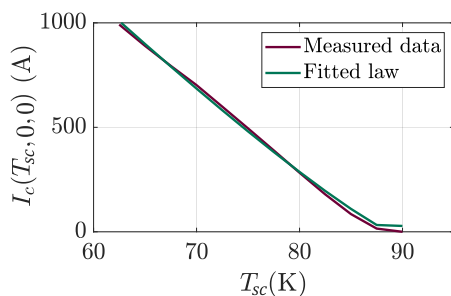
dependence. The related parameters may then have a different meaning. For example, here I_{c0} is the critical current at 0 K.

The voltage across an HTS tape v_{sc} is modeled assuming an E-J constitutive power law [86] as

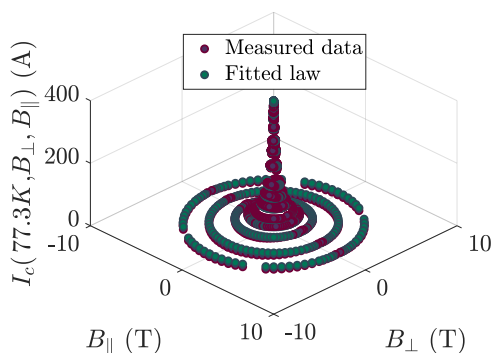
$$v_{sc} = \frac{E_c}{I_c(T_{sc}, B_{\parallel}, B_{\perp})} l_{sc} \left| \frac{i_{sc}}{I_c(T_{sc}, B_{\parallel}, B_{\perp})} \right|^{n_{sc}-1} i_{sc} \quad (IV.2)$$

where i_{sc} is the superconductor current, l_{sc} its length and n_{sc} its index value. In this work, we neglect the dependence of n_{sc} on the temperature and magnetic field.

The dependency of the critical current in terms of temperature and magnetic field for the adopted YBCO tape is provided in [84] and plotted in Fig. IV.4. The HTS material parameters from Eq. (IV.1) are fitted from these measurements and are presented in Table IV.2.



(a) as a function of the temperature.



(b) as a function of the applied magnetic flux density.

Figure IV.4: Amperium Type 8502-350 YBCO tape critical current.

Quantity	Symbol	Value
HTS parameter [A]	I_{c0}	$4.0865 \cdot 10^3$
HTS parameter [K]	T_0	88.8216
HTS parameter [-]	α_T	1.1508
HTS parameter [-]	α_B	1.7465
HTS parameter [-]	k_B	1
HTS parameter [T]	B_0	0.2745
Critical electric field [V/m]	E_c	$1 \cdot 10^{-4}$
Index-value [-]	n_{sc}	30

Table IV.2: Parameters of the Amperium Type 8502-350 YBCO tape fitted from data provided in [84].

IV.1.4 HTS pancake coil

Each HTS pancake coil (PC) is made by co-winding the HTS tape with a corrugated spacer (Fig. IV.5). The support structure is full of holes to favor the circulation of the LN2. The connectors are made of copper. The specifications of an HTS pancake coil are summarized in Table IV.3. The inner radius is chosen to respect the HTS tape minimum bending radius. The number of turns is selected to obtain the required inductance. The other parameters are obtained from the HTS tape data [84] or from our prototype (see Chap. V).

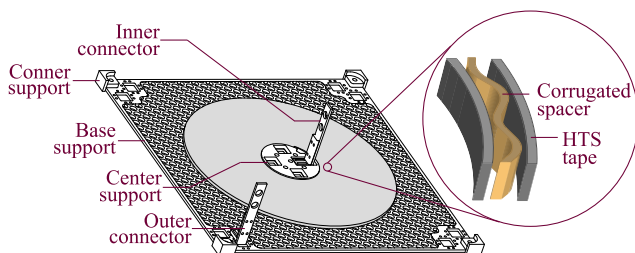


Figure IV.5: HTS pancake.

Quantity	Symbol	Value
Dimensions without connectors [m]		0.4 (W) × 0.4 (L) × $20 \cdot 10^{-3}$ (H)
Coil inner radius [m]	r_{in}	$4.2 \cdot 10^{-2}$
Coil length [m]	l_p	53
Number of turns [-]	N_t	74
Corrugated insulator thickness [m]	t_i	$1.8 \cdot 10^{-3}$
Reinforcement layer resistance [Ω]	$R_{SS,PC}$	$20.14 \cdot 10^3$
Substrate layer resistance [Ω]	$R_{sub,PC}$	107.88
Silver layer resistance [Ω]	$R_{Ag,PC}$	34.20
Copper connector resistance [Ω]	$R_{c,PC}$	$31.15 \cdot 10^{-6}$

Table IV.3: HTS pancake coil specifications.

IV.1.5 HTS double pancake coil

One double pancake coil (DPC) is obtained by stacking two pancake coils and connecting them in series to create addicting flux linkages.

IV.1.6 HTS module

One directly-coupled HTS module is composed of 2 HTS double pancake coils, denoted DPCu and DPCl. The DPCu is connected in series with the upper arm HB-SMs stack. The DPCl is connected in series with the lower arm HB-SMs stack. The DPCs are stacked as shown in Fig. IV.6 so that they have a positive coupling coefficient. The specifications of an HTS module are summarized in Table IV.4.

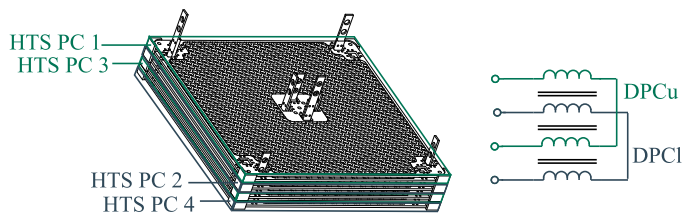


Figure IV.6: HTS module.

Quantity	Symbol	Value
Number of PC per module [m]		4
Vertical clearance between PC [m]	t_h	$4 \cdot 10^{-3}$
Dimensions without connectors [m]		$0.4 \text{ (W)} \times$ $0.4 \text{ (L)} \times$ $8 \cdot 10^{-2} \text{ (H)}$
Weight [kg]		4.85
Self inductance [H]	L_m	$6.6 \cdot 10^{-3}$
Resistance [Ω]	R_m	$124.6 \cdot 10^{-6}$
Coupling coefficient	K_m	0.8788

Table IV.4: HTS module specifications.

We want to estimate the critical current of the HTS module $I_{c,m}$. This is done in three steps, adapting the procedure described in the IEC 61788 [81].

1. First, the local critical current along the DPC length is obtained from Eq. (IV.1). It is a function of the local magnetic flux density. To obtain the field, we use a 2D-axisymmetric magneto-static finite element model implemented in Comsol Multiphysics (Fig. IV.7). We model only the HTS layer and assume a uniform current density distribution. Notice that the inner turns of the coils are subjected to the highest magnetic field.
2. Second, the DPC DC voltage as a function of the DC current, i.e., the I-V characteristic, is obtained by summing Eq. (IV.2) for each turn. Since the local magnetic field is a function of the current of both DPCs, we

obtain a 2-D I-V characteristic that is plotted in Fig. IV.8. The currents in DPCu and DPCl are denoted $i_{sc,m,u}$ and $i_{sc,m,l}$, respectively and their voltage is denoted $v_{sc,m,u}$ and $v_{sc,m,l}$, respectively.

- Third, the critical current is deduced from the 2-D I-V characteristic. For design purpose, we consider the worst case scenario that corresponds to both DPC having the same current i.e. $i_{sc,m,u} = i_{sc,m,l}$. At 77 K, we obtained $I_{c,m} = 234.43$ A which represents a degradation of nearly 40% compared to the tape critical current estimated to be $I_c = 401.2$ A (Fig. IV.3). At 65 K, the estimated critical current is $I_{c,m} = 377.13$ A, 55% higher than at 77 K.

Note that the above method used to estimate the module critical current is based on the approximation that the current density is uniform in the HTS layer tape cross-section. This is not true in reality, but the determination of the current density distribution in an HTS coil is a complex numerical challenge [87], [88]. Anyway, the above procedure is deemed accurate enough for preliminary design purposes.

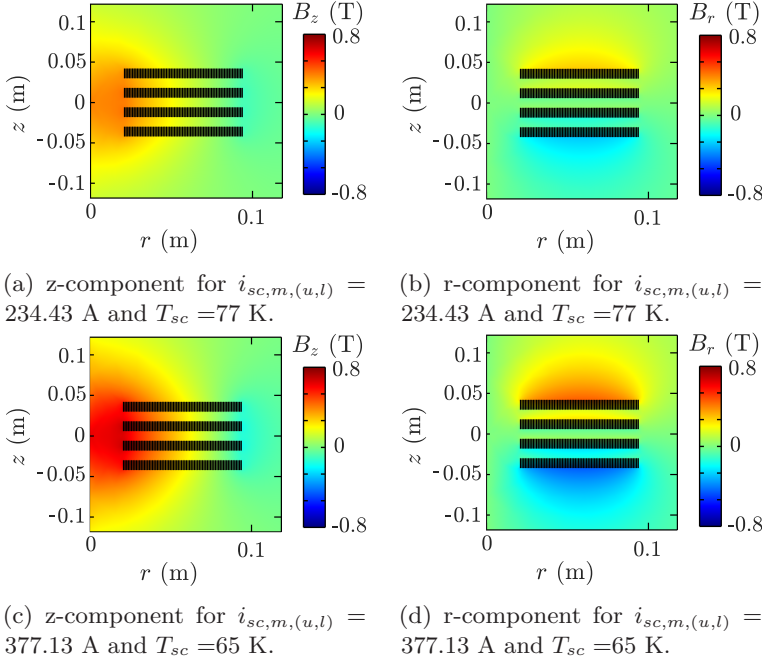


Figure IV.7: HTS Module magnetic flux density distribution for a current equal to the critical current in both DPC. The component parallel to the tape surface is B_z . The one perpendicular to it is B_r .

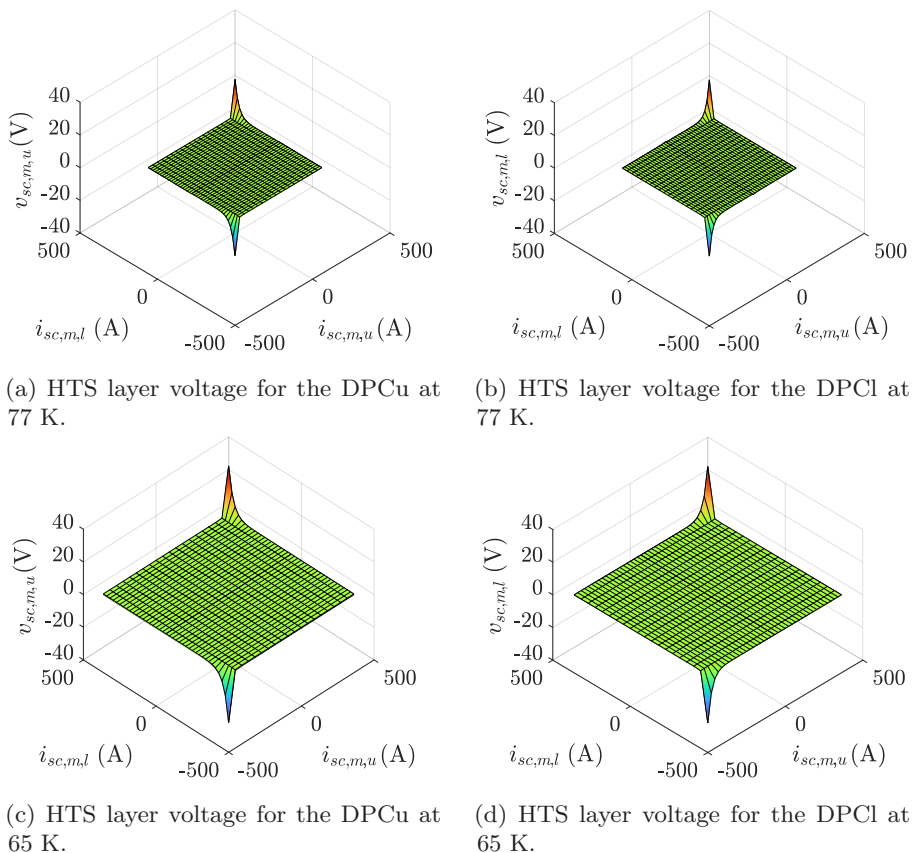


Figure IV.8: 2-D I-V characteristic of each DPC of one HTS module.

IV.1.7 Coupled HTS Arm Coils

To obtain the coupled HTS arm coils, the HTS modules are connected in series and in parallel to meet the required arm coil current and inductance.

The number of parallel modules N_p is determined by imposing a 20% current margin on the device critical current,

$$N_p = \text{ceil} \left(\frac{I_{nom}}{0.8 I_{c,m}} \right) \quad (IV.3)$$

where I_{nom} is the nominal arm coil current.

Once N_p is determined, the number HTS modules in series N_s is determined from the desired arm coil self-inductance L as

$$N_s = \text{ceil} \left(\frac{N_p L}{L_m} \right) \quad (IV.4)$$

where L_m is the module self inductance.

In this study, we consider three MMC configurations:

- MMC #0: an MMC with 400 HB-SMs and conventional uncoupled dry-type air-core arm coils. It corresponds to the reference MMC defined in Section I.4.
- MMC #3: an MMC with 400 HB-SMs and directly-coupled HTS arm coils operating at 77 K.
- MMC #4: an MMC with 400 HB-SMs and directly-coupled HTS arm coils operating at 65 K.

The corresponding specifications are summarized in Table IV.5. The layout of the HTS modules within the cryostat is shown in Fig IV.9. A visual comparison of the coupled HTS arm coils with the reference uncoupled coils is proposed in Fig. IV.10.

	MMC		
	#0	#3	#4
T_{op} [K]	RT	77	65
N_s	-	34	21
N_p	-	8	5
R [Ω]	$32.5 \cdot 10^{-3}$	$0.53 \cdot 10^{-3}$	$0.52 \cdot 10^{-3}$
L [H]	$51.6 \cdot 10^{-3}$	$28.0 \cdot 10^{-3}$	$27.7 \cdot 10^{-3}$
$K_{u,l}$	0	0.8788	0.8788
Conductor's length [m]	$5.98 \cdot 10^3$	$57.64 \cdot 10^3$	$22.26 \cdot 10^3$
Cryostat volume [m ³]	NA	20.65	7.15
Mass [t]	85.00	22.5	7.84

Table IV.5: Coupled HTS arm coils specifications. Data are given for a set of 2 coils. RT denotes the room temperature. The mass includes the weight of HTS modules and of the cryostat full of LN2.

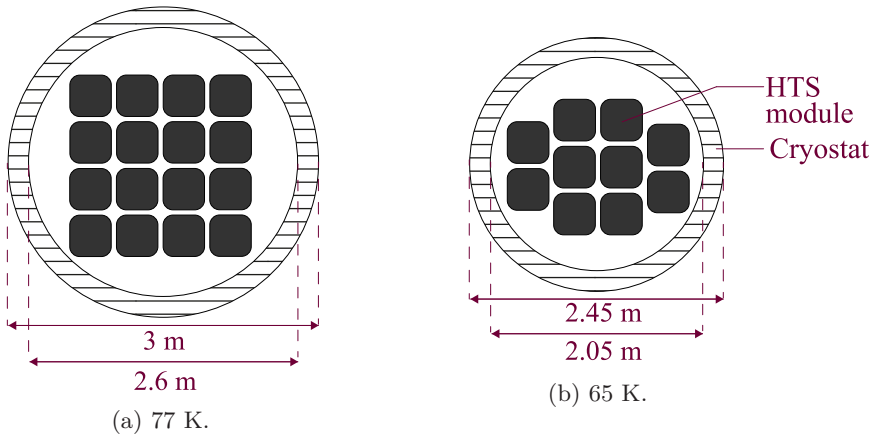


Figure IV.9: HTS modules layout.

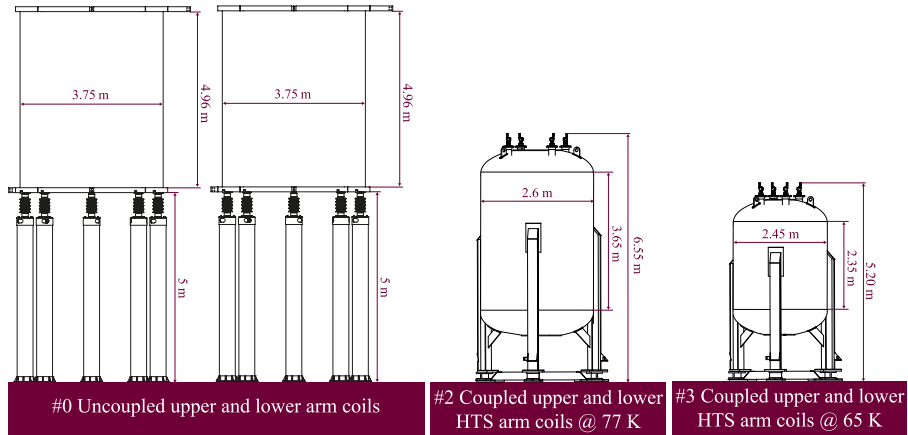


Figure IV.10: Mock-up of the coupled HTS arm coils.

IV.1.8 Refrigeration system

We consider a single refrigeration system for all the HTS arm coils. We adopt an hybrid architecture inspired from [89] and illustrated in Fig. IV.11. It uses a cryocooler as the primary source for refrigeration and one open-cycle LN₂ buffer tank as a backup. This configuration provides the high reliability required for in-grid operation while avoiding the high costs of cryocooler redundancy.

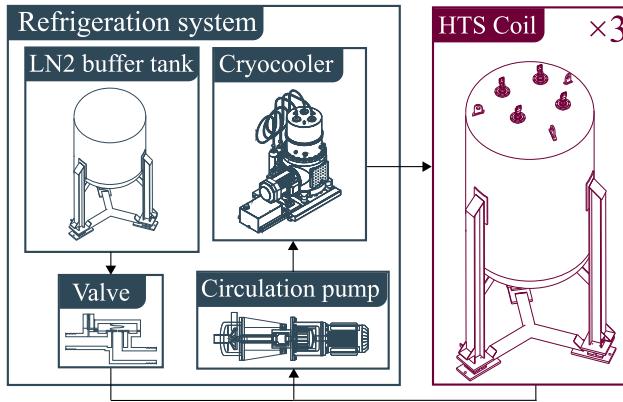
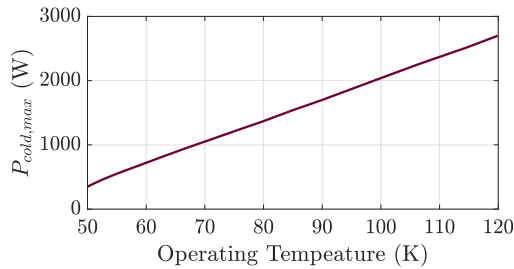
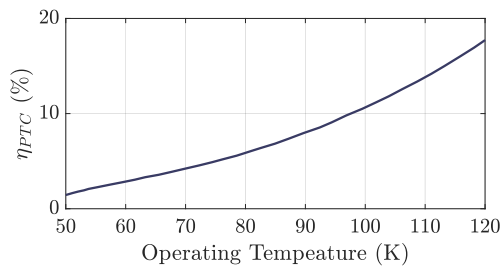


Figure IV.11: Overview of the coupled HTS coils system.

We select a Pulse Tube Cryocooler (PTC) whose parameters are summarized in Table IV.6. The cryocooler capital cost is estimated from [90]. The maximum cooling power $P_{cold,max}$, corresponding to the heat load (power) that can be removed from the cryocooler cold tip while maintaining its temperature, is shown in Fig. IV.12a. The cryocooler efficiency η_c is shown in Fig. IV.12b. For $T_{op} = 77$ K, the PTC efficiency is $\eta_{PTC} = 5.33\%$. For $T_{op} = 65$ K, $\eta_{PTC} = 3.51\%$.



(a) Maximum cooling power.



(b) Efficiency.

Figure IV.12: PTC cooling performances.

Quantity	Symbol	Value
Maximum cooling power @ 77 K [W]	$P_{cold,max}(77)$	1300
Motor electric consumption @ $P_{cold,max}(77)$ [W]	$P_{PTC,e}(77)$	24.4 kW
Additional losses @ $P_{cold,max}(77)$ [W]	P_{add}	2.5 kW
Weight [kg]	M_{PTC}	1300
Dimensions [m]		1.8 (L) × 1.2 (W) × 2.1 (H)
Capital cost [k€]	CC_{PTC}	107.4

Table IV.6: Cryocooler specifications. Cooling power given for a water cooled configuration with 15°C water temperature at the heat rejecter.

We assume that the heat load to be removed from the cryostat is equal to the total active power dissipated in the coils P_{coil} (defined in Section III.2). Note that we neglect the losses generated in the HTS tapes, commonly denominated AC losses [91], since they are deemed small compared to the copper connector losses of HTS pancakes coils. The required number of cryocoolers N_{PTC} is then computed by considering a 20 % margin on the maximum cooling power,

$$N_{PTC} = ceil \left(\frac{P_{coil}}{0.8 P_{cold,max}} \right) \quad (IV.5)$$

And at T_{op} , the electric power consumption of all the cryocoolers is,

$$P_{PTC,e} = \frac{P_{coil}}{\eta_{PTC}} \quad (IV.6)$$

The circulation pump parameters are given in Table IV.7. Each cryostat is equipped with two pumps.

Quantity	Symbol	Value
Flow rate @ 77 K [L/s]		7
Electric power consumption @ 77 K [W]		0.8 kW
Weight [kg]	M_{pump}	120
Dimensions [m]		0.3 (L) × 0.3 (W) × 0.75 (H)
Capital cost [k€]	CC_{pump}	10

Table IV.7: Circulating pump specifications.

The parameters for the LN2 buffer tank are provided in Table IV.8. The cryostat capital cost per unit storage volume is considered 1035.4 €/m³ (value obtained from market prices).

Quantity	Symbol	Value
External Diameter [m]		3
Height [m]		6.5
Storage Capacity [m ³]		21.5
Weight [kg]		$4.69 \cdot 10^3$
Weight with LN2 [kg]	M_{BT}	$22 \cdot 10^3$
Capital Cost [k€]	CC_{BT}	22.2

Table IV.8: LN2 Buffer Tank Specifications.

The nominal electric power consumption of the refrigeration system is computed as

$$P_{RS,e} = \frac{P_{coil}}{\eta_{PTC}} + N_{PTC} P_{add} + 6 P_{pump} \quad (IV.7)$$

IV.2 Steady-State Analysis

In this section, we evaluate the steady-state performances of the proposed cryo-MMCs and compare them with the reference MMC #0. This is done by calculating the performance indicators defined in section III.2 using the DA-HSS model developed in section II and the data from Table IV.5. The results are summarized in Table IV.9.

	MMC		
	#0	#3	#4
P_{cond} [kW]	1860.5	1891.8	1891.8
P_{sw} [kW]	5422.9	5250.6	5268.0
P_{coil} [kW]	677.21	3.98	3.95
$\Delta v_{c,(u,l),p}$ [p.u.]	0.1401	0.1398	0.1379
$WTHD\{v_{\Delta m,p}\}$	$3.9 \cdot 10^{-5}$	$3.65 \cdot 10^{-5}$	$3.47 \cdot 10^{-5}$
$\max\{i_{(u,l),p}\}$ [kA]	1.5316	1.5090	1.5093
$\min\{i_{(u,l),p}\}$ [kA]	-1.3485	-1.2756	-1.2523

Table IV.9: MMCs #0, #3 and #4 Performance indicators evaluated for $P = P_{nom}$ and $Q = Q_{nom}$.

As shown in Table IV.9, conduction and switching losses have similar values for the three MMC configurations. Nevertheless, arm coil electrical losses are 170 times smaller for the MCC #3 and #4, which is due to the HTS arm coils having much smaller Joule losses that are only generated by the connectors of the HTS pancake coils. Notice that refrigeration losses will be included in the subsequent development. Other steady-state performance indicators are improved for MMC #3 and #4 compared to MMC #0.

IV.3 Transient Analysis

In this section, we evaluate the transient performances of the proposed MMCs #3 and #4 and compare them with the reference MMC #0. Since The MMCs #3 and #4 behave similarly, we report here only the results for the MMC #4.

IV.3.1 Modeling

For the transient analysis, we use the same circuit simulation described in section III.5 with the controller's gains for MMC #4 given in Table E.1. But a

specific model is derived and implemented to simulate the coupled HTS arm coils of MMC #4.

In all the time-domain responses presented in this section, dashed lines represent the response of MMC #0 while solid lines represent the response of MMC #4. Also, the waveforms for the phases a , b , and c are represented in purple, green, and blue, respectively.

The coupled HTS arm coils are modeled using a lumped-parameter thermo-electric circuit [92]. Note that we neglect the losses in the HTS tape, commonly called AC losses [91]. An accurate estimation of AC losses in HTS tapes requires complex models that are out of the scope of this thesis [88, 93, 94]. Besides the AC losses are deemed small compared to the copper connector losses of HTS pancakes coils.

IV.3.1.1 Electric Circuit

The coupled HTS arm coils are modeled by the lumped-parameter electric circuit shown in Fig. IV.13. The coupling is modeled by the inductance matrix \mathbf{L}_{coil} ,

$$\mathbf{L}_{coil} = \frac{N_s}{N_p} \begin{bmatrix} 1 & K_{u,l} \\ K_{u,l} & 1 \end{bmatrix} L_m \quad (IV.8)$$

where L_m and $K_{u,l}$ are provided in Table IV.4.

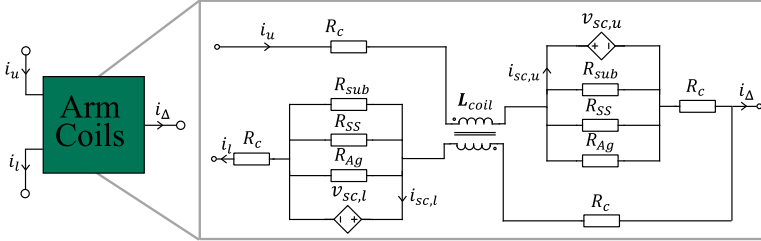


Figure IV.13: Lumped-parameter electric circuit of the coupled HTS arm coils.

The equivalent resistances for the stainless steel, silver, and substrate layers of the tape are determined as

$$R_{c,coil} = \frac{N_s}{N_p} 2 R_{c,PC} \quad (IV.9a)$$

$$R_{sub} = \frac{N_s}{N_p} 2 R_{sub,PC} \quad (IV.9b)$$

$$R_{SS} = \frac{N_s}{N_p} 2 R_{SS,PC} \quad (IV.9c)$$

$$R_{Ag} = \frac{N_s}{N_p} 2 R_{Ag,PC} \quad (IV.9d)$$

where $R_{c,PC}$, $R_{sub,PC}$, $R_{SS,PC}$ and $R_{Ag,PC}$ are provided in Table IV.3 and correspond to the resistances for one pancake coil.

The HTS layer voltage for the upper and lower HTS arm coil, $v_{sc,u}$ and $v_{sc,l}$ are,

$$v_{sc,u} = \frac{N_s}{N_p} v_{sc,m,u} \left(\frac{i_{sc,u}}{N_p}, \frac{i_{sc,l}}{N_p}, T_{sc} \right) \quad (IV.10a)$$

$$v_{sc,l} = \frac{N_s}{N_p} v_{sc,m,l} \left(\frac{i_{sc,u}}{N_p}, \frac{i_{sc,l}}{N_p}, T_{sc} \right) \quad (IV.10b)$$

where $v_{sc,m,u}$ and $v_{sc,m,l}$ are the 2-D I-V characteristics defined from Fig. IV.8.

IV.3.1.2 Thermal Circuit

The HTS layer voltage is a function of the temperature T_{sc} (see Eq.(IV.2)). Therefore we need to build a thermal model. Note that we neglect the temperature-dependence of the resistivity of non-superconducting layers.

The thermal behavior of one HTS module is modeled using a lumped-parameter thermal circuit inspired from [92] and illustrated in Fig. IV.14.

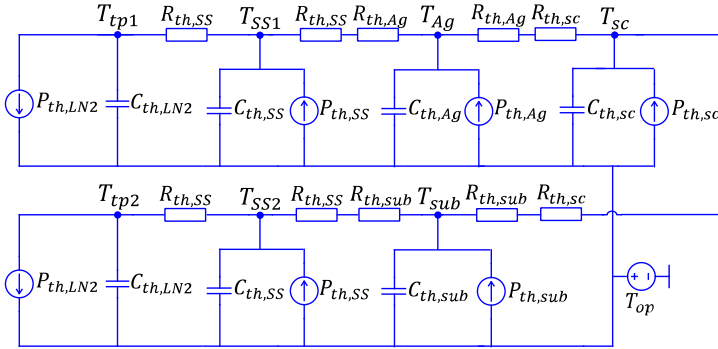


Figure IV.14: Lumped-parameter thermal circuit of one HTS module.

This model assumes homogeneous 1-D heat flow, inside the HTS tape by conduction, and between the tape surface and the liquid nitrogen bath by convection. The thermal circuit elements for the HTS module are provided in Table IV.10.

	Quantity	Symbol	Value
Liquid nitrogen thermal capacity [J/K]		$C_{th,LN2}$	$39.5 \cdot 10^3$
Stainless steel layer thermal resistance [K/W]		$R_{th,SS}$	$1.95 \cdot 10^{-6}$
Silver layer thermal capacity [J/K]		$C_{th,Ag}$	12.7
Silver layer thermal resistance [K/W]		$R_{th,Ag}$	$1.8 \cdot 10^{-9}$
YBCO layer thermal capacity [J/K]		$C_{th,sc}$	4.62
YBCO layer thermal resistance [K/W]		$R_{th,sc}$	$6.29 \cdot 10^{-8}$
Substrate layer thermal capacity [J/K]		$C_{sub,sc}$	539.42
Substrate layer thermal resistance [K/W]		$R_{sub,sc}$	$1.87 \cdot 10^{-6}$

Table IV.10: Thermal circuit parameters for the HTS module.

The power sources modeling the losses inside each layer of the HTS tape in Fig. IV.14 are

$$P_{th,sc} = \frac{1}{N_s N_p} (v_{sc,u} i_{sc,u} + v_{sc,l} i_{sc,l}) \quad (IV.11a)$$

$$P_{th,Ag} = \frac{1}{N_s N_p} R_{Ag,coil} (i_{Ag,u}^2 + i_{Ag,l}^2) \quad (IV.11b)$$

$$P_{th,SS} = \frac{1}{2 N_s N_p} R_{SS,coil} (i_{SS,u}^2 + i_{SS,l}^2) \quad (IV.11c)$$

$$P_{th,sub} = \frac{1}{N_s N_p} R_{sub,coil} (i_{sub,u}^2 + i_{sub,l}^2) \quad (IV.11d)$$

where $i_{Ag,u}$ and $i_{Ag,l}$ are the currents in the HTS tape silver layer of the upper and lower arms, $i_{SS,u}$ and $i_{SS,l}$ the currents in the stainless steel layer for the upper and lower arms and $i_{sub,u}$ and $i_{sub,l}$ the currents in the substrate layer for the upper and lower arms.

The convective heat transfer with the liquid nitrogen bath is written as

$$P_{th,LN2} = w_t 4 l_p (T_{tp} - T_{op}) h_{LN2}(\Delta T) \quad (IV.12)$$

where T_{tp} is the HTS tape boundary temperature, T_{op} is the operating temperature of the LN2 bath, and $h_{LN2}(\Delta T)$ is the convective heat transfer coefficient of the LN2 which depends the temperature difference $\Delta T = T_{tp} - T_{op}$.

The liquid nitrogen convective heat transfer coefficient at atmospheric pressure is fitted from the measurement presented in [95] and plotted in Fig. IV.15. The fitted law for the LN2 convective heat transfer coefficient at

atmospheric pressure is given by

$$h_{LN2}(\Delta T) = 9732 e^{-\left(\frac{\Delta T - 11.39}{7.763}\right)^2} + 3794 e^{-\left(\frac{\Delta T - 23.23}{8.974}\right)^2} + 230.1049 \quad (\text{IV.13})$$

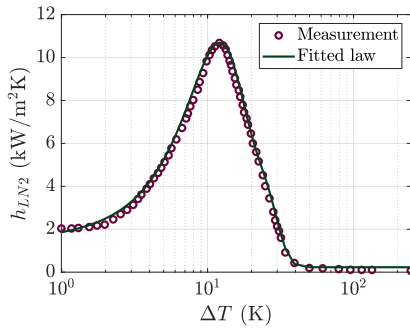
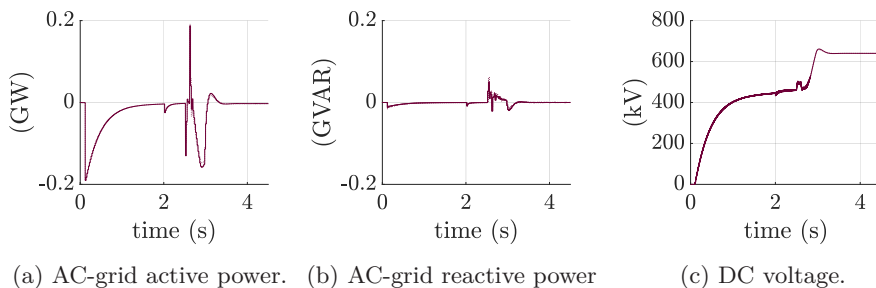


Figure IV.15: Liquid Nitrogen convective heat transfer coefficient at atmospheric pressure. Data from [95].

IV.3.2 Behavior during Normal Operation

The results for the start-up sequence defined in Section III.5.2 are plotted in Fig. IV.16 for MMCs #0 and #4. No significant difference is observed. This tends to confirm that the superconducting coils do not introduce any unexpected instability during the start-up of the converter. A full discussion on the waveforms presented in Fig. IV.16 is provided in Section III.5.2.



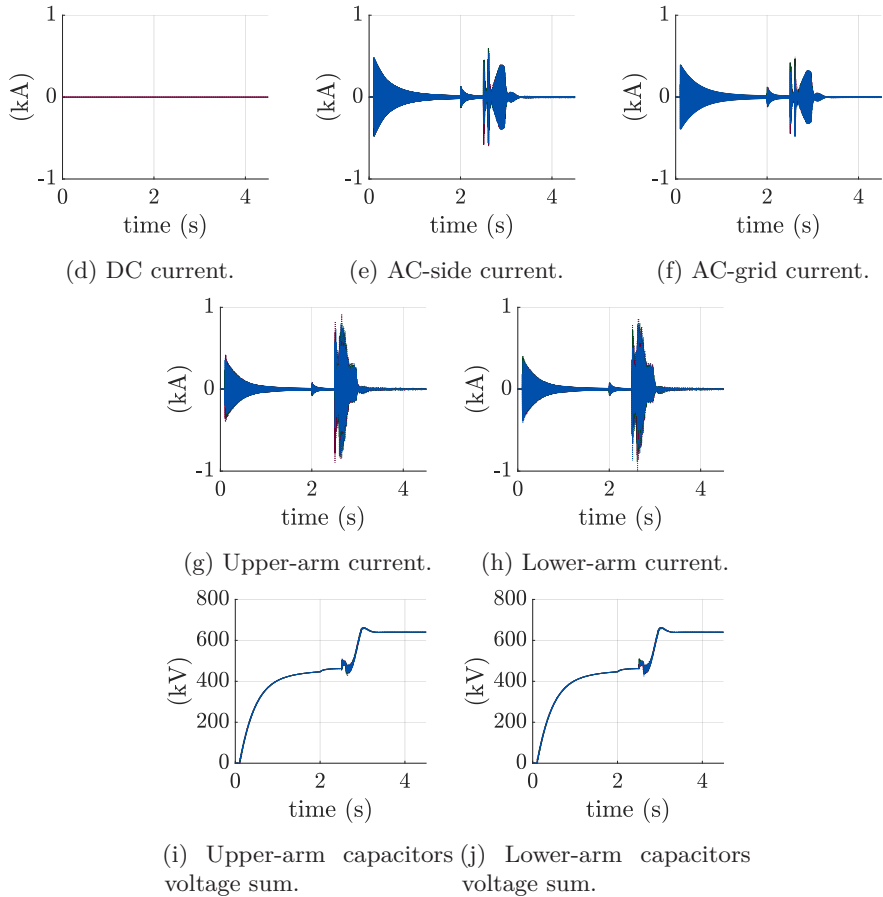
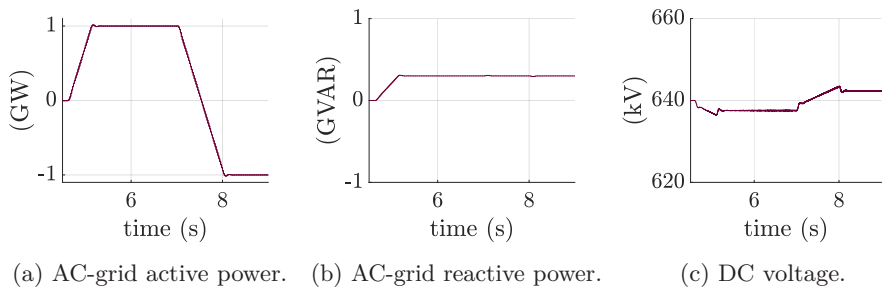
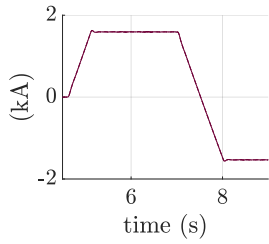


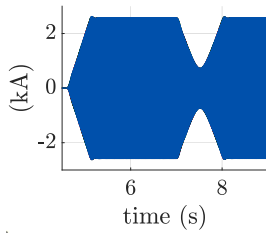
Figure IV.16: Simulation results for the start-up sequence from 0 s to 4.5 s. Dashed lines represent the response of MMC #0 and solid lines represent the response of MMC #4

The results for the operation sequence defined Section III.5 are plotted in Fig. IV.17 for MMCs #0 and #4.

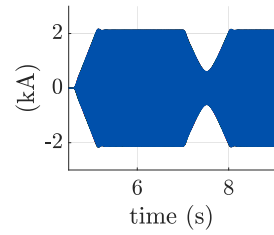




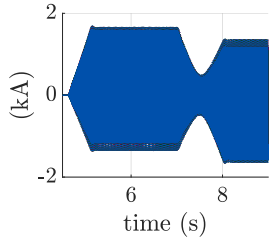
(d) DC current.



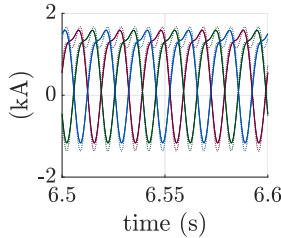
(e) AC-side current.



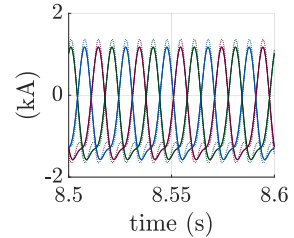
(f) AC-grid current.



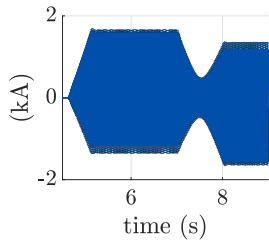
(g) Upper-arm current.



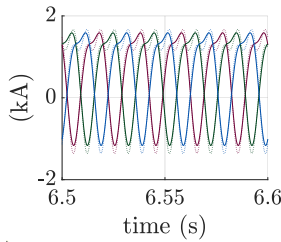
(h) Upper-arm current: zoom between 6.5 s and 6.6 s.



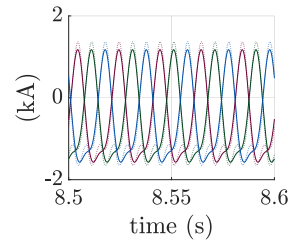
(i) Upper-arm current: zoom between 8.5 s and 8.6 s.



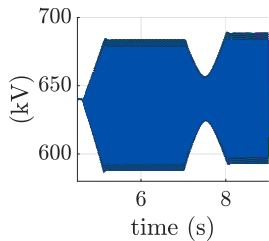
(j) Lower-arm current.



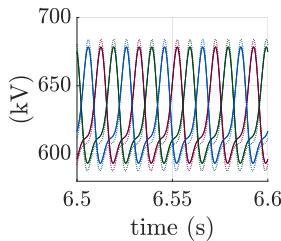
(k) Lower-arm current: zoom between 6.5 s and 6.6 s.



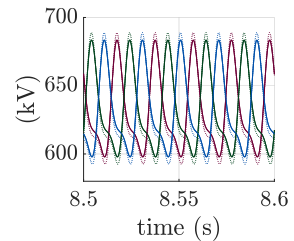
(l) Lower-arm current: zoom between 8.5 s and 8.6 s.



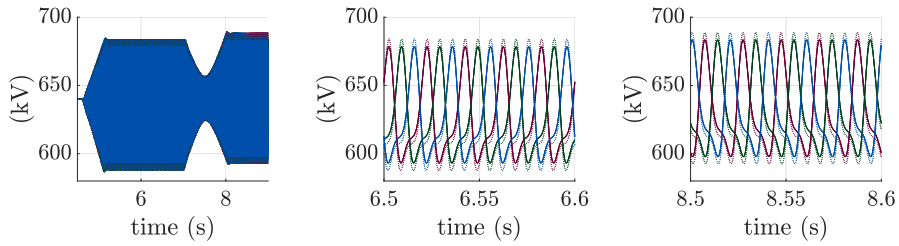
(m) Upper-arm capacitor voltages sum.



(n) Upper-arm capacitor voltages sum: zoom between 6.5 s and 6.6 s.



(o) Upper-arm capacitor voltages sum: zoom between 8.5 s and 8.6 s.



(p) Lower-arm capacitor voltages sum. (q) Lower-arm capacitor voltages sum: zoom between 6.5 s and 6.6 s. (r) Lower-arm capacitor voltages sum: zoom between 8.5 s and 8.6 s.

Figure IV.17: Simulation results for the nominal power transfer from 4.5 s to 9 s. Dashed lines represent the response of MMC #0 and solid lines represent the response of MMC #4

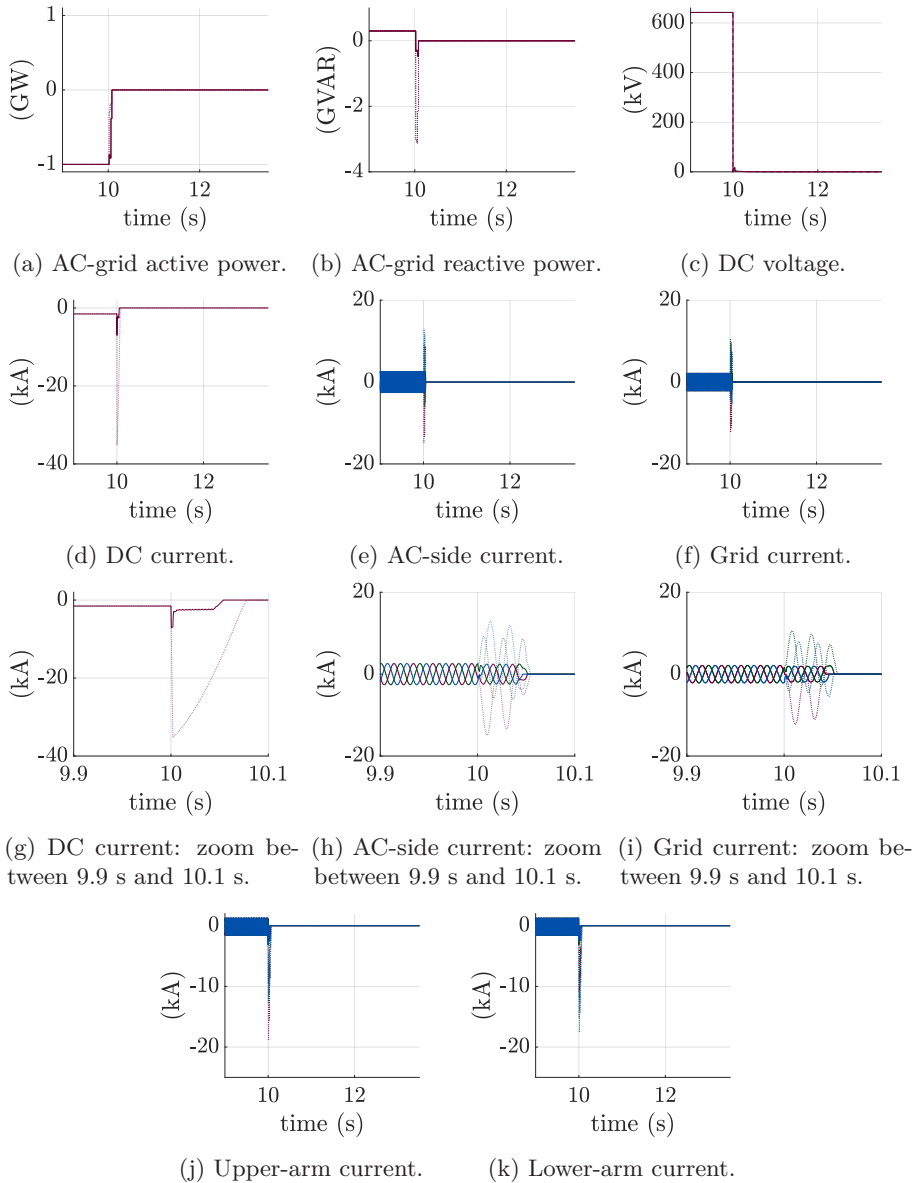
From the results in Figs. IV.17a, IV.17b, IV.17c, IV.17d, IV.17e and IV.17f, we can see that MMC #4, with coupled HTS arm coils, behaves similarly in terms of external dynamics to MMC #0. A detailed analysis of these waveforms is developed in Section III.5.

In Figs. IV.17g and IV.17j, we plot the upper- and lower-arm currents, respectively. In Figs. IV.17h and IV.17k, when $P = 1$ GW, the arm currents oscillate for the MMC #0 between -1.40 kA and 1.67 kA and for the MMC #4 between -1.25 kA and 1.5 kA. In Figs. IV.17i and IV.17l, when $P = -1$ GW, the arm currents oscillate for MMC #0 between -1.65 kA and 1.40 kA while for the MMC #4 between -1.57 kA and 1.17 kA.

In Figs. IV.17m and IV.17p, we plot the sum of the upper- and lower-arm capacitor voltages, respectively. In Figs. IV.17n and IV.17q, when $P = 1$ GW, the arm capacitor voltages sum oscillates between 587.01 kV and 685.23 kV for MMC #0 while for MMC #4 between 593.18 kV and 678.33 kV. In Figs. IV.17o and IV.17r, when $P = -1$ GW, the arm capacitor voltages sum oscillates between 592.11 kV and 690.0 kV for the MMC #0 while for the MMC #4 between 597.84 kV and 683.39 kV.

IV.3.3 Behavior during a Pole-to-Pole Fault

The results for the pole-to-pole fault defined in Section III.5.3 are plotted in Fig. IV.18 for MMCs #0 and #4.



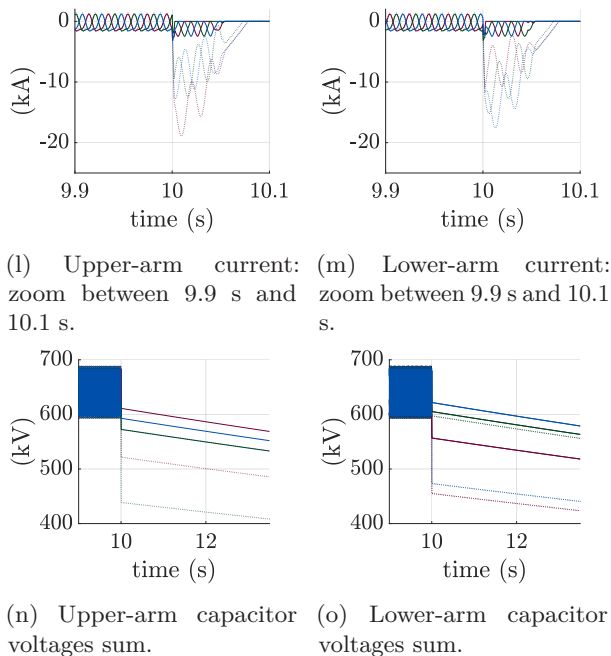


Figure IV.18: Simulation results for the pole-to-pole fault from 9 s to 13.5 s. Dashed lines represent the response of MMC #0 and solid lines represent the response of MMC #4.

The cryo-MMC significantly reduces the AC-grid contribution to the fault. When the fault occurs at $t = 10$ s, the active power drops to zero while the reactive power spikes up to 3.1 GVAR for MMC #0 versus 0.47 GVAR for MMC #4, as shown in Figs. IV.18b and IV.18e.

The DC-surge current is limited to 7 kA with MMC #4 versus 35.23 kA for the MMC #0, as illustrated in Figs IV.18d and IV.18f.

The converter AC-side current, the grid-side current, and the arm currents are limited during the fault by the superconducting arm coils. The peak current on the converter AC side is limited to 2.5 kA for MMC #4 versus 14.9 kA for MMC #0 as shown in Figs. IV.18g and IV.18i. The AC grid peak current is limited to 1.94 kA for MMC #4 versus 12.3 kA for MMC #0 as illustrated in Figs. IV.18h and IV.18j. The peak arm current is limited to 3.15 kA for MMC #4 versus 18.9 A for MMC #0 as shown in Figs. IV.18k, IV.18l, IV.18m and IV.18n.

As illustrated in Figs. IV.18n and IV.18o, the SMs capacitors are discharged during the fault until the converter is blocked. The value of dv/dt of this discharge is smaller for MMC #4 than for MMC #0 due to the highly-resistive current path provided by the superconducting arm coils.

The thermal behavior of the HTS arm coils during fault is shown in

Fig. IV.19. The HTS tape boundary temperature spikes immediately after the fault at 110 K as shown in Fig. IV.19a and the YBCO temperature spikes at 340 K as shown in Fig. IV.19b. Once the converter is blocked at $t = 10.042$ s, the HTS tape cools down and reaches the operating temperature of 65 K at $t = 20$ s. Note that the coil behavior is asymmetrical between the 3 phases as expected for a 3-phase system [82].

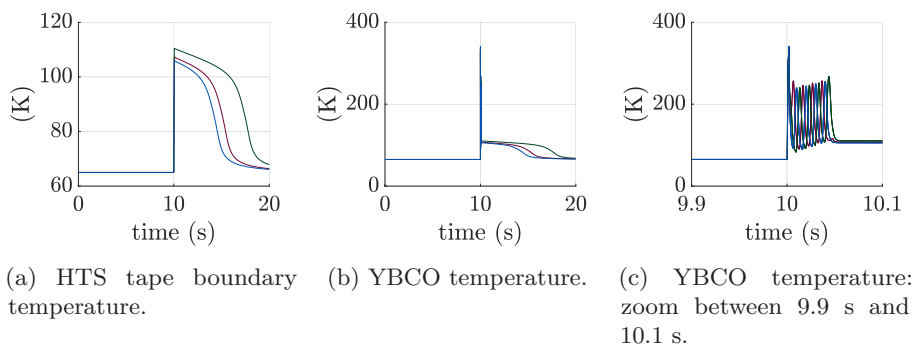


Figure IV.19: HTS coils thermal behavior.

Under the modeled pole-to-pole fault condition, the cryo-MMC reduces the DC-side surge current by 80%, the peak arm currents by 83%, and the peak AC current by 84% compared to the reference MMC. The obtained results validate the thermal design of the proposed coupled HTS arm coils for which temperatures reached 340 K on the HTS layer and 115 K on the HTS tape boundary during the fault.

This study confirms the thermal stability of the proposed HTS coils and demonstrates that the cryo-MMC has the potential to avoid oversizing the converter station to withstand fault conditions thanks to the fault current limitation function provided by the HTS arm coils. Also, the limitation of the DC-fault current may facilitate the deployment of DC-CBs.

IV.4 Economical Assessment

IV.4.1 Conventional Arm Coils

The capital cost of the reference coil for the MMC #0 is estimated by considering a capital cost of 20 k€/MVA for reactors with voltage ratings higher than 230 kV. The conventional arm coils are rated for 40 MVA, and consequently, the capital cost of each arm coils is estimated to be $CC_{coil} = 800$ k€. The total capital cost of coils for the whole MMC #0 is $TCC_{coil} = 4800$ k€.

IV.4.2 HTS Arm Coils

The total capital cost of HTS coils TCC_{coil} (Fig. IV.11) is estimated as

$$TCC_{coil} = 6 CC_{coil} + CC_{RS} \quad (IV.14)$$

where CC_{RS} is the capital cost of the refrigeration system and CC_{coil} is the capital cost of each HTS arm coil.

The capital cost of a single HTS arm coil is

$$CC_{coil} = 2 l_p N_p N_s CC_{tape} + CCV_{cryostat} \frac{V_{cryostat}}{2} \quad (IV.15)$$

where CC_{tape} is the capital cost of the HTS tape per unit length assumed to be 75 €/m, l_p is the length of a single pancake, $V_{cryostat}$ is the storage volume of the coupled upper and lower arm coils' cryostat in m^3 , and $CCV_{cryostat}$ its capital cost per unit volume assumed to be 2000 €/m³. We recall for coupled coils, both arm coils are in the same cryostat.

The capital cost of the refrigeration system is estimated as

$$CC_{RS} = N_{PTC} \cdot CC_{PTC} + CC_{BT} + 6 CC_{pump} \quad (IV.16a)$$

The refrigeration system sizing is presented in Table IV.11. These results are obtained from the data provided in Tables IV.6, IV.7 and IV.8. The number of cryocoolers N_{PTC} in the refrigeration system is obtained from Eq. (IV.5) using the nominal coil's losses given Table IV.9.

	MMC	
	#3	#4
Nominal Cooling Cold Power [kW]	4.54	4.72
N_{PTC}	4	8
Nominal Electric Power Consumption [kW]	72.28	109.55
Refrigeration System dimensions [m]	5.6 (L) × 5.1 (W) × 7 (H)	7.3 (L) × 5.1 (W) × 7 (H)
Mass [kg]	$13.56 \cdot 10^3$	$21.54 \cdot 10^3$
Capital Cost [k€]	511.87	726.67

Table IV.11: Refrigeration system sizing.

Finally, the coil's capital costs for the studied configurations are summarized in Table IV.12.

	MMC		
	#0	#3	#4
CC_{coil} [k€]	800	2176	843
TCC_{coil} [k€]	4800	13569	5840

Table IV.12: Coil's capital cost.

Table IV.12 shows that HTS coils are more expensive than conventional ones, which is mainly due to the higher capital costs of 2G HTS tapes at the present date. Additionally, the operation at 65 K for MMC #4 increases the current transportation capacity of HTS tapes and thereby reduces capital costs compared to the operation at 77 K for MMC #3.

IV.4.3 Cryo-MMC

The capital cost of a HB-MMC can be written in a very simplified manner as

$$CC_{MMC} = CC_{HBSM} + TCC_{Coil} \quad (IV.17)$$

where CC_{HBSM} corresponds to the total costs related to the converter submodules and TCC_{Coil} is the total capital cost of coils provided in Tab. IV.12.

The reference MMC #0 has a capital cost of $CC_{MMC} = 110$ M€ [96], since we have estimated $TCC_{coil} = 4.8$ M€ in Section IV.4.1, we deduce $CC_{HBSM} = 105.2$ M€. The MMC capital cost for the different arm coil configurations is summarized in Table IV.14.

	MMC		
	#0	#3	#4
CC_{MMC} [M€]	110	118.77	111.04
$100 \frac{TCC_{Coil}}{CC_{MMC}}$ [%]	4.36	12.9	5.55

Table IV.13: MMC capital cost for different arm coil configurations.

Table IV.14 shows that the cryo-MMCs, corresponding to the MMCs #3 and #4, are more expensive than the reference MMC #0. Notice that the capital cost of the arm coils corresponds to a small fraction of the MMC #0 capital cost. Even if the arm coils' cost is doubled for MMC #4, the total impact of

the converter's capital cost is still minor. In particular, MMC #4 corresponds to an increase in the capital cost of 2.13% compared to the MMC #0.

To assess the cost of losses for the MMC, we start by computing its annual energy losses AEL as

$$AEL = \begin{cases} 8760 k_u (P_{cond} + P_{sw} + P_{coil}), & \text{for the MMC,} \\ 8760 k_u (P_{cond} + P_{sw} + P_{RS,e}), & \text{for the cryo-MMC.} \end{cases} \quad (IV.18)$$

where k_u is the converter's utilization factor adopted to be $k_u = 0.95$. Notice that we consider a nominal power transfer overall the operation span.

The annual energy losses for the different MMC's configurations is presented in Table IV.14.

	MMC		
	#0	#3	#4
AEL [MWh/year]	$6.6248 \cdot 10^4$	$6.0044 \cdot 10^4$	$6.1152 \cdot 10^4$

Table IV.14: MMC energy loss for different arm coil configurations.

The estimation of the life-cycle cost of the proposed MMCs is calculated here as the sum of the present value of all costs over the time horizon,

$$LCC \triangleq \sum_{t=1}^T \frac{C_t}{(1+r)^t} \quad (IV.19)$$

where r is the discount rate, T is the time horizon and C_t is the cost in the year t calculated as follows.

$$C_t = CC_t + OC_t \quad (IV.20)$$

where CC_t and OC_t represent the capital and the operational cost in the year t . In this study we assume a discount rate of 4% and a operation horizon of 40 years.

The capital cost is assumed to be only composed of the capital cost of the MMC as the initial investment cost, that is

$$CC_t = \begin{cases} CC_{MMC}, & \text{for } t = 0, \\ 0, & \text{otherwise.} \end{cases} \quad (IV.21)$$

The operational cost is assumed to be only composed of the annual energy losses and is calculated as follows,

$$OC_t = MCL \cdot AEL \quad (IV.22)$$

where MCL is the monetary cost of losses assumed to be 60 €/MWh.

The updated cost evolution for the MMC with different arm coil configurations is plotted in Fig. IV.20 for a 40-year time-span.

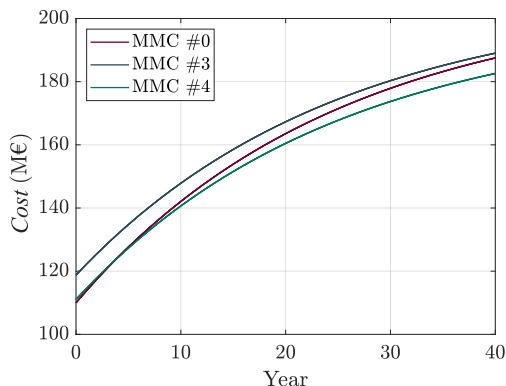


Figure IV.20: Yearly cost evolution for the MMC with different arm coil configurations.

As shown in Fig. IV.20, the MMC #4 has an initial capital cost slightly higher than the MMC #0 and this difference is compensated by the reduced operational cost of MMC #4 which finds a breakeven in 4 years. At 40 years, MMC #0 has an LCC of 187.52 M€ versus 189.03 M€ for MMC #3 and 182.59 M€ for MMC #4.

Another critical aspect of the HTS arm coil system is its contribution to the converter weight and its footprint. These two aspects are significant for offshore applications since it represents an important constraint for the offshore platform. For the reference MMC, the arm coil's mass accounts for 42% of the converter weight [51]. In Table IV.15, we present the mass and the footprint of the proposed design. The HTS arm coil's data consider the mass and footprint of the refrigeration system. MMC #3 reduces the arm coils' mass by 51% while maintaining a similar footprint. MMC #4 reduces the arm coils' mass by 55.5% and their footprint by a factor of 1.6.

	MMC		
	#0	#3	#4
Arm coils mass [t]	255	93.4	61.7
Arm coils footprint [m ²]	140.63	133.21	86.00

Table IV.15: Coupled HTS arm coils mass and footprint, including the refrigeration system.

IV.5 Summary

Directly-coupled HTS arm coils can be designed to reduce the conversion losses and provide a fault current limitation. For instance:

- An HB-MMC with directly-coupled HTS arm coils with $L = 28.3$ mH and $K_{u,l} = 0.8788$ operating at 77 K has smaller arm coils than the reference MMC. The weight of two coupled HTS arm coils (including the refrigeration system) is 31.1 t (a reduction of 63.4%), and its volume is 47 m³ (a reduction of 78.6%). Such MMC has also improved steady-state performances. In particular, the conversion losses are reduced by 9.4%. In addition, the DC-fault current is reduced by 80%. Such converter is estimated to have a capital cost of 118.77 M€ (an increase of 8%) and a life-cycle cost considering 40 years of operation of 189.03 M€ (an increase of 0.8%).
- An HB-MMC with directly-coupled arm HTS coils with $L = 27.7$ mH and $K_{u,l} = 0.8788$ operating at 65 K has smaller arm coils than the reference MMC. The weight of the coupled HTS arm coils (including the refrigeration system) is 20.6 t (a reduction of 75.8%), and its volume is 40.7 m³ (a reduction of 82%). Such MMC has also improved steady-state performances. In particular, the conversion losses are reduced by 7.7%. In addition, the DC-fault current is reduced by 80%. Such converter is estimated to have a capital cost of 111.04 M€ (an increase of 0.95%) and a life-cycle cost considering 40 years of operation of 172.7 M€ (a reduction of 7.9%).

We remind the reader that such technical-economic analysis is based on many assumptions and strongly depends on the cost inputs. The relative values are probably more trustworthy than the absolute values. Therefore the results are to be interpreted with care. In that sense, it seems that a cryo-MMC operating at 65 K is competitive compared to the reference MMC.

Chapter V

Laboratory-Scale Cryo-MMC Prototype

In previous chapters, we have shown that directly-coupled HTS arm coils are a promising solution for HB-MMC, yielding smaller arm coils and providing fault-current limitation. In this chapter, we detail the design, construction, and testing of the world's first cryo-MMC.

The objectives of this chapter are:

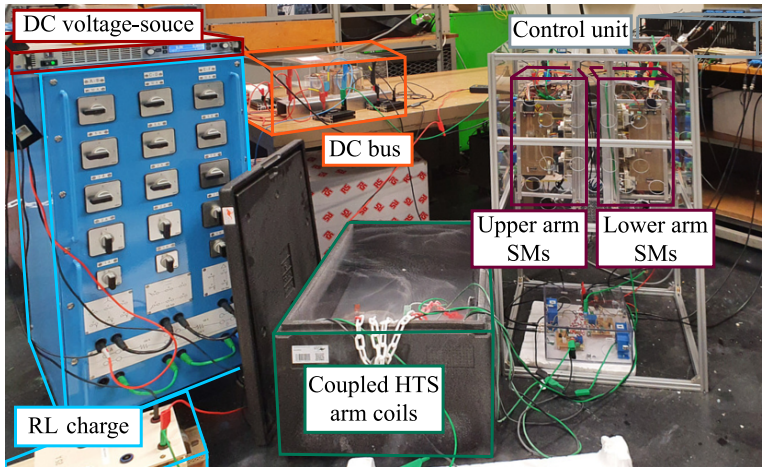
- To validate the construction of the high-temperature superconducting (HTS) module proposed in Chapter IV.
- To demonstrate the proper behavior of a laboratory-scale cryo-MMC prototype during normal operation.
- To compare the performances of a cryo-MMC and of a conventional MMC during normal operation.
- To move the cryo-MMC to a technology readiness level (TRL) of 3-4.

This chapter is organized as follows. Section V.1 summarizes the main technical specifications and overview of the prototype. Section V.2 concludes with experimental results and discussion. In Section V.3, we summarize the essential findings of this chapter.

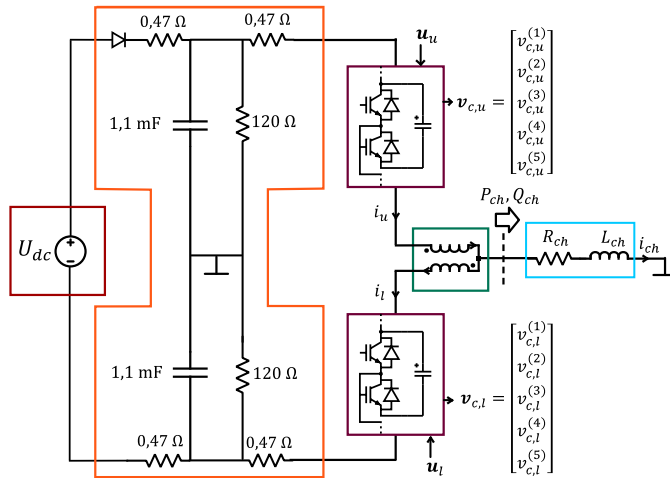
V.1 Prototype Specifications and Overview

Our cryo-MMC prototype and the corresponding test circuit are shown in Fig. V.1. Its specifications are summarized in Table V.1.

The prototype is composed of the following components. A DC-voltage source (in red) is connected through a DC bus (in orange) to the upper- and lower-arm SMs (in purple). These upper- and lower-arm SMs are connected in series with HTS arm coils (in green), and the converter feeds an RL-load (in blue).



(a) Photo.



(b) Electric circuit.

Figure V.1: Cryo-MMC prototype.

Quantity	Symbol	Value
Nominal DC-voltage [V]	U_{dc}	150
Number of submodules per arm	N	5
Submodule capacitance [mF]	C	3.3
Fundamental frequency [Hz]	F_0	50
Load inductance [mH]	L_{ch}	4.25
Load resistance [Ω]	R_{ch}	2

Table V.1: Cryo-MMC prototype specifications.

V.1.1 Arm Submodules

Our prototype has five half-bridge submodules per arm. Their assembly is shown in Fig. V.2. The SM capacitors (KEMET ALS31A332400) have a capacitance of 3.3 mF and are rated for a maximum voltage of 400 V. The IGBT modules (SKM 145GB066D) have a maximum collector-emitter voltage of 600 V and a maximum collector current of 195 A at 25 °C, and they are controlled by the gate driver (SKHI 21A R).

The arm stacks were designed and built as part of the Ph.D. thesis of Gilbert Bergna [67], and the postdoc of Nikola Stankovic [97]. Several updates were required so that they could be used in this project.

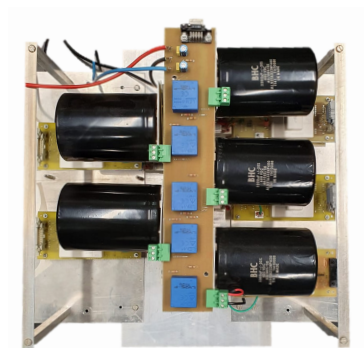


Figure V.2: Cryo-MMC prototype HB-SMs assembly.

V.1.2 Control Structure

The prototype is operated in open loop as illustrated in Fig. V.3a using an OP 5600 real-time target.

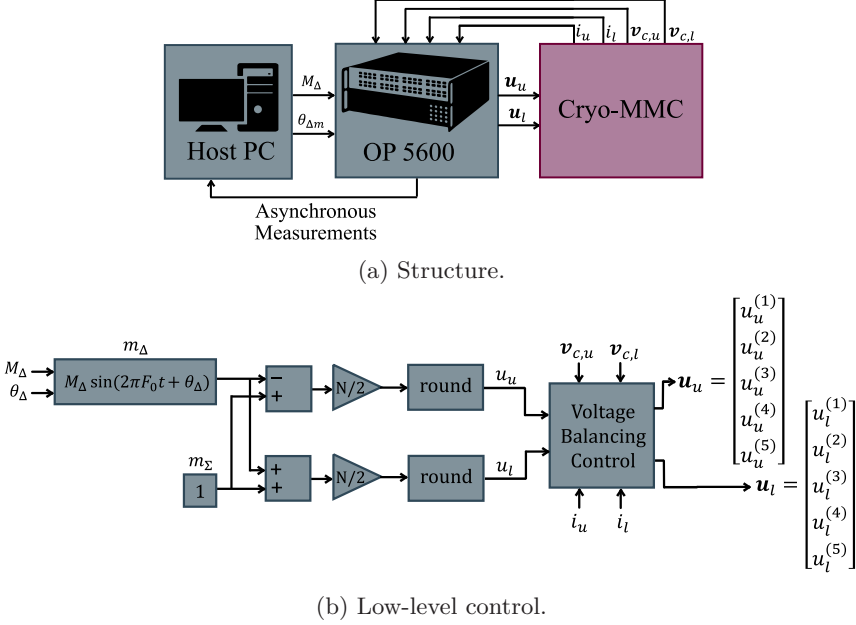


Figure V.3: Cryo-MMC prototype control structure.

The nearest-level modulation (NLM) is implemented using Eq. (E.5) from which the upper- and lower-arm modulation indices, u_u and u_l , respectively, are determined from the Δ -modulation index m_Δ , defined from its amplitude M_Δ and phase θ_Δ as in Eq. (E.8), and the Σ -modulation index adopted to be $m_\Sigma = 1$. To obtain the switching signals of the i -th IGBT for the upper and lower arms, $u_u^{(i)}$ and $u_l^{(i)}$, respectively, we employ the capacitor voltage balancing control illustrated in Fig. E.4, for which the voltage balancing algorithm is implemented as in Fig. E.5.

V.1.3 Uncoupled/Coupled HTS Arm Coils

V.1.3.1 HTS tape

Following the considerations of section IV.1.3, to capitalize on our experience with 1G HTS tapes [98], [99] and to reduce the risks, we selected the 1G BSCCO tape (Sumitomo DI-BSCCO™ HT-CA tape) for this project. The geometric data for that BSCCO tape are summarized in Table V.2. In Fig. V.4, we plot

the measured I-V characteristic of the short sample. It has a critical current of 163 A at 77 K.

Quantity	Value
Critical current [A]	170
Width [mm]	4.5
Thickness [mm]	0.34
Reinforcement thickness [mm]	0.05
Critical double bending diameter [mm]	60

Table V.2: Parameters for the HT-CA BSCCO tape. This tape has a copper reinforcement layer.

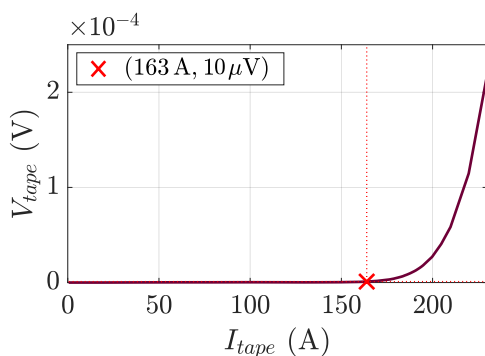


Figure V.4: Measured I-V characteristic of the HT-CA BSCCO tape.

V.1.3.2 HTS pancake coil

Following a similar design to the one proposed in section IV.1.4, we realized and tested a total of 8 HTS pancake coils, denoted #PC1 to #PC8.

A pancake coil is shown in Fig. V.5. Each HTS pancake is wound using $\tilde{47}$ m of BSCCO tape co-wound with a corrugated spacer (Cenpac Mach PP 5 mm). The specifications of an HTS pancake coil are summarized in Table V.3.

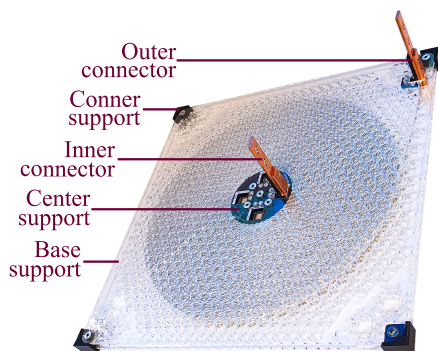


Figure V.5: HTS pancake coil.

Quantity	Symbol	Value
Dimensions without connectors [m]		0.4 (W) × 0.4 (L) × $12.5 \cdot 10^{-3}$ (H)
Coil inner radius [m]	r_{in}	$4.2 \cdot 10^{-2}$
Coil length [m]	l_p	47
Number of turns [-]	N_t	72
Corrugated insulator thickness [m]	t_i	$1.8 \cdot 10^{-3}$

Table V.3: HTS pancake coil specifications.

The base support was laser cut in a 4 mm PMMA plate. The other parts of the pancake were printed using an Ultimaker 3 extended 3D printer with a 2.85 mm diameter PLA filament with a profile of 0.2 mm, an infill factor of 80%, and a printing temperature of 200 °C. The copper connectors are connected to the HTS tape by pressure. The construction process of the HTS pancake is depicted in Fig. V.6.

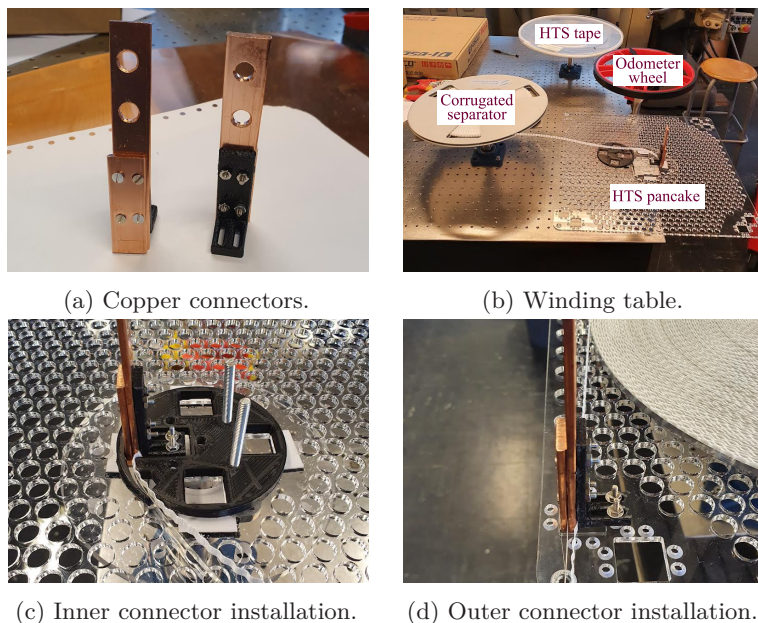


Figure V.6: Winding of an HTS pancake coil.

We measured the (connector) DC-resistance, the inductance, and the critical current of the HTS pancake coils and summarized them in Table V.4. The DC resistance was measured at 20 A and its inductance at 20 A and 50 Hz, both in an LN₂ bath. The critical current was deduced from the measured I-V characteristic as discussed in section IV.1.3. The results show that the characteristic of the HTS pancake coils are quite uniform, and therefore that the conductor has not been degraded during winding. The coil's critical current variation may be due to the variation of the tape critical current along the length.

	HTS pancake coil							
	PC1	PC2	PC3	PC4	PC5	PC6	PC7	PC8
R_{PC} [$\mu\Omega$]	18.3	25.0	22.4	23.8	19.0	19.4	18.5	27.2
L_{PC} [mH]	1.19	1.21	1.23	1.18	1.24	1.20	1.20	1.22
I_c [A]	153	143	141	140	140	155	154	153

Table V.4: Measured HTS pancake coil parameters.

V.1.3.3 Uncoupled/coupled HTS arm coils

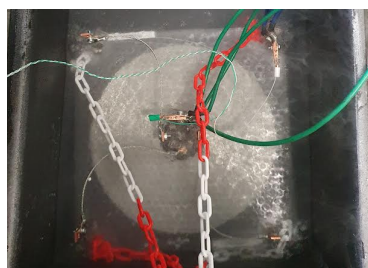
We tested three HB-MMCs with different arm coils configurations:

- MMC #0e: an MMC with 5 HB-SMs and uncoupled copper arm coils operated at room temperature. The Coil #0u integrates the upper arm, and Coil #0l the lower arm.
- MMC #1e: an MMC with 5 HB-SMs and uncoupled HTS arm coils operated in an LN2 bath at 77 K. Coil #1u integrates the upper arm, and Coil #1l the lower arm.
- MMC #2e: an MMC with 5 HB-SMs and HTS directly-coupled arm coils operated in an LN2 bath at 77 K. Coil #2u integrates the upper arm, and Coil #2l the lower arm.

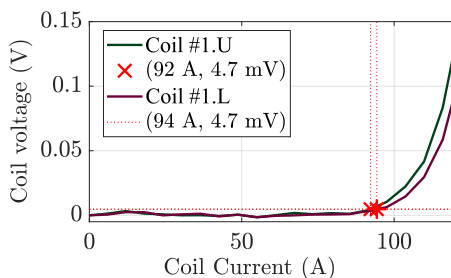
The HTS arm coils were built as follows.

- Coil #1u: built from the series association of HTS pancakes #PC1, #PC2, #PC3, and #PC4, all directly coupled between themselves.
- Coil #1l: built from the series association of HTS pancakes #PC5, #PC6, #PC7, and #PC8, all directly coupled between themselves.
- Coil #2u: built from the series association of HTS pancakes #PC5 and #PC7, directly coupled with Coil #2l.
- Coil #2l: built from the series association of HTS pancakes #PC6 and #PC8, directly coupled with Coil #2u.

The measurements for the HTS coils are presented in Table V.5. The DC-resistance was measured at 20 A, and its self and mutual inductances were measured at 20 A and 50 Hz. The critical current was computed from the normalized I-V measurement [80] shown in Fig. V.7.



(a) Measured I-V characteristic of the HTS Coil #1u.



(b) I-V characteristic.

Figure V.7: HTS Coils #1u and #1l I-V Measurement.

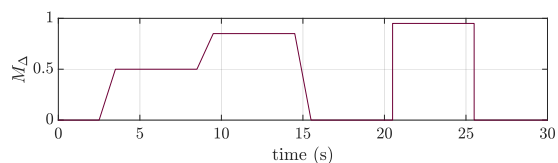
The critical current of Coils #1u and #1l correspond to 55 % of the BSCCO tape critical current of 163 A. And the critical current of Coils #2u and #2l correspond to 74 % of the BSCCO tape critical current. This degradation in critical current is attributed to the coils' self field.

	Coil					
	#0u	#0l	#1u	#1l	#2u	#2l
Number of HTS PCs [-]	0	0	4	4	2	2
R [Ω]	0.20	0.21	$7.47 \cdot 10^{-4}$	$6.41 \cdot 10^{-4}$	$3.74 \cdot 10^{-4}$	$3.2 \cdot 10^{-4}$
L [mH]	4.25	4.27	13.43	13.1	4.1	4.0
M [mH]	0	0	0	0	2.62	2.55
I_c [A]	-	-	92	94	120	122
T_{op} [K]	RT	RT	77	77	77	77

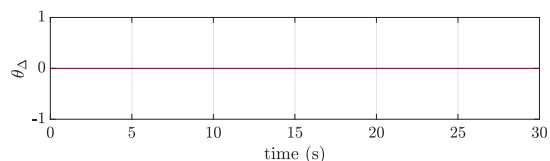
Table V.5: Measured HTS coil parameters. RT stands for room temperature.

V.2 Experimental Results

In this section, we report experimental results for MMCs #0e, #1e and #2e. We consider a repetitive sequence defined by the Δ -modulation index profile shown in Fig. V.8.



(a) Amplitude.



(b) Phase.

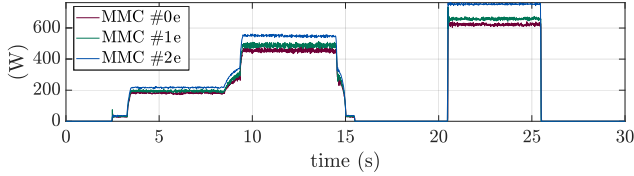
Figure V.8: Δ -modulation index sequence.

The modulation index profile (Fig. V.8) is defined as follows.

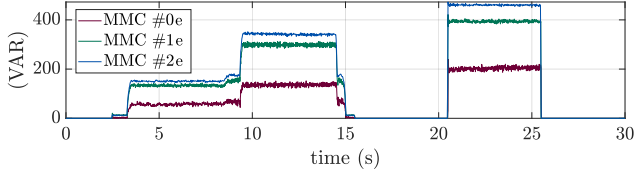
- At $t = 2.5$ s, M_{Δ} ramps up from 0 to 0.5 in 1 s.
- At $t = 8.5$ s, M_{Δ} ramps up from 0.5 to 0.85 in 1 s.
- At $t = 14.5$ s, M_{Δ} ramps down from 0.85 to 0 in 1 s.
- At $t = 20.5$ s, M_{Δ} ramps up from 0 to 0.95 in 1 ms.
- At $t = 25.501$ s, M_{Δ} ramps down from 0.95 to 0 in 1 ms.

V.2.1 Comparison Between Different Arm Coil Configurations

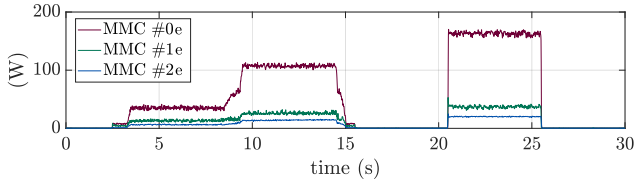
The measured active and reactive power at the RL load are plotted in Figs. V.9a and V.9b, respectively. The measured arm coils' electrical losses, corresponding to the sum of the upper and lower arm coil's electrical losses, are plotted in Fig. V.9c.



(a) RL-load active power.



(b) RL-load reactive power.



(c) Total arm coil losses.

Figure V.9: Measurements for different arm coil configurations.

Note that each converter has a slightly different operating point (active and reactive power). This is because the arm coil resistance and inductance of each converter are different (see Table V.5).

In Table V.6, we summarize the measurements presented in Fig. V.9 for $M_{\Delta} = 0.95$ and $\theta_{\Delta} = 0$. We define the normalized arm coils losses as the arm

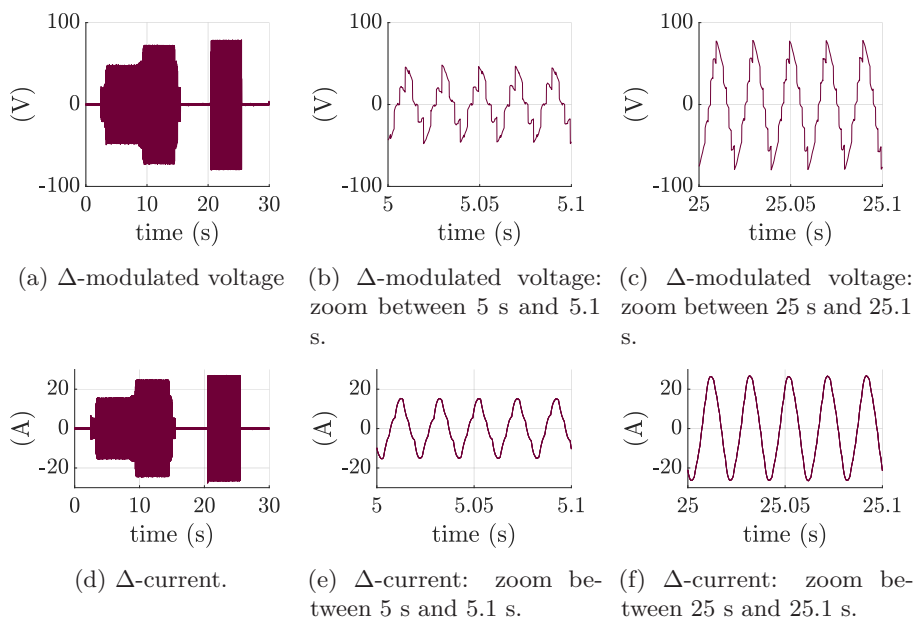
coils losses divided by the active power. The normalized arm coils losses are 4.5 times lower for MMC #1e and 9.8 times lower for MMC #2e compared to MMC #0e.

	MMC #0e	MMC #1e	MMC #2e
Converted active power [W]	626	660	760
Converted reactive power [VAR]	192	388	456
Arm coils losses [W]	164	38	19
Normalized arm coils losses	0.2600	0.0576	0.0263

Table V.6: Measurements for $M_{\Delta} = 0.95$ and $\theta_{\Delta} = 0$.

V.2.2 Cryo-MMC Behavior During Normal Operation

In this part, we present the measurements during regular operation for MMC #2e, which is the configuration selected in Chapter IV as the most suitable for the cryo-MMC. MMC #2e measurements for the modulation index profile considered in Fig. V.8 are presented in Fig. V.10.



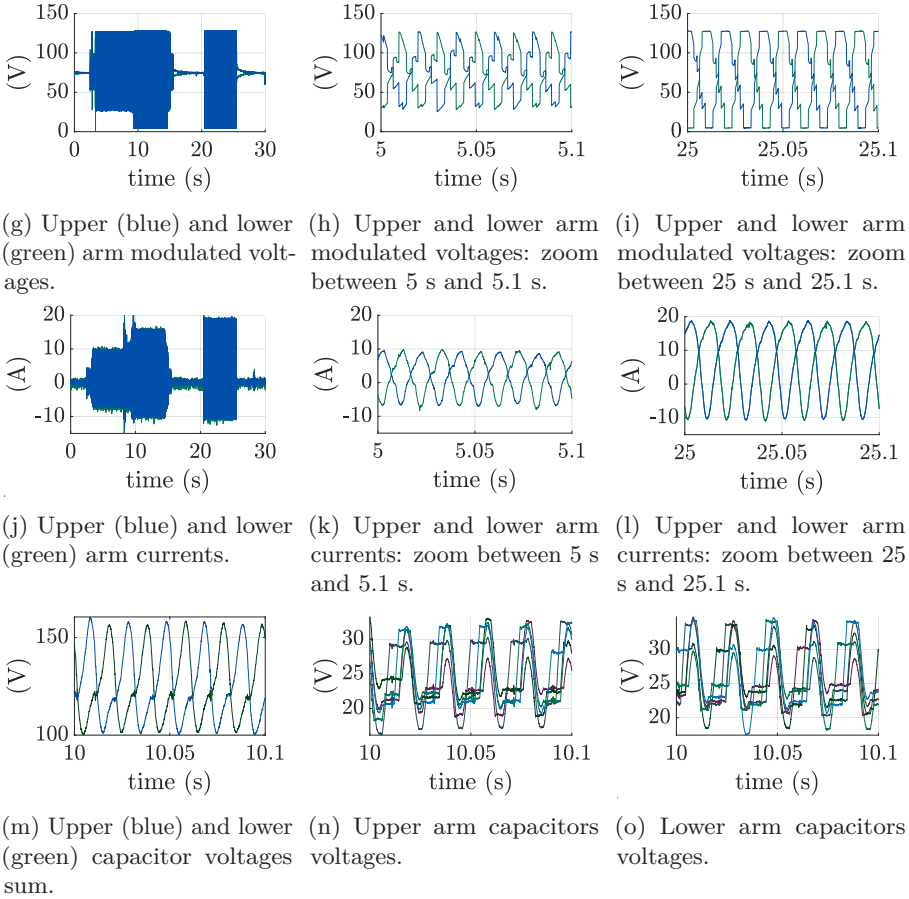


Figure V.10: Measurements for the MMC #2e.

The Δ -modulated voltage is shown in Figs. V.10a, V.10b and V.10c. We identify five voltage levels in Fig. V.10b for $M_{\Delta} = 0.5$, and six voltage levels in Fig. V.10c for $M_{\Delta} = 0.95$.

The Δ -current flowing through the RL-load is shown in Figs. V.10d, V.10e and V.10f. The Δ -modulated voltage harmonics are filtered by arm coils and the load.

The upper- and lower-arm modulated voltages are shown in Figs. V.10g, V.10h and V.10i. We identify four voltages levels in Fig. V.10h for $M_{\Delta} = 0.5$, and five voltage levels in Fig. V.10i for $M_{\Delta} = 0.95$.

The upper- and lower-arm currents are shown in Figs. V.10j, V.10k and V.10l. In Figs. V.10k and V.10l, we can see that the arm currents are composed by a DC component and harmonics.

The sum of capacitor's voltage for the upper and lower arm, shown in Fig. V.10m, oscillates between 100 V and 158 V with a mean value of 125 V. The

individual upper and lower arm capacitor voltages, shown in Figs. V.10n and V.10o, respectively, oscillate between 18.2 V and 34.3 V with a mean value of 25 V.

The cryo-MMC #2e was tested for two hours, repeating the sequence presented in Fig. V.8 for the amplitude of the modulation index every 30 s. The converter behaved as expected. After the test, the I-V characteristics of the HTS arm coils were measured again. They remained unchanged regarding the pre-test conditions, indicating that the HTS coils suffered no degradation during the converter operation.

V.3 Summary

First, we designed, wound and tested successfully 8 inductive high-temperature superconducting pancake coils. Each pancake coil is made of ~ 47 m of 1G HTS tape and has an inductance of ~ 1.2 mH. The pancake coils are connected in series and stacked to obtain the directly-coupled HTS arm coils. We measured a self-inductance of $L = 4$ mH and a coupling coefficient $K_{u,l} = 0.88$. The measured critical current at 77 K is 120 A, corresponding to 74% of the measured critical current of the HTS tape.

Second, the world's first HB-MMC with directly-coupled HTS arm coils (cryo-MMC) has been designed, built, and tested. The prototype is a 1-phase 5-submodule HB-MMC. The prototype operated as expected, in inverter mode for a DC voltage of 150 V up to 760 W. The normalized arm coils losses are 10 times lower for the cryo-MMC compared to the HB-MMC with uncoupled copper arm coils. The reported results confirm the feasibility of integrating high-temperature superconducting coils into an MMC.

From our point of view, the main difficulties for the realization of this prototype were related to the HTS coils. It required the choice of suitable materials which can handle thermal cycling down to 77 K without breaking. The HTS tape needs to be handled carefully during winding, but no major problem occurred and the 8 pancakes coils were functional.

Conclusion

We summarize here the essential findings and propose future research directions.

In Chapter II, a detailed-arm harmonic state-space (DA-HSS) model was developed and validated for the half-bridge MMC. This model makes it possible to accurately calculate the steady-state values of the converter's state variables ten times faster than classical time-domain models. Its key difference from classical state-space models is its ability to inherently account for the harmonics created by the modulation (nearest level modulation here). Future works could apply the same methodology to other power electronic converters where the effect of the modulation harmonics is more critical, such as the 2L-VSC.

In Chapter III, we defined steady-state performance indicators that need to be considered when designing an MMC. These indicators are: the capacitor voltage ripple, the maximum and minimum arm currents, the weighted total harmonic distortion of the AC-modulated voltage, the arm coil losses, and the conduction and switching losses of the solid-state switches. Then, we studied the possibility of magnetically coupling the arm coils of the HB-MMC with the aim of reducing their size. We used the DA-HSS model to size the arm coils of the HB-MMC, for both the uncoupled and directly-coupled cases. Three arm coil configurations were selected and compared using a time-domain transient simulation of a 1 GW ± 320 kV P2P HVDC link. We showed that directly-coupled arm coils can be designed to: keep the same size while improving the performances, or reduce the size while keeping the same performances. For instance, an MMC with directly-coupled arm coils with a self-inductance of $L = 27.3$ mH and a coupling coefficient of $K_{u,l} = 0.6740$ would perform similarly to the reference industrial-scale MMC while reducing the arm coil mass by 43.6% and its volume by 44.7%. Future works could look deeper into the electrical, thermal and mechanical design of conventional dry-type air-core coupled arm coils.

In Chapter IV, we studied the possibility to replace the conventional dry-type air-core arm coils with high-temperature superconducting arm coils to provide a fault current limitation function to the HB-MMC. We designed the HTS arm coils and their refrigeration system considering 1 GW ± 320 kV HB-MMC. We used the DA-HSS model to calculate the steady-state performance indicators. We showed that the cryo-MMC can improve steady-state performance when compared to the reference MMC. A transient analysis confirmed the thermal and electrical stability of the cryo-MMC. The HTS arm coils reduced the DC and AC prospective fault currents by a factor of five. Also, the cryo-MMC can lower the arm coils' mass by a factor of four while reducing their footprint by a factor of 1.6. These two aspects, the mass and the footprint, are significant

for offshore applications since they represent an important constraint for the offshore platform. We assessed the economic cost of a cryo-MMC and showed that the configuration with directly-coupled HTS arm coils operating at 65 K yields an increase in capital cost of 0.96% when compared to the reference MMC. The lower operational losses of the cryo-MMC result in a life cycle-cost reduction by 14.82 M€ at the end of a 40 years operation compared to the reference MMC. Future works could investigate alternative refrigeration system architectures in order to improve the cooling efficiency and thereby reduce the operational losses of the cryo-MMC.

In Chapter V, we described the design, construction, and tests of our laboratory-scale HB-MMC with high temperature superconducting directly-coupled arm coils. We designed, wound, and successfully tested eight inductive high-temperature superconducting pancake coils. Each pancake coil is made of 47 m of 1G HTS tape and has an inductance of ~ 1.2 mH. The pancake coils are connected in series to obtain the directly-coupled HTS arm coils. This is the world's first HB-MMC with directly-coupled HTS arm coils (cryo-MMC) that has been designed, built, and tested. The prototype is a 1-phase 5-submodule HB-MMC. The prototype operated as expected, in inverter mode for a DC voltage of 150 V up to 760 W. The normalized arm coils losses are ten times lower for the cryo-MMC compared to the HB-MMC with uncoupled copper arm coils.

Future works on the cryo-MMC solution can focus on the following aspects.

- The designed refrigeration system in Chapter IV has an efficiency of around 5% at 77 K and 3% at 65 K. Future works should look into more efficient refrigeration systems to reduce the operational costs of the cryo-MMC.
- Studies of the cryo-MMC integration in an HV-MTDC grid should be realized to evaluate the impact of this converter in large DC systems.
- The association of the cryo-MMC and DC-CBs should be analyzed to evaluate the most suitable CB technology in terms of functional and economic aspects. This analysis would also enable comparison between a cryo-MMC associated with a DC-CB with a fault-blocking capable topology, such as the MMC with full-bridge submodules.
- The cryo-MMC fault-current capability still needs to be tested at the laboratory scale.

The cryo-MMC can also provide a suitable solution for MMC-HVDC overhead lines due to its fault-current limitation capability. Currently, MMC-based HVDC overhead lines are unlikely to deploy the classical HB-MMC since they are more fault-prone to a DC short-circuit than cable links due to environmental and weather conditions. The MMC with full-bridge SMs (FB-MMC) is seen as the preferred topology for overhead DC-transmission lines. Still, the association of the cryo-MMC and a DC-circuit breaker can be

Conclusion

a less expensive alternative. While a FB-MMC has a capital cost of 150 M€ [96], the proposed cryo-MMC has an estimated capital cost of 111.04 M€.

The industrialization of the cryo-MMC would require a joint effort between two industries: HVDC power electronic converter manufacturers and superconducting equipment manufacturers. The construction of the HTS arm coils of the cryo-MMC can inspire itself from the successful projects of superconducting fault current limiters all around the globe, as reported in [100, 101, 102, 103].

Appendices

Appendix A

Linear Systems and Harmonic State Space

A.1 Mathematical Preliminaries

Definition A.1.1 (Time-dependent matrix function). A time-dependent matrix function is a mapping which assigns to a given $t \in \mathbb{R}$ a unique complex matrix $\mathbf{F}(t) \in \mathbb{C}^{N \times M}$. Denote by $C(\mathbb{R}, \mathbb{C}^{N \times M})$ the set of time-dependent matrix functions.

Definition A.1.2 (T-periodic matrix function). Consider a time-dependent matrix function $\mathbf{F}(t)$. Denote by $\mathbf{C}_T(\mathbb{R}, \mathbb{C}^{N \times M})$ the set of continuous, T-periodic matrix functions such that $\mathbf{F}(t) \in \mathbf{C}_T \iff \mathbf{F}(t + T) = \mathbf{F}(t)$, $\forall T \in \mathbb{R}_{>0}$, where T is the period of $\mathbf{F}(t)$.

Definition A.1.3 (Causal time-dependent matrix function). A causal time-dependent matrix function is a mapping which assigns to a given $t \geq t_0$, with $t_0 \in \mathbb{R}_{\geq 0}$, a unique complex matrix $\mathbf{F}(t) \in \mathbb{C}^{N \times M}$ and $\mathbf{F}(t) = 0, \forall t < t_0$. Denote by $\mathbf{C}(\mathbb{R}_{\geq t_0}, \mathbb{C}^{N \times M})$ the set of causal time-dependent matrix functions.

Definition A.1.4 (Complex Fourier series). Consider $\mathbf{F}(t) \in \mathbf{C}_T(\mathbb{R}, \mathbb{C}^{N \times M})$. $\mathbf{F}(t)$ can be written as a complex Fourier series,

$$\mathbf{F}(t) = \sum_{k=-\infty}^{\infty} \mathbf{F}_k e^{jk\omega t} \quad (\text{A.1})$$

with

$$\mathbf{F}_k = \frac{1}{T} \int_0^T \mathbf{F}(\tau) e^{-jk\omega\tau} d\tau \quad (\text{A.2})$$

where $k \in \mathbb{Z}$ is the harmonic order, $\omega = \frac{2\pi}{T}$ and $\mathbf{F}_k \in \mathbb{C}^{N \times M}$.

Definition A.1.5 (Inverse of a complex Fourier series). Consider a square matrix function $\mathbf{F}(t) \in \mathbf{C}_T(\mathbb{R}, \mathbb{C}^{N \times N})$ written as a complex Fourier series with Fourier coefficients \mathbf{F}_k . If $\det(\mathbf{F}_k) \neq 0, \forall k \in \mathbb{Z}$, then the inverse of \mathbf{F} is,

$$\mathbf{F}^{-1}(t) = \sum_{k=-\infty}^{\infty} \mathbf{F}_k^{-1} e^{-jk\omega t} \quad (\text{A.3})$$

Definition A.1.6 (Product of complex Fourier series). Consider two T-periodic functions $\mathbf{F}(t) \in \mathbf{C}_T(\mathbb{R}, \mathbb{C}^{N \times M})$ and $\mathbf{G}(t) \in \mathbf{C}_T(\mathbb{R}, \mathbb{C}^{M \times P})$ written as complex

Fourier series,

$$\mathbf{F}(t) = \sum_{q=-\infty}^{\infty} \mathbf{F}_q e^{jq\omega t} \quad (\text{A.4a})$$

$$\mathbf{G}(t) = \sum_{i=-\infty}^{\infty} \mathbf{G}_i e^{ji\omega t} \quad (\text{A.4b})$$

Their product is,

$$\mathbf{F}(t)\mathbf{G}(t) = \sum_{q=-\infty}^{\infty} \sum_{i=-\infty}^{\infty} \mathbf{F}_q \mathbf{G}_i e^{j(q+i)\omega t} \quad (\text{A.5})$$

Let $k = q + i$,

$$\mathbf{F}(t)\mathbf{G}(t) = \sum_{k=-\infty}^{\infty} \sum_{i=-\infty}^{\infty} \mathbf{F}_{k-i} \mathbf{G}_i e^{jk\omega t} \quad (\text{A.6})$$

Definition A.1.7 (Toeplitz transform). Consider a matrix function $\mathbf{M}(t) \in \mathbf{C}_T(\mathbb{R}, \mathbb{C}^{N \times M})$ written as complex Fourier series. The Toeplitz transform \mathcal{T} of $\mathbf{M}(t)$ maps the set of Fourier coefficients $\{\mathbf{M}_k \in \mathbb{C}^{N \times M}\}_{k \in \mathbb{Z}}$ to a matrix of infinite dimension \mathcal{M} ,

$$\begin{aligned} \mathcal{T} : \mathbf{C}_T(\mathbb{R}, \mathbb{C}^{N \times M}) &\rightarrow \mathbb{C}^{\infty \times \infty} \\ \mathbf{M}(t) &\mapsto \mathcal{M} \end{aligned} \quad (\text{A.7})$$

with

$$\mathcal{M} = \begin{bmatrix} \mathbf{M}_0 & \mathbf{M}_{-1} & \mathbf{M}_{-2} & \dots & \dots & \dots & \mathbf{M}_{-\infty} \\ \mathbf{M}_1 & \ddots & \ddots & \ddots & & & \vdots \\ \mathbf{M}_2 & \ddots & \mathbf{M}_0 & \mathbf{M}_{-1} & \mathbf{M}_{-2} & & \vdots \\ \vdots & \ddots & \mathbf{M}_1 & \mathbf{M}_0 & \mathbf{M}_{-1} & & \vdots \\ \vdots & & \mathbf{M}_2 & \mathbf{M}_1 & \mathbf{M}_0 & \ddots & \mathbf{M}_{-2} \\ \vdots & & & \ddots & \ddots & \ddots & \mathbf{M}_{-1} \\ \mathbf{M}_{\infty} & \dots & \dots & \dots & \mathbf{M}_2 & \mathbf{M}_1 & \mathbf{M}_0 \end{bmatrix} \quad (\text{A.8})$$

A.2 Linear Systems

A linear system is a system for which the inputs and outputs are related by a linear differential equation of the form

$$\sum_{p=1}^P \alpha_p(t) \frac{d^p}{dt^p} y_p(t) = \sum_{m=1}^M \beta_m(t) \frac{d^m}{dt^m} \mathbf{u}_m(t) \quad (\text{A.9})$$

where $\mathbf{u}_m(t) \in \mathbb{C}$ denotes the m -th input, $y_p(t) \in \mathbb{C}$ the p -th output, $\alpha_p(t)$ and $\beta_m(t) \in \mathbb{C}$ are complex coefficients, and M and $P \in \mathbb{Z}$ denote the total number of input and output, respectively.

A.2.1 Linear Time-Variant System

A linear time-variant (LTV) system can be written in a state-space representation,

$$\frac{d}{dt}\mathbf{x}(t) = \mathbf{A}(t)\mathbf{x}(t) + \mathbf{B}(t)\mathbf{u}(t) \quad (\text{A.10a})$$

$$\mathbf{y}(t) = \mathbf{C}(t)\mathbf{x}(t) + \mathbf{D}(t)\mathbf{u}(t) \quad (\text{A.10b})$$

with $\mathbf{x}(t) \in C(\mathbb{R}, \mathbb{C}^{N \times 1})$ is the state vector, $\mathbf{u}(t) \in C(\mathbb{R}, \mathbb{C}^{M \times 1})$ is the input or control vector, $\mathbf{A}(t) \in C(\mathbb{R}, \mathbb{C}^{N \times N})$ is the state matrix, $\mathbf{B}(t) \in C(\mathbb{R}, \mathbb{C}^{N \times M})$ is the control matrix, $\mathbf{y}(t) \in C(\mathbb{R}, \mathbb{C}^{P \times 1})$ is the output vector, $\mathbf{C}(t) \in C(\mathbb{R}, \mathbb{C}^{P \times N})$ is the output matrix and $\mathbf{D}(t) \in C(\mathbb{R}, \mathbb{C}^{P \times M})$ is the feed-forward matrix.

Eq. (A.10a) is called the state dynamic equation and Eq. (A.10b) the output equation.

A.2.2 Linear Time-Invariant System

A linear time-invariant system (LTI) is a linear system for which the matrices of (A.10) do not vary with time. It can be written as,

$$\frac{d}{dt}\mathbf{x}(t) = \mathbf{A}\mathbf{x}(t) + \mathbf{B}\mathbf{u}(t) \quad (\text{A.11a})$$

$$\mathbf{y}(t) = \mathbf{C}\mathbf{x}(t) + \mathbf{D}\mathbf{u}(t) \quad (\text{A.11b})$$

with $\mathbf{A} \in \mathbb{C}^{N \times N}$, $\mathbf{B} \in \mathbb{C}^{N \times M}$, $\mathbf{C} \in \mathbb{C}^{P \times N}$ and $\mathbf{D} \in \mathbb{C}^{P \times M}$.

A.2.3 Linear Time-Periodic System

A linear time-periodic system (LTP) is a linear system for which the matrices of (A.10) are T -periodic. It can be written as,

$$\frac{d}{dt}\mathbf{x}(t) = \mathbf{A}(t)\mathbf{x}(t) + \mathbf{B}(t)\mathbf{u}(t) \quad (\text{A.12a})$$

$$\mathbf{y}(t) = \mathbf{C}(t)\mathbf{x}(t) + \mathbf{D}(t)\mathbf{u}(t) \quad (\text{A.12b})$$

with $\mathbf{A}(t) \in \mathbf{C}_T(\mathbb{R}, \mathbb{C}^{N \times N})$, $\mathbf{B}(t) \in \mathbf{C}_T(\mathbb{R}, \mathbb{C}^{N \times M})$, $\mathbf{C}(t) \in \mathbf{C}_T(\mathbb{R}, \mathbb{C}^{P \times N})$ and $\mathbf{D}(t) \in \mathbf{C}_T(\mathbb{R}, \mathbb{C}^{P \times M})$.

Following Eq. (A.1), the terms $\mathbf{A}(t)$, $\mathbf{B}(t)$, $\mathbf{C}(t)$ and $\mathbf{D}(t)$ can be written as complex Fourier series,

$$\mathbf{A}(t) = \sum_{k=-\infty}^{\infty} \mathbf{A}_k e^{jk\omega t} \quad (\text{A.13a})$$

$$\mathbf{B}(t) = \sum_{k=-\infty}^{\infty} \mathbf{B}_k e^{jk\omega t} \quad (\text{A.13b})$$

$$\mathbf{C}(t) = \sum_{k=-\infty}^{\infty} \mathbf{C}_k e^{jk\omega t} \quad (\text{A.13c})$$

$$\mathbf{D}(t) = \sum_{k=-\infty}^{\infty} \mathbf{D}_k e^{jk\omega t} \quad (\text{A.13d})$$

with $\mathbf{A}_k \in \mathbb{C}^{N \times N}$, $\mathbf{B}_k \in \mathbb{C}^{N \times M}$, $\mathbf{C}_k \in \mathbb{C}^{P \times N}$ and $\mathbf{D}_k \in \mathbb{C}^{P \times M}$.

A.3 Solution of Linear Systems

A.3.1 Solution of LTV Systems

In this section, we look for the solution $\mathbf{x}(t)$ of the LTV system (A.10). We follow the resolution described in [104].

Start by computing the homogeneous solution of the LTV system, denoted $\mathbf{x}_h(t)$, using the following equation.

$$\frac{d}{dt} \mathbf{x}_h(t) = \mathbf{A}(t) \mathbf{x}_h(t) \quad (\text{A.14})$$

The solution of Eq. (A.14) is can be found by the following theorem.

Theorem A.3.1. *The solution of the homogeneous LTV system (A.14) forms an N -dimensional vector space. Moreover, there exists a matrix $\Pi(t, t_0) \in \mathbf{C}(\mathbb{R}, \mathbb{C}^{N \times N})$ such that the solution of the initial valued problem (IVP) $\mathbf{x}(t_0) = \mathbf{x}_0$ is given by $\mathbf{x}_h(t) = \Pi(t, t_0) \mathbf{x}_0$.*

The matrix $\Pi(t, t_0)$ is called the principal matrix solution [104, p. 82]. Its columns correspond to the vectors that compose the vector basis of the N -dimensional vector space solutions of (A.14). Some properties of $\Pi(t, t_0)$ are

$$\Pi(t_0, t_0) = \mathbb{I}_N \quad (\text{A.15a})$$

$$\Pi(t, t_1) \Pi(t_1, t_0) = \Pi(t, t_0) \quad (\text{A.15b})$$

$$\Pi(t, t_0)^{-1} = \Pi(t_0, t) \quad (\text{A.15c})$$

where \mathbb{I}_N is the $N \times N$ identity matrix.

From theorem A.3.1, Eq. (A.14) can be rewritten as

$$\frac{d}{dt}\Pi(t, t_0) = \mathbf{A}(t)\Pi(t, t_0) \quad (\text{A.16})$$

Multiply both sides of (A.16) by $\Pi(t, t_0)^{-1}dt$,

$$\left(d\Pi(t, t_0)\right)\Pi(t, t_0)^{-1} = \mathbf{A}(t)dt \quad (\text{A.17})$$

Integrate both sides of Eq. (A.17),

$$\int_{t_0}^t \left(d\Pi(\tau, t_0)\right)\Pi(\tau, t_0)^{-1} = \int_{t_0}^t \mathbf{A}(\tau)d\tau \quad (\text{A.18})$$

Solve Eq. (A.18),

$$\left[\ln\left(\Pi(\tau, t_0)\right)\right]_{t_0}^t = \int_{t_0}^t \mathbf{A}(\tau)d\tau \quad (\text{A.19})$$

$$\ln\left(\Pi(t, t_0)\Pi(t_0, t_0)^{-1}\right) = \int_{t_0}^t \mathbf{A}(\tau)d\tau \quad (\text{A.20})$$

which leads to

$$\Pi(t, t_0) = e^{\int_{t_0}^t \mathbf{A}(\tau)d\tau}\Pi(t_0, t_0) \quad (\text{A.21})$$

Use (A.15a),

$$\Pi(t, t_0) = e^{\int_{t_0}^t \mathbf{A}(\tau)d\tau} \quad (\text{A.22})$$

The solution of the homogeneous LTV system (A.10) is

$$\mathbf{x}_h(t) = e^{\int_{t_0}^t \mathbf{A}(\tau)d\tau}\mathbf{x}_0 \quad (\text{A.23})$$

Subsequently, we look for the solution of the non-homogeneous LTV system (A.10a) which can be found by the method of variation of parameters [104, p. 83]. The method assumes that $\mathbf{x}(t)$ is of the form,

$$\mathbf{x}(t) = \Pi(t, t_0)\mathbf{c}(t) \quad (\text{A.24})$$

with $\mathbf{c}(t) \in C(\mathbb{R}, \mathbb{C}^{N \times 1})$ and $\mathbf{c}(t_0) = \mathbf{x}_0$. Differentiate (A.24),

$$\frac{d}{dt}\mathbf{x}(t) = \left(\frac{d}{dt}\Pi(t, t_0)\right)\mathbf{c}(t) + \Pi(t, t_0)\left(\frac{d}{dt}\mathbf{c}(t)\right) \quad (\text{A.25})$$

Insert (A.24) and (A.25) into (A.10a),

$$\left(\frac{d}{dt}\Pi(t, t_0)\right)\mathbf{c}(t) + \Pi(t, t_0)\left(\frac{d}{dt}\mathbf{c}(t)\right) = \mathbf{A}(t)\Pi(t, t_0)\mathbf{c}(t) + \mathbf{B}(t)\mathbf{u}(t) \quad (\text{A.26})$$

Use (A.16) to obtain

$$\frac{d}{dt}\mathbf{c}(t) = \Pi(t, t_0)^{-1}\mathbf{B}(t)\mathbf{u}(t) \quad (\text{A.27})$$

Use (A.15c) and integrate (A.27) to obtain

$$\mathbf{c}(t) = \mathbf{c}(t_0) + \int_{t_0}^t \Pi(t_0, \tau)\mathbf{B}(\tau)\mathbf{u}(\tau)d\tau \quad (\text{A.28})$$

Given (A.28) with $\mathbf{c}(t_0) = \mathbf{x}_0$ and (A.24), we obtain the solution of the LTV system (A.10a) as

$$\mathbf{x}(t) = \Pi(t, t_0)\mathbf{x}_0 + \Pi(t, t_0) \int_{t_0}^t \Pi(t_0, \tau)\mathbf{B}(\tau)\mathbf{u}(\tau)d\tau \quad (\text{A.29})$$

Use (A.15b),

$$\mathbf{x}(t) = \Pi(t, t_0)\mathbf{x}_0 + \int_{t_0}^t \Pi(t, \tau)\mathbf{B}(\tau)\mathbf{u}(\tau)d\tau \quad (\text{A.30})$$

A.3.2 Solution of LTI Systems

In this section, we look for the solution $\mathbf{x}(t)$ of the LTI system (A.11). An LTI system can be seen as a particular case of the more generic LTV system in which the system's matrices do not vary with time. Consequently, its solution is given by (A.30).

Let us start by computing the LTI system's principal matrix solution $\Pi(t, t_0)$. For an LTI system, (A.22) becomes,

$$\Pi(t, t_0) = e^{\int_{t_0}^t \mathbf{A}d\tau} \quad (\text{A.31})$$

Solve (A.31),

$$\Pi(t, t_0) = e^{\mathbf{A}\cdot(t-t_0)} \quad (\text{A.32})$$

Insert (A.32) into (A.30) to obtain the solution of the LTI system,

$$\mathbf{x}(t) = e^{\mathbf{A}\cdot(t-t_0)}\mathbf{x}_0 + \int_{t_0}^t e^{\mathbf{A}\cdot(t-\tau)}\mathbf{B}\mathbf{u}(\tau)d\tau \quad (\text{A.33})$$

A.3.3 Solution of LTP Systems

In this section, we look for the solution $\mathbf{x}(t)$ of the LTP system (A.12). Since an LTP system is an LTV system, its solution is given by (A.30).

Let us start by computing the LTP system's principal matrix solution $\Pi(t, t_0)$ which is given by the Floquet theorem [104, p. 92].

Theorem A.3.2 (Floquet). *Suppose $\mathbf{A}(t) \in \mathbf{C}_T(\mathbb{R}, \mathbb{C}^{N \times N})$, the principal matrix solution of the LTP system has the form*

$$\Pi(t, t_0) = \mathbf{P}(t, t_0)e^{\mathbf{Q} \cdot (t-t_0)} \quad (\text{A.34})$$

where $\mathbf{P}(t, t_0) \in \mathbf{C}_T(\mathbb{R}, \mathbb{C}^{N \times N})$ and $\mathbf{Q} \in \mathbb{C}^{N \times N}$.

Starting from (A.29),

$$\mathbf{x}(t) = \Pi(t, t_0)\mathbf{x}_0 + \Pi(t, t_0) \int_{t_0}^t \Pi(t_0, \tau) \mathbf{B}(\tau) \mathbf{u}(\tau) d\tau \quad (\text{A.35})$$

Use (A.15c),

$$\mathbf{x}(t) = \Pi(t, t_0)\mathbf{x}_0 + \Pi(t, t_0) \int_{t_0}^t \Pi(\tau, t_0)^{-1} \mathbf{B}(\tau) \mathbf{u}(\tau) d\tau \quad (\text{A.36})$$

The inverse of (A.34) is

$$\Pi(t, t_0)^{-1} = e^{\mathbf{Q} \cdot (t_0-t)} \mathbf{P}(t, t_0)^{-1} \quad (\text{A.37})$$

Insert (A.34) and (A.37) into (A.36) and reorganize it to obtain

$$\begin{aligned} \mathbf{x}(t) = & \mathbf{P}(t, t_0)e^{\mathbf{Q} \cdot (t-t_0)} \mathbf{x}_0 + \\ & \mathbf{P}(t, t_0)e^{\mathbf{Q}t} \int_{t_0}^t e^{-\mathbf{Q} \tau} \mathbf{P}(\tau, t_0)^{-1} \mathbf{B}(\tau) \mathbf{u}(\tau) d\tau \end{aligned} \quad (\text{A.38})$$

Define

$$\tilde{\mathbf{B}}(t, t_0) \triangleq \mathbf{P}(t, t_0)^{-1} \mathbf{B}(t) \quad (\text{A.39})$$

Insert (A.39) into (A.38),

$$\mathbf{x}(t) = \mathbf{P}(t, t_0)e^{\mathbf{Q} \cdot (t-t_0)} \mathbf{x}_0 + \mathbf{P}(t, t_0)e^{\mathbf{Q}t} \int_{t_0}^t e^{-\mathbf{Q} \tau} \tilde{\mathbf{B}}(\tau, t_0) \mathbf{u}(\tau) d\tau \quad (\text{A.40})$$

From the Theorem A.3.2, $\mathbf{P}(t, t_0) \in \mathbf{C}_T(\mathbb{R}, \mathbb{C}^{N \times N})$, thus it can be written as a complex Fourier series,

$$\mathbf{P}(t, t_0) = \sum_{n=-\infty}^{\infty} \mathbf{P}_n(t_0) e^{jn\omega t} \quad (\text{A.41})$$

With its inverse defined by (A.3),

$$\mathbf{P}(t, t_0)^{-1} = \sum_{n=-\infty}^{\infty} \mathbf{P}_n^{-1}(t_0) e^{-jn\omega t} \quad (\text{A.42})$$

Consider $\mathbf{B}(t)$ written as a complex Fourier series (A.13),

$$\tilde{\mathbf{B}}(t, t_0) = \sum_{n=-\infty}^{\infty} \sum_{m=-\infty}^{\infty} \mathbf{P}_n(t_0)^{-1} \mathbf{B}_m e^{j(m-n)\omega t} \quad (\text{A.43})$$

Let $k = m - n$,

$$\tilde{\mathbf{B}}(t, t_0) = \sum_{k=-\infty}^{\infty} \sum_{m=-\infty}^{\infty} \mathbf{P}_{m-k}(t_0)^{-1} \mathbf{B}_m e^{jk\omega t} \quad (\text{A.44})$$

Rewrite (A.44) as

$$\tilde{\mathbf{B}}(t, t_0) = \sum_{k=-\infty}^{\infty} \tilde{\mathbf{B}}_k(t_0) e^{jk\omega t} \quad (\text{A.45})$$

with

$$\tilde{\mathbf{B}}_k(t_0) = \sum_{m=-\infty}^{\infty} \mathbf{P}_{m-k}(t_0)^{-1} \mathbf{B}_m \quad (\text{A.46})$$

Insert (A.46) in (A.40) to obtain the expression of the solution of the non-homogeneous LTP system (A.12),

$$\begin{aligned} \mathbf{x}(t) &= \mathbf{P}(t, t_0) e^{\mathbf{Q} \cdot (t-t_0)} \mathbf{x}_0 + \\ &\quad \mathbf{P}(t, t_0) e^{\mathbf{Q}t} \int_{t_0}^t \sum_{k=-\infty}^{\infty} e^{(jk\omega \mathbb{1}_N - \mathbf{Q})\tau} \tilde{\mathbf{B}}_k(t_0) \mathbf{u}(\tau) d\tau \end{aligned} \quad (\text{A.47})$$

A.4 Transfer Function of Linear Systems

The notion of transfer function (TF) is well established for LTI systems [105, p. 193]. In this section, we discuss the extension of this concept to LTP systems.

A.4.1 Transfer function of LTI Systems

The output of an LTI system $\mathbf{y}(t) \in C(\mathbb{R}, \mathbb{C}^{P \times 1})$ when excited by a non-causal input vector $\mathbf{u}(t) \in C(\mathbb{R}, \mathbb{C}^{M \times 1})$ is given by

$$\mathbf{y}(t) = \mathbf{h}(t) * \mathbf{u}(t) = \int_{-\infty}^{\infty} \mathbf{h}(\tau) \mathbf{u}(t - \tau) d\tau \quad (\text{A.48})$$

where $(*)$ denotes the convolution product and, $\mathbf{h}(t) \in C(\mathbb{R}, \mathbb{C}^{P \times M})$ is the system response to the Dirac delta function.

Let us define a generic exponentially modulated time-invariant (EMTI) signal as

$$\mathbf{v}(t) \triangleq \hat{\mathbf{v}} e^{st} \quad (\text{A.49})$$

with $\hat{\mathbf{v}} \in \mathbb{C}^{M \times 1}$ and $s \in \mathbb{C}$.

An EMTI input vector is written as

$$\mathbf{u}(t) = \hat{\mathbf{u}}e^{st} \quad (\text{A.50})$$

When an LTI system is excited by an EMTI input vector, its response is also the same EMTI signal multiplied by a time-independent factor. Such an input for which the system response is also of the same form is called the characteristic function (also eigenfunction) of the system and it provides the notion of transfer function as we will demonstrate hereafter.

Assume the input vector of the system to be an EMTI signal, from (A.48) we write

$$\mathbf{y}(t) = \int_{-\infty}^{\infty} \mathbf{h}(\tau)e^{-s\tau} d\tau \hat{\mathbf{u}}e^{st} \quad (\text{A.51})$$

Rewrite Eq.(A.51) as

$$\mathbf{y}(t) = \mathbf{H}(s)\mathbf{u}(t) \quad (\text{A.52})$$

with

$$\mathbf{H}(s) \triangleq \mathcal{L}\{\mathbf{h}(t)\} = \int_{-\infty}^{\infty} \mathbf{h}(\tau)e^{-s\tau} d\tau \quad (\text{A.53})$$

Eq. (A.52) shows that an LTI system excited by an EMTI signal produces a response that is the product of the input and the time-independent factor $\mathbf{H}(s)$ defined as the transfer function of the LTI system [105, p. 194]. The function $\mathbf{H}(s) \in \mathbb{C}^{P \times M}$ is also the Laplace transform $\mathcal{L}\{\mathbf{h}(t)\}$ of $\mathbf{h}(t)$ [105, p. 330].

At this point, we can write the output vector of the LTI system as

$$\mathbf{y}(t) = \hat{\mathbf{y}}e^{st} \quad (\text{A.54})$$

Insert Eq. (A.54) into Eq. (A.52) and simplify it to obtain,

$$\hat{\mathbf{y}} = H(s)\hat{\mathbf{u}} \quad (\text{A.55})$$

Both Eqs. (A.52) and (A.55) define the transfer function of an LTI system excited by the non-casual EMTI input as corresponding to the complex factor relating the system's input and output when the system is excited by its eigenfunction. From the transfer function, one can analyze many properties of the LTI systems, such as the internal stability [105, p. 198], for example.

So far, the discussion on the TF of LTI systems has only considered a non-causal input signal. From now on, we focus our study on systems excited by causal inputs where all time-dependent functions are casual as defined in A.1.3. For the LTI system of the form (A.11), the following corollary is derived.

Corollary A.4.1. *When an LTI system of the form (A.11) is excited by a causal EMTI input vector $\mathbf{u}(t) = \hat{\mathbf{u}}e^{st} \in C(\mathbb{R}_{\geq t_0}, \mathbb{C}^{M \times 1})$, the forced response for the state and the output vectors have the form $\mathbf{x}(t) = \hat{\mathbf{x}}e^{st} \in \mathbf{C}(\mathbb{R}_{\geq t_0}, \mathbb{C}^{N \times 1})$ and $\mathbf{y}(t) = \hat{\mathbf{y}}e^{st} \in \mathbf{C}(\mathbb{R}_{\geq t_0}, \mathbb{C}^{P \times 1})$, respectively.*

To demonstrate the Corollary A.4.1, let us insert Eq. (A.50) into Eq. (A.33),

$$\mathbf{x}(t) = e^{\mathbf{A} \cdot (t-t_0)} \mathbf{x}_0 + \int_{t_0}^t e^{\mathbf{A}t} e^{(s\mathbb{1}_N - \mathbf{A})\tau} \mathbf{B} \hat{\mathbf{u}} d\tau \quad (\text{A.56})$$

Integrate (A.56),

$$\mathbf{x}(t) = e^{\mathbf{A} \cdot (t-t_0)} \mathbf{x}_0 + (s\mathbb{1}_N - \mathbf{A})^{-1} e^{\mathbf{A}t} \left(e^{(s\mathbb{1}_N - \mathbf{A})t} - e^{(s\mathbb{1}_N - \mathbf{A})t_0} \right) \mathbf{B} \hat{\mathbf{u}} \quad (\text{A.57})$$

Reorganize (A.57),

$$\mathbf{x}(t) = e^{\mathbf{A} \cdot (t-t_0)} \left(\mathbf{x}_0 - (s\mathbb{1}_N - \mathbf{A})^{-1} \mathbf{B} \hat{\mathbf{u}} e^{st_0} \right) + (s\mathbb{1}_N - \mathbf{A})^{-1} \mathbf{B} \hat{\mathbf{u}} e^{st} \quad (\text{A.58})$$

Insert (A.58) into (A.11) to derive the output vector as

$$\mathbf{y}(t) = \mathbf{C} \mathbf{B} e^{\mathbf{A} \cdot (t-t_0)} \left(\mathbf{x}_0 - (s\mathbb{1}_N - \mathbf{A})^{-1} \mathbf{B} \hat{\mathbf{u}} e^{st_0} \right) + \left(\mathbf{C}(s\mathbb{1}_N - \mathbf{A})^{-1} \mathbf{B} + \mathbf{D} \right) \hat{\mathbf{u}} e^{st} \quad (\text{A.59})$$

In (A.58) and (A.59), we identify two distinct responses to the causal EMTI signal. The first term is called the transient response, and the second is called the forced response of the system [106, p. 57].

The transient response is proportional to $e^{\mathbf{A} \cdot (t-t_0)}$, which can be written as a linear combination of terms of the form $e^{\lambda_i \cdot (t-t_0)}$, where λ_i are eigenvalues of \mathbf{A} . If the system is stable the eigenvalues λ_i are strictly negative, consequently $\lim_{t \rightarrow +\infty} e^{\mathbf{A} \cdot (t-t_0)} \rightarrow 0$.

The forced response is proportional to the EMTI input vector. Hence the definition of transfer function given in (A.52) can be matched by considering only the second term of the equation.

Alternatively, we can search an initial state for which the response of the system is only composed of the forced response,

$$\mathbf{x}_0 = (s\mathbb{1}_N - \mathbf{A})^{-1} \mathbf{B} \hat{\mathbf{u}} e^{st_0} \quad (\text{A.60})$$

Insert (A.60) into (A.58) and (A.59) to obtain

$$\mathbf{x}(t) = (s\mathbb{1}_N - \mathbf{A})^{-1} \mathbf{B} \mathbf{u}(t) \quad (\text{A.61a})$$

$$\mathbf{y}(t) = \left(\mathbf{C}(s\mathbb{1}_N - \mathbf{A})^{-1} \mathbf{B} + \mathbf{D} \right) \mathbf{u}(t) \quad (\text{A.61b})$$

We remark that the state vector and the output vectors of an LTI system excited by a causal EMTI input vector, and under the initial condition given in (A.60), are EMTI signals and $\mathbf{x}(t) = \hat{\mathbf{x}}e^{st}$ with $\hat{\mathbf{x}} \in \mathbb{C}^{N \times 1}$ and $\mathbf{y}(t) = \hat{\mathbf{y}}e^{st}$ with $\hat{\mathbf{y}} \in \mathbb{C}^{P \times 1}$.

From the definition (A.61b), the transfer function of the LTI systems of the form (A.11) is,

$$\mathbf{H}(s) = \mathbf{C}(s\mathbb{I}_N - \mathbf{A})^{-1}\mathbf{B} + \mathbf{D} \quad (\text{A.62})$$

We recall that the transfer function of an LTI system does not provide the system's response for any initial state. For that, one may rely on Eqs. (A.58), (A.59).

A.4.2 Transfer Function of LTP Systems

From the motivation of using all the theories for the analysis and control of LTI systems for LTP systems, we determine the eigenfunction of LTP systems in this section.

A.4.2.1 Response of LTP Systems to the EMTI Signal

The notion of eigenfunction is not directly transferable from LTI to LTP systems. For instance, the causal EMTI input vector does not provide similar results such as LTI systems [106, p. 60].

For instance, let us determine the state vector $\mathbf{x}(t)$ for LTP systems (A.13) when excited by an EMTI signal. Start by inserting Eq. (A.50) into (A.47),

$$\begin{aligned} \mathbf{x}(t) &= \mathbf{P}(t, t_0)e^{\mathbf{Q} \cdot (t-t_0)}\mathbf{x}_0 + \\ &\quad \mathbf{P}(t, t_0)e^{\mathbf{Q}t} \int_{t_0}^t \sum_{m=-\infty}^{\infty} e^{((s+jm\omega)\mathbb{I}_N - \mathbf{Q})\tau} \tilde{\mathbf{B}}_m(t_0)\hat{\mathbf{u}}d\tau \end{aligned} \quad (\text{A.63})$$

Integrate (A.63),

$$\begin{aligned} \mathbf{x}(t) &= \mathbf{P}(t, t_0)e^{\mathbf{Q} \cdot (t-t_0)}\mathbf{x}_0 + \mathbf{P}(t, t_0)e^{\mathbf{Q}t} \cdot \\ &\quad \left[\sum_{m=-\infty}^{\infty} \left((s + jm\omega)\mathbb{I}_N - \mathbf{Q} \right)^{-1} e^{((s+jm\omega)\mathbb{I}_N - \mathbf{Q})\tau} \tilde{\mathbf{B}}_m(t_0)\hat{\mathbf{u}} \right]_{t_0}^t \end{aligned} \quad (\text{A.64})$$

$$\begin{aligned} \mathbf{x}(t) &= \mathbf{P}(t, t_0)e^{\mathbf{Q} \cdot (t-t_0)}\mathbf{x}_0 + \\ &\quad \mathbf{P}(t, t_0)e^{\mathbf{Q}t} \left[\sum_{m=-\infty}^{\infty} \left(e^{((s+jm\omega)\mathbb{I}_N - \mathbf{Q})t} - e^{((s+jm\omega)\mathbb{I}_N - \mathbf{Q})t_0} \right) \cdot \right. \\ &\quad \left. \left((s + jm\omega)\mathbb{I}_N - \mathbf{Q} \right)^{-1} \tilde{\mathbf{B}}_m(t_0)\hat{\mathbf{u}} \right] \end{aligned} \quad (\text{A.65})$$

Reorganize Eq. (A.65) as

$$\begin{aligned} \mathbf{x}(t) = & \mathbf{P}(t, t_0) e^{\mathbf{Q} \cdot (t-t_0)} \left(\mathbf{x}_0 - \right. \\ & \left. \sum_{m=-\infty}^{\infty} \left((s + jm\omega) \mathbb{I}_N - \mathbf{Q} \right)^{-1} \tilde{\mathbf{B}}_m(t_0) \hat{\mathbf{u}} e^{(s+jm\omega)t_0} \right) + \\ & \mathbf{P}(t, t_0) \sum_{m=-\infty}^{\infty} \left((s + jm\omega) \mathbb{I}_N - \mathbf{Q} \right)^{-1} \tilde{\mathbf{B}}_m(t_0) \hat{\mathbf{u}} e^{jm\omega t} e^{st} \quad (\text{A.66}) \end{aligned}$$

Let us determine the output vector $\mathbf{y}(t)$ of the LTP system with the form (A.12) when excited by an EMTI input vector. Insert (A.66) into (A.12b),

$$\begin{aligned} \mathbf{y}(t) = & \mathbf{C}(t) \mathbf{P}(t, t_0) e^{\mathbf{Q} \cdot (t-t_0)} \cdot \\ & \left(\mathbf{x}_0 - \sum_{m=-\infty}^{\infty} \left((s + jm\omega) \mathbb{I}_N - \mathbf{Q} \right)^{-1} \tilde{\mathbf{B}}_m(t_0) \hat{\mathbf{u}} e^{(s+jm\omega)t_0} \right) \\ & + \left(\mathbf{C}(t) \mathbf{P}(t, t_0) \sum_{m=-\infty}^{\infty} \left((s + jm\omega) \mathbb{I}_N - \mathbf{Q} \right)^{-1} \right. \\ & \left. \tilde{\mathbf{B}}_m(t_0) e^{jm\omega t} + \mathbf{D}(t) \right) \hat{\mathbf{u}} e^{st} \quad (\text{A.67}) \end{aligned}$$

To obtain the forced response of the system, assume the following initial state,

$$\mathbf{x}_0 = \sum_{m=-\infty}^{\infty} \left((s + jm\omega) \mathbb{I}_N - \mathbf{Q} \right)^{-1} \tilde{\mathbf{B}}_m(t_0) \hat{\mathbf{u}} e^{(s+j\omega)t_0} \quad (\text{A.68})$$

Insert Eq. (A.68) into Eq. (A.63) to obtain the state vector's forced response,

$$\mathbf{x}_f(t) = \mathbf{P}(t, t_0) \sum_{m=-\infty}^{\infty} \left((s + jm\omega) \mathbb{I}_N - \mathbf{Q} \right)^{-1} \tilde{\mathbf{B}}_m(t_0) \hat{\mathbf{u}} e^{jm\omega t} e^{st} \quad (\text{A.69})$$

Insert (A.41) into (A.69),

$$\begin{aligned} \mathbf{x}_f(t) = & \sum_{n=-\infty}^{\infty} \mathbf{P}_n(t_0) e^{jn\omega t} \cdot \\ & \sum_{m=-\infty}^{\infty} \left((s + jm\omega) \mathbb{I}_N - \mathbf{Q} \right)^{-1} \tilde{\mathbf{B}}_m(t_0) \hat{\mathbf{u}} e^{jm\omega t} e^{st} \quad (\text{A.70}) \end{aligned}$$

Rewrite Eq. (A.70) as

$$\mathbf{x}_f(t) = \sum_{n=-\infty}^{\infty} \sum_{m=-\infty}^{\infty} \mathbf{P}_n(t_0) \left((s + jm\omega) \mathbb{I}_N - \mathbf{Q} \right)^{-1} \tilde{\mathbf{B}}_m(t_0) \hat{\mathbf{u}} e^{j(n+m)\omega t} e^{st} \quad (\text{A.71})$$

Let $k = n + m$,

$$\mathbf{x}_f(t) = \sum_{k=-\infty}^{\infty} \sum_{m=-\infty}^{\infty} \mathbf{P}_{k-m}(t_0) \left((s + jm\omega)\mathbb{I}_N - \mathbf{Q} \right)^{-1} \tilde{\mathbf{B}}_m(t_0) \hat{\mathbf{u}} e^{jk\omega t} e^{st} \quad (\text{A.72})$$

Rewrite Eq. (A.72) as

$$\mathbf{x}_f(t) = \sum_{k=-\infty}^{\infty} \mathbf{x}_k(t_0) \hat{\mathbf{u}} e^{jk\omega t} e^{st} \quad (\text{A.73})$$

with

$$\mathbf{x}_k(t_0) \triangleq \sum_{m=-\infty}^{\infty} \mathbf{P}_{k-m}(t_0) \left((s + jm\omega)\mathbb{I}_N - \mathbf{Q} \right)^{-1} \tilde{\mathbf{B}}_m(t_0) \quad (\text{A.74})$$

Insert Eq. (A.68) into Eq. (A.12b) to obtain the output vector's forced response,

$$\mathbf{y}_f(t) = \sum_{n=-\infty}^{\infty} \mathbf{C}_n e^{jn\omega t} \sum_{m=-\infty}^{\infty} \mathbf{x}_m(t_0) e^{jm\omega t} \hat{\mathbf{u}} e^{st} + \sum_{n=-\infty}^{\infty} \mathbf{D}_n e^{jn\omega t} \hat{\mathbf{u}} e^{st} \quad (\text{A.75})$$

Use (A.6) to simplify,

$$\mathbf{y}_f(t) = \sum_{k=-\infty}^{\infty} \left(\sum_{m=-\infty}^{\infty} \mathbf{C}_{k-m} \mathbf{x}_m(t_0) + \mathbf{D}_k \right) e^{jk\omega t} \hat{\mathbf{u}} e^{st} \quad (\text{A.76})$$

Although Eq. (A.73) provide a relation between $\mathbf{x}(t)$ and $\mathbf{u}(t)$ and Eq. (A.76), between $\mathbf{y}(t)$ and $\mathbf{u}(t)$, the function relating them is time-dependent, demonstrating that the EMTP signal is not the eigenfunction of the LTP system.

A.4.2.2 Response of LTP systems to Exponentially Modulated Time-Periodic Signal

In the quest to find the eigenfunction for LTP systems, Wereley [106] proposed to use the exponentially modulated time-periodic (EMTP) signal as the input vector.

An EMTP signal is the product of a T-periodic signal and a complex exponential. Using the complex Fourier form, it can be written as,

$$\mathbf{v}(t) \triangleq \sum_{k=-\infty}^{\infty} \mathbf{v}_k e^{jk\omega t} e^{st} \quad (\text{A.77})$$

As it turns out, an EMTP signal is indeed the eigenfunction of an LTP system, which is recalled in the following corollary.

Corollary A.4.2. *When an LTP system of the form (A.12) is excited by a causal EMTP input $\mathbf{u}(t) = \sum_{m=-\infty}^{\infty} \mathbf{u}_m e^{jm\omega t} e^{st}$, the forced response for the state and output vectors are EMTP vectors.*

To demonstrate the Corollary A.4.2, we assume the input vector $\mathbf{u}(t)$ as a causal EMTP signal,

$$\mathbf{u}(t) = \sum_{m=-\infty}^{\infty} \mathbf{u}_m e^{jm\omega t} e^{st} \quad (\text{A.78})$$

Let us determine the state vector $\mathbf{x}(t)$ of the LTP system with the form (A.12) when excited by an EMTP input vector. Insert Eq. (A.78) into Eq. (A.47),

$$\begin{aligned} \mathbf{x}(t) = & \mathbf{P}(t, t_0) e^{\mathbf{Q} \cdot (t-t_0)} \mathbf{x}_0 + \\ & \mathbf{P}(t, t_0) e^{\mathbf{Q}t} \int_{t_0}^t e^{-\mathbf{Q}\tau} \sum_{n=-\infty}^{\infty} \tilde{\mathbf{B}}_n(t_0) e^{jn\omega\tau} \sum_{m=-\infty}^{\infty} \mathbf{u}_m e^{jm\omega\tau} e^{s\tau} d\tau \end{aligned} \quad (\text{A.79})$$

Let $k = m + n$,

$$\begin{aligned} \mathbf{x}(t) = & \mathbf{P}(t, t_0) e^{\mathbf{Q} \cdot (t-t_0)} \mathbf{x}_0 + \\ & \mathbf{P}(t, t_0) e^{\mathbf{Q}t} \int_{t_0}^t \sum_{k=-\infty}^{\infty} \sum_{m=-\infty}^{\infty} e^{((s+jk\omega)\mathbb{1}_N - \mathbf{Q})\tau} \tilde{\mathbf{B}}_{k-m}(t_0) \mathbf{u}_m d\tau \end{aligned} \quad (\text{A.80})$$

Integrate (A.80),

$$\begin{aligned} \mathbf{x}(t) = & \mathbf{P}(t, t_0) e^{\mathbf{Q} \cdot (t-t_0)} \mathbf{x}_0 + \mathbf{P}(t, t_0) e^{\mathbf{Q}t} \cdot \\ & \left[\sum_{k=-\infty}^{\infty} \sum_{m=-\infty}^{\infty} e^{((s+jk\omega)\mathbb{1}_N - \mathbf{Q})\tau} ((s+jk\omega)\mathbb{1}_N - \mathbf{Q})^{-1} \tilde{\mathbf{B}}_{k-m}(t_0) \mathbf{u}_m \right]_{t_0}^t \end{aligned} \quad (\text{A.81})$$

$$\begin{aligned} \mathbf{x}(t) = & \mathbf{P}(t, t_0) e^{\mathbf{Q} \cdot (t-t_0)} \mathbf{x}_0 + \\ & \mathbf{P}(t, t_0) e^{\mathbf{Q}t} \left(\sum_{k=-\infty}^{\infty} \sum_{m=-\infty}^{\infty} \left(e^{((s+jk\omega)\mathbb{1}_N - \mathbf{Q})t} - e^{((s+jk\omega)\mathbb{1}_N - \mathbf{Q})t_0} \right) \cdot \right. \\ & \left. ((s+jk\omega)\mathbb{1}_N - \mathbf{Q})^{-1} \tilde{\mathbf{B}}_{k-m}(t_0) \mathbf{u}_m \right) \end{aligned} \quad (\text{A.82})$$

Reorganize Eq. (A.82) as,

$$\begin{aligned} \mathbf{x}(t) = & \mathbf{P}(t, t_0) e^{\mathbf{Q} \cdot (t-t_0)} \\ & \left(\mathbf{x}_0 - \sum_{k=-\infty}^{\infty} \sum_{m=-\infty}^{\infty} \left((s+jk\omega)\mathbb{1}_N - \mathbf{Q} \right)^{-1} \tilde{\mathbf{B}}_{k-m}(t_0) \mathbf{u}_m e^{(s+jk\omega)t_0} \right) \end{aligned}$$

$$+ \mathbf{P}(t, t_0) \sum_{k=-\infty}^{\infty} \sum_{m=-\infty}^{\infty} \left((s + jk\omega)\mathbb{1}_N - \mathbf{Q} \right)^{-1} \tilde{\mathbf{B}}_{k-m}(t_0) \mathbf{u}_m e^{jk\omega t} e^{st} \quad (\text{A.83})$$

Let us now determine the output vector $\mathbf{y}(t)$ of the LTP system with the form (A.12) when excited by an EMTP input vector. Insert Eq. (A.83) into Eq. (A.12b),

$$\begin{aligned} \mathbf{y}(t) = \mathbf{C}(t) & \left(\mathbf{P}(t, t_0) e^{\mathbf{Q} \cdot (t-t_0)} \right. \\ & \left(\mathbf{x}_0 - \sum_{k=-\infty}^{\infty} \sum_{m=-\infty}^{\infty} \left((s + jk\omega)\mathbb{1}_N - \mathbf{Q} \right)^{-1} \tilde{\mathbf{B}}_{k-m}(t_0) \mathbf{u}_m e^{(s+jk\omega)t_0} \right) + \\ & \left. \mathbf{P}(t, t_0) \sum_{k=-\infty}^{\infty} \sum_{m=-\infty}^{\infty} \left((s + jk\omega)\mathbb{1}_N - \mathbf{Q} \right)^{-1} \tilde{\mathbf{B}}_{k-m}(t_0) \mathbf{u}_m e^{jk\omega t} e^{st} \right) + \\ & \mathbf{D}(t) \sum_{k=-\infty}^{\infty} \mathbf{u}_k e^{jk\omega t} e^{st} \quad (\text{A.84}) \end{aligned}$$

Reorganize Eq. (A.85) as

$$\begin{aligned} \mathbf{y}(t) = \mathbf{C}(t) & \left(\mathbf{P}(t, t_0) e^{\mathbf{Q} \cdot (t-t_0)} \right. \\ & \left(\mathbf{x}_0 - \sum_{k=-\infty}^{\infty} \sum_{m=-\infty}^{\infty} \left((s + jk\omega)\mathbb{1}_N - \mathbf{Q} \right)^{-1} \tilde{\mathbf{B}}_{k-m}(t_0) \mathbf{u}_m e^{(s+jk\omega)t_0} \right) \\ & + \sum_{k=-\infty}^{\infty} \sum_{m=-\infty}^{\infty} \left(\left(\mathbf{P}(t, t_0) (s + jk\omega)\mathbb{1}_N - \mathbf{Q} \right)^{-1} \tilde{\mathbf{B}}_{k-m}(t_0) \right) \mathbf{u}_m + \\ & \left. \mathbf{D}(t) \mathbf{u}_k \right) e^{jk\omega t} e^{st} \quad (\text{A.85}) \end{aligned}$$

To obtain the input vector's forced response, assume the following initial state,

$$\mathbf{x}_0 \triangleq \sum_{k=-\infty}^{\infty} \sum_{m=-\infty}^{\infty} \left((s + jk\omega)\mathbb{1}_N - \mathbf{Q} \right)^{-1} \tilde{\mathbf{B}}_{k-m}(t_0) \mathbf{u}_m e^{(s+jk\omega)t_0} \quad (\text{A.86})$$

Insert Eq. (A.86) into Eq. (A.83) to obtain the forced response for the state vector,

$$\begin{aligned} \mathbf{x}_f(t) = \mathbf{P}(t, t_0) & \sum_{k=-\infty}^{\infty} \sum_{m=-\infty}^{\infty} \left((s + jk\omega)\mathbb{1}_N - \mathbf{Q} \right)^{-1} \\ & \tilde{\mathbf{B}}_{k-m}(t_0) \mathbf{u}_m e^{jk\omega t} e^{st} \quad (\text{A.87}) \end{aligned}$$

Insert Eq. (A.41) into Eq. (A.87),

$$\mathbf{x}_f(t) = \sum_{n=-\infty}^{\infty} \sum_{k=-\infty}^{\infty} \sum_{m=-\infty}^{\infty} \mathbf{P}_n(t_0) \left((s + jk\omega)\mathbb{I}_N - \mathbf{Q} \right)^{-1} \tilde{\mathbf{B}}_{k-m}(t_0) \mathbf{u}_m e^{j(n+k)\omega t} e^{st} \quad (\text{A.88})$$

Let $p = n + k$,

$$\mathbf{x}_f(t) = \sum_{p=-\infty}^{\infty} \sum_{k=-\infty}^{\infty} \sum_{m=-\infty}^{\infty} \mathbf{P}_{p-k}(t_0) \left((s + jm\omega)\mathbb{I}_N - \mathbf{Q} \right)^{-1} \tilde{\mathbf{B}}_{k-m}(t_0) \mathbf{u}_m e^{jp\omega t} e^{st} \quad (\text{A.89})$$

Rewrite Eq. (A.89) as

$$\mathbf{x}_f(t) = \sum_{p=-\infty}^{\infty} \mathbf{x}_p(t_0) e^{jp\omega t} e^{st} \quad (\text{A.90})$$

with

$$\mathbf{x}_p(t_0) \triangleq \sum_{k=-\infty}^{\infty} \sum_{m=-\infty}^{\infty} \mathbf{P}_{p-k}(t_0) \left((s + jm\omega)\mathbb{I}_N - \mathbf{Q} \right)^{-1} \tilde{\mathbf{B}}_{k-m}(t_0) \mathbf{u}_m \quad (\text{A.91})$$

Insert Eq. (A.90) into Eq. (A.12b) to the output vector's forced response,

$$\mathbf{y}_f(t) = \sum_{n=-\infty}^{\infty} \mathbf{C}_n e^{jn\omega t} \sum_{k=-\infty}^{\infty} \mathbf{x}_k(t_0) e^{jk\omega t} e^{st} + \sum_{n=-\infty}^{\infty} \mathbf{D}_n e^{jn\omega t} \sum_{k=-\infty}^{\infty} \mathbf{u}_k e^{jk\omega t} e^{st} \quad (\text{A.92})$$

Reorganize Eq. (A.92) as

$$\mathbf{y}_f(t) = \sum_{n=-\infty}^{\infty} \sum_{k=-\infty}^{\infty} \mathbf{C}_n \mathbf{x}_k(t_0) + \mathbf{D}_n \mathbf{u}_k e^{j(n+k)\omega t} e^{st} \quad (\text{A.93})$$

Let $q = k + n$,

$$\mathbf{y}_f(t) = \sum_{q=-\infty}^{\infty} \sum_{k=-\infty}^{\infty} \mathbf{C}_{q-k} \mathbf{x}_k(t_0) + \mathbf{D}_{q-k} \mathbf{u}_k e^{jq\omega t} e^{st} \quad (\text{A.94})$$

Rewrite Eq. (A.94) as

$$\mathbf{y}_f(t) = \sum_{q=-\infty}^{\infty} \mathbf{y}_q(t_0) e^{jq\omega t} e^{st} \quad (\text{A.95})$$

with

$$\mathbf{y}_q(t_0) = \sum_{k=-\infty}^{\infty} \mathbf{C}_{q-k} \mathbf{x}_k(t_0) + \mathbf{D}_{q-k} \mathbf{u}_k \quad (\text{A.96})$$

Eqs.(A.90) and (A.95) show that, when an LTP system is excited by an EMTP input vector, the systems' forced response for the state and the output vectors $\mathbf{x}(t)$ and $\mathbf{y}(t)$ are also EMTP signals.

A.4.2.3 Harmonic State Space Representation and Transfer Function of LTP Systems

From (A.94) it is hard to visualize a time-independent factor between the input and the output vectors. Wereley [106] proposed an alternative representation of the problem using the Theorem A.4.2.

As stated in the Theorem A.4.2, an LTP system excited by a EMTP input vector, has EMTP state and output vectors as forced response. We adopt all the vectors of (A.12) as,

$$\mathbf{x}_f(t) = \sum_{k=-\infty}^{\infty} \mathbf{x}_k e^{jk\omega t} e^{st} \quad (\text{A.97a})$$

$$\mathbf{u}_f(t) = \sum_{k=-\infty}^{\infty} \mathbf{u}_k e^{jk\omega t} e^{st} \quad (\text{A.97b})$$

$$\mathbf{y}_f(t) = \sum_{k=-\infty}^{\infty} \mathbf{y}_k e^{jk\omega t} e^{st} \quad (\text{A.97c})$$

with $\mathbf{x}_k \in \mathbb{C}^{N \times 1}$, $\mathbf{u}_k \in \mathbb{C}^{M \times 1}$ and $\mathbf{y}_k \in \mathbb{C}^{P \times 1}$.

Insert Eq. (A.97) into Eq. (A.12),

$$\begin{aligned} \frac{d}{dt} \sum_{k=-\infty}^{\infty} \mathbf{x}_k e^{jk\omega t} e^{st} &= \sum_{n=-\infty}^{\infty} \mathbf{A}_n e^{jn\omega t} \sum_{m=-\infty}^{\infty} \mathbf{x}_m e^{jm\omega t} e^{st} + \\ &\quad \sum_{n=-\infty}^{\infty} \mathbf{B}_n e^{jn\omega t} \sum_{m=-\infty}^{\infty} \mathbf{u}_m e^{jm\omega t} e^{st} \end{aligned} \quad (\text{A.98a})$$

$$\begin{aligned} \sum_{k=-\infty}^{\infty} \mathbf{y}_k e^{jk\omega t} e^{st} &= \sum_{n=-\infty}^{\infty} \mathbf{C}_n e^{jn\omega t} \sum_{m=-\infty}^{\infty} \mathbf{x}_m e^{jm\omega t} e^{st} + \\ &\quad \sum_{n=-\infty}^{\infty} \mathbf{D}_n e^{jn\omega t} \sum_{m=-\infty}^{\infty} \mathbf{u}_m e^{jm\omega t} e^{st} \end{aligned} \quad (\text{A.98b})$$

Use (A.6) to simplify Eq. (A.98) as

$$\sum_{k=-\infty}^{\infty} (s + jk\omega) \mathbf{x}_k e^{jk\omega t} e^{st} = \sum_{k=-\infty}^{\infty} \sum_{m=-\infty}^{\infty} \mathbf{A}_{k-m} \mathbf{x}_m e^{jk\omega t} e^{st} + \sum_{k=-\infty}^{\infty} \sum_{m=-\infty}^{\infty} \mathbf{B}_{k-m} \mathbf{u}_m e^{jk\omega t} e^{st} \quad (\text{A.99a})$$

$$\sum_{k=-\infty}^{\infty} \mathbf{y}_k e^{jk\omega t} e^{st} = \sum_{k=-\infty}^{\infty} \sum_{m=-\infty}^{\infty} \mathbf{C}_{k-m} \mathbf{x}_m e^{jk\omega t} e^{st} + \sum_{k=-\infty}^{\infty} \sum_{m=-\infty}^{\infty} \mathbf{D}_{k-m} \mathbf{u}_m e^{jk\omega t} e^{st} \quad (\text{A.99b})$$

Simplify Eq. (A.99) as,

$$\sum_{k=-\infty}^{\infty} (s + jk\omega) \mathbf{x}_k = \sum_{k=-\infty}^{\infty} \sum_{m=-\infty}^{\infty} \mathbf{A}_{k-m} \mathbf{x}_m + \sum_{k=-\infty}^{\infty} \sum_{m=-\infty}^{\infty} \mathbf{B}_{k-m} \mathbf{u}_m \quad (\text{A.100a})$$

$$\sum_{k=-\infty}^{\infty} \mathbf{y}_k = \sum_{k=-\infty}^{\infty} \sum_{m=-\infty}^{\infty} \mathbf{C}_{k-m} \mathbf{x}_m + \sum_{k=-\infty}^{\infty} \sum_{m=-\infty}^{\infty} \mathbf{D}_{k-m} \mathbf{u}_m \quad (\text{A.100b})$$

From Eq.(A.100), we write the k -th harmonic amplitude of the input and output vectors as

$$(s + jk\omega) \mathbf{x}_k = \sum_{m=-\infty}^{\infty} \mathbf{A}_{k-m} \mathbf{x}_m + \sum_{m=-\infty}^{\infty} \mathbf{B}_{k-m} \mathbf{u}_m \quad (\text{A.101a})$$

$$\mathbf{y}_k = \sum_{m=-\infty}^{\infty} \mathbf{C}_{k-m} \mathbf{x}_m + \sum_{m=-\infty}^{\infty} \mathbf{D}_{k-m} \mathbf{u}_m \quad (\text{A.101b})$$

Eq.(A.101) defines an infinite system of equations, relating the amplitude of the harmonic components of the system vectors. We can rewrite (A.101) in a matrix form.

The HTF $\mathcal{H}(s)$ presents an infinite dimensional matrix structure,

$$\mathcal{H}(s) = \begin{bmatrix} \ddots & \vdots & \vdots & \vdots & \\ \cdots & H_{-1,-1}(s) & H_{-1,0}(s) & H_{-1,1}(s) & \cdots \\ \cdots & H_{0,-1}(s) & H_{0,0}(s) & H_{0,1}(s) & \cdots \\ \cdots & H_{1,-1}(s) & H_{1,0}(s) & H_{1,1}(s) & \cdots \\ & \vdots & \vdots & \vdots & \ddots \end{bmatrix} \quad (\text{A.108})$$

The element $H_{n,m}(s)$ is the relation between the $n - th$ output harmonic with $m - th$ input harmonic.

A.4.2.4 Truncated Harmonic State Space Representation

The truncated HSS representation is obtained from Eq.(A.104) when the vectors of (A.97) are truncated to the $N_h - th$ harmonic,

$$\mathbf{x}(t) \stackrel{hyp.}{=} e^{st} \sum_{k=-N_h}^{N_h} \mathbf{x}_k e^{jk\omega t} \quad (\text{A.109a})$$

$$\mathbf{u}(t) \stackrel{hyp.}{=} e^{st} \sum_{k=-N_h}^{N_h} \mathbf{u}_k e^{jk\omega t} \quad (\text{A.109b})$$

$$\mathbf{y}(t) \stackrel{hyp.}{=} e^{st} \sum_{k=-N_h}^{N_h} \mathbf{y}_k e^{jk\omega t} \quad (\text{A.109c})$$

The vectors of (A.102) are rewritten as,

$$\mathbf{X} \triangleq [\mathbf{x}_{-N_h}^T \quad \cdots \quad \mathbf{x}_0^T \quad \cdots \quad \mathbf{x}_{N_h}^T]^T \quad (\text{A.110a})$$

$$\mathbf{U} \triangleq [\mathbf{u}_{-N_h}^T \quad \cdots \quad \mathbf{u}_0^T \quad \cdots \quad \mathbf{u}_{N_h}^T]^T \quad (\text{A.110b})$$

$$\mathbf{Y} \triangleq [\mathbf{y}_{-N_h}^T \quad \cdots \quad \mathbf{y}_0^T \quad \cdots \quad \mathbf{y}_{N_h}^T]^T \quad (\text{A.110c})$$

Use Eq. (A.110) to rewrite Eq.(A.101) as,

$$\begin{aligned}
 s \begin{bmatrix} \mathbf{x}_{-N_h} \\ \vdots \\ \mathbf{x}_0 \\ \vdots \\ \mathbf{x}_{N_h} \end{bmatrix} &= \begin{pmatrix} \begin{bmatrix} \mathbf{A}_0 & \cdots & \mathbf{A}_{-N_h} & \cdots & \mathbf{A}_{-2N_h} \\ \vdots & \ddots & \vdots & \ddots & \vdots \\ \mathbf{A}_{N_h} & \cdots & \mathbf{A}_0 & \cdots & \mathbf{A}_{-N_h} \\ \vdots & \ddots & \vdots & \ddots & \vdots \\ \mathbf{A}_{2N_h} & \cdots & \mathbf{A}_{N_h} & \cdots & \mathbf{A}_0 \\ -jN\omega\mathbb{I}_N & \mathbf{0}_N & \cdots & \cdots & \mathbf{0}_N \\ \mathbf{0}_N & \ddots & \ddots & \ddots & \vdots \\ \vdots & \ddots & \mathbf{0}_N & \ddots & \vdots \\ \vdots & \ddots & \ddots & \ddots & \mathbf{0}_N \\ \mathbf{0}_N & \cdots & \cdots & \mathbf{0}_N & jN\omega\mathbb{I}_N \end{bmatrix} - \begin{bmatrix} \mathbf{x}_{-N_h} \\ \vdots \\ \mathbf{x}_0 \\ \vdots \\ \mathbf{x}_{N_h} \end{bmatrix} + \\
 &\quad \begin{bmatrix} \mathbf{B}_0 & \cdots & \mathbf{B}_{-N_h} & \cdots & \mathbf{B}_{-2N_h} \\ \vdots & \ddots & \vdots & \ddots & \vdots \\ \mathbf{B}_{N_h} & \cdots & \mathbf{B}_0 & \cdots & \mathbf{B}_{-N_h} \\ \vdots & \ddots & \vdots & \ddots & \vdots \\ \mathbf{B}_{2N_h} & \cdots & \mathbf{B}_{N_h} & \cdots & \mathbf{B}_0 \end{bmatrix} \begin{bmatrix} \mathbf{u}_{-N_h} \\ \vdots \\ \mathbf{u}_0 \\ \vdots \\ \mathbf{u}_{N_h} \end{bmatrix}
 \end{pmatrix} \quad (\text{A.111a})
 \end{aligned}$$

$$\begin{aligned}
 \begin{bmatrix} y_{-N_h} \\ \vdots \\ y_0 \\ \vdots \\ y_{N_h} \end{bmatrix} &= \begin{bmatrix} \mathbf{C}_0 & \cdots & \mathbf{C}_{-N_h} & \cdots & \mathbf{C}_{-2N_h} \\ \vdots & \ddots & \vdots & \ddots & \vdots \\ \mathbf{C}_{N_h} & \cdots & \mathbf{C}_0 & \cdots & \mathbf{C}_{-N_h} \\ \vdots & \ddots & \vdots & \ddots & \vdots \\ \mathbf{C}_{2N_h} & \cdots & \mathbf{C}_{N_h} & \cdots & \mathbf{C}_0 \end{bmatrix} \begin{bmatrix} \mathbf{x}_{-N_h} \\ \vdots \\ \mathbf{x}_0 \\ \vdots \\ \mathbf{x}_{N_h} \end{bmatrix} + \quad (\text{A.111b})
 \end{aligned}$$

$$\begin{aligned}
 &\quad \begin{bmatrix} \mathbf{D}_0 & \cdots & \mathbf{D}_{-N_h} & \cdots & \mathbf{D}_{-2N_h} \\ \vdots & \ddots & \vdots & \ddots & \vdots \\ \mathbf{D}_{N_h} & \cdots & \mathbf{D}_0 & \cdots & \mathbf{D}_{-N_h} \\ \vdots & \ddots & \vdots & \ddots & \vdots \\ \mathbf{D}_{2N_h} & \cdots & \mathbf{D}_{N_h} & \cdots & \mathbf{D}_0 \end{bmatrix} \begin{bmatrix} \mathbf{u}_{-N_h} \\ \vdots \\ \mathbf{u}_0 \\ \vdots \\ \mathbf{u}_{N_h} \end{bmatrix} \quad (\text{A.111c})
 \end{aligned}$$

From Eq.(A.111), we conclude that to describe the system dynamics up to the N_h -th harmonic, the matrices of Eq.(A.10) have to be decomposed up to $2N_h$ -th harmonic,

$$\mathbf{A}(t) = \sum_{k=-2N_h}^{2N_h} \mathbf{A}_k e^{jk\omega t} \quad (\text{A.112a})$$

$$\mathbf{B}(t) = \sum_{k=-2N_h}^{2N_h} \mathbf{B}_k e^{jk\omega t} \quad (\text{A.112b})$$

$$\mathbf{C}(t) = \sum_{k=-2N_h}^{2N_h} \mathbf{C}_k e^{jk\omega t} \quad (\text{A.112c})$$

$$\mathbf{D}(t) = \sum_{k=-2N_h}^{2N_h} \mathbf{D}_k e^{jk\omega t} \quad (\text{A.112d})$$

Appendix B

Data for a 1 GW ± 320 kV Point-to-Point MMC-Based Link

The data summarized in this appendix is obtained from the CIGRE B4 benchmark presented in the technical brochure 832 [49].

Quantity	Symbol	Value	Ref.
Rated active power [MW]	P_{nom}	1 000	[49, p. 56]
Rated reactive power [MVar]	Q_{nom}	300	[49, p. 56]
Rated DC voltage [kV]	U_{dc}	± 320	[49, p. 56]
Number of submodules per arm	N	400	[49, p. 56]
Submodule capacitance [mF]	C	11	[49, p. 56]
Arm coil inductance [mH]	L	50.9	Appendix C
Arm coil resistance [m Ω]	R	90.4	Appendix C
Start-up resistance [pu]	$R_{startup}$	3.6	[49, p. 56]
Star-point resistance [Ω]	R_r	$5 \cdot 10^3$	[49, p. 56]

Table B.1: Modular multilevel converter parameters.

Quantity	Symbol	Value
Grid voltage L-L RMS [kV]	V_g	400
Grid frequency [Hz]	F_0	50
3-phase short-circuit level [GVA]	SCL	9
X/R ratio	XR	7
Grid Thevenin parameter [Ω]	R_s	0.5963
Grid Thevenin parameter [H]	L_s	0.0133
Grid Thevenin parameter [Ω]	R_p	709
Grid Thevenin parameter [H]	L_{sp}	0.012
Grid Thevenin parameter [Ω]	R_{sp}	0.19
Grid Thevenin parameter [Ω]	R_{spp}	78

Table B.2: AC-grid parameters [49, p. 177].

Quantity	Symbol	Value
Rated apparent power [MVA]	S_t	1060
Voltage primary side (Y-g) L-L RMS [kV]	U_{prim}	440
Voltage secondary side (Δ) L-L RMS [kV]	U_{sec}	330
Leakage inductance [p.u.]	L_f	0.18
Winding resistance [p.u.]	R_f	0.006
Primary-side grounding inductance [H]	L_{tg}	0.127

Table B.3: Transformer parameters [49, p. 181].

Quantity	Symbol	Value
Length [km]	l_{cable}	70
Resistance per unit length [Ω/km]	R_{cable}	0.011
Capacitance per unit length [F/km]	C_{cable}	$0.2185 \cdot 10^{-6}$
Inductance per unit length [H/km]	L_{cable}	$2.615 \cdot 10^{-3}$

Table B.4: DC cable parameters [49, p. 78].

Appendix C

Design of Dry-Type Air-Core Coils

In this appendix, an approach to designing uncoupled and coupled dry-type air-core coils (Fig. C.1) is developed. Uncoupled dry-type air-core coils are employed as the arm coils of industrial modular multilevel converters in HVDC applications [69, p. 96].

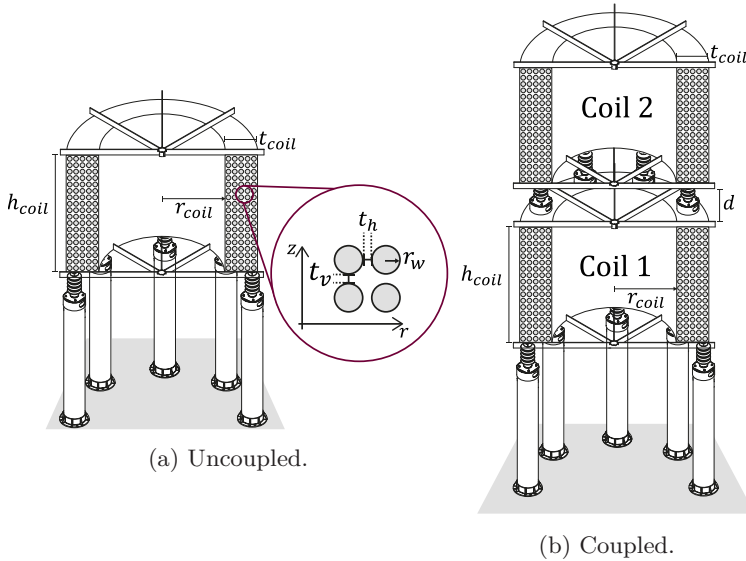


Figure C.1: Dry-type air-core coils.

C.1 Coil parameters

C.1.1 Coil Inductance

The self inductance of the n -th circular turn, denoted by $L_{n,n}$, and the mutual inductance between the n -th and the m -th turns, denoted by $L_{n,m}$, can be calculated analytically [107] as follows.

The self inductance of a circular coil is given by [107, Eq. (4.27)]

$$L_{n,n} = \mu_0 \sqrt{(r_n + r_w) r_n} \left(\left(\frac{2}{k_n} - k_n \right) \mathbf{K}(k_n) - \frac{2}{k_n} \mathbf{E}(k_n) \right) \quad (\text{C.1})$$

with

$$k_n = \frac{2 \sqrt{(r_n + r_w) r_n}}{2 r_n + r_w} \quad (\text{C.2a})$$

$$\mathbf{K}(k) = \int_0^{\frac{\pi}{2}} \frac{1}{\sqrt{1 - k^2 \sin^2(\theta)}} d\theta \quad (\text{C.2b})$$

$$\mathbf{E}(k) = \int_0^{\frac{\pi}{2}} \sqrt{1 - k^2 \sin^2(\theta)} d\theta \quad (\text{C.2c})$$

where $n \in \{1, \dots, N_{turns}\}$, r_n denotes the internal radius of the n -th circular loop and r_w is the conductor radius.

The mutual inductance between two different circular coils $L_{n,m}$ is given by [107, Eq. (4.59)]

$$L_{n,m} = \mu_0 \sqrt{(r_n + r_w)(r_m + r_w)} \left(\left(\frac{2}{k_{n,m}} - k_{n,m} \right) \mathbf{K}(k_{n,m}) - \frac{2}{k_{n,m}} \mathbf{E}(k_{n,m}) \right) \quad (\text{C.3})$$

with

$$k_{n,m} = \sqrt{\frac{(r_n + r_w)(r_m + r_w)}{(r_n + r_m + r_w)^2 + d_{n,m}^2}} \quad (\text{C.4})$$

with $n \in \{1, \dots, N_{turns}\}$, $m \in \{1, \dots, N_{turns}\}$, and $n \neq m$ and $d_{n,m}$ is the distance between the two coils' center.

C.1.2 Single Coil Inductance

Assuming a single air-core coil as illustrated in Fig. C.1a composed of N_{turns} circular turns connected in series, the coil self inductance is

$$L = \sum_{n=1}^{N_{turns}} \sum_{m=1}^{N_{turns}} L_{n,m} \quad (\text{C.5})$$

where $L_{n,m}$ is the inductance between the n -th and the m -th turns. N_{turns} is given by

$$N_{turns} = N_v N_h \quad (\text{C.6})$$

where N_v and N_h are the number of turns in z- and r-directions, respectively.

C.1.3 Coupled Coils Inductance

Assuming two identical coil as illustrated in Fig. C.1b each one composed of N_{turns} circular turns connected in series, each coil self inductance is

$$L_1 = \sum_{n=1}^{N_{turns}} \sum_{m=1}^{N_{turns}} L_{n,m} \quad (C.7a)$$

$$L_2 = \sum_{n=N_{turns}+1}^{2N_{turns}} \sum_{m=N_{turns}+1}^{2N_{turns}} L_{n,m} \quad (C.7b)$$

The mutual inductance between coils is

$$M_{1,2} = \sum_{n=1}^{N_{turns}} \sum_{m=N_{turns}+1}^{2N_{turns}} L_{n,m} \quad (C.8a)$$

$$M_{2,1} = \sum_{n=N_{turns}+1}^{2N_{turns}} \sum_{m=1}^{N_{turns}} L_{n,m} \quad (C.8b)$$

Since we consider two identical coils, it follows that

$$L_1 = L_2 = L \quad (C.9a)$$

$$M_{1,2} = M_{2,1} = M \quad (C.9b)$$

The coupling coefficient between two identical coupled coils is

$$K = \frac{M}{L} \quad (C.10)$$

C.1.4 Coil Resistance

The resistance of the air-core coil shown in Fig. C.1 can be estimated as

$$R = \varrho_c \frac{l_{coil}}{\pi r_w^2} \quad (C.11)$$

where ϱ_c is the conductor resistivity, and l_{coil} is the total length of the coil.

C.1.5 Other parameters

The total length of this coil l_{coil} is given by

$$l_{coil} = N_v \sum_{n=1}^{N_h} 2 \pi r_n \quad (C.12)$$

The width, height and volume of the coil's active part are computed as

$$w_{coil} = N_h 2 r_w + (N_h - 1) t_h \quad (\text{C.13a})$$

$$h_{coil} = N_v 2 r_w + (N_v - 1) t_v \quad (\text{C.13b})$$

$$V_{coil} = \pi (r_{coil} + w_{coil})^2 h_{coil} \quad (\text{C.13c})$$

The mass of conductor in the coil is given by

$$M_{cond} = \rho_c N_v \sum_{n=1}^{N_h} 2\pi^2 r_n r_w^2 \quad (\text{C.14})$$

where ρ_c is the conductor specific mass.

The total mass of the coil is computed as

$$M_{coil} = \alpha_{coil} M_{cond} \quad (\text{C.15})$$

where α_{coil} is the ratio between conductor and coil masses.

C.2 Design

The conductor radius r_w is computed from the coil nominal current I_{nom} and the maximum current density J_{max} as

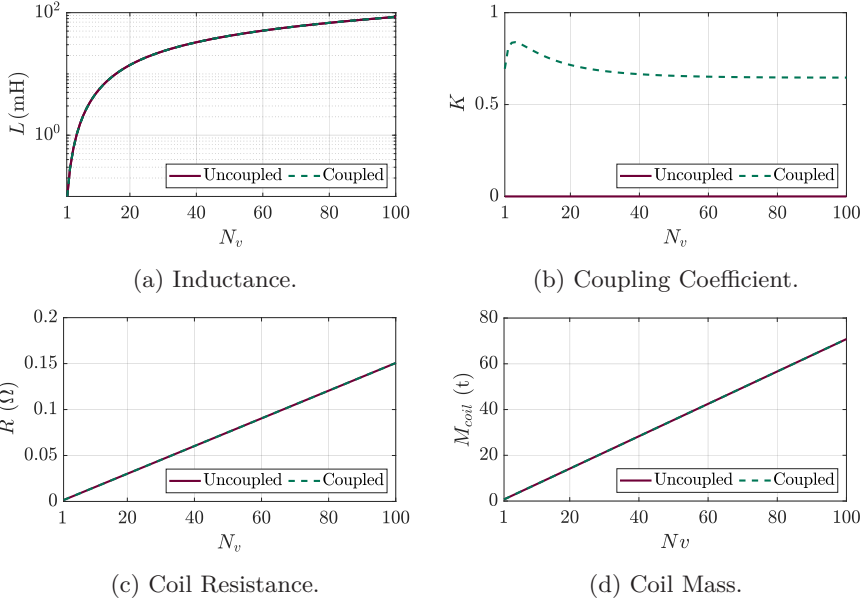
$$r_w = \sqrt{\frac{I_{nom}}{\pi J_{max}}} \quad (\text{C.16})$$

We adopt $I_{nom} = 1750$ A and $J_{max} = 2$ A/mm² with yields $r_w = 19.6$ mm. The vertical and horizontal separations between turns are adopted to be $t_h = 135$ mm and $t_v = 50$ mm. In our design we adopt a constant number of turns in horizontal direction of $N_h = 5$ and we take the number of turns in the vertical direction $N_v \in \{1, \dots, 100\}$. This leads to a total of one hundred designs for uncoupled arm coils and one hundred designs for coupled arm coils.

In Table C.1, we summarize the parameters used to design the various air-core aluminum coils. In Fig. C.2, we plot the evolution of the coils inductance and other derived quantities in terms of the number of vertical turns N_v .

Quantity	Symbol	Value
Internal coil radius [m]	r_{coil}	1.25
Nominal current [A]	I_{nom}	1750
Maximum current density [A/mm ²]	J_{max}	2
Conductor radius [mm]	r_w	19.6
Horizontal separation thickness [mm]	t_h	135
Vertical separation thickness [mm]	t_v	50
Number of turns in horizontal direction	N_h	5
Coiling window width [m]	w_{coil}	0.7
Aluminium resistivity [Ω /m]	ρ_c	$2.65 \cdot 10^{-8}$
Aluminium density [kg/m ³]	ρ_c	2710
Conductor/coil mass ratio	α_{coil}	6
Clearance between coupled coils [m]	d	0.5

Table C.1: Parameters for the dry-type air-core aluminium coil.


 Figure C.2: Dry-type air-core aluminium coil inductance, resistance, mass and volume as a function of N_v for the parameters listed in Table C.1.

Appendix D

Losses Calculation for the Modular Multilevel Converter

In this appendix, we develop a semi-analytical method to compute the conduction and switching losses of an MMC with half-bridge submodules. The HB-SMs conventions are given in Fig. D.1. Many of the variables used here were introduced the Section II.2.

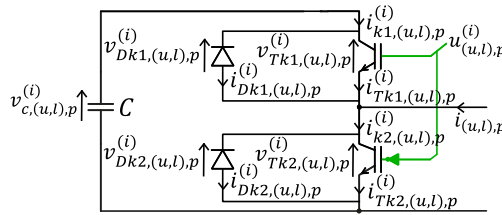


Figure D.1: Converter for the i -th SM in the upper and lower arm of phase p .

The i -th SM's switches currents in the upper and lower arm of the phase p are given by Eq. (II.3) as

$$i_{k1,(u,l),p}^{(i)} = -u_{(u,l),p}^{(i)} i_{(u,l),p} \quad (\text{D.1a})$$

$$i_{k2,(u,l),p}^{(i)} = \left(1 - u_{(u,l),p}^{(i)}\right) i_{(u,l),p} \quad (\text{D.1b})$$

Next, the diodes and transistors currents are given by

$$i_{Tk1,(u,l),p}^{(i)} = \begin{cases} -u_{(u,l),p}^{(i)} i_{(u,l),p}, & \text{when } i_{(u,l),p} < 0, \\ 0, & \text{otherwise.} \end{cases} \quad (\text{D.2a})$$

$$i_{Dk1,(u,l),p}^{(i)} = \begin{cases} -u_{(u,l),p}^{(i)} i_{(u,l),p}, & \text{when } i_{(u,l),p} > 0, \\ 0, & \text{otherwise.} \end{cases} \quad (\text{D.2b})$$

$$i_{Tk2,(u,l),p}^{(i)} = \begin{cases} \left(1 - u_{(u,l),p}^{(i)}\right) i_{(u,l),p}, & \text{when } i_{(u,l),p} > 0, \\ 0, & \text{otherwise.} \end{cases} \quad (\text{D.2c})$$

$$i_{Dk2,(u,l),p}^{(i)} = \begin{cases} \left(1 - u_{(u,l),p}^{(i)}\right) i_{(u,l),p}, & \text{when } i_{(u,l),p} < 0, \\ 0, & \text{otherwise.} \end{cases} \quad (\text{D.2d})$$

D.1 Conduction Losses

In order to investigate the conduction losses, the voltage over switches can be written from Eq. (II.3) with a slight modification to include the on-state voltage of the solid-state devices as

$$v_{Tk1,(u,l),p}^{(i)} = \left(1 - u_{(u,l),p}^{(i)}\right) v_{c,(u,l),p}^{(i)} + u_{(u,l),p}^{(i)} v_{CE,k1,(u,l),p}^{(i)} \quad (\text{D.3a})$$

$$v_{Dk1,(u,l),p}^{(i)} = \left(1 - u_{(u,l),p}^{(i)}\right) v_{c,(u,l),p}^{(i)} + u_{(u,l),p}^{(i)} v_{F,k1,(u,l),p}^{(i)} \quad (\text{D.3b})$$

$$v_{Tk2,(u,l),p}^{(i)} = u_{(u,l),p}^{(i)} v_{c,(u,l),p}^{(i)} + \left(1 - u_{(u,l),p}^{(i)}\right) v_{CE,k2,(u,l),p}^{(i)} \quad (\text{D.3c})$$

$$v_{Dk2,(u,l),p}^{(i)} = u_{(u,l),p}^{(i)} v_{c,(u,l),p}^{(i)} + \left(1 - u_{(u,l),p}^{(i)}\right) v_{F,k2,(u,l),p}^{(i)} \quad (\text{D.3d})$$

where $v_{CE,k1,(u,l),p}^{(i)}$ and $v_{CE,k2,(u,l),p}^{(i)}$ are the on-state collector-emitter voltages of the transistors Tk1 and Tk2 of the i -th SM, respectively, and $v_{F,k1,(u,l),p}^{(i)}$ and $v_{F,k2,(u,l),p}^{(i)}$ are the forward voltages of the diodes Dk1 and Dk2 of the i -th SM, respectively.

The on-state voltages of the transistors and diodes are obtained from 2-D linear scattered interpolators for the transistor's on-state collector-emitter voltage and the diode's forward voltage. Denoted by $v_{CE}(i_d, T_j)$ and $v_F(i_d, T_j)$, respectively, in terms of the component's current i_d and its junction temperature T_j . This work considers that all the solid-state devices have the same junction temperature T_j . These interpolators are determined from the data sheet of a given IGBT module. The typical characteristics for these quantities are illustrated in Fig. D.2 for an IGBT module with a rated collector-emitter voltage of $V_{CE} = 4.5$ kV and a rated collector current of $I_C = 3$ kA.

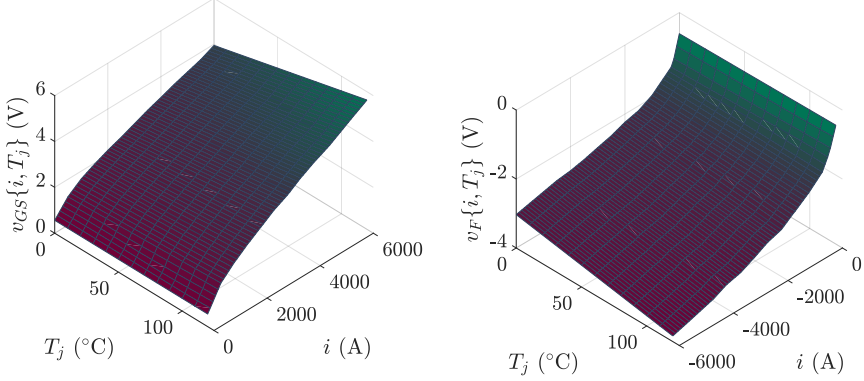
From the interpolators v_{CE} and v_F , the on-state voltages for the components of the i -th SM are written as

$$v_{CE,k1,(u,l),p}^{(i)} = v_{CE} \left(i_{Tk1,(u,l),p}^{(i)}, T_j \right) \quad (\text{D.4a})$$

$$v_{F,k1,(u,l),p}^{(i)} = v_F \left(i_{Dk1,(u,l),p}^{(i)}, T_j \right) \quad (\text{D.4b})$$

$$v_{CE,k2,(u,l),p}^{(i)} = v_{CE} \left(i_{Tk2,(u,l),p}^{(i)}, T_j \right) \quad (\text{D.4c})$$

$$v_{F,k2,(u,l),p}^{(i)} = v_F \left(i_{Dk2,(u,l),p}^{(i)}, T_j \right) \quad (\text{D.4d})$$



(a) Transistor's on-state collector-emitter voltage.

(b) Diode's on-state forward voltage.

 Figure D.2: Typical transistor's on-state collector-emitter voltage and diode's on-state forward voltage for an IGBT module with a rated collector-emitter voltage $V_{CE} = 4.5$ kV and a rated collector current $I_C = 3$ kA.

The instantaneous conduction losses of the switching devices can be computed from Eqs. (D.2), (D.3) as

$$p_{Tk1,(u,l),p}^{(i)} = v_{Tk1,(u,l),p}^{(i)} i_{Tk1,(u,l),p}^{(i)} \quad (\text{D.5a})$$

$$p_{Dk1,(u,l),p}^{(i)} = v_{Dk1,(u,l),p}^{(i)} i_{Dk1,(u,l),p}^{(i)} \quad (\text{D.5b})$$

$$p_{Tk2,(u,l),p}^{(i)} = v_{Tk2,(u,l),p}^{(i)} i_{Tk2,(u,l),p}^{(i)} \quad (\text{D.5c})$$

$$p_{Dk2,(u,l),p}^{(i)} = v_{Dk2,(u,l),p}^{(i)} i_{Dk2,(u,l),p}^{(i)} \quad (\text{D.5d})$$

From Eqs. (D.2),(D.3),(D.4), we can rewrite (D.5) as

$$p_{Tk1,(u,l),p}^{(i)} = \begin{cases} -u_{(u,l),p}^{(i)} v_{CE} \left(-u_{(u,l),p}^{(i)} i_{(u,l),p}, T_j \right) i_{(u,l),p}, & \text{when } i_{(u,l),p} < 0, \\ 0, & \text{otherwise.} \end{cases} \quad (\text{D.6a})$$

$$p_{Dk1,(u,l),p}^{(i)} = \begin{cases} -u_{(u,l),p}^{(i)} v_F \left(-u_{(u,l),p}^{(i)} i_{(u,l),p}, T_j \right) i_{(u,l),p}, & \text{when } i_{(u,l),p} > 0, \\ 0, & \text{otherwise.} \end{cases} \quad (\text{D.6b})$$

$$p_{Tk2,(u,l),p}^{(i)} = \begin{cases} \left(1 - u_{(u,l),p}^{(i)} \right) v_{CE} \left(\left(1 - u_{(u,l),p}^{(i)} \right) i_{(u,l),p}, T_j \right) i_{(u,l),p}, & \text{when } i_{(u,l),p} > 0, \\ 0, & \text{otherwise.} \end{cases} \quad (\text{D.6c})$$

$$p_{Dk2,(u,l),p}^{(i)} = \begin{cases} \left(1 - u_{(u,l),p}^{(i)}\right) v_{CE} \left(\left(1 - u_{(u,l),p}^{(i)}\right) i_{(u,l),p}, T_j \right) i_{(u,l),p}, \\ \text{when } i_{(u,l),p} < 0, \\ 0, \text{ otherwise.} \end{cases} \quad (\text{D.6d})$$

The sum of the conduction losses for each SM component of an arm can be computed from (D.6) as

$$p_{Tk1,(u,l),p} = \sum_{i=1}^N p_{Tk1,(u,l),p}^{(i)} = \begin{cases} -u_{(u,l),p} v_{CE} \left(-i_{(u,l),p}, T_j \right) i_{(u,l),p}, \\ \text{when } i_{(u,l),p} < 0, \\ 0 \text{ otherwise.} \end{cases} \quad (\text{D.7a})$$

$$p_{Dk1,(u,l),p} = \sum_{i=1}^N p_{Dk1,(u,l),p}^{(i)} = \begin{cases} -u_{(u,l),p} v_F \left(-i_{(u,l),p}, T_j \right) i_{(u,l),p}, \\ \text{when } i_{(u,l),p} > 0 \\ 0 \text{ otherwise.} \end{cases} \quad (\text{D.7b})$$

$$p_{Tk2,(u,l),p} = \sum_{i=1}^N p_{Tk2,(u,l),p}^{(i)} = \begin{cases} (N - u_{(u,l),p}) v_{CE} \left(i_{(u,l),p}, T_j \right) i_{(u,l),p}, \\ \text{when } i_{(u,l),p} > 0 \\ 0 \text{ otherwise.} \end{cases} \quad (\text{D.7c})$$

$$p_{Dk2,(u,l),p} = \sum_{i=1}^N p_{Dk2,(u,l),p}^{(i)} = \begin{cases} (N - u_{(u,l),p}) v_F \left(i_{(u,l),p}, T_j \right) i_{(u,l),p}, \\ \text{when } i_{(u,l),p} < 0 \\ 0 \text{ otherwise.} \end{cases} \quad (\text{D.7d})$$

Eq. (D.7) shows that one can calculate the conduction loss of a single inserted SM in an arm, and then multiply the result by the number of inserted SMs in the corresponding arm, which is given by $u_{(u,l),p}$, to obtain the total conduction losses of the inserted SMs. In the same way, one can calculate the conduction loss of a single non-inserted SM in an arm, and then multiply the result by the number of non-inserted SMs in the corresponding arm, which is given by $N - u_{(u,l),p}$, to obtain the total conduction losses of the non-inserted SMs. This analysis holds true as long as all the solid-state devices have the same junction temperature T_j and v_{CE} and v_F are linear interpolators.

The average conduction losses for each SM component of an arm over a fundamental period is computed as

$$P_{Tk1,(u,l),p} = \int_{(k-1) T_0}^{k T_0} p_{Tk1,(u,l),p} dt \quad (\text{D.8a})$$

$$P_{Dk1,(u,l),p} = \int_{(k-1)T_0}^k T_0 p_{Dk1,(u,l),p} dt \quad (\text{D.8b})$$

$$P_{Tk2,(u,l),p} = \int_{(k-1)T_0}^k T_0 p_{Tk2,(u,l),p} dt \quad (\text{D.8c})$$

$$P_{Dk2,(u,l),p} = \int_{(k-1)T_0}^k T_0 p_{Dk2,(u,l),p} dt \quad (\text{D.8d})$$

Finally, the average conduction losses for each phase of the MMC are computed as

$$P_{cond,p} = \left(P_{Tk1,u,p} + P_{Tk2,u,p} + P_{Dk1,u,p} + P_{Tk2,u,p} \right. \\ \left. + P_{Tk1,l,p} + P_{Tk2,l,p} + P_{Dk1,l,p} + P_{Tk2,l,p} \right) \quad (\text{D.9})$$

D.2 Switching Losses

To calculate the switching losses, we need to determine all the switching instants at each arm of the converter. Suppose that $N_{sw,(u,l),p}$ switching events take place for the upper and lower arm of the phase p over a fundamental operation period. The finite set of switching instants for the upper and lower arm of the phase p is defined as

$$\mathbf{t}_{sw,(u,l),p} = \{t_{(u,l),p}^{(1)}, \dots, t_{(u,l),p}^{(N_{sw,(u,l),p})}\} \quad (\text{D.10})$$

To determine the elements of $\mathbf{t}_{sw,(u,l),p}$ we compute the forward difference on the arm modulation index defined as

$$\Delta u_{(u,l),p}(t_h) = u_{(u,l),p}(t_h) - u_{(u,l),p}(t_{h-1}) \quad (\text{D.11})$$

where $t_h \in \mathbb{R}_{\geq 0}$.

Subsequently, the k -th switching instant can be obtained from the following condition,

$$t_{(u,l),p}^{(k)} = t_h, \text{ when } \left| \Delta u_{(u,l),p}(t_{(u,l),p}^{(k)}) \right| > 0, \forall k \in \{1, \dots, N_{sw,(u,l),p}\} \quad (\text{D.12})$$

Additionally, we define eight subsets of $\mathbf{t}_{sw,(u,l),p}$ for each arm as

$$\mathbf{t}_{ON,Tk1,(u,l),p} = \{t_{ON,Tk1,(u,l),p}^{(1)}, \dots, t_{ON,Tk1,(u,l),p}^{(N_{ON,Tk1})}\} \quad (\text{D.13a})$$

$$\mathbf{t}_{OFF,Tk1,(u,l),p} = \{t_{OFF,Tk1,(u,l),p}^{(1)}, \dots, t_{OFF,Tk1,(u,l),p}^{(N_{OFF,Tk1})}\} \quad (\text{D.13b})$$

$$\mathbf{t}_{ON,Dk1,(u,l),p} = \{t_{ON,Dk1,(u,l),p}^{(1)}, \dots, t_{ON,Dk1,(u,l),p}^{(N_{ON,Dk1})}\} \quad (D.13c)$$

$$\mathbf{t}_{OFF,Dk1,(u,l),p} = \{t_{OFF,Dk1,(u,l),p}^{(1)}, \dots, t_{OFF,Dk1,(u,l),p}^{(N_{OFF,Dk1})}\} \quad (D.13d)$$

$$\mathbf{t}_{ON,Tk2,(u,l),p} = \{t_{ON,Tk2,(u,l),p}^{(1)}, \dots, t_{ON,Tk2,(u,l),p}^{(N_{ON,Tk2})}\} \quad (D.13e)$$

$$\mathbf{t}_{OFF,Tk2,(u,l),p} = \{t_{OFF,Tk2,(u,l),p}^{(1)}, \dots, t_{OFF,Tk2,(u,l),p}^{(N_{OFF,Tk2})}\} \quad (D.13f)$$

$$\mathbf{t}_{ON,Dk2,(u,l),p} = \{t_{ON,Dk2,(u,l),p}^{(1)}, \dots, t_{ON,Dk2,(u,l),p}^{(N_{ON,Dk2})}\} \quad (D.13g)$$

$$\mathbf{t}_{OFF,Dk2,(u,l),p} = \{t_{OFF,Dk2,(u,l),p}^{(1)}, \dots, t_{OFF,Dk2,(u,l),p}^{(N_{OFF,Dk2})}\} \quad (D.13h)$$

where $(N_{ON,Tk1}, N_{OFF,Tk1})$, $(N_{ON,Dk1}, N_{OFF,Dk1})$, $(N_{ON,Dk2}, N_{OFF,Dk2})$, $(N_{ON,Tk2}, N_{OFF,Tk2})$ and $(N_{ON,Dk2}, N_{OFF,Dk2})$ denotes the total number of on and off switching events of the components Tk1, Dk1, Tk2 and Dk2 respectively.

Moreover, the elements of these subsets are obtained from the elements of $\mathbf{t}_{sw,(u,l),p}$ from the following conditions,

$$t_{ON,Tk1,(u,l),p}^{(n)} = t_{(u,l),p}^{(k)}, \text{ if } \Delta u_{(u,l),p} \left(t_{(u,l),p}^{(k)} \right) > 0 \text{ and } i_{(u,l),p} \left(t_{(u,l),p}^{(k)} \right) < 0 \\ \forall k \in \{1, \dots, N_{sw,(u,l),p}\}, \forall n \in \{1, \dots, N_{ON,Tk1}\} \quad (D.14a)$$

$$t_{OFF,Tk1,(u,l),p}^{(n)} = t_{(u,l),p}^{(k)}, \text{ if } \Delta u_{(u,l),p} \left(t_{(u,l),p}^{(k)} \right) < 0 \text{ and } i_{(u,l),p} \left(t_{(u,l),p}^{(k)} \right) < 0 \\ \forall k \in \{1, \dots, N_{sw,(u,l),p}\}, \forall n \in \{1, \dots, N_{OFF,Tk1}\} \quad (D.14b)$$

$$t_{ON,Dk1,(u,l),p}^{(n)} = t_{(u,l),p}^{(k)}, \text{ if } \Delta u_{(u,l),p} \left(t_{(u,l),p}^{(k)} \right) > 0 \text{ and } i_{(u,l),p} \left(t_{(u,l),p}^{(k)} \right) > 0 \\ \forall k \in \{1, \dots, N_{sw,(u,l),p}\}, \forall n \in \{1, \dots, N_{ON,Dk1}\} \quad (D.14c)$$

$$t_{OFF,Dk1,(u,l),p}^{(n)} = t_{(u,l),p}^{(k)}, \text{ if } \Delta u_{(u,l),p} \left(t_{(u,l),p}^{(k)} \right) < 0 \text{ and } i_{(u,l),p} \left(t_{(u,l),p}^{(k)} \right) > 0 \\ \forall k \in \{1, \dots, N_{sw,(u,l),p}\}, \forall n \in \{1, \dots, N_{OFF,Dk1}\} \quad (D.14d)$$

$$t_{ON,Tk2,(u,l),p}^{(n)} = t_{(u,l),p}^{(k)}, \text{ if } \Delta u_{(u,l),p} \left(t_{(u,l),p}^{(k)} \right) < 0 \text{ and } i_{(u,l),p} \left(t_{(u,l),p}^{(k)} \right) > 0 \\ \forall k \in \{1, \dots, N_{sw,(u,l),p}\}, \forall n \in \{1, \dots, N_{ON,Tk2}\} \quad (D.14e)$$

$$t_{OFF,Tk2,(u,l),p}^{(n)} = t_{(u,l),p}^{(k)}, \text{ if } \Delta u_{(u,l),p} \left(t_{(u,l),p}^{(k)} \right) > 0 \text{ and } i_{(u,l),p} \left(t_{(u,l),p}^{(k)} \right) > 0 \\ \forall k \in \{1, \dots, N_{sw,(u,l),p}\}, \forall n \in \{1, \dots, N_{OFF,Tk2}\} \quad (\text{D.14f})$$

$$t_{ON,Dk2,(u,l),p}^{(n)} = t_{(u,l),p}^{(k)}, \text{ if } \Delta u_{(u,l),p} \left(t_{(u,l),p}^{(k)} \right) < 0 \text{ and } i_{(u,l),p} \left(t_{(u,l),p}^{(k)} \right) < 0 \\ \forall k \in \{1, \dots, N_{sw,(u,l),p}\}, \forall n \in \{1, \dots, N_{ON,Dk2}\} \quad (\text{D.14g})$$

$$t_{OFF,Dk2,(u,l),p}^{(n)} = t_{(u,l),p}^{(k)}, \text{ if } \Delta u_{(u,l),p} \left(t_{(u,l),p}^{(k)} \right) > 0 \text{ and } i_{(u,l),p} \left(t_{(u,l),p}^{(k)} \right) < 0 \\ \forall k \in \{1, \dots, N_{sw,(u,l),p}\}, \forall n \in \{1, \dots, N_{OFF,Dk2}\} \quad (\text{D.14h})$$

We can now define 2-D linear scattered interpolators to determine the switching energy of transistors during its switching on and off, respectively $E_{ON,T}(i_d, T_j)$, $E_{OFF,T}(i_d, T_j)$ and the switching energy of diodes during its switching off $E_{OFF,D}(i_d, T_j)$ as a function of the commutated current i and the junction temperature T_j . The typical characteristics for these quantities are illustrated in Fig. D.3 for an IGBT module with a rated collector-emitter voltage $V_{CE} = 4.5$ kV and a rated collector current $I_C = 3$ kA.

The total switching energies relative to each component of the HB-SM for a given phase arm are written as

$$E_{ON,Tk1,(u,l),p} = \sum_{n=1}^{N_{ON,Tk1,(u,l),p}} \left(\left| \Delta u_{(u,l),p} \left(t_{ON,Tk1,(u,l),p}^{(n)} \right) \right| \cdot E_{ON,T} \left(i_{(u,l),p} \left(t_{ON,Tk1,(u,l),p}^{(n)} \right), T_j \right) \right) \quad (\text{D.15a})$$

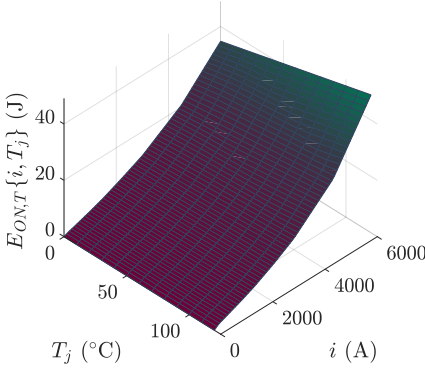
$$E_{OFF,Tk1,(u,l),p} = \sum_{n=1}^{N_{OFF,Tk1,(u,l),p}} \left(\left| \Delta u_{(u,l),p} \left(t_{OFF,Tk1,(u,l),p}^{(n)} \right) \right| \cdot E_{OFF,T} \left(i_{(u,l),p} \left(t_{OFF,Tk1,(u,l),p}^{(n)} \right), T_j \right) \right) \quad (\text{D.15b})$$

$$E_{OFF,Dk1,(u,l),p} = \sum_{n=1}^{N_{ON,Dk1,(u,l),p}} \left(\left| \Delta u_{(u,l),p} \left(t_{OFF,Dk1,(u,l),p}^{(n)} \right) \right| \cdot E_{OFF,D} \left(i_{(u,l),p} \left(t_{OFF,Dk1,(u,l),p}^{(n)} \right), T_j \right) \right) \quad (\text{D.15c})$$

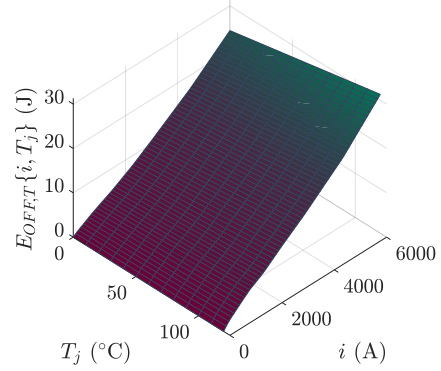
$$E_{ON,Tk2,(u,l),p} = \sum_{n=1}^{N_{ON,Tk2,(u,l),p}} \left(\left| \Delta u_{(u,l),p} \left(t_{ON,Tk2,(u,l),p}^{(n)} \right) \right| \cdot E_{ON,T} \left(i_{(u,l),p} \left(t_{ON,Tk2,(u,l),p}^{(n)} \right), T_j \right) \right) \quad (\text{D.15d})$$

$$E_{OFF,Tk2,(u,l),p} = \sum_{n=1}^{N_{OFF,Tk2,(u,l),p}} \left(\left| \Delta u_{(u,l),p} \left(t_{OFF,Tk2,(u,l),p}^{(n)} \right) \right| \cdot E_{OFF,T} \left(i_{(u,l),p} \left(t_{OFF,Tk2,(u,l),p}^{(n)} \right), T_j \right) \right) \quad (D.15e)$$

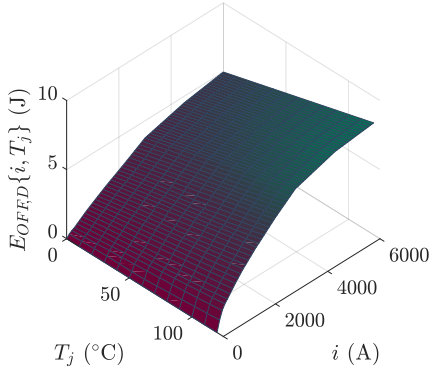
$$E_{OFF,Dk2,(u,l),p} = \sum_{n=1}^{N_{ON,Dk2,(u,l),p}} \left(\left| \Delta u_{(u,l),p} \left(t_{ON,Dk2,(u,l),p}^{(n)} \right) \right| \cdot E_{OFF,D} \left(i_{(u,l),p} \left(t_{ON,Dk2,(u,l),p}^{(n)} \right), T_j \right) \right) \quad (D.15f)$$



(a) Transistor's on-switching energy.



(b) Transistor's off-switching energy.



(c) Diode's off-switching energy.

Figure D.3: Typical transistor switching energies for an IGBT module with a rated collector-emitter voltage $V_{CE} = 4.5$ kV and a rated collector current $I_C = 3$ kA.

The average switching losses over a fundamental period relative to each component of the HB-SM for a given phase arm are written from Eq. (D.15) as

$$P_{ON,Tk1,(u,l),p} = \frac{E_{ON,Tk1,(u,l),p}}{T_0} \quad (\text{D.16a})$$

$$P_{OFF,Tk1,(u,l),p} = \frac{E_{OFF,Tk1,(u,l),p}}{T_0} \quad (\text{D.16b})$$

$$P_{OFF,Dk1,(u,l),p} = \frac{E_{OFF,Dk1,(u,l),p}}{T_0} \quad (\text{D.16c})$$

$$P_{ON,Tk2,(u,l),p} = \frac{E_{ON,Tk2,(u,l),p}}{T_0} \quad (\text{D.16d})$$

$$P_{OFF,Tk2,(u,l),p} = \frac{E_{OFF,Tk2,(u,l),p}}{T_0} \quad (\text{D.16e})$$

$$P_{OFF,Dk2,(u,l),p} = \frac{E_{OFF,Dk2,(u,l),p}}{T_0} \quad (\text{D.16f})$$

Finally, the average switching losses for each phase of the MMC are computed as

$$\begin{aligned} P_{sw,p} = & (P_{ON,Tk1,u,p} + P_{OFF,Tk1,u,p} + P_{OFF,Dk1,u,p} \\ & + P_{ON,Tk2,u,p} + P_{OFF,Tk2,u,p} + P_{OFF,Dk2,u,p} \\ & + P_{ON,Tk1,l,p} + P_{OFF,Tk1,l,p} + P_{OFF,Dk1,l,p} \\ & + P_{ON,Tk2,l,p} + P_{OFF,Tk2,l,p} + P_{OFF,Dk2,l,p}) \quad (\text{D.17}) \end{aligned}$$

Appendix E

Grid-Following Control of the Modular Multilevel Converter

An MMC can be either operated in grid-following or grid-forming control [108]. The difference between these strategies falls essentially on the control variable. In grid-forming mode, the MMC controls the AC frequency and voltage amplitude based on droop control [109, 110, 111] or virtual synchronous machine control strategies [111, 110, 112]. In grid-following mode [55, 111, 113, 114], the MMC controls the active power or the DC voltage and the reactive power. In MMC-HVDC links connected to weak AC systems, such as a wind turbine plant, the converter connected to the turbines is operated in grid-forming mode. Alternatively, in P2P links between two strong AC systems, both converters are operated in grid-following mode. In this appendix, we discuss the control structure of an MMC operated in grid-following control, for which typical structure is illustrated in Fig. (E.1).

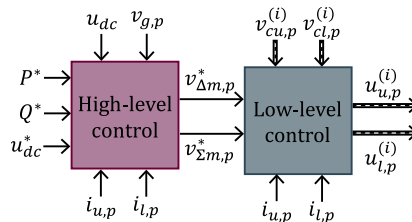


Figure E.1: Typical control structure for the MMC in grid-following operation.

The control structure of the MMC represented in Fig. (E.1) can be divided in low- and high-level structures. The high-level control is responsible for generating the modulated voltages references, $v_{\Sigma m,p}^*$ and $v_{\Delta m,p}^*$, which are usually obtained from classical PI controllers that aim to control the converter's internal and external dynamics. The low-level control is responsible for converting the modulated voltages references, $v_{\Sigma m,p}^*$ and $v_{\Delta m,p}^*$, into the individual switching patterns of SMS, $u_{m,u,p}^{(i)}$ and $u_{m,l,p}^{(i)}$.

E.1 Low-Level Control

The low-level control structure considered in this study is presented in Fig. E.2.

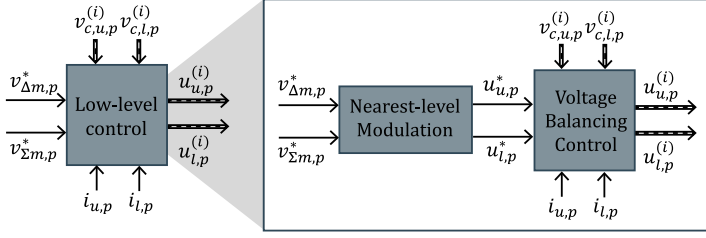


Figure E.2: Low-level control structure for the MMC.

To synthesize a multilevel AC-modulated voltage from multiple voltage levels, the SMs must follow a coordinated switching pattern. The low-level control of the MMC aims to generate these patterns to impose a specific AC-modulated voltage at the fundamental frequency to control the converter's operation point.

E.1.1 Nearest-Level Modulation

The Nearest-Level Modulation (NLM), illustrated in Fig. E.3, is the most widespread modulation technique in MMC-HVDC applications. It generates the number of SMs to be inserted in the upper and lower arms, $u_{u,p}^*$ and $u_{l,p}^*$, respectively, to synthesize the desired AC-modulated voltage based on an analytical formula.

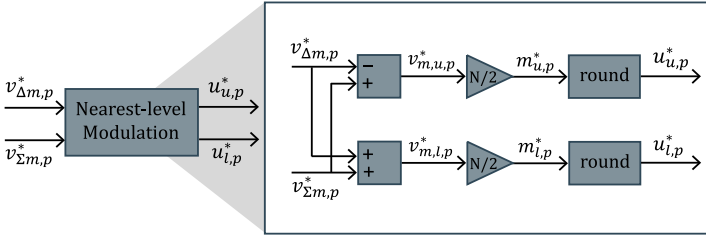


Figure E.3: Nearest-level modulation scheme.

From the references of the modulated voltages $v_{\Delta m,p}^*$ and $v_{\Sigma m,p}^*$, we can write the references for the upper and lower arm modulated voltages from Eqs. (II.20e),(II.20f) as

$$v_{m,u,p}^* = v_{\Sigma m,p}^* - v_{\Delta m,p}^* \quad (\text{E.1a})$$

$$v_{m,l,p}^* = v_{\Sigma m,p}^* + v_{\Delta m,p}^* \quad (\text{E.1b})$$

The references for the upper and lower arm modulation indexes, $v_{m,u,p}^*$ and $v_{m,l,p}^*$ respectively, are defined as

$$m_{u,p}^* \triangleq \frac{v_{m,u,p}^*}{U_{dc}} = \frac{v_{\Sigma m,p}^* - v_{\Delta m,p}^*}{U_{dc}} \quad (\text{E.2a})$$

$$m_{l,p}^* \triangleq \frac{v_{m,l,p}^*}{U_{dc}} = \frac{v_{\Sigma m,p}^* + v_{\Delta m,p}^*}{U_{dc}} \quad (\text{E.2b})$$

where U_{dc} is the rated DC voltage.

Define the Δ and the Σ modulation indices,

$$m_{\Delta,p}^* \triangleq \frac{2v_{\Delta m,p}^*}{U_{dc}} \quad (\text{E.3a})$$

$$m_{\Sigma,p}^* \triangleq \frac{2v_{\Sigma m,p}^*}{U_{dc}} \quad (\text{E.3b})$$

Using the definition (E.3), rewrite Eq. (E.2) as

$$m_{u,p}^* = \frac{1}{2} (m_{\Sigma,p}^* - m_{\Delta,p}^*) \quad (\text{E.4a})$$

$$m_{l,p}^* = \frac{1}{2} (m_{\Sigma,p}^* + m_{\Delta,p}^*) \quad (\text{E.4b})$$

The NLM generates the references for the upper and lower arm switching functions as

$$u_{u,p}^* = \text{round}(N m_{u,p}^*) = \text{round}\left(\frac{N}{2} (m_{\Sigma,p}^* - m_{\Delta,p}^*)\right) \quad (\text{E.5a})$$

$$u_{l,p}^* = \text{round}(N m_{l,p}^*) = \text{round}\left(\frac{N}{2} (m_{\Sigma,p}^* + m_{\Delta,p}^*)\right) \quad (\text{E.5b})$$

where the function $\text{round}\{\cdot\}$ rounds up to the nearest integer.

If the converter is operated in open loop, $v_{\Delta m,p}^*$ and $v_{\Sigma m,p}^*$ are imposed as

$$\begin{bmatrix} v_{\Delta m,a}^* \\ v_{\Delta m,b}^* \\ v_{\Delta m,c}^* \end{bmatrix} = \begin{bmatrix} V_{\Delta m,1}^* \cos(\omega_0 t + \theta_{\Delta,1}^*) \\ V_{\Delta m,1}^* \cos\left(\omega_0 t - \frac{2\pi}{3} + \theta_{\Delta,1}^*\right) \\ V_{\Delta m,1}^* \cos\left(\omega_0 t + \frac{2\pi}{3} + \theta_{\Delta,1}^*\right) \end{bmatrix} \quad (\text{E.6a})$$

$$v_{\Sigma m,p}^* = \frac{U_{dc}}{2} \quad (\text{E.6b})$$

where $V_{\Delta m,1}^*$ and $\theta_{\Delta,1}^*$ are references for the Δ -modulated voltage amplitude and angle, respectively.

Using Eq.(E.6), we can rewrite Eq.(E.3) as

$$\begin{bmatrix} m_{\Delta,a}^* \\ m_{\Delta,b}^* \\ m_{\Delta,c}^* \end{bmatrix} = \begin{bmatrix} M_{\Delta,1}^* \cos(\omega_0 t + \theta_{\Delta,1}^*) \\ M_{\Delta,1}^* \cos\left(\omega_0 t - \frac{2\pi}{3} + \theta_{\Delta,1}^*\right) \\ M_{\Delta,1}^* \cos\left(\omega_0 t + \frac{2\pi}{3} + \theta_{\Delta,1}^*\right) \end{bmatrix} \quad (\text{E.7a})$$

$$m_{\Sigma,p}^* = 1 \quad (\text{E.7b})$$

with

$$M_{\Delta,1}^* = \frac{2V_{\Delta m,1}^*}{U_{dc}} \quad (\text{E.8})$$

Notice that the NLM does not provide the individual switching patterns of SMs. The choice of which SMs to insert is performed by the voltage balancing control that aims to balance the capacitor voltages between the SM in each arm.

E.1.2 Voltage-Balancing Control

The voltage-balancing control (VBC) is responsible for generating the switching functions of the individual SMs for the upper and lower arm, $u_{u,p}^{(i)}$ and $u_{l,p}^{(i)}$, respectively, based on the references of the upper and lower arm switching functions, $u_{u,p}^*$ and $u_{l,p}^*$, respectively, as illustrated in Fig. (E.4). Equally important, the VBC aims to balance the capacitor voltages between the SMs of an arm.

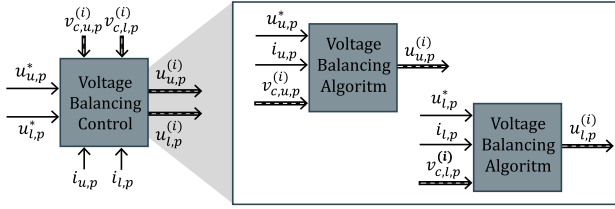


Figure E.4: Voltage balancing control scheme.

In order to evaluate the performance of a VBC, we define three metrics. The first metric corresponds to the average switching frequency of SMs defined as

$$F_{SM} \triangleq \frac{N_{on}}{T_0 N} \quad (\text{E.9})$$

where N_{on} is the number of turn-on events during a fundamental period.

The second and the third metrics correspond to the individual and the total capacitor's voltage ripples defined respectively as,

$$\Delta v_{c,(u,l),p}^{(i)} \triangleq \frac{N}{V_{c,(u,l),p,0}} \left(\max_{t \in [(k-1)T_0, kT_0]} \{v_{c,(u,l),p}^{(i)}\} - \min_{t \in [(k-1)T_0, kT_0]} \{v_{c,(u,l),p}^{(i)}\} \right) \quad (\text{E.10})$$

usually required to be smaller than 20%. The average switching frequency of SMs using the CSF-VBA is $F_{SM} = 170$ Hz.

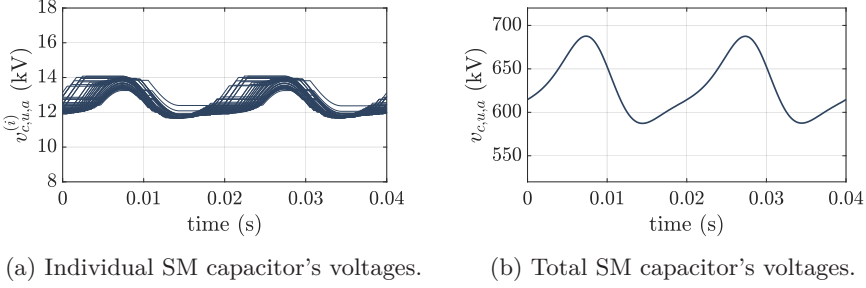


Figure E.6: Individual and total SM capacitor's voltages using the CSF-VBA. Simulation for the thesis's study case with $N = 50$ and $C = 3.3$ mF for $P = 1$ GW and $Q = 300$ MVar.

E.2 High-Level Control

The high-level control loop can independently control the internal and external dynamics of the MMC. The external dynamics of the MMC corresponds to its AC- and DC-side dynamics, and the internal dynamics correspond to the SM capacitor's voltage fluctuations and circulating current dynamics.

The external dynamics control has a cascaded structure and is composed of inner and outer control loops. The inner Δ -current control loop based on the dq decomposition of Eq. (II.22) at the fundamental frequency. The dq - Δ -current control loop is employed to control, independently, the d - Δ - and the q - Δ -currents. Cascaded with the d - Δ -current control, an outer loop can control the active power, the DC voltage, or the AC frequency. Cascaded with the q - Δ -current control, an outer loop can control the reactive power or the AC voltage amplitude.

The internal-dynamics control loops fall out of the scope of this thesis, and no further discussion will be provided on this subject.

The high-level control structure considered in this study is presented in Fig. E.7. This control structure supposes a balanced condition where the three-phases voltages and currents have the same amplitude with a 120° phase-shift between phases. Furthermore, only the MMC's external dynamics are controlled in closed loop.

E.2.1 External Dynamics Control: Inner Control Loop

The dq - Δ -current loop implements a decoupled control of the d and q components of the fundamental-frequency component of $i_{\Delta,p}$. The derivation of the dq - Δ -current control structure can be found in [115].

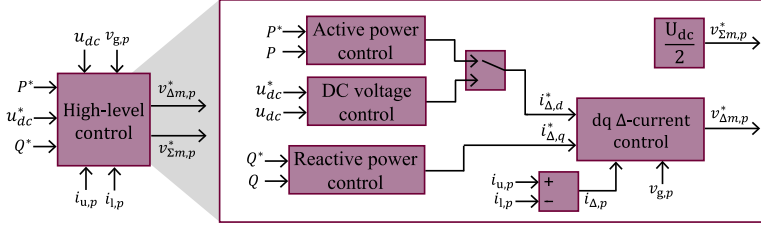


Figure E.7: High-level control structure for the MMC in grid-following operation.

A three-phase variable $\mathbf{f}_{a,b,c}$ can be decomposed into dq0 components as follows.

$$\mathbf{f}_{d,q,0} = K_P(\theta_{dq}) \mathbf{f}_{a,b,c} \quad (\text{E.12})$$

with

$$\mathbf{f}_{a,b,c} = \begin{bmatrix} f_a & f_b & f_c \end{bmatrix}^T \quad (\text{E.13a})$$

$$\mathbf{f}_{d,q,0} = \begin{bmatrix} f_d & f_q & f_0 \end{bmatrix}^T \quad (\text{E.13b})$$

$$K_P(\theta_{dq}) = \frac{2}{3} \begin{bmatrix} \cos(\theta_{dq}) & \cos(\theta_{dq} - \frac{2\pi}{3}) & \cos(\theta_{dq} + \frac{2\pi}{3}) \\ \sin(\theta_{dq}) & \sin(\theta_{dq} - \frac{2\pi}{3}) & \sin(\theta_{dq} + \frac{2\pi}{3}) \\ \frac{1}{2} & \frac{1}{2} & \frac{1}{2} \end{bmatrix} \quad (\text{E.13c})$$

where θ_{dq} is the Park transformation angle and f_d , f_q and f_0 are respectively the direct, the quadrature and the homopolar components of $\mathbf{f}_{a,b,c}$.

Also, the inverse park transformation is given by

$$\mathbf{f}_{a,b,c} = K_P^{-1}(\theta_{dq}) \mathbf{f}_{d,q,0} \quad (\text{E.14})$$

with

$$K_P^{-1}(\theta_{dq}) = \begin{bmatrix} \cos(\theta_{dq}) & \sin(\theta_{dq}) & 1 \\ \cos(\theta_{dq} - \frac{2\pi}{3}) & \sin(\theta_{dq} - \frac{2\pi}{3}) & 1 \\ \cos(\theta_{dq} + \frac{2\pi}{3}) & \sin(\theta_{dq} + \frac{2\pi}{3}) & 1 \end{bmatrix} \quad (\text{E.15})$$

Eq. (II.22) can be decomposed using the the Park transformation defined in Eqs. (E.12) and (E.14) as

$$L_\Delta K_P(\theta_{dq}) \frac{d}{dt} K_P^{-1}(\theta_{dq}) \begin{bmatrix} i_{\Delta,d} \\ i_{\Delta,q} \\ i_{\Delta,0} \end{bmatrix} + R_\Delta \begin{bmatrix} i_{\Delta,d} \\ i_{\Delta,q} \\ i_{\Delta,0} \end{bmatrix} = \begin{bmatrix} v_{\Delta,m,d} \\ v_{\Delta,m,q} \\ v_{\Delta,m,0} \end{bmatrix} - \begin{bmatrix} v_{g,d} \\ v_{g,q} \\ v_{g,0} \end{bmatrix} \quad (\text{E.16})$$

Notice that for the balanced condition, the homopolar components are zero.

The angle of the Park's transform θ_{dq} is obtained from a phase-locked loop which usually imposes $v_{g,q} = 0$ [115]. As a result, the PLL angle is synchronized with the grid voltage angle of phase a ,

$$\theta_{dq} = \omega_0 t + \theta_g \quad (\text{E.17})$$

where θ_g is the phase of the grid voltage.

With the PLL angle given by Eq. (E.17) and since a three-phase balanced system is considered, Eq. (E.16) leads to

$$L_\Delta \begin{bmatrix} s & \omega_0 \\ -\omega_0 & s \end{bmatrix} \begin{bmatrix} i_{\Delta,d} \\ i_{\Delta,q} \end{bmatrix} + R_\Delta \begin{bmatrix} i_{\Delta,d} \\ i_{\Delta,q} \end{bmatrix} = \begin{bmatrix} v_{\Delta m,d} \\ v_{\Delta m,q} \end{bmatrix} - \begin{bmatrix} v_{g,d} \\ v_{g,q} \end{bmatrix} \quad (\text{E.18})$$

From Eq. (E.18), the transfer function for the dq - Δ -currents can be written as

$$H_i(s) = \frac{i_{\Delta,d}}{v_{\Delta m,d} - v_{g,d} - \omega_0 L_\Delta i_{\Delta,q}} = \frac{i_{\Delta,q}}{v_{\Delta m,q} - v_{g,q} + \omega_0 L_\Delta i_{\Delta,d}} = \frac{1}{L_\Delta s + R_\Delta} \quad (\text{E.19})$$

Subsequently, we can imagine a PI-based control-loop for the dynamics presented in Eq. (E.19). Start by defining a generic PI-controller as

$$C(k_p, k_i) = \frac{k_p s + k_i}{s} \quad (\text{E.20})$$

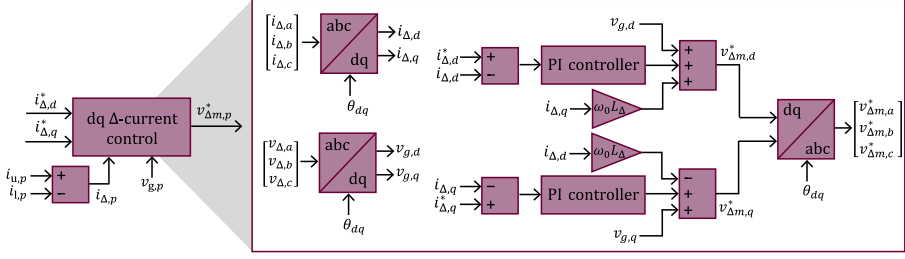
The dq - Δ -current controller's equations are written as

$$\begin{bmatrix} C(k_p, k_i, k_{i,i}) & 0 \\ 0 & C(k_p, k_i, k_{i,i}) \end{bmatrix} \left(\begin{bmatrix} i_{\Delta,d}^* \\ i_{\Delta,q}^* \end{bmatrix} - \begin{bmatrix} i_{\Delta,d} \\ i_{\Delta,q} \end{bmatrix} \right) + \begin{bmatrix} v_{g,d} \\ v_{g,q} \end{bmatrix} + \begin{bmatrix} 0 & \omega_0 L_\Delta \\ -\omega_0 L_\Delta & 0 \end{bmatrix} \begin{bmatrix} i_{\Delta,d} \\ i_{\Delta,q} \end{bmatrix} = \begin{bmatrix} v_{\Delta m,d}^* \\ v_{\Delta m,q}^* \end{bmatrix} \quad (\text{E.21})$$

The reference for the Δ -modulated voltage in the abc frame can be obtained from its dq components using the inverse Park's transform as

$$\begin{bmatrix} v_{\Delta m,a}^* \\ v_{\Delta m,b}^* \\ v_{\Delta m,c}^* \end{bmatrix} = K_P^{-1}(\theta_{dq}) \begin{bmatrix} v_{\Delta m,d}^* \\ v_{\Delta m,q}^* \\ 0 \end{bmatrix} \quad (\text{E.22})$$

The classical dq - Δ -current control for the MMC is presented in Fig. E.8.


 Figure E.8: Inner dq - Δ -current control.

E.2.1.1 External Dynamics Control: Outer Control Loop

The apparent power transferred to the grid can be written in terms of dq variables as

$$S = \frac{3}{2} (v_{g,d} + jv_{g,q}) (i_{\Delta,d} - ji_{\Delta,q}) \quad (\text{E.23})$$

which yields

$$S = \frac{3}{2} (v_{g,q}i_{\Delta,d} + v_{g,q}i_{\Delta,q}) + j\frac{3}{2} (v_{g,q}i_{\Delta,d} - v_{g,d}i_{\Delta,q}) \quad (\text{E.24})$$

from which we can identify the active and reactive power as

$$P = \frac{3}{2} (v_{g,d}i_{\Delta,d} + v_{g,q}i_{\Delta,q}) \quad (\text{E.25a})$$

$$Q = \frac{3}{2} (v_{g,q}i_{\Delta,d} - v_{g,d}i_{\Delta,q}) \quad (\text{E.25b})$$

We recall that the dq frame is oriented such that $v_{g,q} = 0$. Thus Eq. (E.25) is simplified to

$$P = \frac{3}{2} v_{g,d} i_{\Delta,d} \quad (\text{E.26a})$$

$$Q = -\frac{3}{2} v_{g,d} i_{\Delta,q} \quad (\text{E.26b})$$

It is worth noticing that thanks to the choice of the angle made in (E.17), the active and reactive power can be independently controlled.

The transfer function for active and reactive power can be written from Eq. (E.26) as

$$H_{PQ}(s) = \frac{P}{i_{\Delta,d}} = \frac{Q}{-i_{\Delta,q}} = \frac{3}{2} v_{g,d} \quad (\text{E.27})$$

We can write a PI-control for the dynamics presented in (E.27) as

$$\begin{bmatrix} C(k_{p,PQ}, k_{i,PQ}) & 0 \\ 0 & C(k_{p,PQ}, k_{i,PQ}) \end{bmatrix} \left(\begin{bmatrix} P^* \\ Q^* \end{bmatrix} - \begin{bmatrix} P \\ Q \end{bmatrix} \right) = \begin{bmatrix} i_{d\Delta}^* \\ -i_{q\Delta}^* \end{bmatrix} \quad (\text{E.28})$$

The classical PQ control structure is illustrated in Fig. E.9.

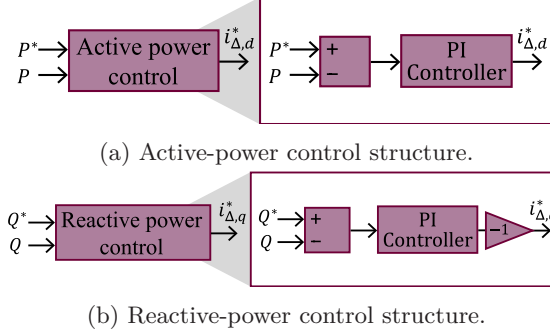


Figure E.9: Active and reactive power control structures.

Another possibility is to control the DC voltage u_{dc} using the d- Δ -current control loop. The DC-side power can be written as

$$u_{dc}i_{dc} = \frac{3}{2}v_{g,d}i_{\Delta,d} \quad (\text{E.29})$$

with i_{dc} given by

$$i_{dc} = i_{u,a} + i_{u,b} + i_{u,c} \quad (\text{E.30})$$

From (II.20a), Eq. (E.30) can be rewritten as

$$i_{dc} = \frac{i_{\Delta,a} + i_{\Delta,b} + i_{\Delta,c}}{2} + i_{\Sigma,a} + i_{\Sigma,b} + i_{\Sigma,c} \quad (\text{E.31})$$

Since we consider a balanced three-phase system, it follows that

$$i_{dc} = i_{\Sigma,a} + i_{\Sigma,b} + i_{\Sigma,c} \quad (\text{E.32})$$

Add the equations (II.40) for each phase to obtain

$$\begin{aligned} \frac{d}{dt}v_{\Sigma,c,a} + \frac{d}{dt}v_{\Sigma,c,b} + \frac{d}{dt}v_{\Sigma,c,c} = & - \left(\frac{u_{\Delta,a}}{4C}i_{\Delta,a} + \frac{u_{\Delta,b}}{4C}i_{\Delta,b} + \frac{u_{\Delta,c}}{4C}i_{\Delta,c} \right) \\ & + \left(\frac{u_{\Sigma,a}}{2C}i_{\Sigma,a} + \frac{u_{\Sigma,b}}{2C}i_{\Sigma,b} + \frac{u_{\Sigma,c}}{2C}i_{\Sigma,c} \right) \end{aligned} \quad (\text{E.33})$$

Then let us adopt the following assumptions,

$$v_{\Sigma,c,p} \stackrel{\text{hyp.}}{=} u_{dc} \quad (\text{E.34a})$$

$$u_{\Sigma,p} \stackrel{\text{hyp.}}{=} N \quad (\text{E.34b})$$

$$\frac{u_{\Delta,a}}{4C}i_{\Delta,a} + \frac{u_{\Delta,b}}{4C}i_{\Delta,b} + \frac{u_{\Delta,c}}{4C}i_{\Delta,c} \stackrel{\text{hyp.}}{=} 0 \quad (\text{E.34c})$$

Using (E.34), Eq. (E.33) simplifies to

$$3 \frac{d}{dt} u_{dc} = \frac{N}{2C} (i_{\Sigma,a} + i_{\Sigma,b} + i_{\Sigma,c}) \quad (\text{E.35})$$

Replace Eq. (E.32) into Eq. E.35 to obtain

$$\frac{6C}{N} \frac{d}{dt} u_{dc} = i_{dc} \quad (\text{E.36})$$

Finally, insert Eq. (E.36) into Eq. (E.29),

$$\frac{6C}{N} u_{dc} \frac{d}{dt} u_{dc} = \frac{3}{2} v_{g,d} i_{\Delta,d} \quad (\text{E.37})$$

which yields

$$\frac{3C}{N} \frac{d}{dt} u_{dc}^2 = \frac{3}{2} v_{g,d} i_{\Delta,d} \quad (\text{E.38})$$

The transfer function for dc-voltage can be written from Eq. (E.38) as

$$H_U(s) = \frac{u_{dc}^2}{i_{\Delta,d}} = \frac{N v_{g,d}}{4C s} \quad (\text{E.39})$$

A PI-based control for the dynamic presented in (E.39) can be written as

$$C(k_p, U, k_i, U) ((u_{dc}^*)^2 - (u_{dc})^2) = i_{\Delta,d}^* \quad (\text{E.40a})$$

The DC-voltage control structure is presented in Fig. E.10.

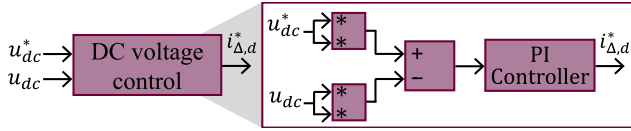


Figure E.10: DC-voltage control structure.

E.2.1.2 Controller's Tuning

The procedure to tune the gain of controllers for VSCs can be found in [116, 117].

From a control point of view, the dynamic behavior of the VBC is taken into account by means of a first-order transfer function,

$$H_{VBC}(s) = \frac{v_{\Delta m,d}}{v_{\Delta m,d}^*} = \frac{v_{\Delta m,q}}{v_{\Delta m,q}^*} = \frac{1}{T_{SM} s + 1} \quad (\text{E.41})$$

where $T_{SM} = 1/F_{SM}$ is the average switching period of SMs.

The open-loop transfer function of the inner Δ -current control is obtained using Eqs. (E.19) and (E.41) as

$$H_{OL,i}(s) = \frac{v_{\Delta m,d}}{i_{\Delta,d}^* - i_{\Delta,d}} = \frac{v_{\Delta m,q}}{i_{\Delta,q}^* - i_{\Delta,q}} = C(k_{p,i}, k_{i,i}) H_{VBC}(s) H_i(s) = \frac{k_{p,i}}{s} \frac{s + k_{i,i}}{T_{SM} s + 1} \frac{1}{L_{\Delta} s + R_{\Delta}} \quad (\text{E.42})$$

To calculate the gains of the inner-current controller, we compensate the pole of $H_i(s)$ in Eq. (E.42) and place the cutting frequency at one tenth of F_{SM} leading to

$$w_{c,i} = \frac{2\pi F_{SM}}{10} \quad (\text{E.43})$$

$$k_{i,i} = R_{\Delta} \sqrt{(w_{c,i} T_{SM})^2 + w_{c,i}^2} \quad (\text{E.44})$$

$$k_{p,i} = k_{i,i} \frac{L_{\Delta}}{R_{\Delta}} \quad (\text{E.45})$$

Moreover, the open-loop transfer functions for the PQ and the DC-voltage control are obtained using Eqs. (E.27) and (E.39) as

$$H_{OL,PQ}(s) = \frac{v_{\Delta m,d}}{P^* - P} = \frac{v_{\Delta m,q}}{Q^* - Q} = H_{CL,i}(s) H_{PQ}(s) \quad (\text{E.46})$$

$$H_{OL,U}(s) = \frac{v_{\Delta m,d}}{(u_{dc}^*)^2 - (u_{dc})^2} = H_{CL,i}(s) H_U(s) \quad (\text{E.47})$$

where $H_{CL,i}(s)$ denotes the closed-loop transfer function of the inner dq - Δ -current control loop given by

$$H_{CL,i}(s) = \frac{i_{\Delta,d}}{i_{\Delta,d}^*} = \frac{i_{\Delta,q}}{i_{\Delta,q}^*} = \frac{k_{p,i} s + k_{i,i}}{L_{\Delta} T_{SM} s^3 + (L_{\Delta} + R_{\Delta} T_{SM}) s^2 + (R_{\Delta} + k_{p,i} s) + k_{i,i}} \quad (\text{E.48})$$

Since the external dynamics control has a cascaded structure, the inner control loop must be faster than the outer control loops. Consequently, we choose for the outer control loops a cutting frequency that is one tenth of the cutting frequency of the inner control loop. As a result, only the static response of $H_{CL,i}(s)$ is considered in Eq. (E.47) which is simplified to

$$H_{OL,PQ}(s) \approx H_{CL,i}(0) H_{PQ}(s) = \frac{k_{p,PQ} s + k_{i,PQ}}{s} \frac{3}{2} v_{g,d} \quad (\text{E.49})$$

$$H_{OL,U}(s) \approx H_{CL,i}(0) H_U(s) = \frac{k_{p,U} s + k_{i,U}}{s} \frac{N}{4Cs} v_{g,d} \quad (\text{E.50})$$

To calculate the gains of the PQ outer controller, we employ an integral action to place its cutting frequency ten times smaller than $w_{c,i}$, leading to

$$w_{c,PQ} = \frac{2\pi F_{SM}}{100} \quad (\text{E.51})$$

$$k_{i,PQ} = \frac{2w_{c,PQ}}{3v_{g,d}} \quad (\text{E.52})$$

$$k_{p,PQ} = 0 \quad (\text{E.53})$$

The gains of the DC-voltage outer controller are computed to impose its phase margin at 60° and its cutting frequency ten times smaller than $w_{c,i}$, leading to

$$w_{c,U} = \frac{2\pi F_{SM}}{100} \quad (\text{E.54})$$

$$k_{i,U} = \frac{2C w_{c,U}^2}{N v_{g,d}} \quad (\text{E.55})$$

$$k_{p,U} = \frac{2\sqrt{3}C w_{c,U}}{N v_{g,d}} \quad (\text{E.56})$$

The controller's gains for the reference 1 GW and ± 320 kV MMC #0 defined in Section I.4, considering $F_{SM} = 150$ Hz are provided in Table E.1. We also provided the controller's gain for the various MMC configuration studied in Chapters III and IV.

Quantity	Symbol	MMC #0	MMC #1	MMC #2	MMC #4
Current controller proportional gain [V/A]	$k_{p,i}$	11.00	9.28	8.81	8.71
Current controller integral gain [V/(A s)]	$k_{i,i}$	137.85	137.84	137.26	136.07
Power controller proportional gain [1/(V)]	$k_{p,PQ}$	0	0	0	0
Power controller integral gain [1/(V s)]	$k_{i,PQ}$	$1.904 \cdot 10^{-5}$	$1.904 \cdot 10^{-5}$	$1.904 \cdot 10^{-5}$	$1.904 \cdot 10^{-5}$
DC-voltage controller proportional gain [A/V ²]	$k_{p,U}$	$4.83 \cdot 10^{-8}$	$4.83 \cdot 10^{-8}$	$4.83 \cdot 10^{-8}$	$4.83 \cdot 10^{-8}$
DC-voltage controller integral gain [A/(V ² s)]	$k_{i,U}$	$2.62 \cdot 10^{-8}$	$2.62 \cdot 10^{-8}$	$2.62 \cdot 10^{-8}$	$2.62 \cdot 10^{-8}$

Table E.1: Controller's parameters for the MMCs #0, #1, #2 and #4.

In Fig. E.11c, the open-loop bode diagrams of the proposed control structures are plotted, which confirm the frequency separation of the inner and the outer control loops and their robust phase margins.

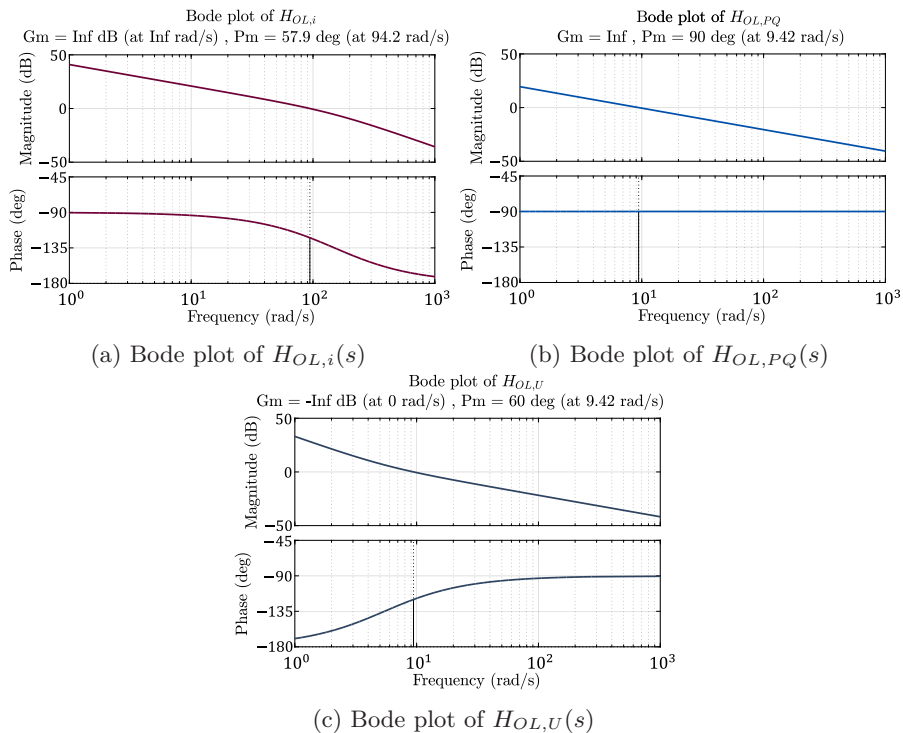


Figure E.11: Open-loop bode diagrams of the proposed control structures considering $F_{SM} = 150$ Hz.

Bibliography

- [1] P. EGROT and R. Coelho-Medeiros. “Convertisseur Alternatif-Continu de Type MMC”. French pat. 3110304. May 18, 2020.
- [2] P. Egrot and R. Coelho-Medeiros. “Convertisseur Alternatif-Continu de Type MMC”. French pat. 2004974. May 18, 2020.
- [3] C. Sulzberger. “Triumph of AC - from Pearl Street to Niagara”. In: *IEEE Power and Energy Magazine* 1.3 (May 2003), pp. 64–67.
- [4] “Triumph of AC. 2. The Battle of the Currents”. In: *IEEE Power and Energy Magazine* 1.4 (July 2003), pp. 70–73.
- [5] W. Long and S. Nilsson. “HVDC Transmission: Yesterday and Today”. In: *IEEE Power and Energy Magazine* 5.2 (Mar. 2007), pp. 22–31.
- [6] N. Iwamuro and T. Laska. “IGBT History, State-of-the-Art, and Future Prospects”. In: *IEEE Transactions on Electron Devices* 64.3 (Mar. 2017), pp. 741–752.
- [7] M. Callavik, P. Lundberg, and O. Hansson. “NORDBLINK Pioneering VSC-HVDC Interconnector between Norway and Germany”. In: (), p. 6.
- [8] *List of HVDC Projects*. Aug. 12, 2021. URL: https://en.wikipedia.org/w/index.php?title=List_of_HVDC_projects&oldid=1038501598 (visited on 08/26/2021).
- [9] *Changji-Guquan UHVDC Link*. URL: <https://www.hitachiabb-powergrids.com/references/hvdc/changji-guquan-uhvdc-link> (visited on 09/13/2021).
- [10] P. L. Francos, S. S. Verdugo, H. F. Álvarez, S. Guyomarch, and J. Loncle. “INELFE — Europe’s first integrated onshore HVDC interconnection”. In: *2012 IEEE Power and Energy Society General Meeting*. 2012, pp. 1–8.
- [11] *Nord Sea Link*. URL: <https://www.hitachiabb-powergrids.com/ch/en/references/hvdc/nsl-link> (visited on 09/27/2021).
- [12] M. P. Bahrman and B. K. Johnson. “The ABCs of HVDC Transmission Technologies”. In: *IEEE Power and Energy Magazine* 5.2 (Mar. 2007), pp. 32–44.
- [13] D. Van Hertem and M. Ghandhari. “Multi-Terminal VSC HVDC for the European Supergrid: Obstacles”. In: *Renewable and Sustainable Energy Reviews* 14.9 (Dec. 1, 2010), pp. 3156–3163.
- [14] D. Jovicic. “Introduction to Line Commutated HVDC”. In: *High Voltage Direct Current Transmission*. John Wiley & Sons, Ltd, 2019, pp. 1–12.

- [15] D. Van Hertem, O. Gomis-Bellmunt, and J. Liang. “Comparison of HVAC and HVDC Technologies”. In: *HVDC Grids: For Offshore and Supergrid of the Future*. IEEE, 2016, pp. 79–96.
- [16] K. Sharifabadi, L. Harnefors, H.-P. Nee, S. Norrnga, and R. Teodorescu. “MMC-HVDC Transmission Technology and MTDC Networks”. In: *Design, Control, and Application of Modular Multilevel Converters for HVDC Transmission Systems*. IEEE, 2016, pp. 336–372.
- [17] D. Van Hertem, O. Gomis-Bellmunt, and J. Liang. “HVDC Grid Layouts”. In: *HVDC Grids: For Offshore and Supergrid of the Future*. IEEE, 2016, pp. 171–191.
- [18] D. Jovicic. “VSC HVDC Applications and Topologies, Performance and Cost Comparison with LCC HVDC”. In: *High Voltage Direct Current Transmission*. John Wiley & Sons, Ltd, 2019, pp. 137–163.
- [19] *Let’s Build a Global Power Grid*. IEEE Spectrum. July 28, 2015. URL: <https://spectrum.ieee.org/lets-build-a-global-power-grid> (visited on 09/13/2021).
- [20] Y. Shu and W. Chen. “Research and Application of UHV Power Transmission in China”. In: *High Voltage 3* (Jan. 2018).
- [21] *China’s State Grid Corp Crushes Power Transmission Records*. IEEE Spectrum. Jan. 10, 2019. URL: <https://spectrum.ieee.org/chinas-state-grid-corp-crushes-power-transmission-records> (visited on 09/13/2021).
- [22] European Commission. Joint Research Centre. Institute for Energy and Transport. *HVDC Submarine Power Cables in the World :State of the Art Knowledge*. 2015. URL: <https://data.europa.eu/doi/10.2790/957356> (visited on 09/13/2021).
- [23] *DolWin3 - TenneT*. URL: <https://www.tennet.eu/our-grid/offshore-projects-germany/dolwin3/> (visited on 09/13/2021).
- [24] European Commission. Directorate-General for Energy. *Energy Roadmap 2050*. 2012.
- [25] IEA. *Net Zero by 2050 - A Roadmap for the Global Energy Sector*. 2021.
- [26] IRENA. *Global Energy Transformation: A Roadmap to 2050*. 2019.
- [27] D. Van Hertem, O. Gomis-Bellmunt, and J. Liang. “Energy Scenarios: Projections on Europes Future Generation and Load”. In: *HVDC Grids: For Offshore and Supergrid of the Future*. IEEE, 2016, pp. 25–42.
- [28] ENTSO-E. *Ten-Year Network Development Plan 2020*. Aug. 15, 2021.
- [29] ENTSO-E. *HVDC Links in System Operations*. Dec. 2, 2019.
- [30] D. Van Hertem, O. Gomis-Bellmunt, and J. Liang. “Drivers for the Development of HVDC Grids”. In: *HVDC Grids: For Offshore and Supergrid of the Future*. IEEE, 2016, pp. 3–24.

- [31] E. Pierri, O. Binder, N. G. A. Hemdan, and M. Kurrat. “Challenges and Opportunities for a European HVDC Grid”. In: *Renewable and Sustainable Energy Reviews* 70 (Apr. 1, 2017), pp. 427–456.
- [32] J. A. Ansari, C. Liu, and S. A. Khan. “MMC Based MTDC Grids: A Detailed Review on Issues and Challenges for Operation, Control and Protection Schemes”. In: *IEEE Access* 8 (2020), pp. 168154–168165.
- [33] D. Gómez A., J. D. Páez, M. Cheah-Mane, J. Maneiro, P. Dworakowski, O. Gomis-Bellmunt, and F. Morel. “Requirements for Interconnection of HVDC Links with DC-DC Converters”. In: *IECON 2019 - 45th Annual Conference of the IEEE Industrial Electronics Society*. IECON 2019 - 45th Annual Conference of the IEEE Industrial Electronics Society. Vol. 1. Oct. 2019, pp. 4854–4860.
- [34] F. Wang, L. Bertling, A. T. Le, A. Mannikoff, and J. Blennow. “An Overview Introduction of VSC-HVDC: State-of-Art and Potential Applications in Electric Power Systems”. In: *Cigrè International Symposium, Bologna, Italy, Sept. 2011*. (2011).
- [35] B. Abrahamsson. “Estlink HVDC Light in 19 Months”. In: *2007 IET Power Convention*. 2007 IET Power Convention. Sept. 2007, pp. 1–34.
- [36] *Cross Sound Cable | Hitachi Energy*. URL: <https://www.hitachienergy.com/references/hvdc/cross-sound-cable> (visited on 01/04/2022).
- [37] K. Sharifabadi, L. Harnefors, H.-P. Nee, S. Norrga, and R. Teodorescu. “Introduction to Modular Multilevel Converters”. In: *Design, Control, and Application of Modular Multilevel Converters for HVDC Transmission Systems*. IEEE, 2016, pp. 7–59.
- [38] R. Marquardt. “Stromrichterschaltungen mit verteilten Energiespeichern”. German pat. 10103031A1. Rainer Marquardt. July 25, 2002.
- [39] R. Marquardt. “Modular Multilevel Converters: State of the Art and Future Progress”. In: *IEEE Power Electronics Magazine* 5.4 (Dec. 2018), pp. 24–31.
- [40] L. G. Franquelo, J. Rodriguez, J. I. Leon, S. Kouro, R. Portillo, and M. A. Prats. “The Age of Multilevel Converters Arrives”. In: *IEEE Industrial Electronics Magazine* 2.2 (June 2008), pp. 28–39.
- [41] A. Marquez, J. I. Leon, S. Vazquez, L. G. Franquelo, and M. Perez. “A Comprehensive Comparison of Modulation Methods for MMC Converters”. In: *IECON 2017 - 43rd Annual Conference of the IEEE Industrial Electronics Society*. IECON 2017 - 43rd Annual Conference of the IEEE Industrial Electronics Society. Oct. 2017, pp. 4459–4464.
- [42] J.-M. Lee, J.-W. Park, D.-W. Kang, J.-P. Lee, D.-W. Yoo, and J.-M. Lee. “Comparison of Capacitor Voltage Balancing Methods for 1GW MMC-HVDC Based on Real-Time Digital Simulator and Physical Control Systems”. In: *Journal of Power Electronics* 19.5 (2019), pp. 1171–1181.

- [43] M. Moranchel, E. J. Bueno, F. J. Rodriguez, and I. Sanz. “Implementation of Nearest Level Modulation for Modular Multilevel Converter”. In: *2015 IEEE 6th International Symposium on Power Electronics for Distributed Generation Systems (PEDG)*. 2015 IEEE 6th International Symposium on Power Electronics for Distributed Generation Systems (PEDG). June 2015, pp. 1–5.
- [44] H. Pereira, V. Mendes, L. Harnefors, and R. Teodorescu. “Comparison of 2L-VSC and MMC-Based HVDC Converters: Grid Frequency Support Considering Reduced Wind Power Plants Models”. In: *Electric Power Components and Systems* (Feb. 1, 2018), pp. 1–10.
- [45] W. Leterme, I. Jahn, P. Ruffing, K. Sharifabadi, and D. Van Hertem. “Designing for High-Voltage Dc Grid Protection: Fault Clearing Strategies and Protection Algorithms”. In: *IEEE Power and Energy Magazine* 17.3 (May 2019), pp. 73–81.
- [46] *Protection and Local Control of HVDC-grids*. e-cigre. Aug. 20, 2018. URL: <https://e-cigre.org/publication/739-protection-and-local-control-of-hvdc-grids> (visited on 01/04/2022).
- [47] D. Jovicic, G. Tang, and H. Pang. “Adopting Circuit Breakers for High-Voltage Dc Networks: Appropriating the Vast Advantages of Dc Transmission Grids”. In: *IEEE Power and Energy Magazine* 17.3 (May 2019), pp. 82–93.
- [48] G. Konstantinou, J. Zhang, S. Ceballos, J. Pou, and V. G. Agelidis. “Comparison and Evaluation of Sub-Module Configurations in Modular Multilevel Converters”. In: *2015 IEEE 11th International Conference on Power Electronics and Drive Systems*. 2015 IEEE 11th International Conference on Power Electronics and Drive Systems. June 2015, pp. 958–963.
- [49] *Guide for Electromagnetic Transient Studies Involving VSC Converters*. e-cigre. Apr. 16, 2021. URL: <https://e-cigre.org/publication/832-guide-for-electromagnetic-transient-studies-involving-vsc-converters> (visited on 12/07/2021).
- [50] *HVDC PLUS Brochure*.
- [51] N. Evans, P. Dworakowski, M. Al-Kharaz, S. Hegde, E. Perez, and F. Morel. “Cost-Performance Framework for the Assessment of Modular Multilevel Converter in HVDC Transmission Applications”. In: *IECON 2019 - 45th Annual Conference of the IEEE Industrial Electronics Society*. IECON 2019 - 45th Annual Conference of the IEEE Industrial Electronics Society. Lisbon, Portugal: IEEE, Oct. 2019, pp. 4793–4798.
- [52] H. Saad, S. Dennetière, J. Mahseredjian, P. Delarue, X. Guillaud, J. Peralta, and S. Nguéfeu. “Modular Multilevel Converter Models for Electromagnetic Transients”. In: *IEEE Transactions on Power Delivery* 29.3 (June 2014), pp. 1481–1489.

- [53] J. Peralta, H. Saad, S. Denetiere, J. Mahseredjian, and S. Nguefeu. “Detailed and Averaged Models for a 401-Level MMC–HVDC System”. In: *IEEE Transactions on Power Delivery* 27.3 (July 2012), pp. 1501–1508.
- [54] H. Saad, J. Peralta, S. Denetière, J. Mahseredjian, J. Jatskevich, J. A. Martinez, A. Davoudi, M. Saeedifard, V. Sood, X. Wang, J. Cano, and A. Mehrizi-Sani. “Dynamic Averaged and Simplified Models for MMC-Based HVDC Transmission Systems”. In: *IEEE Transactions on Power Delivery* 28.3 (July 2013), pp. 1723–1730.
- [55] K. Shinoda, J. Freytes, A. Benchaib, J. Dai, H. Saad, and X. Guillaud. “Energy Difference Controllers for MMC without DC Current Perturbations”. In: Oct. 25, 2016.
- [56] B. Džonlaga, L. Quéval, and J.-C. Vannier. “Impact of the Arm Resistance and Inductance on the PQ Diagram of a Modular Multilevel Converter”. In: *2019 20th International Symposium on Power Electronics (Ee)*. 2019 20th International Symposium on Power Electronics (Ee). Oct. 2019, pp. 1–6.
- [57] D. Jovic and A. A. Jamshidifar. “MMC Converter Detailed Phasor Model Including Second Harmonic”. In: *IEEE PES Innovative Smart Grid Technologies, Europe*. IEEE PES Innovative Smart Grid Technologies, Europe. Oct. 2014, pp. 1–5.
- [58] G. Bergna-Diaz, J. Freytes, X. Guillaud, S. D’Arco, and J. A. Suul. “Generalized Voltage-Based State-Space Modeling of Modular Multilevel Converters With Constant Equilibrium in Steady State”. In: *IEEE Journal of Emerging and Selected Topics in Power Electronics* 6.2 (June 2018), pp. 707–725.
- [59] J. Lyu, X. Zhang, X. Cai, and M. Molinas. “Harmonic State-Space Based Small-Signal Impedance Modeling of a Modular Multilevel Converter With Consideration of Internal Harmonic Dynamics”. In: *IEEE Transactions on Power Electronics* 34.3 (Mar. 2019), pp. 2134–2148.
- [60] Z. Xu, B. Li, S. Wang, S. Zhang, and D. Xu. “Generalized Single-Phase Harmonic State Space Modeling of the Modular Multilevel Converter With Zero-Sequence Voltage Compensation”. In: *IEEE Transactions on Industrial Electronics* 66.8 (Aug. 2019), pp. 6416–6426.
- [61] P. De Rua and J. Beerten. “Generalization of Harmonic State-Space Framework to Delayed Periodic Systems for Stability Analysis of the Modular Multilevel Converter”. In: *IEEE Transactions on Power Delivery* (2021), pp. 1–1.

- [62] R. Coelho-Medeiros, B. Džonlaga, J.-C. Vannier, J. Dai, L. Queval, and P. Egrot. “A Comparison between Different Models of the Modular Multilevel Converter”. In: *2020 22nd European Conference on Power Electronics and Applications (EPE'20 ECCE Europe)*. 2020 22nd European Conference on Power Electronics and Applications (EPE'20 ECCE Europe). Sept. 2020, P.1–P.10.
- [63] Q. Chen, J. Lyu, R. Li, and X. Cai. “Impedance Modeling of Modular Multilevel Converter Based on Harmonic State Space”. In: *2016 IEEE 17th Workshop on Control and Modeling for Power Electronics (COMPEL)*. 2016 IEEE 17th Workshop on Control and Modeling for Power Electronics (COMPEL). June 2016, pp. 1–5.
- [64] J. Lyu, X. Zhang, Z. Ma, and X. Cai. “A Novel DC-Side-Port Impedance Modeling of Modular Multilevel Converters Based on Harmonic State Space Method”. In: *2018 International Power Electronics Conference (IPEC-Niigata 2018 -ECCE Asia)*. 2018 International Power Electronics Conference (IPEC-Niigata 2018 -ECCE Asia). May 2018, pp. 4162–4167.
- [65] Z. Xu, B. Li, L. Han, J. Hu, S. Wang, S. Zhang, and D. Xu. “A Complete HSS-Based Impedance Model of MMC Considering Grid Impedance Coupling”. In: *IEEE Transactions on Power Electronics* 35.12 (Dec. 2020), pp. 12929–12948.
- [66] H. Zong, C. Zhang, J. Lyu, X. Cai, M. Molinas, and F. Rao. “Generalized MIMO Sequence Impedance Modeling and Stability Analysis of MMC-HVDC With Wind Farm Considering Frequency Couplings”. In: *IEEE Access* 8 (2020), pp. 55602–55618.
- [67] G. B. Diaz. “Modular Multilevel Converter Control for HVDC Operation : Optimal Shaping of the Circulating Current Signal for Internal Energy Regulation”. PhD thesis. CentraleSupélec ; Norwegian University of Science and Technology (Trondheim, Norvège), July 3, 2015.
- [68] L. F. Chaparro and A. Akan. “Chapter 11 - Discrete Fourier Analysis”. In: *Signals and Systems Using MATLAB (Third Edition)*. Ed. by L. F. Chaparro and A. Akan. Academic Press, Jan. 1, 2019, pp. 637–720.
- [69] K. Sharifabadi, L. Harnefors, H.-P. Nee, S. Norrga, and R. Teodorescu. “Main-Circuit Design”. In: *Design, Control, and Application of Modular Multilevel Converters for HVDC Transmission Systems*. IEEE, 2016, pp. 60–132.
- [70] M. Zygmanowski, B. Grzesik, and R. Nalepa. “Capacitance and Inductance Selection of the Modular Multilevel Converter”. In: *2013 15th European Conference on Power Electronics and Applications (EPE)*. 2013 15th European Conference on Power Electronics and Applications (EPE). Sept. 2013, pp. 1–10.

- [71] D. Jovcic and A. A. Jamshidifar. “MMC Converter Detailed Phasor Model Including Second Harmonic”. In: *IEEE PES Innovative Smart Grid Technologies, Europe*. IEEE PES Innovative Smart Grid Technologies, Europe. Oct. 2014, pp. 1–5.
- [72] A. Marzoughi, R. Burgos, D. Boroyevich, and Y. Xue. “Investigation and Design of Modular Multilevel Converter in AFE Mode with Minimized Passive Elements”. In: Sept. 20, 2015.
- [73] A. O. Arslan, M. Kurtoglu, F. Eroglu, and A. M. Vural. “Optimal Selection of Arm Inductance and Switching Modulation for Three-Phase Modular Multilevel Converters in Terms of DC Voltage Utilization, Harmonics and Efficiency”. In: *Journal of Power Electronics* 19.4 (2019), pp. 922–933.
- [74] B. Džonlaga. “Contribution to the Sizing of the Modular Multilevel Converter”. These de doctorat. Université Paris-Saclay (ComUE), Sept. 25, 2019.
- [75] A. F. Christe. “Galvanically Isolated Modular Converter”. Lausanne: EPFL, 2018. 194 pp.
- [76] D. G. Holmes and T. A. Lipo. “Harmonic Distortion”. In: *Pulse Width Modulation for Power Converters: Principles and Practice*. IEEE, 2003, pp. 57–94.
- [77] H. Saad, S. Denetière, and J. Mahseredjian. “On Modelling of MMC in EMT-Type Program”. In: *2016 IEEE 17th Workshop on Control and Modeling for Power Electronics (COMPEL)*. 2016 IEEE 17th Workshop on Control and Modeling for Power Electronics (COMPEL). June 2016, pp. 1–7.
- [78] W. R. Leon Garcia, P. Tixador, B. Raison, A. Bertinato, B. Luscan, and C. Creusot. “Technical and Economic Analysis of the R-Type SFCL for HVDC Grids Protection”. In: *IEEE Transactions on Applied Superconductivity* 27.7 (Oct. 2017), pp. 1–9.
- [79] M. W. Rupich. “4 - Second-Generation (2G) Coated High-Temperature Superconducting Cables and Wires for Power Grid Applications”. In: *Superconductors in the Power Grid*. Ed. by C. Rey. Woodhead Publishing Series in Energy. Woodhead Publishing, Jan. 1, 2015, pp. 97–130.
- [80] IEC61788-3. *DC Critical Current of Ag- and/or Ag Alloy-Sheathed Bi-2212 and Bi-2223 Oxide*. 2006.
- [81] IEC61788-26:2020. *Superconductivity - Part 26: Critical Current Measurement - DC Critical Current of RE-Ba-Cu-O Composite Superconductors*. 2020.

- [82] J. J. Pérez-Chávez, F. Trillaud, L. M. Castro, L. Quéval, A. Polasek, and R. de Andrade Junior. “Generic Model of Three-Phase (RE)BCO Resistive Superconducting Fault Current Limiters for Transient Analysis of Power Systems”. In: *IEEE Transactions on Applied Superconductivity* 29.6 (Sept. 2019), pp. 1–11.
- [83] J. Kozak, M. Majka, T. Janowski, S. Kozak, G. Wojtasiewicz, and B. Kondratowicz-Kucewicz. “Tests and Performance Analysis of Coreless Inductive HTS Fault Current Limiters”. In: *IEEE Transactions on Applied Superconductivity* 21.3 (June 2011), pp. 1303–1306.
- [84] N. Strickland. “A High-Temperature Superconducting (HTS) Wire Critical Current Database”. In: (Oct. 29, 2021).
- [85] Y. B. Kim, C. F. Hempstead, and A. R. Strnad. “Critical Persistent Currents in Hard Superconductors”. In: *Physical Review Letters* 9.7 (Oct. 1, 1962), pp. 306–309.
- [86] D. van der Laan, H. van Eck, B. ten Haken, J. Schwartz, and H. ten Kate. “Temperature and Magnetic Field Dependence of the Critical Current of Bi/Sub 2/Sr/Sub 2/Ca/Sub 2/Cu/Sub 3/O/Sub x/ Tape Conductors”. In: *IEEE Transactions on Applied Superconductivity* 11.1 (Mar. 2001), pp. 3345–3348.
- [87] M. Zhang, J.-H. Kim, S. Pamidi, M. Chudy, W. Yuan, and T. A. Coombs. “Study of Second Generation, High-Temperature Superconducting Coils: Determination of Critical Current”. In: *Journal of Applied Physics* 111.8 (Apr. 15, 2012), p. 083902.
- [88] L. Quéval, V. Zermeno, and F. Grilli. “Numerical Models for Ac Loss Calculation in Large-Scale Applications of HTS Coated Conductors”. In: *Superconductor Science and Technology* 29.2 (Feb. 2016).
- [89] Y.-H. Kim, S.-K. Lee, H.-M. Jang, Y.-W. Kim, K.-T. Lee, C.-Y. Choi, C.-H. Ryu, H.-J. Kim, S.-D. Hwang, H.-S. Yang, S.-H. Sohn, and J.-H. Lim. “The Application of the Cryogenic System on the HTS Power Cable Circuit in Actual Grid”. In: *Cryogenics. Special Issue: ACASC 2011* 52.12 (Dec. 1, 2012), pp. 661–666.
- [90] M. Green. “The Cost of Coolers for Cooling Superconducting Devices at Temperatures at 4.2 K, 20 K, 40 K and 77 K”. In: *IOP Conference Series: Materials Science and Engineering* 101 (Dec. 18, 2015), p. 012001.
- [91] P. Zhou, G. Ma, and L. Quéval. “Transition Frequency of Transport Ac Losses in High Temperature Superconducting Coated Conductors”. In: *Journal of Applied Physics* 126.6 (Aug. 14, 2019), p. 063901.
- [92] W. T. B. de Sousa. “Transient Simulations of Superconducting Fault Current Limiters”. Rio de Janeiro: Universidade Federal do Rio de Janeiro, 2015.

- [93] E. Pardo, J. Souc, and J. Kovac. “AC Loss in ReBCO Pancake Coils and Stacks of Them: Modelling and Measurement”. In: *Superconductor Science & Technology* 25 (Sept. 12, 2011).
- [94] B. Shen, F. Grilli, and T. Coombs. “Review of the AC Loss Computation for HTS Using the H-Formulation”. In: *Superconductor Science and Technology* 33.3 (Mar. 1, 2020), p. 033002. arXiv: 1908.02176.
- [95] H. Merte and J. A. Clark. “Boiling Heat-Transfer Data for Liquid Nitrogen at Standard and Near-Zero Gravity”. In: *Advances in Cryogenic Engineering*. Ed. by K. D. Timmerhaus. Advances in Cryogenic Engineering. Boston, MA: Springer US, 1962, pp. 546–550.
- [96] “Introduction to DC Grids”. In: *High Voltage Direct Current Transmission*. John Wiley & Sons, Ltd, 2019, pp. 371–377.
- [97] N. Stanković, M. J. Jiménez Carrizosa, A. Arzandé, P. Egrot, and J.-C. Vannier. “An HVDC Experimental Platform with MMC and Two-Level VSC in the Back-to-Back Configuration”. In: *2016 IEEE 25th International Symposium on Industrial Electronics (ISIE)*. 2016 IEEE 25th International Symposium on Industrial Electronics (ISIE). June 2016, pp. 436–441.
- [98] L. Quéval, O. Despouys, F. Trillaud, and B. Douine. “Feasibility Study of a Superconducting Power Filter for HVDC Grids”. In: *2020 22nd European Conference on Power Electronics and Applications (EPE'20 ECCE Europe)*. 2020 22nd European Conference on Power Electronics and Applications (EPE'20 ECCE Europe). Sept. 2020, P.1–P.7.
- [99] S. Fawaz, H. Menana, B. Douine, and L. Queval. “DC Modeling and Characterization of HTS Coils with Non Uniform Current Density Distribution”. In: *Superconductor Science and Technology* 34.12 (Nov. 2021), p. 124001.
- [100] P. Tixador. “Development of Superconducting Power Devices in Europe”. In: *Physica C: Superconductivity and its Applications*. Proceedings of the 22nd International Symposium on Superconductivity (ISS 2009) 470.20 (Nov. 1, 2010), pp. 971–979.
- [101] A. Hobl, S. Krämer, S. Elschner, C. Jänke, J. Bock, and J. Schramm. “Superconducting Fault Current Limiters — A New Tool for the “Grid of the Future””. In: *CIREN 2012 Workshop: Integration of Renewables into the Distribution Grid*. CIREN 2012 Workshop: Integration of Renewables into the Distribution Grid. May 2012, pp. 1–4.
- [102] H.-P. Kraemer, W. Schmidt, H. Cai, B. Gamble, D. Madura, T. MacDonald, J. McNamara, W. Romanosky, G. Snitchler, N. Lallouet, F. Schmidt, and S. Ahmed. “Superconducting Fault Current Limiter for Transmission Voltage”. In: *Physics Procedia* 36 (2012), pp. 921–926.

- [103] M. Moyzykh, D. Gorbunova, P. Ustyuzhanin, D. Sotnikov, K. Baburin, A. Maklakov, E. Magommedov, A. Shumkov, A. Telnova, V. Shcherbakov, D. Kumarov, L. Sabirov, M. Medovik, A. Kadyrbaev, S. Alexandrov, I. Mikoyan, S. Samoilenkov, and A. Vavilov. “First Russian 220 kV Superconducting Fault Current Limiter (SFCL) For Application in City Grid”. In: *IEEE Transactions on Applied Superconductivity* 31.5 (Aug. 2021), pp. 1–7.
- [104] G. Teschl. *Ordinary differential equations and dynamical systems*. Jan. 2008.
- [105] B. Lathi and R. Green. *Linear Systems and Signals*. The Oxford Series in Electrical and Computer Engineering. Oxford University Press, 2018.
- [106] N. Wereley. *Analysis and control of linear periodically time varying systems*. Massachusetts, United States of America, Jan. 1990.
- [107] C. R. Paul. “The Concept of Loop Inductance”. In: *Inductance: Loop and Partial*. IEEE, 2010, pp. 117–194.
- [108] D. Pattabiraman, R. H. Lasseter., and T. M. Jahns. “Comparison of Grid Following and Grid Forming Control for a High Inverter Penetration Power System”. In: *2018 IEEE Power Energy Society General Meeting (PESGM)*. 2018 IEEE Power Energy Society General Meeting (PESGM). Aug. 2018, pp. 1–5.
- [109] J. Freytes, P. Rault, F. Gruson, F. Colas, and X. Guillaud. “Dynamic Impact of MMC Controllers on DC Voltage Droop Controlled MTDC Grids”. In: *2016 18th European Conference on Power Electronics and Applications (EPE'16 ECCE Europe)*. 2016 18th European Conference on Power Electronics and Applications (EPE'16 ECCE Europe). Sept. 2016, pp. 1–10.
- [110] R. Ofir, U. Markovic, P. Aristidou, and G. Hug. “Droop vs. Virtual Inertia: Comparison from the Perspective of Converter Operation Mode”. In: *2018 IEEE International Energy Conference (ENERGYCON)*. 2018 IEEE International Energy Conference (ENERGYCON). June 2018, pp. 1–6.
- [111] K. Sharifabadi, L. Harnefors, H.-P. Nee, S. Norrga, and R. Teodorescu. “Dynamics and Control”. In: *Design, Control, and Application of Modular Multilevel Converters for HVDC Transmission Systems*. IEEE, 2016, pp. 133–213.
- [112] S. D’Arco, G. Guidi, and J. A. Suul. “Operation of a Modular Multilevel Converter Controlled as a Virtual Synchronous Machine”. In: *2018 International Power Electronics Conference (IPEC-Niigata 2018 -ECCE Asia)*. 2018 International Power Electronics Conference (IPEC-Niigata 2018 -ECCE Asia). May 2018, pp. 782–789.

- [113] H. Saad, X. Guillaud, J. Mahseredjian, S. Denetière, and S. Nguéfeu. “MMC Capacitor Voltage Decoupling and Balancing Controls”. In: *IEEE Transactions on Power Delivery* 30.2 (Apr. 2015), pp. 704–712.
- [114] G. Bergna, J. A. Suul, E. Berne, P. Egrot, J.-C. Vannier, and M. Molinas. “Analysis of Modular Multilevel Converters under Unbalanced Grid Conditions with Different Load Current Control Strategies and Lagrange-Based Differential Current Control”. In: *2013 1st International Future Energy Electronics Conference (IFEEC)*. 2013 1st International Future Energy Electronics Conference (IFEEC). Nov. 2013, pp. 669–674.
- [115] A. Yazdani and R. Iravani. “Grid-Imposed Frequency VSC System: Control in dq-Frame”. In: *Voltage-Sourced Converters in Power Systems: Modeling, Control, and Applications*. IEEE, 2010, pp. 204–244.
- [116] S. D’Arco, J. A. Suul, and O. B. Fosso. “Automatic Tuning of Cascaded Controllers for Power Converters Using Eigenvalue Parametric Sensitivities”. In: *IEEE Transactions on Industry Applications* 51.2 (Mar. 2015), pp. 1743–1753.
- [117] L. Quéval and H. Ohsaki. “Back-to-Back Converter Design and Control for Synchronous Generator-Based Wind Turbines”. In: *2012 International Conference on Renewable Energy Research and Applications (ICRERA)*. 2012 International Conference on Renewable Energy Research and Applications (ICRERA). Nov. 2012, pp. 1–6.

Titre : Cryo-MMC : un convertisseur modulaire multiniveau avec des bobines de bras supraconductrices couplées

Mots clés : Haute tension courant continu, convertisseur modulaire multiniveau, bobines supraconductrices à haute température.

Résumé : Dans cette thèse, nous étudions un convertisseur modulaire multiniveau (MMC) avec des bobines de bras supraconductrices couplées. Cette topologie est appelée « cryo-MMC ». Nous dimensionnons des bobines supraconductrices en couplage direct utilisant des rubans supraconducteurs à haute température critique (HTS) et leur système de refroidissement. L'application considérée est un lien haute tension courant continu à ± 320 kV et 1 GW. Nous évaluons numériquement les performances en régime permanent et transitoire du cryo-MMC, qui permettent de confirmer sa stabilité thermique et électrique. En particulier, lors d'un défaut DC pôle-à-pôle, les bobines supraconductrices réduisent les courants DC et AC

par un facteur cinq. D'un point de vue technico-économique, le cryo-MMC est jugé viable

Le concept proposé réduit la masse des bobines de bras d'un facteur de quatre et divise leur empreinte au sol par un facteur de 1,6 par rapport au cas de référence, ce qui est particulièrement intéressant pour les applications embarquées en mer. Finalement sa capacité de limiter les courants de défaut peut simplifier la protection des futurs réseaux HVDC. Nous présentons la toute première preuve expérimentale de ce concept avec un cryo-MMC à 5 niveaux et détaillons le dimensionnement, la réalisation et la caractérisation en régime permanent de ce prototype.

Title : Cryo-MMC : a Modular Multilevel Converter with Superconducting Coupled Arm Coils

Keywords : High-voltage direct current, modular multilevel converter, high-temperature superconducting coils.

Abstract : In this thesis, we study a Modular Multilevel Converter (MMC) with high temperature superconducting (HTS) coupled arm coils. This topology is called "cryo-MMC". We design directly-coupled HTS arm coils wound with HTS conductors and their cooling system. The considered application is a point-to-point high-voltage direct-current (HVDC) link rated at ± 320 kV and 1 GW. We numerically assess the steady-state and transient performance of the cryo-MMC, which confirms its thermal and electrical stability. The HTS arm coils reduce the DC and AC prospective fault currents by a factor of five during a pole-to-

pole DC fault.

From a techno-economic point of view, the cryo-MMC is deemed feasible, This topology reduces the arm coils mass by a factor of four while reducing their footprint by a factor of 1.6 compared to a reference case, which is particularly advantageous for offshore applications. Finally, its fault-current limitation capability could simplify the protection of future HVDC grids. We propose the first experimental proof of this concept with a 5-level cryo-MMC. We detail its design, construction and report the steady-st